Titre: Title:	Development of Electrodeposited Nickel-Tungsten Composite Materials with Effective Additives for Tribological and Corrosion Resistance Applications
Auteur: Author:	Mina Dadvand
Date:	2022
Type:	Mémoire ou thèse / Dissertation or Thesis
Référence: Citation:	Dadvand, M. (2022). Development of Electrodeposited Nickel-Tungsten Composite Materials with Effective Additives for Tribological and Corrosion Resistance Applications [Ph.D. thesis, Polytechnique Montréal]. PolyPublie. https://publications.polymtl.ca/10565/

POLYTECHNIQUE MONTRÉAL

affiliée à l'Université de Montréal

Development of Electrodeposited Nickel-Tungsten Composite Materials with Effective Additives for Tribological and Corrosion Resistance Applications

MINA DADVAND

Département de génie chimique

Thèse présentée en vue de l'obtention du diplôme de *Philosophiae Doctor*

Génie des matériaux

Septembre 2022

POLYTECHNIQUE MONTRÉAL

affiliée à l'Université de Montréal

Cette thèse intitulée :

Development of Electrodeposited Nickel-Tungsten Composite Materials with Effective Additives for Tribological and Corrosion Resistance Applications

présentée par **Mina DADVAND**

en vue de l'obtention du diplôme de *Philosophiae Doctor*

a été dûment acceptée par le jury d'examen constitué de :

L'Hocine YAHIA, président
Oumarou SAVADOGO, membre et directeur de recherche
Jamal CHAOUKI, membre
Joshua C. BYERS, membre externe

DEDICATION

This thesis is dedicated to my parents
for their love, support, and encouragement

ACKNOWLEDGEMENTS

I thank Professor Oumarou Savadogo for the opportunity to study for my Ph.D. under his supervision. Working under his supervision has been very enjoyable and I have learned new things and grown a lot. He encouraged me to be confident, independent, and responsible.

I also thank all my colleagues, including our research associate Kentaro Oishi for their suggestions and comments on my work.

Lastly, I thank my parents for all their love and encouragement, without whom I would never have enjoyed so many opportunities.

RÉSUMÉ

Le développement de revêtements à haute performance contre l'usure et la corrosion est très important pour économiser de l'énergie dans de nombreuses applications industrielles, prolonger la durée de vie de divers composants d'ingénierie et également pour protéger les pièces contre diverses défaillances telles que l'usure, la corrosion, l'oxydation et la fatigue sous une grande variété de circonstances.

Parmi les différentes techniques de fabrication de revêtements telles que le dépôt chimique en phase vapeur (CVD), le dépôt physique en phase vapeur (PVD) et l'électrodéposition, cette dernière a été largement acceptée pour l'ingénierie de la surface. En effet, celle–ci confère des propriétés d'usure et de corrosion souhaitables en raison de sa moindre complexité et de son coût relativement faible. . L'avantage unique de la technique d'électrodéposition par rapport aux autres méthodes de fabrication est une meilleure liaison interfaciale entre le matériau de revêtement et le substrat, et un contrôle précis de l'épaisseur et de la composition chimique des revêtements en modifiant de manière appropriée les paramètres de dépôt tels que le potentiel ou le courant.

Le chrome électrodéposé, en particulier le chrome dur (HCr), a été utilisé dans diverses industries telles que l'automobile, l'aérospatiale et les industries minières en raison de son excellente dureté, de ses performances d'usure, de ses propriétés anticorrosion et de son faible coefficient de frottement. Cependant, pendant le processus d'électrodéposition, de la fumée de chrome hexavalent (Cr^{6+}) est générée, qui est extrêmement toxique et dangereuse pour l'environnement. Le tungstène–nickel électrodéposé (NiW), au contraire, s'est avéré être le meilleur remplacement possible des revêtements HCr existants en raison de ses performances exceptionnelles en matière de dureté, de corrosion et d'usure.

Ces dernières années, les composites à matrice métallique (MMC) avec d'excellentes performances, ont été largement utilisés dans les applications aérospatiales, automobiles et électroniques. Il convient également de mentionner que l'incorporation de particules céramiques insolubles (telles que le carbure de silicium (SiC), le dioxyde de cérium (CeO_2) et le nitrure de bore hexagonal (hBN) dans la matrice NiW pourrait encore améliorer les performances mécaniques, tribologiques et de corrosion du Revêtements NiW en raison de la dureté extrêmement élevée du SiC, du très faible coefficient de frottement du hBN, ainsi que des propriétés anticorrosion du SiC, du CeO_2 et du hBN.

Dans ce travail de recherche, un processus d'électrodéposition spécial utilisant une forme d'onde de courant inverse pulsé (PRC) bien conçue, et une chimie de bain spécialement formulée, a été utilisée pour produire un revêtement nano–structuré de nickel–tungstène (NiW). Le matériau résultant doit démontrer des performances de corrosion et de tribologie exceptionnelles par rapport au NiW classique électro–déposé en courant continu à partir de bains de dépôt contenant des ingrédients similaires, notamment une source d'ions nickel, un agent complexant, un réducteur de contrainte, un azurant, un affineur de grain, et un agent mouillant. Le NiW déposé par DC, présentait une structure de phase amorphe dominante, tandis que le NiW déposé à partir de la même chimie de bain, mais en utilisant la forme d'onde PRC a démontré une structure principalement cristalline avec de meilleures performances de corrosion et de tribologie.

De plus, des charges céramiques, comprenant des particules d'oxyde de cérium (CeO_2), de carbure de silicium (SiC) et de nitrure de bore hexagonal (hBN) ont été ajoutées dans la chimie du bain NiW pour produire des composites de NiW–CeO_2, NiW–SiC, NiW–hBN, NiW–SiC–CeO_2 et NiW–SiC–hBN par des procédés d'électrodéposition DC. De plus, la microstructure, la corrosion et les performances tribologiques des composites NiW–SiC, NiW–CeO_2 et NiW–SiC–CeO_2 électro–déposés par PRC ont été comparées à celles de la forme d'onde CC. L'ajout de SiC, CeO_2 et hBN sur l'amélioration de la corrosion et des performances tribologiques de NiW a été déterminé. Différents tests de corrosion électrochimique, notamment des tests de polarisation potentio–dynamique (PP) et de polarisation potentio–dynamique cyclique (CPP), ont été utilisés pour évaluer les performances de corrosion des dépôts. La spectrométrie de masse des ions secondaires à temps de vol (TOF–SIMS) et la spectroscopie photo électronique à rayons X (XPS) ont été utilisées pour étudier les divers produits de corrosion sur les dépôts. La diffraction des rayons X (XRD) et la microscopie électronique à transmission (TEM) ont été employées pour analyser la structure granulaire des revêtements. De plus, les propriétés tribologiques, y compris la dureté et la résistance à l'usure des dépôts, ont été étudiées.

ABSTRACT

The development of high wear and corrosion performance coatings is very crucial to save energy in many industrial applications, extend the lifetimes of various engineering components, and also to protect the parts against various failures such as wear, corrosion, oxidation, and fatigue under a wide variety of circumstances.

Among the different coating fabrication techniques such as chemical vapor deposition (CVD), physical vapor deposition (PVD), and electrodeposition, the latter has received widespread acceptance for engineering the surface to impart desirable wear and corrosion properties owing to its less complexity and relatively low cost. The unique advantage of the electrodeposition technique over the other fabrication methods is improved interfacial bonding between the coating material–substrate and precise controlling of the thickness and chemical composition of the coatings by suitably altering the deposition parameters such as potential or current.

Electrodeposited chromium, especially hard chrome (HCr) has been used in various industries such as automobile, aerospace, and mining industries due to its excellent hardness, wear performance, anticorrosion properties, and low coefficient of friction. However, during the electrodeposition process, hexavalent chromium (Cr^{6+}) fumes are generated which are extremely toxic and hazardous to the environment. The electrodeposited nickel tungsten (NiW), on the contrary, was found to be the best possible replacement for the existing HCr coatings due to its outstanding hardness, corrosion, and wear performance.

In recent years, metal matrix composites (MMCs) with excellent performance, have been widely used in aerospace, automotive, and electronics, applications. It is also noteworthy to mention that the incorporation of insoluble ceramic particulates (such as silicon carbide (SiC), cerium dioxide (CeO_2), and hexagonal boron nitride (hBN)) into NiW matrix could further improve the mechanical, tribological, and corrosion performance of the NiW coatings owing to the extremely high hardness of SiC, the very low friction coefficient of hBN, along with anticorrosion properties of SiC, CeO_2, and hBN.

In this research work, a special electrodeposition process utilizing a well–designed pulsed reverse current (PRC) waveform and specially formulated bath chemistry was used to produce a nanostructured coating of nickel–tungsten (NiW). The word “special electroplating process “refers to a customized process including:

1) Using defined ingredients (types and concentrations) to make up the electroplating bath solution. The ingredients included the followings:
    - A source of metallic ions to be deposited (Ni and W) through the addition of their appropriate salts for example; nickel sulfate and sodium tungstate
    - An appropriate stress reducer to minimize the residual stress within the deposited material. The well-known stress reducers used in overall nickel-plating processes are based on benzothiazole derivatives. For this work, low-cost and commercially available sodium salt of 6,2-benzothiazol-1,1,3-trione known as sodium saccharin was selected.
    - An appropriate surfactant to provide a complete wetting of substrate and to eliminate pores formation resulting from hydrogen bubbles adsorption onto the substrate surface. There is a variety of such surfactants available on the market. The selection of surfactant type for this work was based on solubility in the plating solution, effectiveness in reducing porosity as well as the cost
    - An appropriate grain refiner and brightener to ensure uniform deposition across the substrate surface. In general, there are a variety of such additives commercially available for nickel plating. Among them are the additives based on the propargyl skeleton. Examples are: RALU®PLATE HBOPS-Na, RALU®PLATE POPS-liquid, RASCHIG RALU®PLATE PPS, and RALU®PLATE PPS-OH; However, the manufacturer of these additives (Raschig Inc) does not disclose the exact composition of such additives. Considering the fact that all these typical grain refiners/brighteners belong to the propargyl family and also knowing that the existence of the -C≡C- bond within the molecular skeleton plays an important role as a grain refiner and brightener (especially if this triple carbon-carbon bond exist at the end of the molecular chain), POPDH (Propargyl-oxo-Propane-2,3-Dihydroxy) was selected for this work. This chemical is also commercially available
2) Using an optimized electroplating bath temperature to keep a high deposition rate and at the same time not to degrade the composition and properties of the coated material.
3) Using appropriate agitation mode to create a uniform flow pattern across the plating bath to ensure uniform current density distribution across the substrate being plated as well as uniform thickness of the deposited material throughout the substrate without forming any porosity.

The resulting material should demonstrate outstanding corrosion and tribological performances compared to classic DC electrodeposited NiW from deposition baths containing similar ingredients including the source of nickel ions, complexing agent, stress reducer, brightener and grain refiner, and wetting agent. DC deposited NiW displayed a dominant amorphous phase structure; whereas, the NiW deposited from the same bath chemistry but using PRC waveform demonstrated mostly crystalline structure with better corrosion and tribological performances.

In addition, ceramic fillers including cerium oxide (CeO_2), silicon carbide (SiC), and hexagonal boron nitride (hBN) particles were added into the NiW bath chemistry to produce composites of NiW–CeO_2, NiW–SiC, NiW–hBN, NiW–SiC–CeO_2, and NiW–SiC–hBN through DC electrodeposition processes.

As well, the microstructure, corrosion, and tribological performances of PRC–electrodeposited NiW–SiC, NiW–CeO_2, and NiW–SiC–CeO_2 composites were compared to that of DC waveform. The addition of SiC, CeO_2, and hBN on the improvement of the corrosion and tribological performances of NiW was determined. Various electrochemical corrosion tests including potentiodynamic polarization (PP) and cyclic potentiodynamic polarization (CPP) tests were employed to evaluate the corrosion performances of the deposits. Time–of–Flight Secondary Ion Mass Spectrometry (TOF–SIMS) and X–ray Photoelectron Spectroscopy (XPS) were used to investigate the various corrosion products on deposits. X–ray diffraction (XRD) and transmission electron microscopy (TEM) were used to analyze the grain structure of the coatings. As well, tribological properties including the hardness, and wear resistance of the deposits were investigated.

TABLE OF CONTENTS

LIST OF TABLES

LIST OF FIGURES

LIST OF SYMBOLS AND ABBREVIATIONS

This list presents the symbols and abbreviations used in the thesis or dissertation in alphabetical order, along with their meanings.

Symbol	Description
BF–STEM	Bright Field Scanning Transmission Electron Microscopy
CPP	Cyclic Potentiodynamic Polarization
DF–STEM	Dark Field Scanning Transmission Electron Microscopy
DC	Direct Current
EDS	Energy–dispersive X–ray Spectroscopy
PP	Potentiodynamic Polarization
PRC	Pulse Reverse Current
SEM	Scanning Electron Microscope
TOF–SIMS	Time–of–Flight Secondary Ion Mass Spectrometry
XPS	X–ray Photoelectron Spectroscopy
XRD	X–ray Diffraction

CHAPTER 1 INTRODUCTION

Electrodeposited chromium (Cr) coatings have found extensive engineering applications due to their excellent corrosion and wear resistance properties. [1] The intrinsic properties of Cr such as high hardness and low friction coefficient have provided excellent wear and erosion resistance for many industrial applications such as aircraft landing gear, helicopter dynamic components and propeller hubs, hydraulic actuator rods and cylinders, gas turbine engines, etc. [1] The electrodeposition process of Cr coating as well as its properties and performance have been established very well in many industrial applications. [2] In fact, material designers specify Cr as a reference/standard material for protective coating in many applications due to its minimal performance risks. However, in some particular applications, their performance may not be adequate, and it may just be considered a coating with the most available data. Despite many beneficial properties and low production costs associated with electrodeposition of Cr, the electrolyte used for electrodeposition contains toxic hexavalent chromium Cr(VI) ions. As well, the electrodeposition of Cr suffers from low electrolyte efficiencies resulting in low deposition rate, high energy consumption, and formation of toxic hexavalent chromium vapors. As well, their intrinsic brittleness may cause formation of micro– or macro–cracks within deposits. Although these cracks may not influence the wear and erosion performance, but they diminish the corrosion resistance of the coatings. Therefore, researchers have made extensive efforts into finding an alternative solution. Moreover, Cr deposits may weaken the fatigue resistance of engineering as a result of residual tensile stresses and cracks. [3,4]

Extensive research has been performed to explore alternative technologies and materials to electrodeposition of chromium. Examples are: thermal spray, plasma vapor deposition, electroless and electrodeposition of Cr–free coatings. Over the last decade, thermally sprayed tungsten carbide–cobalt (WC–Co) and tungsten carbide–cobalt–chromium (WC–Co–Cr) coatings have been approved by the Hard Chromium Alternatives Team (HCAT) accepted by aerospace industry and other low–volume and line–of–sight coating applications. However, for high–volume production and non–line–of–sight deposition process, electrodeposition has been proved as feasible, more appropriate, and more economically viable technology. Traditionally, majority of electrodeposition process has been based on nickel (Ni) and its alloys. Nickel (Ni) is the most commonly used metal in electrodeposition as the continuous metallic phase due to several factors such as availability, cost, feasibility of deposition, and its unique properties. [1] However, nickel itself is moderately resistant to corrosion and its resistance can be improved

when it is alloyed with other transition metals such as copper, molybdenum, chromium, iron, tungsten, etc. Among such materials, NiW alloys have drawn considerable attention in recent years in a broad range of engineering applications. [5] It is also noteworthy to mention that presence of insoluble ceramic particulates such as SiC, CeO_2 and hBN within the NiW matrix could greatly enhance the mechanical, tribological and corrosion properties of the coating and this could be possibly due to extremely high hardness of SiC, very low friction coefficient of hBN, and the great role of SiC, CeO_2, and hBN as physical barriers to anodic faradaic current flow.

In this research work, NiW alloy was selected as an interesting metallic matrix for producing its composite with ceramic particles including SiC, CeO_2 and hBN. It was shown that the electrodeposition of NiW alloy from specially formulated bath chemistry and optimized deposition conditions could generate coatings with outstanding tribological and corrosion properties. These materials may be considered suitable candidates as alternatives to carcinogenic and hazardous chromium hexavalent Cr (VI) based coatings. [6] SiC particles were selected due to their interesting properties such as high hardness, high thermal stability, and excellent oxidation resistance. hBN particles were selected due to their extremely low friction of coefficient, and CeO_2 particles were selected due to the outstanding corrosion protection properties. CeO_2 is the most stable cerium oxide in which, cerium has oxidation state of +4 which is more stable than the another oxidation state i.e., Ce^{+3}. [7] To our best knowledge, electrodeposition of NiW reinforced with CeO_2, SiC, and hBN particles is a new material and no research has been done to explore the corrosion and tribological properties of such deposit.

Watts's bath with addition of an appropriate source of tungstate ions such as sodium tungstate was initially used to obtain NiW coatings. The bath contained a mixture of nickel sulfate and nickel chloride, boric acid, together with some additives as brighteners and stress reducers. The operating pH of these typical electrolytes was limited to a narrow range due to pH dependency of the precipitation of nickel hydroxide and nickel tungstate. Later, it was realized the use of citrate ions in electrolyte improves the stability of electrolyte as well as the properties of the deposits. The electrolyte contained nickel sulfate as source of nickel ions, sodium tungstate as source of tungstate ions, and trisodium citrate as complexing agent for both nickel and tungstate ions. It was reported that the addition of ammonium ions citrate based electrolytes improves the cathodic current efficiency. The concentration ratio of citrate to ammonium ions in electrolyte could also influence the properties of the deposits. [8, 9]

Electrolytes based on sulfamate–citrate have been also reported. It was shown that the solution pH had significant influence on the W content, microhardness, and grain size of deposits. The sulfamate based bath produces NiW deposits with low residual tensile stress. [10, 11] Matsui et al. [12] reported a sulfamate based bath containing nickel sulfamate and nickel chloride as sources of nickel ions, sodium tungstate as a source of tungstate ions, and propionic acid as complexing agent. Other reported electrolytes were based on different types of complexing agents such as gluconate, glycine, and triethanolamine. It was reported that the most cathodic current efficiency and the highest W content were achieved by using a mixture of these three complexing agents. It was also reported that the NiW deposits obtained from an electrolyte containing a mixture of citric acid and glycolic acid displayed substantially higher hardness, wear and corrosion resistance compared to those obtained from citrate baths.

Alloys of tungsten (W) are famous for their good corrosion performance and excellent tribological and mechanical properties. It was found that the hardness of electrodeposited NiW alloys is quite higher (almost 2–3 times) than that of pure nickel (Ni) [7, 13]. NiW containing 10 wt.% of W produced deposits with microhardness of approximately 600 Vickers that was increased up to 800 Vickers after annealing at 650oC. Attempts have been made to electrodeposit nano–crystalline NiW where the W component controls the grain size of Ni resulting in the enhancement of tribological, and mechanical properties [13, 14]. However, in some study it was realized that NiW deposit with an average grain size of 5–63 nm demonstrated higher corrosion rate in acidic solution (pH 3) than in alkaline (pH 10) containing 3.5 wt.% NaCl environments. The observation was explained by the fact that the corrosion performance of nano–crystalline NiW is controlled by two main competing factors: (1) W content that promotes the formation of passivation film and (2) the total surface areas of grain boundaries considering the fact the grain boundaries act as the active locations for corrosion reaction. [15]

NiW alloys have found many applications such as barrier coating in electronics, corrosion and wear protection on many engineering tools. NiW alloy was used in hot embossing and injection molding processes where the use of metallic microstructures as mold inserts requires materials with high hardness and good wear performance in order to obtain the replication into polymers and ceramics. It was reported [16] that NiW alloys displayed improved corrosion resistance, wear resistance, and catalytic activity for hydrogen. It was shown [17,18] that the content of W in the electrodeposited NiW alloy has substantial effect on hardness, wear– and corrosion

resistance of the deposit. From our knowledge, no work on the microstructure properties and applications of NiW containing SiC and CeO_2 has been reported in the literature until now.

Nickel–tungsten composite coatings usually are deposited from Watts type or sulfamate bath by reinforcing different nanoparticles (i.e. SiC [6, 19], SiO_2 [20], CeO_2 [20, 21], WC [22], Diamond [11, 23], Al_2O_3 [24, 25, 26, 27, 28], GO (Grapheme oxide) [29, 30, 31], B_4C [32], PCTFE (Polychlorotrifluoroethylene) [33], TiC [34], CrO_2 [35], Sil (Silicate) [36], B (Boron) [37, 38], MWCNT [39, 40], BN (Born nitride) [41, 42, 43], TiO_2 [49], ZrO_2 [43, 44, 45, 46, 47, 48, 49, 50], Co (Cobalt) [51, 52, 53], Cu (Copper) [24, 54], Si3N4 [43, 55], TN [43, 50, 56, 57], Y_2O_3 [58], and PTFE [59, 60, 61]).

In general, co–deposition process is governed by electrophoretic migration of dispersed metallic, or non–metallic particles (micron, or sub–micron size) in the electrolyte followed by incorporation of these particles into a metal deposit [62, 63]. Currently, there are two models developed for co–deposition of solid particles into the metal matrix, Guglielmi and Kurozaki, in which Guglielmi's model is the most adopted one since it has been checked with different co–deposition systems such as: Ni−SiC, Ni−TiO_2, Ni– Al_2O_3, Cu–Al_2O_3, Cr–C, Zn–Ni particles, Co–SiC, and Ni–MoS_2. Guglielmi model is based on a two–step adsorption process. The first step involves loose physical adsorption of the charged solid particles on the cathode surface by Vander Walls forces and the second steps involve strong electrochemical adsorption and entrapment of these particles by Coulomb force within the metal matrix. The main drawback of this model is that it does not consider the particle characteristics and mass transfer effect (e.g. nature of particle, the bath components, the hydrodynamic conditions. etc) during electrodeposition process. [62, 63]

A widely accepted model developed by Kurozaki, includes the movement of the solid particles from the solution to the cathode surface by agitation. [62, 63]

This model is developed in the following steps:

(1) Uniform dispersion and transportation of solid particles to the electric double layer by mechanical agitation

(2) Transportation of the Charged particles to cathode surface by electrophoresis.

(3) Adsorption of solid particles at cathode surface by Columbic force between particles and adsorbed anions followed by incorporation of the particles into growing metal.

Figure 1.1 represents five consecutive steps of co–deposition process. The regions include: formation of ionic clouds around the particles; convection movement towards the cathode (convection layer, typical length < 1 mm); diffusion through a hydrodynamic boundary layer (diffusion layer, typical dimensions of hundreds of μm); electrical double layer (typical dimensions of nm) followed by adsorption and incorporation of particles. [64]

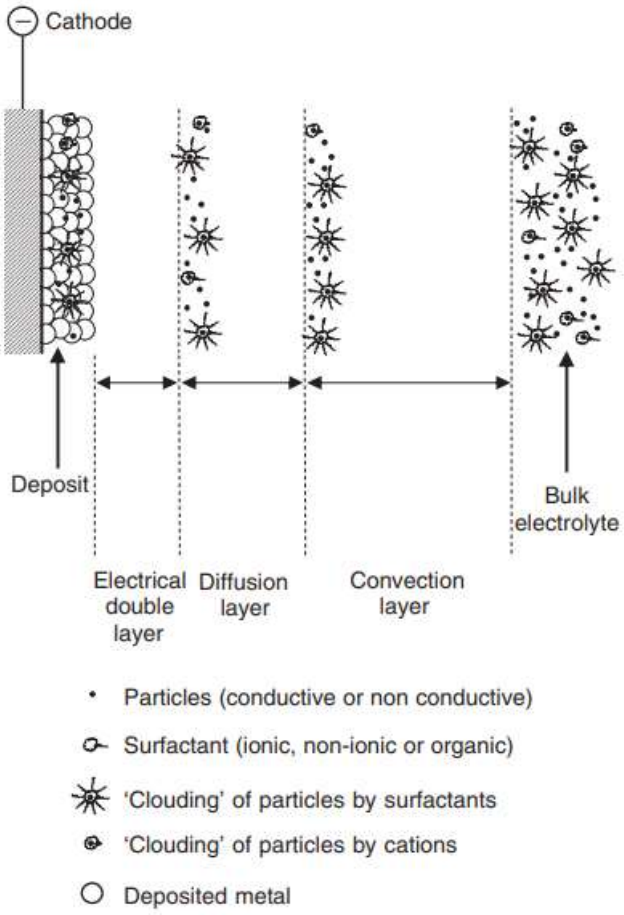

Figure 1.1 Mechanisms of particle co–deposition into a metal deposit. [64]

The major advancement in this field was made during the 1960–1970s especially in Europe mainly for seeking of various coating materials with outstanding wear performance due to the increasing demands for automotive and aerospace applications. Most publications during these years were related to electrodeposition of composite Ni or cobalt (Co) reinforced with hard ceramic particles such as silicon carbide (SiC) and tungsten carbide (WC). One example was the development of nickel (Ni)–SiC composite for automotive engine related applications by

BWM and Porsche. [65] Later during the 1970s, electrodeposition of composite coatings based on Ni reinforced with alumina (Al_2O_3), graphite, and polymeric fillers such as polytetrafluoroethylene (PTFE) for tribological applications and corrosion protection became attractive [66]. Nowadays, the concept of electrodeposition of composite coatings has gained recognition in the field of metal finishing and obtained a great deal of interests by research sectors in various industries to invest on further development of such materials through electrodeposition process [66]. A great variety of ceramic, organic, and diamond particles have been used as the dispersed phase within Ni matrix [67]. In recent years, electrodeposition of NiW composites have received a great deal of attention due to its impressive corrosion and wear resistance compared to other electrodeposited Ni based alloys in composite with fillers. [68] Electrodeposited NiW reinforced with SiC particles in which the properties of deposited NiW were enhanced by co–depositing with SiC [36, 61, 69, 70, 71, 72, 73, 74] has been reported in literature. As well, extensive research works on electrodeposition of NiW for various industrial applications have been published. [6] There are also few publications describing the electrodeposition of NiCe with enhanced corrosion properties of Ni resulting from co–deposition of Ce. [75]

Hosseini et al. [76] investigated the corrosion performance of DC electrodeposited NiW–SiC composite coatings as well as the influence of SiC particle concentration in the plating bath on the composition of composite coatings. It was found that addition of SiC particle into NiW matrix had a significant influence on the morphology, chemical composition, and corrosion performance of the coatings. The resultant NiW–SiC coatings were smoother, and more corrosion resistant compared to NiW coatings presumably due to the lower dissolution rate of nickel and tungsten of the alloy coating. Allahyarzadeh et al. [77] reported the corrosion performance of multilayer PRC electrodeposited NiW coating on carbon steel substrates. The coating was composed of two nickel–tungsten layers with alternating chemical compositions of 25 wt% and 11 wt%. Despite the fact that multilayer coatings possessed considerable resistance against pitting corrosion, corrosion resistance was reduced in the presence of chloride ions due to preferential dissolution of nickel and decrease in passive region area. However, the multilayer coating had higher corrosion resistance compared to monolithic coatings.

The applied current waveform can be either direct current (DC), pulse current (PC), or pulse reverse current (PRC). DC electrodeposition method by far is the most convenient and cost efficient method of electrodeposition. However, it requires the use of additives to control the

microstructure and properties as well as current distribution. Generally, the coatings developed by DC method are non–uniform and brittle. [78]

During the DC electrodeposition process, the negatively charged layer formed around the cathode charges to a certain thickness preventing the approach of ions towards the substrate, whereas in PC electrodeposition process, this layer is discharged periodically during the TOFF. The discharge of the layer allows the ions pass through the layer and approaches the substrate. The locations in electrodeposition bath with higher current density are depleted from the ions faster than the locations with lower current densities. The OFF–time of the pulse allows the ions to migrate towards the depleted areas. Therefore, ions with more uniform distribution will be available for reduction during the TON [78–79]. Figure 1.2 represents a schematic diagram of a typical pulse current waveform.

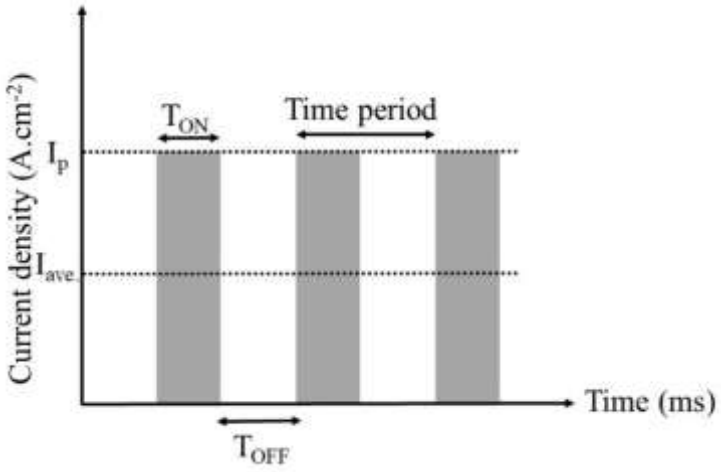

Figure 1.2 A schematic diagram of a typical pulse current waveform.

In PC method, the three independent parameters (i.e. TOFF, TON, and Ip) can be varied to obtain a deposit with desired properties. In PC method, the duty cycle (γ) is described as the percentage of total time of a cycle: [80]

$$\text{Duty cycle} = \frac{\text{TON}}{\text{TON+TOFF}} = \text{TON} \times \text{f} \qquad (1)$$

Where f is frequency or the reciprocal of the cycle duration (T):

$$f = \frac{1}{TON+TOFF} = \frac{1}{T} \qquad (2)$$

The deposition rate of the PC and DC will be the same if the average applied current density (IA) in PC is equivalent to the applied current density in DC electrodeposition process. The average applied current density in PC is described by equation (3):

$$IA = IP \times \gamma \qquad (3)$$

In recent years, pulsed reverse current (PRC) electrodeposition method has gained a considerable attention from researchers and industry since it offers a higher level of control over the chemical composition and deposit structure by appropriate selection of the electrodeposition parameters with minimal additive consumption. In PRC method, the applied current is interrupted and a reversed current is introduced into the electrodeposition cycle for a certain duration. The diffusion layer is replenished in similar to PC process. As well, the protrusions on the surface selectively are dissolved during the reverse resulting in more uniform deposit. The introduction of PRC waveform with high frequency may reduce or eliminate the use of additives in electrodeposition bath chemistry. Some of these additives may have negative impact on ductility and electrical conductivity of electrodeposited material. Figure 1.3 displays a typical reversed pulse current waveform.

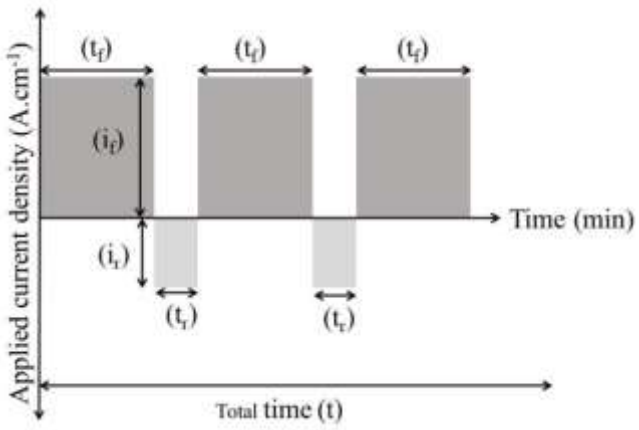

Figure 1.3 A schematic diagram of a typical reversed pulse current waveform.

.

It should be stated that there are two notable parameters in PRC process: average current and duty cycle. Average current density (I*A) is described by the following equation: [81]

$$I^*A = \frac{I(f) \times t(f) - I(r) \times t(r)}{t(f) + t(r)} \qquad (4)$$

Where I(f) is the forward current density, I(r) is the reversed current density, t(f) is the duration of the forward pulse, and t(r) is the duration of the reversed pulse. The duty cycle in PRC electrodeposition is calculated by the following equation:

$$Y^* = \frac{t(f)}{t(f)+t(r)} \qquad (5)$$

The coatings obtained by PRC technique are more compact and uniform due to their finer grain size and they also exhibit better mechanical and corrosion properties compared to DC and PC electrodeposited coatings. The PRC changes the concentration of ions by adsorption and desorption at the interface of cathode and electrolyte. Deposition and dissolution occur during the cathodic and anodic cycle, respectively. Therefore, the composition, microstructure and properties of the deposited material are altered.

It has been also reported that PRC deposited coatings with high tungsten content generate crack–free coatings with lower defects compared to those produced by DC with the same tungsten content. The main cause for cracking of DC deposited NiW with high tungsten content was attributed to formation of residual tensile stress as a result of hydrogen evolution over the cathode, whereas in PRC technique, the evolved hydrogen is consumed during the anodic or reversal scan through its re–oxidation on the surface of cathode. [77, 82–83]

NiW composite coatings exhibit better corrosion resistance compared to pure nickel and nickel tungsten coatings. It has been found that the co–deposition of the nickel and nickel tungsten with solid particles inhibits the crystal growth of nickel and promotes new nucleation sites. This will lead to a fine–grain structure and thus effectively enhances the corrosion resistance of the coating. Addition of these particles will also act as physical barriers against initiation and propagation of corrosive pits by decrease of corrosion current density and shifting the corrosion potential of composite coatings towards nobler values. [84, 85, 86]

Pitting corrosion is a localized breakdown of the passive film as a result of accelerated dissolution of the material. The formation of passive films on many engineering metallic materials provides better corrosion protection substantially. [87–88] However, the passive films on metal surface can breakdown locally resulting in exposure of the unprotected underneath metal. Cyclic potentiodynamic polarization (CPP) technique is a rapid method used for qualitatively evaluating the susceptibility of a metal to localized corrosion in a corrosive environment. During the cyclic polarization test, the potential is scanned in anodic direction and then the scan direction is reversed once the measured current density approaches a certain value. [87–89] The pitting characteristics of specimen are represented by the size and position of the hysteresis loop. In CPP method, parameters such as pitting or breakdown potential (E_p or E_b), protection or re–passivation potential (E_{prot} or E_{rep}), passivation current density (i_p), anodic to cathodic transition potential, hysteresis, and anodic nose or active–passive transition potential can be utilized to evaluate the corrosion behavior of materials. The relative locations of pitting and protection potentials to corrosion potential (Ecorr) are used to investigate the pitting resistance of the material. [87–88] The number of articles that have been published on corrosion behavior of electrodeposited NiW alloys and their composites are limited. [90, 91, 92, 93, 94, 95] Most of such studies were conducted to investigate the general corrosion behavior of these alloys and their composites using potentiodynamic polarization method in different corrosive media. For example, Wu and et al. [96] investigated the influence of brightener, 2–butyne–1, 4–diol on plating process and structures of Ni–W electrodeposit. The resultant coatings were fully bright and smooth. However, the addition of 2–butyne–1, 4–diol into electrodeposition bath, resulted in gradual decrease of W content followed by rapid drop of current efficiency with increase of its concentration.

Attempts have been made to further improve the properties of electrodeposited NiW. Examples are: i) reducing the grain size of deposits by means of applying pulsed reverse current waveform; ii) fabricating of NiW composites with various types, sizes, and shapes of fillers such as ceramic fillers (eg., alumina, zirconia, titania, titanium nitride, hexagonal boron nitride, cubic boron nitride, etc.), glass, carbon nanotubes, graphene, etc.

Addition of hard ceramic particles to NiW alloy matrix and controlling its grain size into the nanocrystalline regime through modification of current waveform parameters, could greatly enhance the hardness of NiW alloys from ~1 GPa to as much as ~7 GPa. Ceramic particles could act as barriers against dislocation and grain boundary sliding thus improving hardness of

composite coatings. The increase in hardness of composite coatings is attributed to the contribution of Orowan strengthening mechanism and grain refinement due to Hall–Petch effect. The influence of co–deposited particles on hardness of the alloy matrix mainly depends on the type, volume content of reinforcements as well as size and distribution of these particles in the metal matrix. [97, 98, 99]

NiW reinforced with SiC [19, 20, 21, 22, 23], Diamond [11, 23], Al_2O_3 (Aluminum oxide) [24, 25, 26, 27], GO (Graphene oxide) [29, 30, 31], TiC (Titanium carbide) [34], CrO_2 [35], B (Boron) [37, 38], MWCNT [39, 40], BN (Boron nitride) [41, 42], ZrO_2 [42, 44, 45, 46, 47, 48, 49, 50, 100], Si3N4 (Silicon nitride) [42, 55], TN (Titanium nitride) [42,43, 44, 45, 46, 47, 48, 49, 50, 51,52, 53, 54, 55, 56, 101], Y_2O_3 (Yttrium oxide) [50], and PTFE (Polytetrafluoroethylene) [59]) exhibit better wear resistance compared to pure nickel and NiW coatings. The improvement in wear resistance of the composite coatings is mainly attributed to reinforced second phase particles in the nickel matrix. These reinforced particles act as barriers to nickel grain growth and plastic deformation of nickel under loading resulting in higher hardness coatings with improved wear performance. [102]

This thesis is organized as follows: Chapter 1 serves to introduce the subject of the research and the objectives; Chapter 2 presents background information and a comprehensive literature review on NiW composite coatings. Objectives, Methodology, and experimental method used for fabrication and characterization of the coating samples and the novelty contributions to the articles are discussed in Chapter 3, 4, and 5; Chapter 6 discusses the results of highly corrosion–resistant pulsed–reverse current electrodeposited NiW and NiW–SiC composites on brass substrate; Chapter 7 investigates the pitting corrosion and mechanical properties of DC and PRC electrodeposited NiW coatings on brass substrate; Chapter 8 discusses the effect of PRC waveform on tribological and mechanical properties of electrodeposited NiW alloys on brass substrate; Chapter 9 provides results on effect of hBN on corrosion and wear performances of DC electrodeposited NiW and NiW–SiC; Chapter 10 discusses the synthesis and characterization of novel NiW–CeO_2 composite coating with enhanced corrosion and wear resistance; Chapter 11 is allocated to present the results on synthesis and characterization of novel NiW–SiC–CeO_2 composite coating on brass substrate with enhanced corrosion and wear resistance, and finally Chapter 12 and 13 presents the summary of all results, and includes recommendations and possible future research work.

In this thesis, the main results are presented in a form of six articles. In all articles, Mina dadvand participated in the definition of the project, design of experiments, fabrication and characterization of all samples, plotting all the graphs, interpretation of the experimental results, and preparation of the articles. Oumarou savadogo supervised the project, and he commented on the organization, analysis of the results and on the preparation of the articles.

Chapter 6 (Article 1): Highly corrosion–resistant pulsed–reverse current electrodeposited nickel tungsten and nickel tungsten–silicon carbide composites

Authors: Mina Dadvand, Oumarou Savadogo

Chapter 7 (Article 2): Pitting corrosion and mechanical properties of direct current and pulsed reverse current electrodeposited nickel–tungsten coatings

Authors: Mina Dadvand, Oumarou Savadogo

Chapter 8 (Article 3): Effect of pulse reverse current waveform on tribological and mechanical properties of electrodeposited nickel–tungsten alloys on brass substrate

Authors: Mina Dadvand, Oumarou Savadogo

Chapter 9 (Article 4): Effect of hBN on corrosion and wear performances of DC electrodeposited NiW and NiW–SiC

Authors: Mina Dadvand, Oumarou Savadogo

Chapter 10 (Article 5): Synthesis and characterization of novel NiW–SiC–CeO_2 composite coating with enhanced corrosion and wear resistance

Authors: Mina Dadvand, Oumarou Savadogo

Chapter 11 (Article 6): Synthesis and characterization of novel NiW–CeO_2 composite coating with enhanced corrosion and wear resistance

Authors: Mina Dadvand, Oumarou Savadogo

CHAPTER 2 LITERATURE REVIEW

2.1 NiW Composite Coatings

2.1.1 NiW–B_4C Composite Coatings

He et al. [32] investigated the micro–hardness and corrosion performance of the pulse electrodeposited NiW and NiW–B_4C composite coatings utilizing potentiodynamic polarization, Electrochemical Impedance Spectroscopy (EIS), and Vickers micro–hardness. Their results exhibited that the addition of B_4C nanoparticles into the NiW alloy matrix can greatly improve the surface morphology and the corrosion resistance of the composite coatings. It was observed that the obtained NiW–B_4C from the bath containing 2 $g.L^{-1}$ B_4C nanoparticles had the best surface morphology, the highest micro–hardness, and the outstanding corrosion resistance. According to polarization results (Figure 2.1), corrosion potential (Ecorr) shifted to more noble values and corrosion current density (icorr) decreased with increase of the concentration of B_4C in the plating bath from 0 to 2 $g.L^{-1}$. When the concentration of B_4C nanoparticles is exceeded 2 $g.L^{-1}$, the corrosion potential gradually decreased, while the corrosion current rose slightly. Figure 2.2 displays the Nyquist plots and the fitted plots for the NiW alloy and NiW–B_4C composite coatings. All electrodeposited coatings exhibited a semicircular arc with different sizes. The larger arcs represent the higher corrosion resistance. Among all coatings, NiW–B_4C (2 $g.L^{-1}$ B_4C) composite coatings displays the larger size, therefore the better corrosion performance.

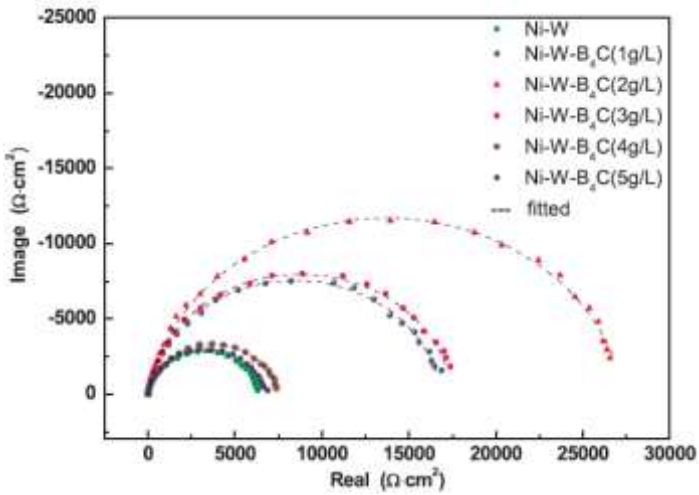

Figure 2.1 The polarization curves of NiW alloy and NiW–B_4C composite coatings with different concentration of B_4C nanoparticles. [32]

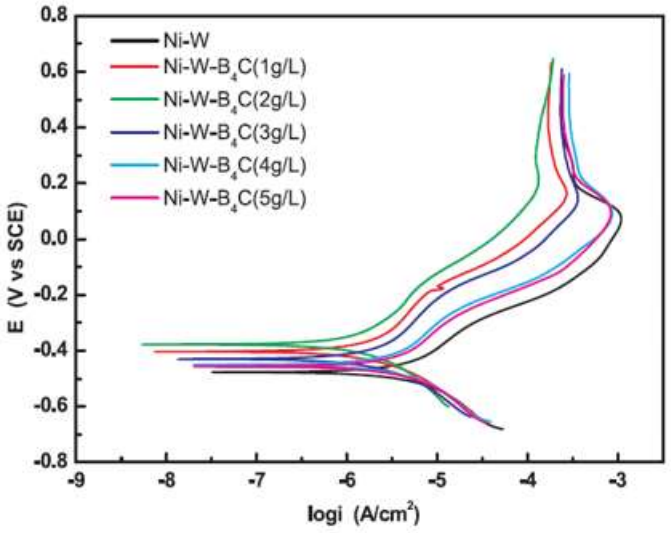

Figure 2.2 Nyquist plots and the fitted plots for the NiW alloy coating and NiW–B_4C composite coatings. [32]

Results also indicated that the NiW–B_4C (2 $g.L^{-1}$) composite coating exhibited the highest micro–hardness (1176 HV) compared to that of the NiW coating (557 HV). This was attributed to the presence of B_4C particles hindering the sliding and dislocation movement of the grain boundaries. On the other hand uniform dispersion of the B_4C particles in the NiW coatings along with grains refinement and dispersion strengthening effect improved the hardness of the coatings. [103]

2.1.2 NiW–SiC Composite Coatings

The co–deposition of SiC nanoparticles in NiW alloy coatings significantly improves mechanical, corrosion and tribological properties of the coatings. SiC nanoparticles are frequently co–deposited with metal matrix to produce the hard and wear resistant coatings due to their low cost, high hardness, good thermal stability, wear resistance, and oxidation resistance. [104]

Li et al. investigated the wear and corrosion performance of NiW–SiC and compared it to Ni and NiW alloy coating. They found that the composite coating exhibits improved wear performance than metal coatings. The wear rate decreased from Ni 2.2 mg cm^{-2} to NiW 1.4

mg cm^{-2} then to NiW/SiC 0.52 mg cm^{-2}. This was attributed to the high hardness of SiC. It was also reported that the incorporation of SiC nanoparticles in the NiW matrix enhanced the anti–corrosion performance of the coatings when the current density was less than 2 $A.dm^{-2}$, then decreased with the increase of the current density. Improvement in corrosion performance of the nano–composite coating was attributed to the presence of the SiC within the NiW matrix covering the surface defects, refining the grains, and acting as a physical barrier against the corrosion attack. [19]

Wasekar et al. [6] investigated the influence of SiC on mechanical properties of pulsed electrodeposited NiW nano–composite coatings. Their results indicated that increase in pulse frequency and decrease in duty cycle increased the SiC content of the nanocrystalline NiW coating. The increase in content of SiC was attributed to pulse current effect at the interface of cathode–solution leading to changes in thickness of pulsating diffusion layer. As shown in Figure 2.3, Maximum SiC content in the coating was obtained when the pulsating diffusion layer thickness was equal to SiC particle size (0.35 μm). It was also observed that the hardness and elastic modulus of NiW–SiC nano–composite coatings was enhanced with increase of the SiC content as per rule of mixtures and subsequently reduced above 5 vol.% SiC. Deterioration of mechanical properties with increase of SiC above 5 vol.% SiC is associated with grain size refinement beyond the Hall–Petch inflection point leading to an "inverse Hall–Petch" behavior in which hardness decreases with finer grain size. As shown in Figure 2.4, Hall–Petch inflection point is ~5 nm which is much lower than the Hall–Petch inflection (breakdown) point for NiW alloy which is ~10 nm. Such a decrease is associated with the presence of SiC particles in NiW alloy matrix which restrain the dislocation movement (Cobel creep/grain boundary sliding) at finest grain size below the inflection point. [6]

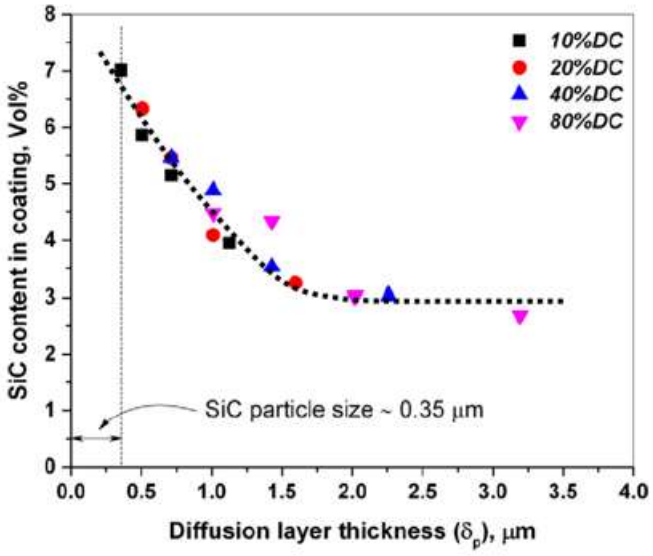

Figure 2.3 Variation in SiC content of NiW–SiC nano–composite coatings as a function of diffusion layer thickness for different duty cycles. [18]

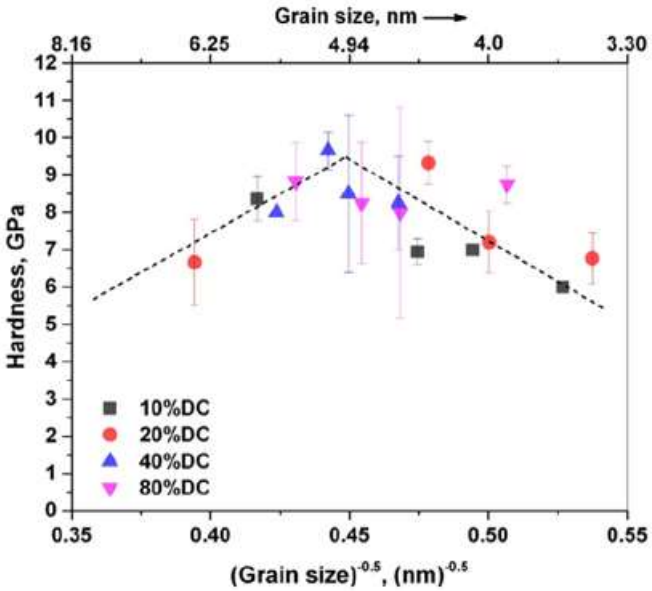

Figure 2.4 Hall–Petch plot for NiW/SiC nano–composite coatings deposited at different duty cycles. [18]

2.1.3 NiW–Diamond Composite Coatings

Diamond co–deposition into the NiW alloy matrix could significantly enhance the mechanical properties, thermal resistance, and wear performance of the NiW coatings due to its extreme hardness, good oxidation resistance, good chemical stability, and good wear resistance. However, the major challenge is to ensure the uniform distribution of diamond particles within the metal matrix. It was reported that the incorporation of diamond particles into NiW matrix increased the grain size from 18 to 23 nm. Therefore, this incorporation was achieved by means of a chemical bonding with the metal alloy matrix and not merely by means of any cohesive forces or physical adhesion. This result could assist to enhance the level of incorporation of diamond particles and to obtain uniform distribution of diamond particles in the coatings. [10]

Hou et al. [11] investigated the wear resistance of electrodeposited NiW/diamond composite coatings. It was stated that the incorporation of diamond particles into alloy matrix led to improved microhardness as well as significant increase of the anti–wear performance of the coatings. This which can be attributed to the particle strengthening and dispersion strengthening effect of the diamond. They also reported that the reinforcement of diamond particles will inhibit the deposition of NiW alloy and it was observed that the diamond content of NiW/diamond composite coating increased with increasing diamond content in the electrodeposition bath. As shown in Figure 2.5, the maximum hardness and anti–wear performance was achieved when the content of diamond particles in the plating bath was 21 vol.%.

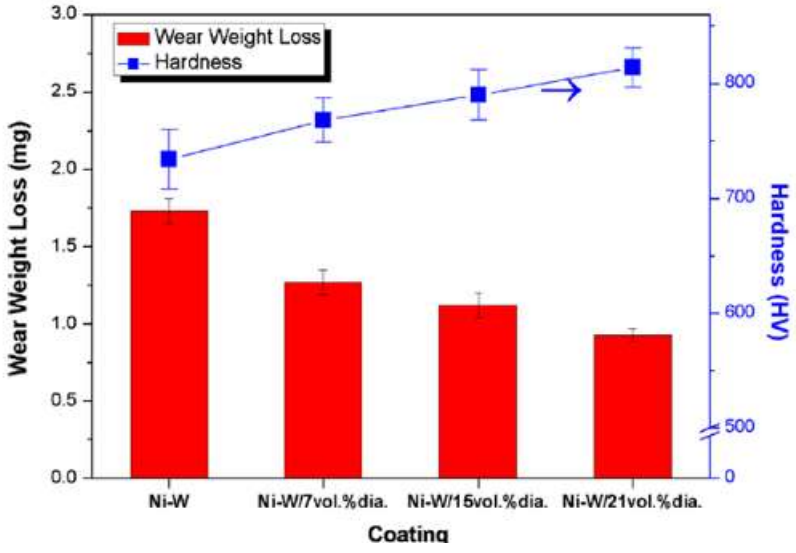

Figure 2.5 Effect of diamond content on wear weight loss and micro–hardness of NiW/diamond composite coatings. [11]

2.1.4 NiW–Al_2O_3 Composite Coatings

Co–deposition of Al_2O_3 nanoparticles with NiW alloy matrix has attracted attention of the scientists due to their high hardness, good thermal conductivity, wear resistance and relatively their low price. Hou et al. [11] investigated the wear resistance of pulse electrodeposited Ni–W/Al_2O_3 composite coatings. They found that effect of reinforcement of alumina on hardness of NiW was insignificant. However it had a great influence on tribological properties of the NiW coatings. The lowest reported friction coefficient (0.25) and wear rate (1.05 mg) was obtained when the alumina content in the electrodeposition bath was 10 $g.L^{-1}$.

Allahyarzadeh et al. [24] studied the wear performance of the functionally graded (FG) electrodeposited NiW/Al_2O_3 nano–composite coating. They found that the wear resistance of FG–coatings were greatly enhanced by addition of Al_2O_3 nanoparticles and the lowest wear rate was obtained at a higher fixed frequency (with continuous variation of duty cycle) or a lower constant duty cycle (with continuous changes of frequency). They also reported that the coefficient of friction (COF) results were approximately the same for all six FG–NC coatings deposited at various frequency and duty cycles. However, the greater COF of was obtained for NiW coating compared to the pure Ni which was attributed to presence of W in the structure.

Allahyarzadeh et al. [24] performed electrochemical experiments to analyze corrosion behavior of functionally graded nano–composite (FGNC) NiW–Al_2O_3, NiW, and pure Ni coatings deposited at different frequencies. They measured the electrochemical values by polarization test in a 3.5wt% NaCl solution and they found that the corrosion potential of (FGNC) NiW–Al_2O_3 is nobler than the NiW and pure Ni coatings as shown in Figure 2.6. This potential shift to the more positive values could be attributed to the presence of Al_2O_3 particles in the NiW matrix of FGNC coatings. According to polarization results, the FGNC coatings exhibited less corrosion current densities (less than about 40%) and no significant difference in corrosion current densities of NiW and pure Ni coatings was observed. The polarization results also indicated that the coatings deposited at higher frequencies had the least corrosion resistance compared to those developed at lower frequencies.

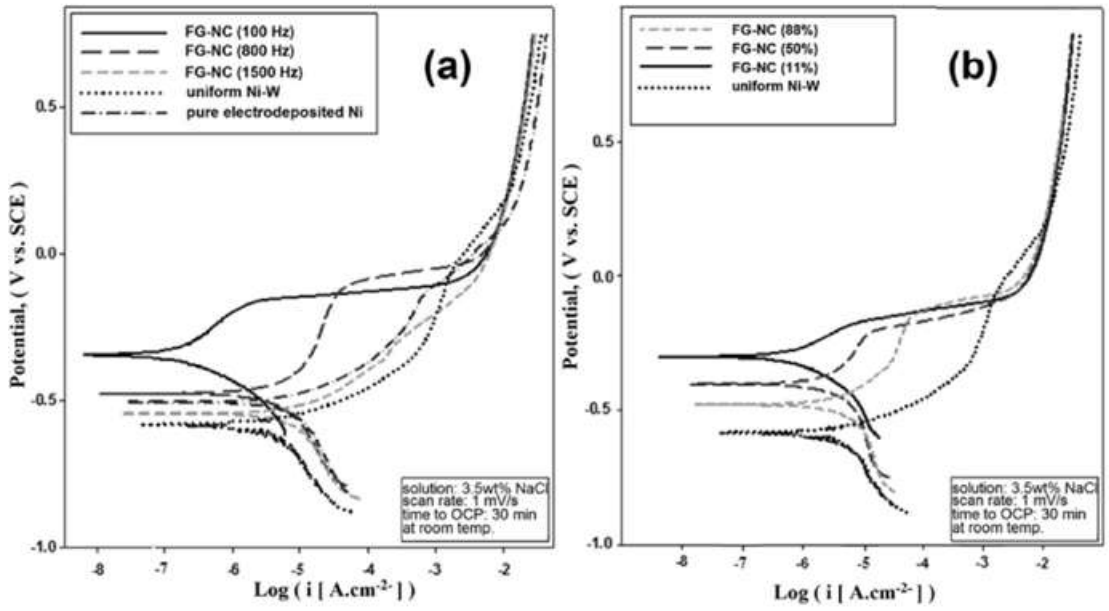

Figure 2.6 Potentiodynamic polarization curve for electrodeposited FG–NC, NiW and pure Ni coatings in the 3.5wt% NaCl. [24]

2.1.5 NiW–GO Composite Coatings

Graphene oxide (GO) has received considerable interest in many researches due to its special structure and characteristics. A critical challenge in electrodeposition of GO composite coating is uniform dispersion of GO in the metal matrix due to its hydrophobic surface. Therefore, appropriate surfactants and ultrasonic vibration are frequently used for the stability of micro and nano–size GO in electrodeposition bath as well as homogeneous distribution of these particles in the composite coating. [105]

Zhang et al. [31] studied and investigated the hardness, wear mechanism and the tribological behavior of electrodeposited NiW–GO composite coatings utilizing high–speed reciprocating friction and wear tester. Their results indicated that presence of GO nanoparticles in the metal matrix had a significant influence on the microstructure and grain size of the NiW–GO composite coatings. As shown in Figure 2.7, NiW–GO contains a finer cauliflower–like structure with smaller nodules in comparison with the corresponding NiW coatings. As it was stated, the co–deposited GO nanoparticles in the alloy matrix improved the hardness, wear, and tribological performance of NiW–GO composite coatings. This was attributed to dispersion strengthening and particle enhancement effects due to presence of GOs in the coating. The

optimum GO concentration in the electrodeposition bath to obtain the highest microhardness and wear resistance was 0.15 $g.L^{-1}$.The reported microhardness value and the wear rate was HV688 and 1.66×10^{-6} $mm^3.N^{-1}.m^{-1}$ respectively.

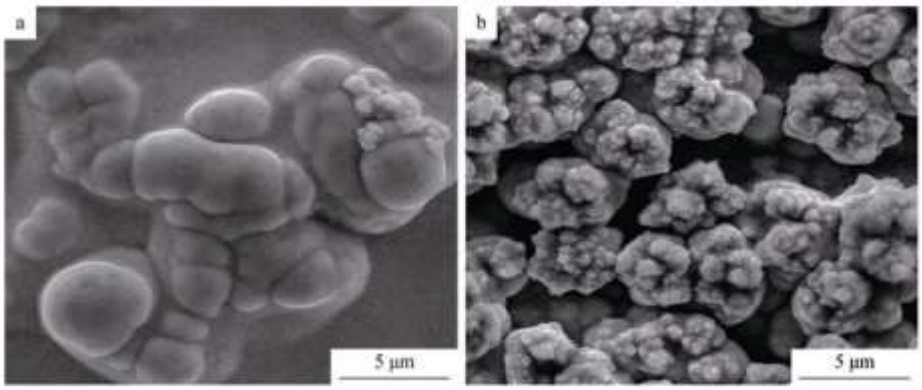

Figure 2.7 SEM images of surface morphology: a) NiW coating, b) NiW–GO composite coating with 0.15 $g.L^{-1}$ GO in electrodeposition bath. [31]

2.1.6 NiW–TiC Composite Coatings

Dilek et al. [34] investigated the tribological and corrosion performance of the pulsed electrodeposited submicron–sized TiC reinforced NiW coatings. It was observed that NiW–TiC deposited from the bath containing 15 $g.L^{-1}$ TiC concentration displayed the best corrosion and tribological performance. This was attributed to microstrain and lattice distortion of NiW matrix due to presence of TiC.

As shown in Figure 2.8, heavy plastic deformation, cracks and grooves along the sliding direction can be observed on the worn surface of un–reinforced NiW coating and therefore the adhesive wear was identified as the dominant wear mechanism. However, NiW–TiC coatings were smoother and contained less and wider cracks.

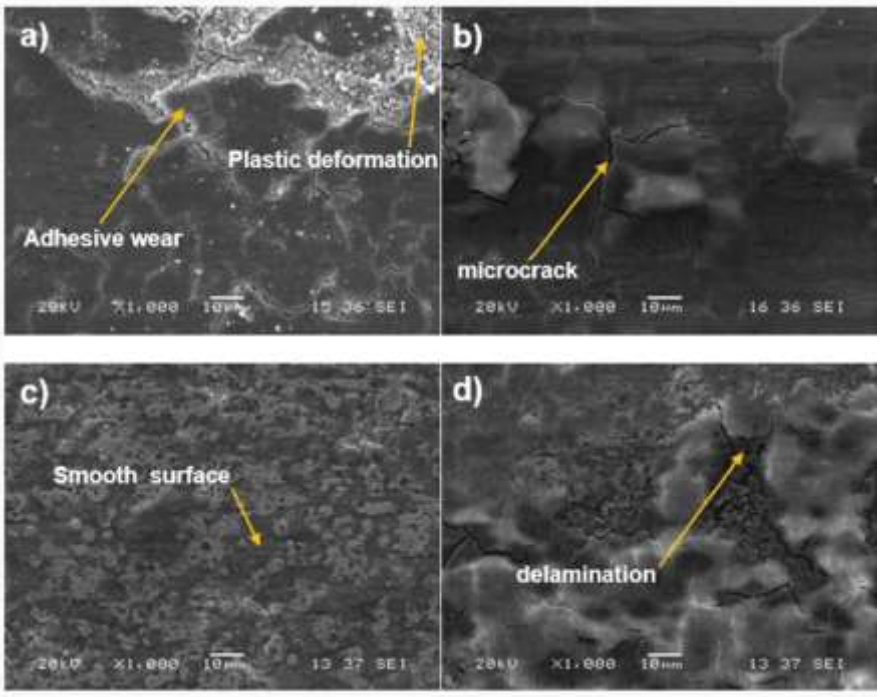

Figure 2.8 SEM morphology from the worn surfaces of the NiW and NiW–TiC composite coating electrodeposited at different TiC concentrations: (a) 0 $g.L^{-1}$; (b) 5 $g.L^{-1}$, (c) 15 $g.L^{-1}$,(d) 30 $g.L^{-1}$. [34]

2.1.7 NiW–Co (Al_2O_3) Composite Coatings

Allahyarzadeh et al. [106] studied the electrochemical and wear properties of the pulsed reverse electrodeposited NiW–Co (Al_2O_3) nano–composite. Results indicated that Al_2O_3 particles enhanced the corrosion resistance of the nano–composite three times and wear resistance up to 2.5 times. As shown in SEM images taken from the worn surface of the coatings in Figure 2.9, it was observed that the increase of the deposition frequency, decreased the wear damages and reduced the plastic deformation signs of the coatings that were electrodeposited by instantaneous variations of duty cycle and thus enhance the wear resistance of the coatings. The improvement in wear resistance was attributed to grain refinement due to presence of the alumina particles in the coating which reduced the material loss by transforming the wear mechanism from sliding into rolling mode.

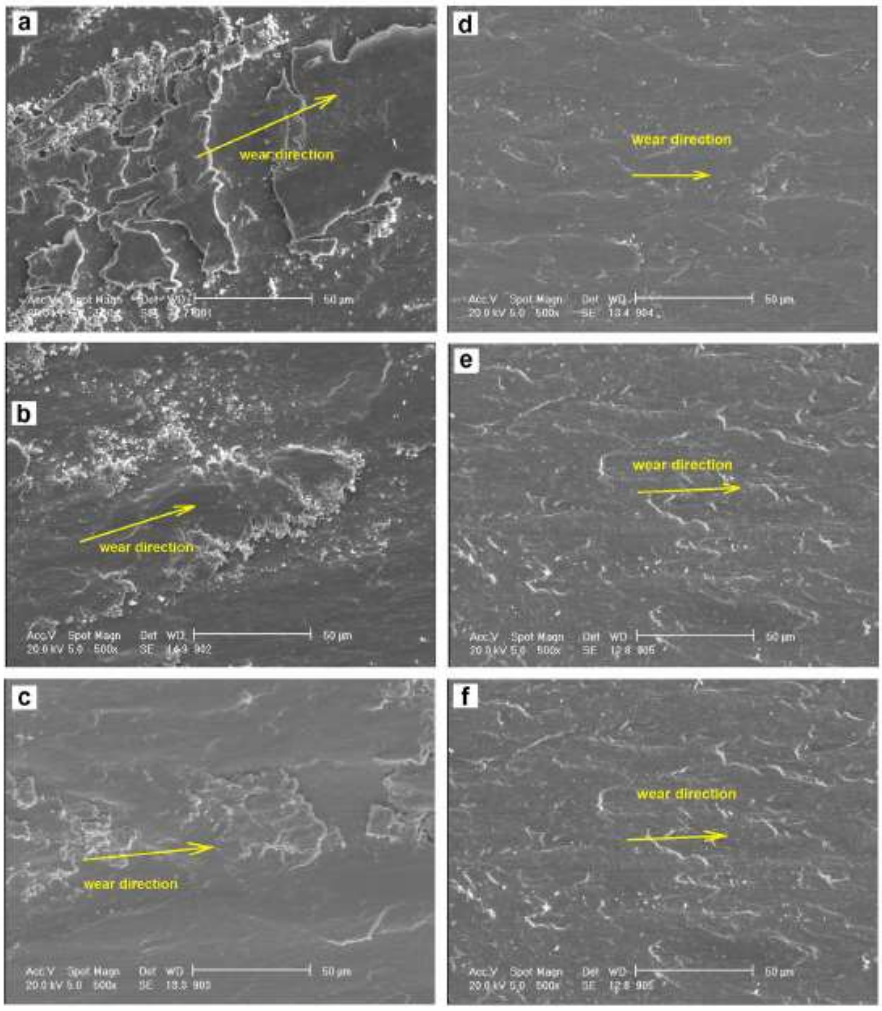

Figure 2.9 SEM images from worn surfaces of NiW–Co (Al_2O_3) coatings deposited at various frequencies: 10f (a and b), 250f (c and d), 500f (e and f). [106]

2.1.8 NiW– CrO_2 Composite Coatings

Nyambura et al. [35] characterized the corrosion and wear behavior of the electrodeposited NiW/Cr_2O_3 nano–composite coatings. They found that the wear resistance in Ni–W/Cr_2O_3 is superior to un–reinforced NiW coatings and the highest wear resistance was achieved when the concentration of Cr_2O_3 in the electrodeposition bath was 10 $g.L^{-1}$. The high wear resistance of the nano–composite coating was attributed to the presence of Cr_2O_3 nanoparticles acting as fibers in the NiW matrix and preventing initiation and propagation of micro–cracks. Presence Cr_2O_3 in the NiW matrix transformed the wear mechanism from sliding mode to rolling mode. The results also indicated that NiW–Cr_2O_3 exhibited lower COF (+0.48) compared to that of

NiW coating (0.6) and this was as a result of Cr_2O_3 adsorption into the nano–composites structure. It was also realized that the highest corrosion resistance was achieved when NiW/Cr_2O_3 nano–composite was electrodeposited at current density of 1 $A.dm^{-2}$ from the electrodeposition bath containing 40 $g.L^{-1}$ W and 10 $g.L^{-1}$ Cr_2O_3 respectively.

2.1.9 NiW–B (Boron) Composite Coatings

Qin et al. [38] investigated the wear properties of NiW–B composite coatings utilizing a reciprocating–sliding tribometer. They found that the wear performance of NiW coating was enhanced with incorporation of boron particles due to polishing effect of the boron particles. It was also observed that the friction coefficient of NiW/B composite coatings was lower than that of NiW coating. The lowest friction coefficient and the highest wear performance was obtained when the concentration of boron in the electrodeposition bath was 3 $g.L^{-1}$.

2.1.10 NiW–CNTs Composite Coatings

Fan et al. [39] investigated and compared the morphology, electrochemical, mechanical, and the tribological behavior of pulsed current electrodeposited NiW–MWCNTs nano–composite coatings. XRD and SEM results indicated that the NiW–MWCNTs deposits possessed more uniform and compact surface structure than NiW coating. This was attributed to uniform dispersion of MWCNTS in the NiW alloy matrix which resulted in strengthening of the coating. As shown in Figure 2.10, scuffing, abrasive grooves, and some large wear debris can be observed on the SEM images taken from the wear tracks of NiW–MWCNTs and NiW coatings. The main wear mechanism of NiW alloy was identified as adhesive wear combined with abrasive wear. However, in NiW–MWCNT coatings, less abrasive grooves with less depth and width was observed and the worn surface of the coatings were smoother which could be due to the dispersion strengthening effect of MWCNTs. Results also indicated that the NiW–MWCNTs nano–composite coatings exhibited better corrosion performance compared to NiW coating and this was due to presence of the MWCNTS particles acting as physical barrier against the corrosion attack and thus hindering the dissolution of Ni through absorbing on the anodic sites.

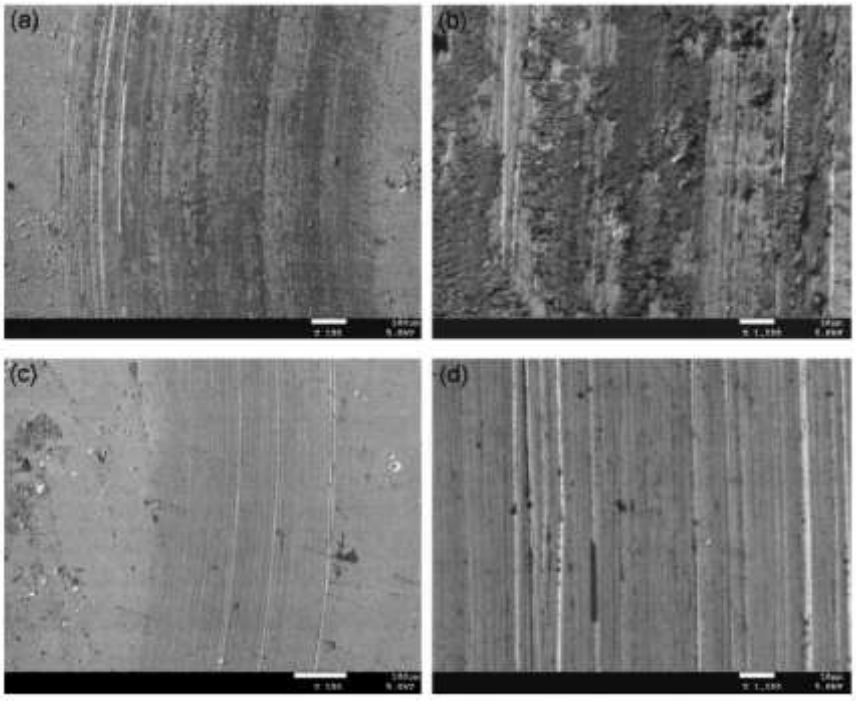

Figure 2.10 SEM morphology from general view and inside of the wear track of the NiW alloy (a, b) and NiW–MWCNTs (2 $g.L^{-1}$) composite coating (c, d). [39]

He et al. [40] studied the effect of mechanical and ultrasound agitation on the properties of pulse electrodeposited NiW/MWCNTs composite coatings. They found that the surface of the NiW/MWCNTs composite coatings prepared using mechanical stirring was non–uniform and coarse due to agglomeration and uneven dispersion of the MWCNTs. This lead to low microhardness, corrosion resistance, and anti–wear performance of the composite coating. Unlike mechanical stirring, ultrasound stirring evenly distributed the MWCNTs within the NiW coatings, resulting in smoother surface, better microhardness, higher tribological and corrosion performance.

2.1.11 Ni–B/ NiW–BN Duplex Composite Coatings

Li et al. [42] evaluated the anti–wear properties of novel electrodeposited Ni–B/ NiW–BN duplex composite coating utilizing an abrasion tester based on ASTM D6037–2013 under dry sliding, room temperature and 45–50% humidity conditions. They found that the co–deposition

of BN nanoparticles with NiW had influence on the content of Ni and W of the deposits, improvement in hardness, and wear resistance of the duplex composite coating. It was also observed that the incorporation of graphite–like BN nanoparticles into spherical–like NiW matrix enhanced the surface roughness and reduced the porosity. The maximum wear performance was achieved when the concentration of BN in the electrodeposition bath was 5 $g.L^{-1}$. They also reported that highest microhardness and best corrosion resistance, and wear performance was achieved when the ultrasonic agitation power was 70W.

2.1.12 NiW– ZrO_2 Composite Coatings

ZrO_2 (extremely refractory compound) is commonly used as the second phase in composites due to its high hardness (13 GPa), high temperature oxidation resistance, low thermal conductivity (11×10^{-6} K^{-1}), high density (6 g/cm^3), wear resistance and an excellent combination of high fracture toughness (~10 MPa $m^{1/2}$) and high flexural strength (~1 GPa). [46, 107]

Zhao et al. [100] investigated the micro–hardness and wear performance of NiW–ZrO_2 nano–composite coating. They found that the addition of ZrO_2 into NiW matrix leads to an improved microhardness, wear resistance of the material and this was due to dispersion and particle strengthening provided by ZrO_2 nanoparticles. ZrO_2 also may act as solid–lubricant between the contact surfaces reducing the material loss rate from the coating. It was also observed that NiW–ZrO_2 nano–composite exhibited the highest corrosion performance compared to NiW coating which was attributed to adsorption of ZrO_2 nanoparticles on the cathode surface, and thus reduction in active surface area of the cathode.

Lehman et al. [45] studied the corrosion performance and wear behavior of electrodeposited NiW coatings modified by ZrO_2 particles. They found that the wear resistance of the NiW–ZrO_2 coatings increases with increase of the ZrO_2 content. However, coatings with more than about 5 wt% ceramic content become brittle and display much lower wear performance. This was attributed to weak interfacial debonding between particle and NiW matrix with increase of ceramic phase content.

Results also indicated that the corrosion resistance of NiW/ZrO_2 nano–composite coatings were higher compared to NiW coating and increased with increasing content of the ceramic phase.

This was mainly due to a reduction in active surface area of the cathode by the adsorption of an increasing amount of inert ceramic particles.

The same group of researchers also studied the influence of the current density on tribological (wear resistant, friction coefficient) properties of NiW nano–composite coatings reinforced with zirconia particles. Their results indicated that NiW/ZrO_2 nano–composite coatings exhibited high wear resistance and this was attributed to increase of resistance to plastic deformation by addition of ZrO_2 particles to NiW alloy matrix. However, the major wear mechanism was abrasive for all coatings at various current densities (in the range of 5–12 A/dm^2). Current density did not have a significant influence on the friction coefficient and wear index of composite coatings (of 2–3.5 wt.% ZrO_2, 45–55 wt.% W) . The scratch test results also demonstrated that the coatings electrodeposited at currents below than 7 A/dm^2 and containing above 2.5 wt.% ZrO_2 particles exhibit brittle characteristics starting at relatively low load of about 1.5 N. [46]

2.1.13 NiW–P–SiO_2–CeO_2 Composite Coatings

Xu et al. [20] investigated the effect of heat treatment and reinforcement of NiW–P with nanoparticles such as SiO_2 and CeO_2 on micro–hardness and surface properties of the coating. Results indicated that the nano–SiO_2 and nano–CeO_2 particles were dispersed homogeneously within the NiW–P alloy coating and there was a strong interfacial bonding between the metal matrix, nano–SiO_2, and nano–CeO_2 particles. They also reported that, when the composite coating was heat treated at 400^{o}C for duration of 3h, micro–hardness increased from 641 Hv to 1338 Hv and abrasivity decreased from 3.76 mg/(cm^2·h) to 0.78 mg/(cm^2·h). As shown in XRD results (Figure 2.11), after heat treatment at 400°C for 1h, the diffraction peak becomes narrower, the crystallite size becomes larger, and a large number of peaks related to Ni_3P phase appear which explains the ease in migration ability of phosphorous atom in the coating during the heat treatment.

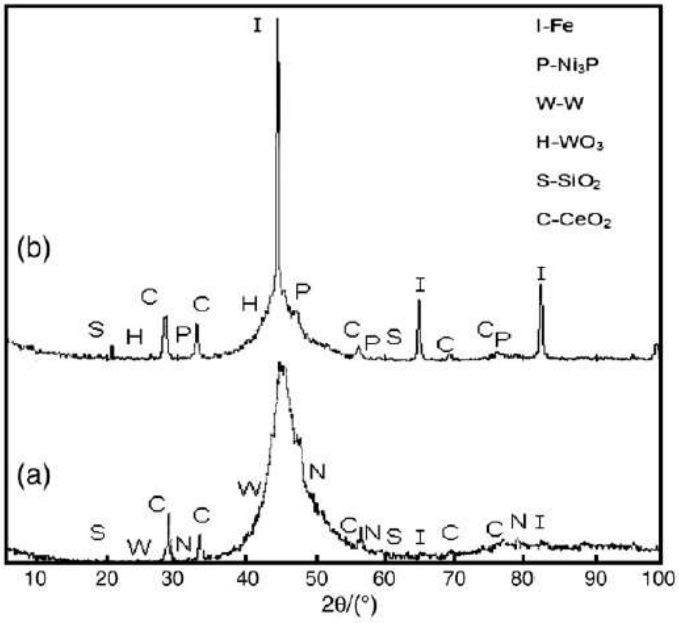

Figure 2.11 X–ray diffraction patterns of NiW–P–SiO_2–CeO_2 composite coatings. (a) phase structure of the coating before heat treatment (as–deposited). (b) phase structure of the coating after heat treatment at 400°C for 1 h. [66]

2.1.14 NiW–ZrO_2–CeO_2 Composite Coatings

Li et al. [108] studied the Structure, surface properties and corrosion resistance of electrodeposited NiW/ZrO_2 nanocrystalline films co–deposited with CeO_2 nanoparticles. They found that NiW/ZrO_2–CeO_2 films exhibited excellent corrosion resistance in corrosive environment. As shown in Nyquist plots in Figure 2.12, the optimal corrosion resistance of coating was obtained at duty cycle of 70% (48.51 kΩ cm^2), average current (I_{av}) of 6 Adm^{-2} (33.58 kΩ cm^2), frequency of 1500 Hz (51 kΩ cm^2), and when duration of electrodeposition was 40 min (70.19 kΩ cm^2). Results also indicated that the incorporation of ZrO_2 in the coating was beneficial to the improvement of the hardness and wear resistance which were highly dependent on the electrodeposition process parameters. For example, the amount of embedded nanoparticles first increased and then decreased when I_{av} exceeded the 6 Adm^{-2}, and this affected the composition, structure, hardness and wear behavior of the composites. The decrease of the hardness at high I_{av} was attributed to the change of composition and the formation of defects in the microstructure. It was also reported that the maximum hardness and

wear resistance were obtained at duty cycle of 70%, frequency of 1500, and when the electrodeposition duration was 40 min.

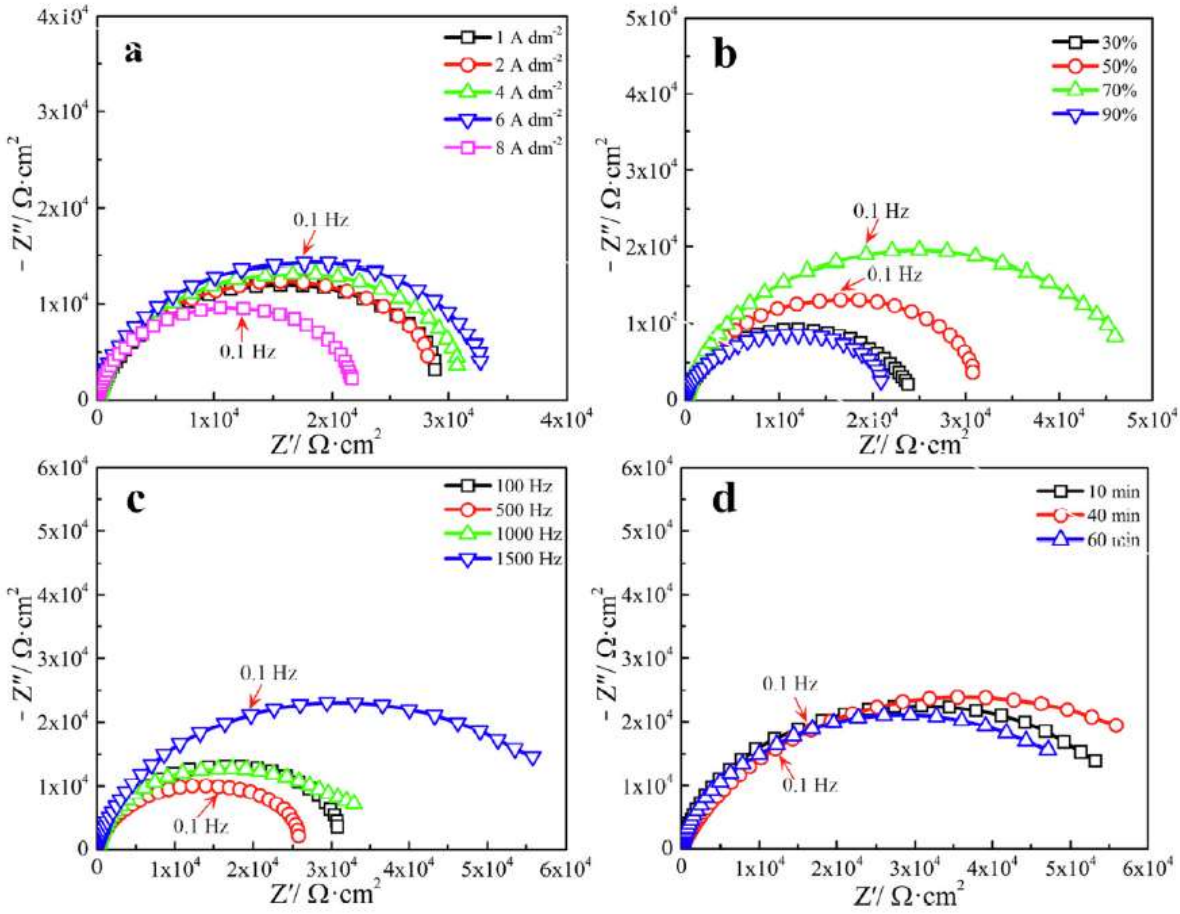

Figure 2.12 Nyquist plots of NiW/ZrO_2–CeO_2 nano–composite fabricated under different (a) average current, (b) duty cycle, (c) frequency and (d) duration in 3.5 wt% NaCl aqueous solution. [108]

2.1.15 NiW–PCTFE Composite Coatings

Hosseini et al. [33] evaluated the corrosion, mechanical and structural properties of NiW–PCTFE nano–composite coating. As shown in Figure 2.13, it was observed that the co–deposition of PCTFE particles into the NiW matrix changed the structure and morphology of the NiW coatings, refined the grain size, and decreased the size of the nodules. The results also indicated that the increase of the PCTFE concentration in the electrodeposition bath, decreased

the microhardness and increased the elastic behavior of the coating. The lowest friction of coefficient was obtained when the concentration of PCTFE in the electrodeposition bath was 4 and 8 $g.L^{-1}$. It was also realized that the corrosion resistance of the NiW coating could be enhanced by incorporation of the PCTFE particles. However, when the PCTFE concentration exceeds the 4 $g.L^{-1}$, corrosion performance of the coating deteriorates.

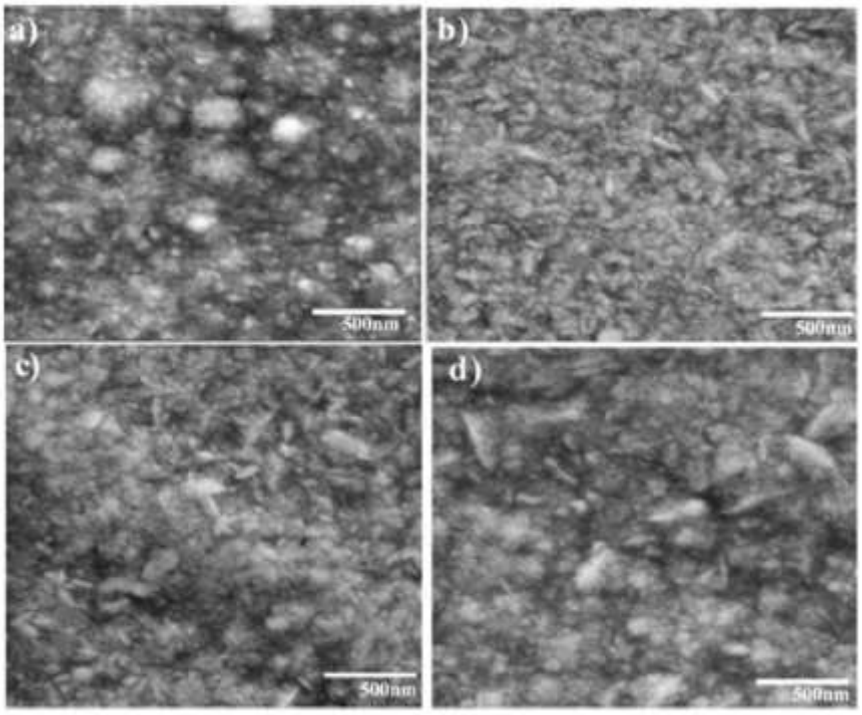

Figure 2.13 SEM micrographs of the surface of a) pure NiW, b) NiW–PCTFE 4 $g.L^{-1}$, c) 8 g. L^{-1} and d) 20 $g.L^{-1}$ coatings.

2.1.16 NiW–Si_3N_4 Composite Coatings

Sassy et al. [36] studied the electroplating mechanism and physicochemical proprieties of deposited NiW–Silicate composite alloy. They found that the NiW composite coatings electrodeposited from silicate–citrate–ammonia bath improved the morphology and the corrosion resistance of copper substrate. The high corrosion resistance of NiW–Silicate was attributed to the long–term stability of NiW–Silicate composite coating into chloride media which resulted in decrease of corrosion currents and increase of corrosion potentials during potentiostatic polarization test. They also observed that NiW–Silicate possessed smooth and

homogeneous surface containing refined and compact grains with cauliflower like–morphology, while NiW coating exhibited a rough and porous structure containing big pores and imperfections.

2.1.17 NiW–TiN Composite Coatings

Zhang et al. [56] investigated the wear and corrosion resistance of pulse electrodeposited NiW–TiN nano–composite coatings. They found that the co–deposition of TiN nanoparticles with NiW matrix could improve hardness and promote grain refinement due to the high surface energy of TiN nanoparticles. The formed nano–crystalline structure resulted in enhancement in corrosion resistance, mechanical properties, and the anti–wear capability, leading to the long life–time in harsh environments.

2.1.18 NiW–Y_2O_3–ZrO_2 Composite Coatings

Zhang et al. [58] studied the influence of electrodeposition current density, temperature and addition of particles on surface morphology and corrosion properties of NiW–Y_2O_3–ZrO_2 nano–composite coating. Coatings with outstanding corrosion performance with crack–free, fine, and uniform surface morphology were obtained at temperature of 60°C, current density of 1.5 A.dm^{-2}, Y_2O_3 and ZrO_2 concentration in the electrodeposition bath was 10 g. L^{-1}. The value of corrosion current density and corrosion rate of nano–composite were reported (2.81×10^{-7}A cm^{-2}) and (0.0033 mm a^{-1}) respectively, which were smaller by an order of magnitude than that of NiW coating (6.67×10^{-6} A cm^{-2}, 0.0779 mm a^{-1}). The high corrosion resistance of nano–composite coatings was firstly attributed to presence of Y_2O_3 and ZrO_2 in NiW matrix acting as physical barriers against the corrosive environment and secondly it was related to the influence of these nanoparticles on formation of microcells causing uniform corrosion and increasing the resistance of the coatings to localized form of corrosion attack.

2.1.19 NiW–Y_2O_3–TN Composite Coatings

Li et al. [57] evaluated the surface properties and corrosion performance of the electrodeposited NiW/TiN–Y_2O_3 nano–crystalline coating. Their results indicated that the co–deposition of TiN

and Y_2O_3 particles with NiW alloy improved the hardness and corrosion resistance of the NiW composite coating. It was also observed that the nano–crystalline coatings exhibited crack–free, compact, and spherical nodular–like morphology. The maximum hardness and wear performance were obtained at the duty cycle of 50%, frequency of 100 Hz, 6 A/cm^2 and duration time of 60 min, while the maximum corrosion resistance was obtained at duty cycle of 70%, frequency of 1000 Hz, average current density of 4 Adm^{-2}, and duration time of 40 min. Therefore, the coating does not own the maximum hardness under the parameters for the best corrosion resistance.

2.1.20 NiW– PTFE Composite Coatings

Farzaneh et al. [59] investigated the electrochemical, structural, and nano tribological behavior of NiW–PTFE nano–composite coatings prepared by tartrate bath. Their results indicated that the NiW/PTFE nano–composite demonstrated higher electrochemical and tribological performance than NiW coating. This was attributed to grain refinement, modification of structure, and reduction of the capacitance of the double layer values by presence of PTFE particles. It was also reported that the corrosion rate and surface roughness of the nano–composite coating was 55 times less than NiW coating when the concentration of PTFE in the electrodeposition bath was 8 $g.L^{-1}$.

Sangeetha et al. [61] studied the corrosion performance of pulsed electrodeposited NiW/PTFE nano–composite and compared it to that of the NiW coating deposited on mild steel substrate. They found that, the NiW/PTFE nano–composite coating exhibited better corrosion performance, lower friction coefficient, moderate microhardness, smoother surface, and excellent hydrophobicity (109.9°) than the NiW alloy coating. This was attributed to chemically inert and solid–lubricant nature of the NiW/PTFE nano–composite coatings.

2.1.21 NiW–WC Composite Coatings

Boonyongmaneerat et al. [109] investigated the effects of WC addition on structure and hardness of electrodeposited NiW coatings. They found that the microstructure, and hardness of the composite could be greatly influenced by parameters such as current density, WC content,

and particle size. These parameters have influence on transportation rates of the plating metals and particles, and the evolution of hydrogen in the electrodeposition baths. It was concluded that the reduction of the particle size of WC improves the uniformity of WC in the deposit, resulting in enhanced hardness which surpasses that of NiW alloys. The most significant hardness enhancement (~10 GPa) was observed when the WC content in the plating bath was increased from 0.2 $g.L^{-1}$ to 1 $g.L^{-1}$. The reported optimum applied current density to obtain non–porous and uniform structure was 0.15 $A.cm^{-2}$.

Figure 2.14 displays the hardness of NiW–WC composites as a function of WC content in a plating bath which were electrodeposited using different current densities and inclusion sizes.

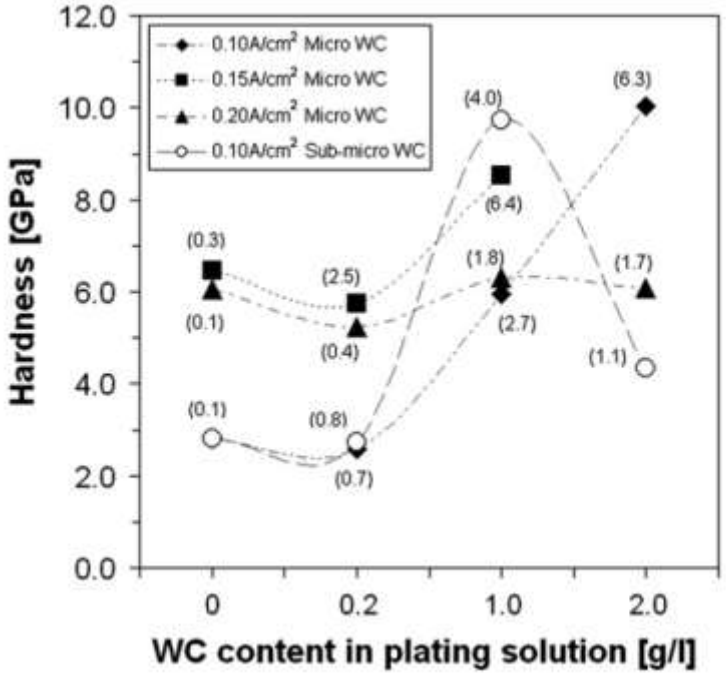

Figure 2.14 The hardness of NiW–WC as a function of WC content in a plating solution electrodeposited at various current densities. [109]

2.1.22 NiW–Co Composite Coatings

Oliveira et al. [51] investigated the influence of the current density, temperature and bath pH on properties of electrodeposited NiW–Co alloys. The corrosion test results demonstrated that the highest corrosion performance with lowest corrosion current density (5.817×10^{-6} A/cm^2)

and the highest polarization resistance (5251 U cm^2) was obtained when the coatings were deposited at the conditions of 100 mA/cm^2 (current density), 55ºC (temperature), and 8 (pH).

In a similar study, Portela et al. [52] investigated the influence of electrodeposition parameter on morphology and anticorrosive properties of the NiW–Co coatings. The highest corrosion resistance was obtained when the coatings had rough surface morphology and grain size of 28 nm and were electrodeposited at the lowest temperature of 353.15 K and the lowest current density of 100 A/m^2.

According to literature, there is no research activities reported on electrodeposition of NiW–CeO_2 and NiW–SiC–CeO_2, NiW–hBN, and NiW–SiC–hBN composites and investigation on their microstructure, corrosion, and tribological properties. Therefore, following research objectives and methodology were proposed.

CHAPTER 3 OBJECTIVES AND METHODOLOGY

The main objective of our project is to develop a low–cost coating material with outstanding corrosion and tribological properties as a potential replacement for hard chromium by means of electrodeposition process. The specific objectives are as follows:

- Deposition of nickel–tungsten (NiW) from an electrolyte containing nickel sulfate as source of nickel ions, sodium tungstate as a source of tungstate ions, citric acid as a complexing agent, sodium saccharin as stress reducer, and an effective grain refiner to reduce the grain size of deposit.
- Fabrication of NiW composites with silicon carbide (SiC), cerium oxide (CeO_2), and hexagonal boron nitride (hBN).
- Characterization of the electrochemical, physic–chemical, mechanical and tribological properties of the above coatings.
- Making correlation between the deposition parameters, composition, structure, and properties of deposits such as mechanical (nano–hardness, elastic modulus), tribological (wear rate, coefficient of friction), and corrosion resistance of the coatings.
- Determination of the best coating composition, which may apply to aerospace, automobile, or electronic sectors.

To address these objectives, the methodology is based on the following:

- The utilization of the DC method and pulse reverse current waveforms to fabricate NiW and its composite with SiC, CeO_2, and hBN.
- The utilization of appropriate grain refiner to reduce the grain size of deposit in order to enhance its corrosion, mechanical, and tribological properties.
- Optimization of the concentration of electrolyte ingredients to achieve stable electrolyte with respect to bath life and preventing the formation of any precipitate forms of nickel hydroxide and nickel tungstate in electrolyte.
- Optimization of experimental parameters of electrodeposition process including applied current density in the case of DC electrodeposition, forward and reversed current densities and pulse durations in the case of reversed pulse electrodeposition, operating bath temperature, and electrolyte pH. The intention of such optimization was to obtain

a decent coating of NiW having an optimum content of W, pit–free and defect–free, homogeneous in thickness across a wide range of surface, and enhance corrosion, mechanical, and tribological performances.

CHAPTER 4 EXPERIMENTAL METHOD

In this chapter we present an overview on the experimental methodology applied in this research work including the coating deposition and characterization methods. First, the electrodeposition bath makeup, substrate preparation, and electrodeposition bath setup were briefly discussed. Then, characterization methods for morphology, composition, and grain structure, mechanical, tribological, and corrosion properties were addressed in the second part.

4.1 Electrodeposition bath makeup

The Nickel (Ni) electrodeposition was carried in a bath containing: nickel sulfate ($NiSO_4.6H_2O$) as a source of nickel ions, citric acid as complexing agent, o–Benzoic sulfimide (sodium saccharin, $C_7H_5NO_3S$) as stress reducer, propargyl–oxopropane-2, 3–dihydroxy as a grain refiner and brightener and DuPont™ Capstone® Fluorosurfactant F–63 as a wetting agent. The nickel tungsten (NiW) coating was electrodeposited onto a brass substrate by dissolving of sodium tungstate dehydrate ($Na_2WO_4.2H_2O$) as a source of tungstate ions in the same electroplating bath that was used for Ni electrodeposition. NiW−SiC electrodeposition bath was prepared by adding SiC particles (20 and 40 $g.L^{-1}$) and a dispersant agent such as polyethyleneimine into the optimized NiW bath. NiW−CeO_2 and NiW−SiC−CeO_2 baths were prepared by adding certain amounts of CeO_2 and mixture of SiC and CeO_2 into the optimized NiW electrodeposition bath, respectively.

In this formulation, citric acid is a most commonly used complexing agent to prevent direct reaction between nickel and tungstate ions by forming complexes with both tungstate (WO_4^{2-}) and nickel (Ni^{2+}) ions. Such direct interaction would cause formation of non–soluble nickel tungstate compound in electrolyte [22–23]. Sodium saccharin was utilized in electrodeposition bath as a grain refiner and stress reliever to reduce the internal stress within the electrodeposited coating materials by increasing the overpotential on the surface of the cathode. [85, 110]

In order to obtain a uniform deposit with mirror–finish surface, propargyl–oxo–propane-2, 3–dihydroxy was used as a grain refiner and brightener. This compound increases the nucleation sites for the reduction of nickel ions on the surface of brass substrate resulting decrease in grain size of nickel. As well, this compound contains an acetylene–type of bonding (i.e. –C≡C–H) at the end of its molecular chain. This typical bond has a high tendency to be adsorbed at high current density areas of substrate during the electrodeposition providing better control over

diffusion of Ni ions towards the cathode [25]. Lastly, Capstone® fluoro–surfactant FS–63 (DuPont™) was selected as the most effective low foaming type wetting agent to lower the surface tension and l facilitate release of gas bubbles from the surface of electrodes [26]. The composition and electrodeposition operating conditions used for NiW and NiW–SiC are summarized in Table 4.1. Figure 4.1 displays the chemical formula of the plating bath ingredients.

Table 4.1 Electrodeposition electrolyte ingredients and experimental parameters

Chemical compound	**Concentration**
Nickel sulfate	29.5–30 ($g.L^{-1}$)
Sodium tungstate	58–60 ($g.L^{-1}$)
Citric acid	63–67 ($g.L^{-1}$)
Ammonia	58 ($ml.L^{-1}$)
Sulfuric acid	As needed
Propargyl–oxo propane-2,3–dihydroxy	0.9–1 ($g.L^{-1}$)
DuPontTM Capstone® Fluoro–surfactant FS– 63	1.8-2 ($g.L^{-1}$)
Sodium saccharin	0.5–1 ($g.L^{-1}$)
Polyethyleneimine branched, Mn~600 by GPC	0.5 ($g.L^{-1}$)
Experimental parameters	
pH	7.8–8.0
Temperature	58–61 ^{o}C

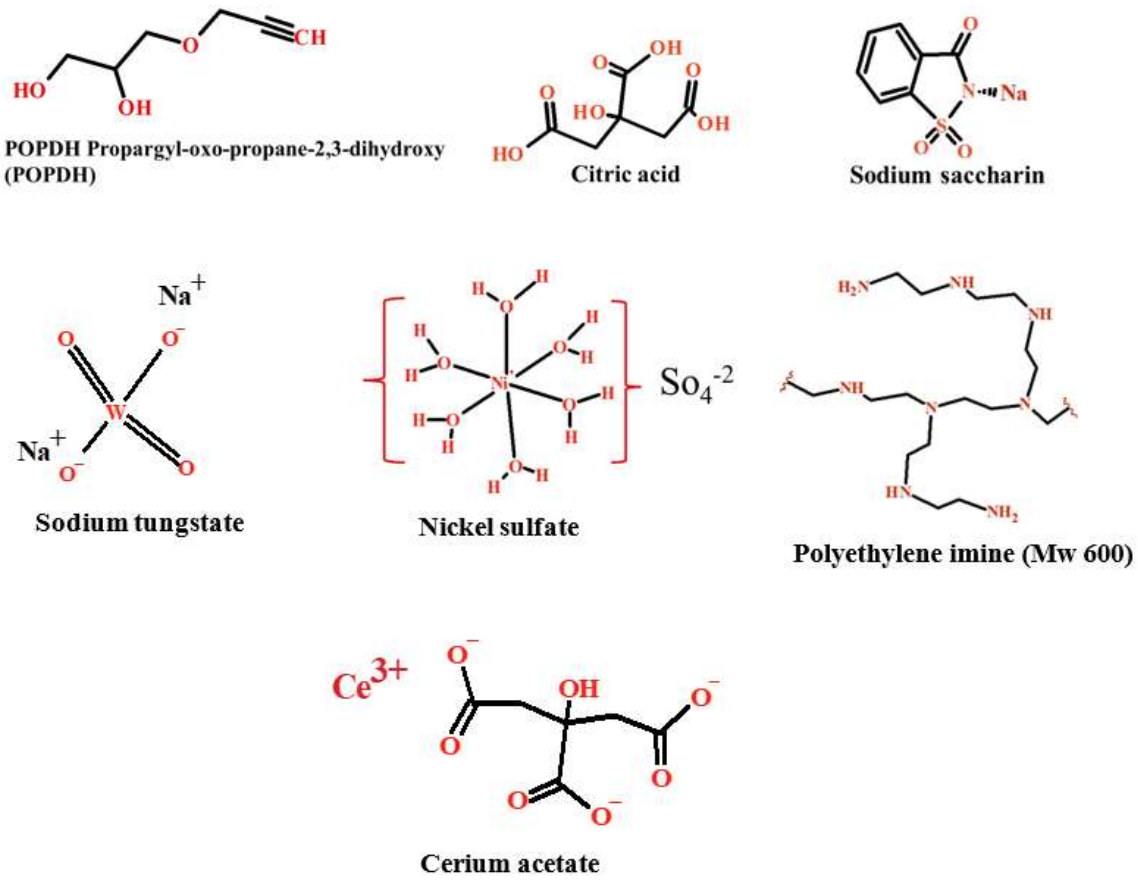

Figure 4.1 Chemical formula of plating bath ingredients.

4.2 Sample preparation

The surface of brass substrates were degreased, activated and rinsed prior to electrodeposition process. Substrates were immersed into 50 $g.L^{-1}$ alkaline soap solution (TEC1001; Technic Inc.) at temperature of about 50°C for approximately 1 min followed by rinsing with deionized (DI) water. The substrate was then activated by immersing into dilute sulfuric acid (10% v/v) at room temperature for about 10 sec followed by rinsing with DI water. In order to determine the cleanliness of the substrate, water break test was performed. In this testing protocol, the substrate was gently rinsed with deionized water following the final rinse step. The substrate was considered clean if the water completely wets the surface.

4.3 Electrodeposition setup

The bath optimization including the type and concentrations of the solution ingredients, solution pH, operating temperature, and deposition duration will be initiated in beaker–scale and it can be scaled up to larger volume using the accessories as demonstrated in Figure 4.2. The anode was platinized titanium mesh (2 cm width and 5 cm length) and the cathode was a surface pre–treated brass substrate with the same dimension as anode. Two such anodes, spaced about 10 cm apart, were supported in plating cell by using clamps and the cathode was placed between the anodes, 5 cm apart from each anode. Reversed pulse plating power supply will be used to provide both direct current (DC) and pulsed reverse (PR) waveforms to electrodeposition bath. Immersion heater connected to temperature controller will be used to keep the solution temperature at optimized value. A filter pump (Flo King Filter System Inc.) connected to polypropylene filter will be used to provide adequate agitation and to keep the solution free of particulates during the deposition. Platinized titanium mesh bars will be used as anodes.

The initial electrodeposition experiments were performed inside a hull cell (Figure 4.3) equipped with heater, thermostat air agitation and air pump to characterize and improve the current density distribution throughout the substrate surface. A platinized titanium mesh sheet was used as anode and brass substrate was used as cathode.

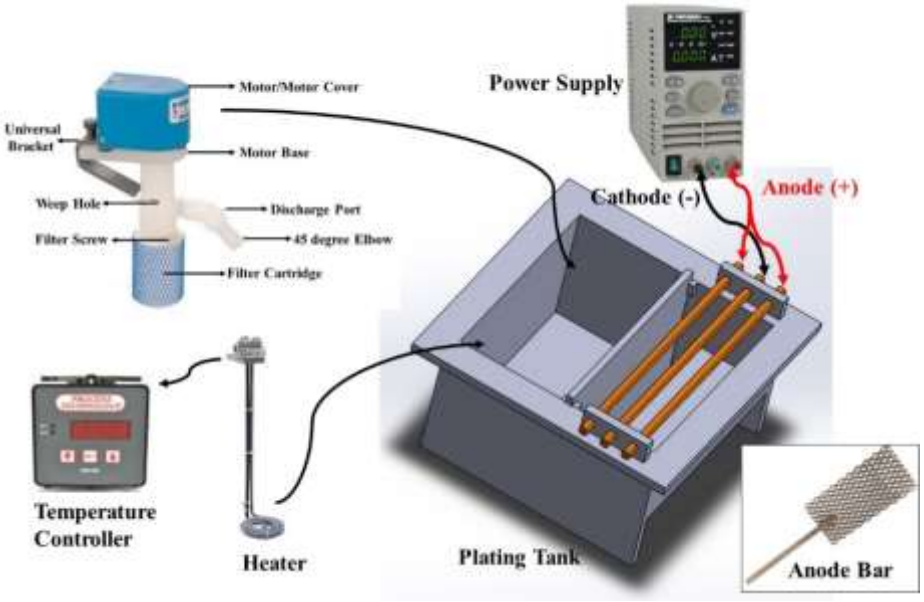

Figure 4.2 Schematic diagram of plating setup in large scale (10-liter plating bath).

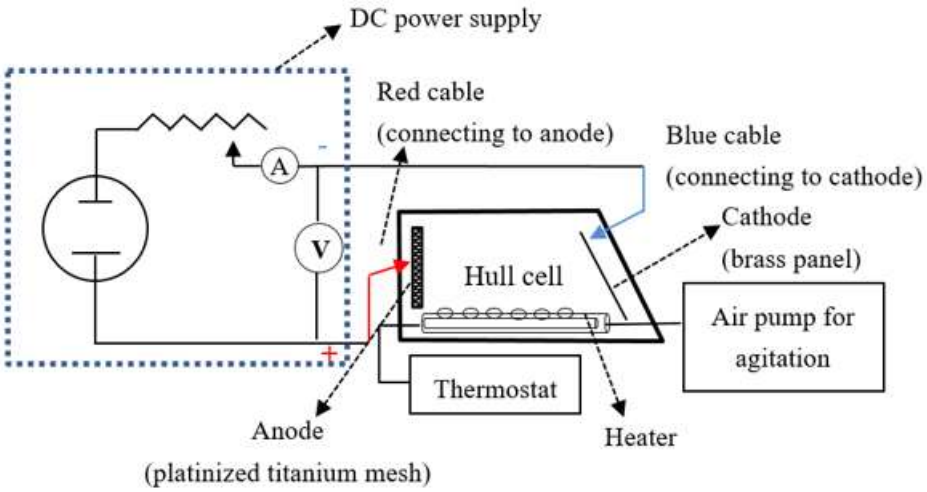

Figure 4.3 Schematic diagram of hull cell equipped with thermostat and air agitation.

4.4 Optimization of PRC waveform

A current waveform (Figure 4.4) composed of direct current (DC, 0.14 A.cm^{-2}, 3 min) and pulsed reverse (0.15 A.cm^{-2} and 16 ms forward, 0.11 A.cm^{-2} and 9 ms reversed) were used to electrodeposit NiW–SiC composite.

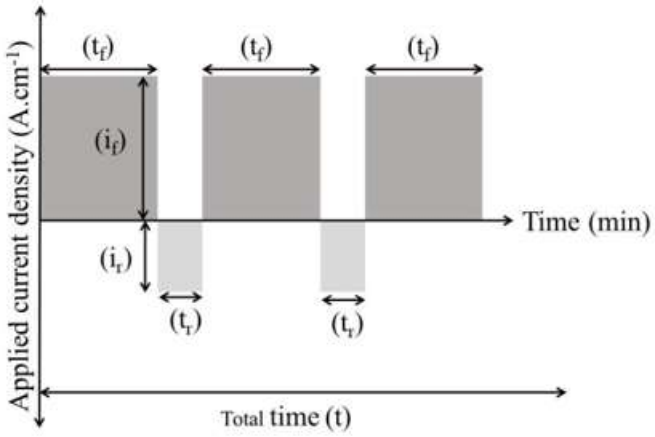

Figure 4.4 Pulsed reverse waveform; i_f = 0.15 A.cm^{-2}; i_r = 0.11 A.cm^{-2}; t_f = 16 ms; t_r = 9 ms; and total time =30 min, i_f = forward current density. i_r = reversed current density; t_f = forward pulse duration; t_r = pulse reverse duration.

4.5 Characterization of deposits

4.5.1 Morphology and composition

The tungsten content, grain size and surface morphology of the deposits were characterized by energy dispersive spectroscopy (EDS), transmission electron microscopy (TEM, Jeol JEM–2100F), scanning transmission electron microscopy (STEM, Hitachi Model HT7700), X–ray diffraction (XRD, Bruker), and scanning electron microscopy (SEM, Joel 7600 TFE), respectively. A Gallium Focused Ion Beam (Ga–FIB, Hitachi FB–2000A) was also used to extract from the NiW coated samples, the thin lamellae (~100 nm) that were observed with the TEM. As well, Time–of–Flight Secondary Ion Mass Spectrometry (*TOF–SIMS;* PHI TRIFT V nanoTOF) and X–ray photoelectron spectroscopy (XPS, Thermo Scientific Aluminum–kα) were used to characterize the surface film on deposits before and after potentiodynamic corrosion test in order to obtain information about the change in chemical composition on the surface of deposits after corrosion testing.

4.5.2 Wear properties

In this research work, two types of Pin–on–disk tribometers were employed to evaluate the wear resistance and to measure the coefficient of friction of the coatings (Rtec Instruments and a custom–built tribometer). The tests were performed under dry air conditions and ambient temperature. The coefficients of friction were measured according to ASTM Standard G99–05 (2010). Spherical AISI 52100 steel balls and alumina balls with a diameter of 1.6 mm and 4.7 mm were used for the pin specimen. Two sets of parameters were used to evaluate the coefficients of friction. In one set, the sliding velocity and the sliding distance were 100 mm/s and 1000 m and the applied load was 2 N. The coefficients of friction were continuously recorded with respect to the sliding distance. Each friction experiment was repeated six times and the average results were reported. The volume of the worn tracks was measured using a 3D profilometer (Bruker ContourX–100). In the second set, the sliding velocity and the number of revolutions were 180 mm/s and 3500, respectively. The applied load was also 1 N. The volume of the worn tracks were measured using a Profilometer (Bruker Dektak XT). Each friction experiment was repeated three times and the average results were reported.

Wear performance of the composite coating is mainly determined by distribution and properties of incorporated particles. Uniform distribution of reinforced particles in the composite coatings can greatly influence the hardness and wear performance of the composite coatings. [111]

In general, the wear mechanism mainly depends on the load, sliding velocity, hardness and surface roughness, lubrication etc and it can be classified into three types: abrasive wear, fatigue wear, and adhesive wear as shown in Figure 4.5. [112]

Abrasive wear usually occurs when hard and rough surface pass over a softer surface. In this wear type, when the asperity is not strong enough, it can be removed and becomes a debris particle between the contact surfaces. Otherwise, the asperity may cause scratches on the softer surface and produce a cutting debris. [112]

Fatigue wear generally occurs when a number of cycles are needed to generate wear debris. Periodical force may induce the creation of surface and subsurface cracks resulting in severe damage and failure of the system. The last wear type is adhesive wear which is caused by localized atomic bonding between the two solid surfaces and is stronger than the strength of either of the materials. During the process, Material can be transferred from one surface to the other. [112, 113]

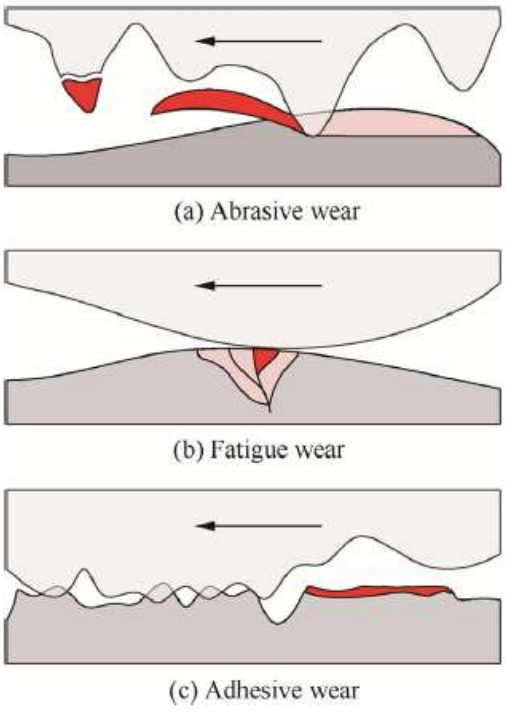

Figure 4.5 Different wear mechanisms. [112]

4.5.3 Corrosion properties

Potentiostat (Princeton Applied Research Potentiostat/Galvanostat Model 273A) was used for studying of pitting corrosion behaviors of the deposits. The potentiostat was equipped with CorrWare software enabling to apply potential scans remotely through the software. Potentiodynamic polarization (PP) scans were performed from -0.6 to 1.0 V vs. Ecorr at room temperature and 5 $mV.s^{-1}$ scan rate. Similarly, cyclic potentiodynamic polarization (CPP) scans were performed from -0.6 to 1.0 V in forward scan at room temperature and 5 $mV.s^{-1}$ scan rate and from 1.0 to -1.0 V in reversed scan with 5 $mV.s^{-1}$ scan rate. For all the PP and CPP experiments, silver/silver sulfate electrode and graphite rod were used as reference and counter electrodes, respectively. Figure 4.6 displays the schematic diagram of the experimental setup for performing of corrosion tests. As it can be seen, the surface of the specimen was covered with an insulating 3M tape to expose 1 cm^2 of the surface to corrosive liquid (artificial sea water). The composition of the artificial sea water is summarized in Table 4.2.

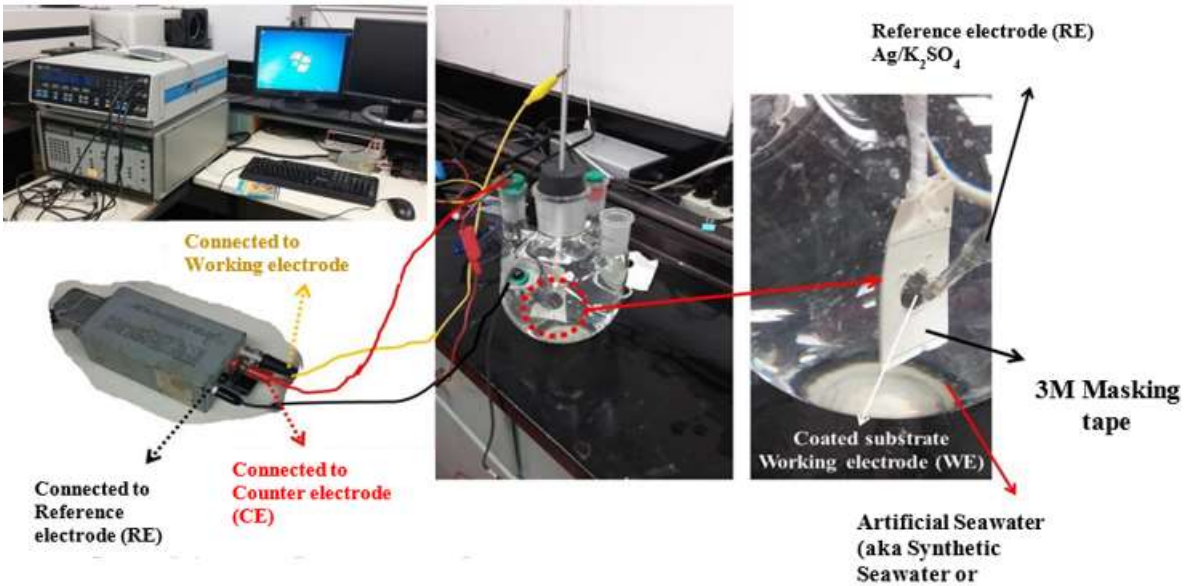

Figure 4.6 Experimental setup for performing PP and CPP corrosions tests.

Table 4.2 Composition of artificial seawater

Ingredients	**Concentration (wt.%)**
NaCl	58.49
Na_2SO_4	9.75
$CaCl_2$	2.765
KCl	1.645
$NaHCO_3$	0.477
KBr	0.238
H_3BO_3 $SrCl_2.6H_2O$	0.071 0.095
NaF	0.007
$MgCl_2$	26.46

The corrosion current density (I_{corr}) and corrosion potential (Ecorr) were determined from the intersection point of the individual cathodic and anodic slopes of Tafel curves at which the anodic current exactly equals the cathodic current. [114]

Polarization resistance (R_p) measurements are used to determine the protective ability of electrodeposited coatings in the corrosive environment. R_p value is inversely proportional to the I_{Corr}. Therefore, higher polarization resistance means lower corrosion current. [115, 116]

Polarization resistance (R_p) can be calculated as follows: [115, 116]

$$Rp = \frac{\beta a \,.\, \beta c}{2.3\,(ICorr)(\beta a+\beta c)} \qquad (6)$$

where i_{corr}, R_p, β_a, and β_c are the corrosion current density (A/cm^2), the polarization resistance (Ω. cm^2), the anodic Tafel slope (volts or millivolts /decade of current), and the cathodic Tafel slope (volts or millivolts /decade of current), respectively. The quantity of $\frac{\beta a \times \beta c}{\beta a+\beta c}$ refers to the Tafel constant. Figure 4.7 displays a typical potentiodynamic polarization plot. [116]

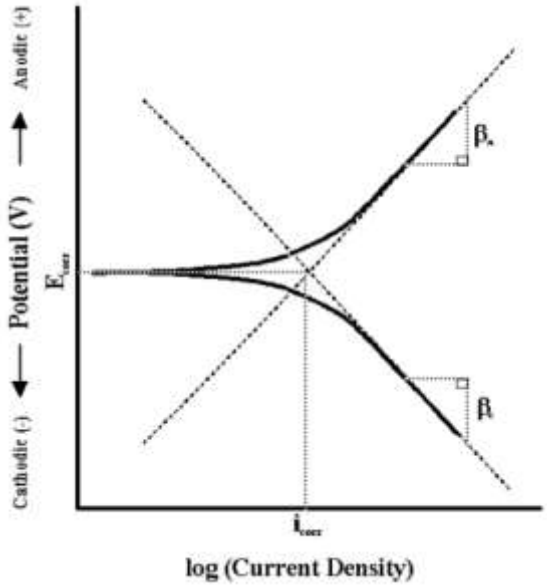

Figure 4.7 Typical potentiodynamic polarization plot. [116]

The I_{corr} value may also be used to calculate the corrosion rate (CR) as follows: [117]

$$CR = \frac{ICorr \,.\, K.\, EW}{d.A} \qquad (7)$$

Where I_{Corr} is the corrosion current, K is the constant factor (=3272), E_w is Equivalent weight (grams/equivalent), d is NiW density (g/cm^3) and A is surface area of working electrode (cm^2).

4.5.4 Mechanical properties

The hardness and elastic modulus were evaluated by using a nano–indenter (Nanomechanics, Inc) with a conical diamond indenter tip (90 degrees, 5µm radius spherical end). The pre–test parameters are displayed in Table 4.3.

Table 4.3 Pre–test parameters for nano–indentation

Parameters	**Value**
Target load (mN)	200
Target depth (nm)	5000
Poisson's Ratio of Sample	0.3
Target Indentation Strain Rate (s^{-1})	0.2
Target Frequency (Hz)	100
Surface Approach Velocity ($nm.s^{-1}$)	100
Hold Maximum Load Time (s)	1

During the nanoindentation process, the indenter tip is pressed into the sample surface and the response of interest is recorded as the load–displacement curve which is often called the P–h curve. [118]

In Nano–indentation process, target load **s**pecifies the load at which the indentation test will terminate. This value also determines the load at which the average results will be reported. Poisson's ratio of the sample was used in calculating the elastic modulus from indentation data. Target Indentation Strain Rate method attempts to maintain a constant indentation strain rate during loading and this value sets that strain rate. The loading algorithm of a constant indentation strain rate test follows a constant $\frac{dp/dt}{P}$, where P is load and t is time. The result is an exponential load rate. This is an important loading condition for strain rate sensitive materials. In order to obtain reliable statistics, 100 indents on various locations for each specimen were performed. [119, 120, 121]

Figures 4.8 and 4.9 display the typical nano–indentation load–displacement curve and indentation profile.

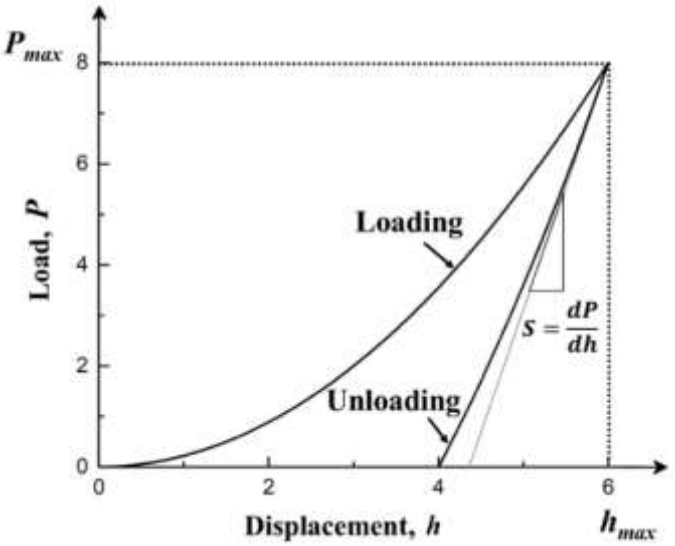

Figure 4.1. Typical load–displacement curve. [122]

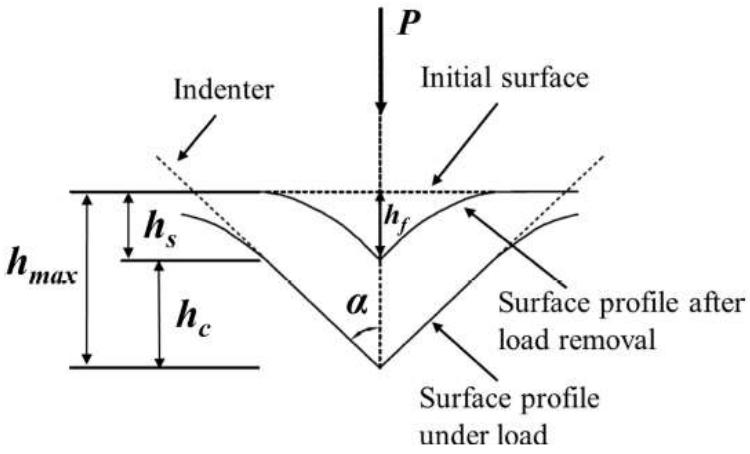

Figure 4.8 Schematic diagram of parameters after unloading. [68]

h_f , h_s, and h_c are identified as indentation depth after unloading, the elastic displacement of the surface at the perimeter and the maximum contact depth at maximum loading point, respectively. It can be concluded that maximum displacement (h_{max}) is obtained by the following equation: [67, 68]

$$h_{max} = h_c + h_s \qquad (8)$$

Equivalent modulus (E_r) and hardness (H) by Oliver & Pharr method, can be defined by the following formula:

$$H = \frac{Pmax}{Ac} \quad (9)$$

$$E_r = \frac{S\sqrt{\Pi}}{2\beta\sqrt{Ac}} \quad (10)$$

where Pmax is the maximum applied load, A_c is the projected contact area of a perfect Berkovich indenter, S is the slope of the unload at the maximum displacement point (hmax), and β is the parameter related to the shape of the indenter. For the Berkovich indenter, the value of β is 1.14.

A_c and S can be calculated by the following formula: [67, 68]

$$Ac = 24.5\ h_c^2 \quad (11)$$

$$S = \frac{dp}{dh} = \alpha m\ (h_{max} - h_f)^{(m-1)} \quad (12)$$

The elastic modulus of the tested material, E, can be related to the equivalent modulus using the following formula: [67, 68]

$$\frac{1}{Er} = \frac{1-\nu 2}{E} + \frac{1-\nu i2}{Ei} \quad (13)$$

where E_i and ν_i are the elastic modulus and Poisson's ratio of the indenter material, respectively. For diamond indenter: Ei = 1141 GPa, ν_i = 0.07. ν is the Poisson's ratio of the sample, which is assumed to be 0.38 (measured by tensile experiments).

CHAPTER 5 NOVELTY CONTRIBUTIONS TO ALL ARTICLES

Novel contribution to Article 1:

The novelty related to this article is to compare the influence of applied DC and PRC deposition methods on corrosion and tribological performances of NiW-SiC composite materials. To the best of our knowledge, there is no such comparison has been reported in literature.

Novel contribution to Article 2:

The novelty related to this article is to investigate for the first time the pitting corrosion behavior of DC and PRC electrodeposited Ni and NiW coatings using cyclic polarization as well as their mechanical properties by nano–indentation technique.

Novel contribution to Article 3:

The novelty related to this article is to fabricate NiW coating with outstanding mechanical, wear performance, and very low coefficient of friction through precise control of the tungsten (W) content of the deposit through applying a well–designed PRC waveform and using a novel derivative of propargyl compound as a grain refiner and brightener into the deposition bath.

Novel contribution to Article 4:

The novelty to this article was to fabricate a new composite of NiW–SiC–hBN and investigate their microstructure and properties. In this article, the influence of hBN on wear performance and corrosion resistance of DC deposited NiW and NiW–SiC was investigated. It was found that the addition of hBN to NiW matrix enhanced the wear resistance significantly due to high lubricity of hBN. Also, addition of SiC to NiW–hBN improved corrosion resistance significantly by shifting of corrosion potential to more positive values and lowering the corrosion current density.

Novel contribution to Article 5:

The novelty to this article was to fabricate new composites of NiW–CeO_2 and NiW–SiC–CeO_2 composites and investigate their microstructure, corrosion, and tribological properties. It was found that the incorporating of CeO_2 and SiC ceramic particles within the NiW matrix enhanced the corrosion and tribological performance of the deposit and PRC–NiW–SiC–CeO_2 possessed

superior corrosion and wear performance compared to the DC and PRC electrodeposited NiW and NiW–SiC coatings.

Novel contribution to Article 6:

The novelty to this article was to fabricate a new composite of NiW–CeO_2 by DC and PRC electrodeposition processes and investigate their microstructure and properties. It was found that the incorporating of CeO_2 ceramic particles within NiW matrix enhanced the corrosion and wear performance of the deposit and PRC–NiW–CeO_2 possessed superior corrosion and wear performance compared to the DC and PRC electrodeposited Ni and NiW coatings.

CHAPTER 6 ARTICLE 1: HIGHLY CORROSION–RESISTANT PULSED–REVERSE CURRENT ELECTRODEPOSITED NICKEL TUNGSTEN AND NICKEL TUNGSTEN–SILICON CARBIDE COMPOSITES

Authors: Mina Dadvand, Oumarou Savadogo

Article Accepted Prior to Revision: Journal of Applied Electrochemistry, 16 May 2022

Abstract

A detailed analysis of the effect of well–designed pulse–reverse current (PRC) waveform parameters as well as formulation of bath chemistry on the film properties of nickel–tungsten (NiW) and nickel tungsten–silicon carbide (NiW–SiC) coatings on brass substrates are presented. The coatings prepared using PRC, demonstrated outstanding corrosion resistance when exposed to corrosive liquid (artificial sea water) compared to that of direct–current (DC) waveform. In particular, the inclusion of SiC particles within NiW deposit significantly improved corrosion resistance of the coatings. The effect of the concentration of SiC particles in the electrolyte on the surface morphology of coating and its corrosion properties are also Investigated.

Keywords: nickel tungsten–silicon carbide composites, pulsed reverse current electrodeposition, direct current electrodeposition, and Corrosion properties.

6.1 Introduction

In general, corrosion and wear are considered as the main factors resulting in the failure of the mechanical parts. Various coating materials have been developed to enhance the lifetime of engineering parts in harsh environments. [1–5] Some metal matrix composites (MMCs) have been considered as promising class of such materials due to their both enhanced mechanical and corrosion properties. These materials are fabricated by incorporating of reinforcement

phase in the metallic matrix. In fact, a metal composite material is composed of at least two components, one being a metal (host), and the other component (filler) could be a different metal, or a ceramic, or an organic compound. The addition of filler enhances the properties of host material [1–3]. Composite coating materials can be produced through either vacuum–based or non–vacuum–based deposition methods. Coatings produced through non–vacuum–based processes are attractive industrially due to less complexity and lower cost. Among the non–vacuum–based metallic coatings, metallic–ceramic composites are the most promising candidates regarding several factors: resistance against various harsh environments, durability against numerous wearing conditions, lower cost, and less complexity in scaling up the coating process to large volume productions. Metallic–ceramic composites are based on combination of metallic and ceramic components that provides unique possibilities to tailor the mechanical and corrosion properties with respect to numerous applications. One of the most important techniques for fabricating of MMCs is electrodeposition process in which the filler particles are suspended in an electrodeposition electrolyte and co–deposited with metal layer to form a composite coating [5–8]. DC electrodeposition method by far is the most convenient and cost efficient method of electrodeposition. However, it requires the use of additives to control the microstructure and properties as well as current distribution. Generally, the coatings developed by DC method are non–uniform and brittle. Recently, pulsed reverse current electrodeposition method has gained a considerable attention from researchers and industry since it offers a higher level of control over the chemical composition and deposit structure by appropriate selection of the electrodeposition parameters with minimal additive consumption. The coatings obtained by PRC technique are more compact and uniform due to their finer grain size and they also exhibit better mechanical and corrosion properties compared to DC electrodeposited coatings. [9–12]

Nickel (Ni) is the most commonly used metal in electrodeposition as the continuous metallic phase due to several factors such as availability, cost, feasibility of deposition, and its unique properties. However, nickel itself is moderately resistant to corrosion and its resistance can be improved when it is alloyed with other transition metals such as copper, molybdenum, chromium, iron, and tungsten. Among such materials, Ni–W alloys have drawn considerable attention in recent years in a broad range of engineering applications. It is also noteworthy to mention that presence of insoluble particulates such as SiC within the NiW matrix could greatly

enhance the corrosion properties of the coating and this could be possibly due to blockage in anodic faradaic current flow. [4–6]

Few studies have been reported on both DC and PRC electrodeposited NiW and also DC electrodeposited NiW–SiC composites. [4–21] Hosseini et al. [5] investigated the corrosion performance of DC electrodeposited NiW–SiC composite coatings as well as the influence of SiC particle concentration in the plating bath on the composition of composite coatings. It was found that addition of SiC particle into NiW matrix had a significant influence on the morphology, chemical composition, and corrosion performance of the coatings.

The resultant NiW–SiC coatings were smoother, and more corrosion resistant compared to NiW coatings presumably due to the lower dissolution rate of nickel and tungsten of the alloy coating [5]. In a similar study done by Yao and et al. [11] results on corrosion behaviour of DC electrodeposited NiW and NiW–SiC nano–composite indicated that NiW–SiC had better corrosion resistance compared to NiW alloy coating possibly due to reinforced SiC particles, acting as inert physical barriers against creation and propagation of defect corrosion. Allahyarzadeh and et al. [22] reported the corrosion performance of multilayer PRC electrodeposited NiW coating on carbon steel substrates. The coating was composed of two nickel–tungsten layers with alternating chemical compositions of 25 wt% and 11 wt%. Despite the fact that multilayer coatings possessed considerable resistance against pitting corrosion, corrosion resistance was reduced in the presence of chloride ions due to preferential dissolution of nickel and decrease in passive region area. However, the multilayer coating had higher corrosion resistance compared to monolithic coatings. Herein, we report the first study on PRC electrodeposition of NiW, reinforced with micrometer size SiC particles, from an electrolyte containing a propargyl derivative as both grain refiner and brightener and investigate their corrosion performance of such coating. The resulting coatings in this approach were crack–free, uniform and exhibited superior corrosion properties.

6.2 Experimental

6.2.1 Electrodeposition bath formulation

The Ni electrodeposition electrolyte was composed of nickel sulfate ($NiSO_4.6H_2O$) as a source of nickel ions, citric acid as complexing agent, *o*–Benzoic sulfimide (sodium saccharin, $C_7H_5NO_3S$) as stress reducer, propargyl–oxopropane-2,3–dihydroxy as a grain refiner and brightener and DuPont™ Capstone® Fluorosurfactant F–63 as a wetting agent. The NiW plating bath was prepared by addition of sodium tungstate dehydrate ($Na_2WO_4.2H_2O$) as a source of tungstate ions into the same electroplating bath that was used for Ni electrodeposition. And finally, NiW–SiC bath was made by adding SiC particles and a dispersant agent such as polyethyleneimine into NiW plating solution. The composition and operating conditions used for electrodeposition condition of NiW and NiW–SiC are summarized in Table 6.1.

Table 6.1 Composition and Operating Condition of the Electrodeposition Baths

Chemical Compound and Operating Condition	**Concentration**		
	Ni	**NiW**	**NiW–SiC**
Nickel sulfate ($g.L^{-1}$) as a source of nickel ions	29.5–30	29.5–30	29.5–30
Sodium tungstate ($g.L^{-1}$) as a source of tungstate ions	None	58–60	58–60
Citric acid ($g.L^{-1}$) as complexing agent	63–67	63–67	63–67
Ammonia ($ml.L^{-1}$)	~65	~65	~65
Sulfuric acid ($g.L^{-1}$)	As needed	As needed	As needed
Propargyl–oxo–propane–2,3–dihydroxy ($g.L^{-1}$) as grain refiner and brightener	0.9–1	0.9–1	0.9–1
DuPont™ Capstone® Fluoro–surfactant FS–63 ($g.L^{-1}$) as wetting agent	1.8–2	1.8–2	1.8–2
Sodium saccharin ($g.L^{-1}$) as stress reducer	0.5–1	0.5–1	0.5–1
Polyethyleneimine branched, M_n ~600 by GPC ($g.L^{-1}$) as dispersing agent	None	None	0.5
SiC particles (320 grit,)	None	None	20
Experimental condition			
pH	7.8–8.0	7.8–8.0	7.8–8.0
Temperature (ºC)	58–61	58–61	58–61
Duration of electrodeposition (min)	30	30	30

6.2.2 Sample preparation

The surface of brass panel substrates were cleaned (degreased) and activated prior to electrodeposition process. The substrates were first immersed into 50 $g.L^{-1}$ alkaline soap solution (TEC1001; Technic Inc.) at temperature of about 50ºC for approximately 1 min followed by rinsing with deionized (DI) water. The substrates were then activated by immersing into dilute sulfuric acid (10% v/v) at room temperature for about 10 sec followed by rinsing with DI water. Water break test was performed to evaluate the cleanness of the substrates. In this testing protocol, the substrate was gently rinsed with deionized water following the final rinse step. The substrate was considered clean if the water completely wets the surface.

6.2.3 Electrodeposition setup

The electrodeposition setup was composed of an electrodeposition tank containing electrolyte, a pump (Flo King Filter System Inc.) to provide adequate agitation, electrodes (anode and cathode), and a pulsed reverse plating power supply. The electrodeposition bath was placed inside a water circulating bath operating at 60ºC temperature. A pulse reverse power supply (Model pe8005, Plating Electronic GmbH, Germany) was used to apply direct current (DC) and pulse reverse current (PRC) waveforms to electrodeposition bath. The anode used in this work was platinized titanium mesh (2 cm width and 5 cm length) and the cathode was a surface pre–treated brass substrate with the same dimension as anode. Two such anodes, spaced about 10 cm apart, were supported in plating cell by using clamps and the cathode was placed between the anodes, 5 cm apart from each anode.

The initial electrodeposition experiments were performed inside a hull cell equipped with heater, thermostat air agitation and air pump to characterize and improve the current density distribution throughout the substrate surface. A platinized titanium mesh sheet was used as anode and brass substrate was used as cathode.

6.2.4 Optimization of applied waveforms

A current waveform composed of direct current (DC, 0.04 $A.cm^{-2}$, 3 min) and pulsed reverse (0.15 $A.cm^{-2}$ and 16 ms forward, 0.11 $A.cm^{-2}$ and 9 ms reversed) were used to electrodeposit NiW–SiC composite.

6.2.5 Materials characterization

The tungsten content, surface morphology of the deposits, grain size were characterized by energy dispersive spectroscopy (EDS), scanning electron microscopy (SEM, Joel 7600 TFE), and X–ray diffraction (XRD, Bruker D8 Advance), respectively. As well, Time–of–Flight Secondary Ion Mass Spectrometry (TOF–SIMS, PHI TRIFT V nanoTOF), and X–ray photoelectron spectroscopy (XPS, Thermo Scientific Aluminum–kα) was used to characterize the surface film on deposits before and after potentiodynamic corrosion test in order to obtain information about the change in chemical composition on the surface of deposits after corrosion testing. Potentiostat (Princeton Applied Research Potentiostat/Galvanostat Model 273A) was used to investigate the corrosion behavior of the deposits. The potentiostat was equipped with CorrWare software enabling to apply potential scans remotely through the software. Potentiodynamic polarization (PP) scans were performed from -0.6 to 1.0 V vs. E_{corr} at room temperature and 5 $mV.s^{-1}$ scan rate. For all the PP experiments, silver/silver sulfate electrode and graphite rod were used as reference and counter electrodes, respectively. The surface of the specimen was covered with an insulating 3M tape to expose 1 cm^2 of the surface to corrosive liquid (artificial sea water). Table 6.2 shows the composition of the artificial seawater.

Table 6.2 Composition of Artificial Sea Water

Ingredients	**Concentrations (wt%)**
NaCl	58.49
Na_2SO_4	9.75
$CaCl_2$	2.765
KCl	1.645
$NaHCO_3$	0.477
KBr	0.238
H_3BO_3	0.071
$SrCl_2.6H_2O$	0.095
NaF	0.007
$MgCl_2$	26.46

To further enhance NiW coating properties on brass substrates, we studied the effect of SiC addition to electrolyte bath as well as its concentration in both DC and PRC electrodeposited NiW–SiC composite coatings. The morphology of NiW–SiC composites deposited from

electrolyte bath containing 20 to 40 $g.L^{-1}$ SiC particles was investigated using EDS analysis and SEM micrographs.

6.3 Results and discussion

During the pulsed reverse electrodeposition process, the applied current density is interrupted periodically and a reversed or stripping time is introduced into the cycle. Therefore, the diffusion layer around the substrate (cathode) is replenished and also the protrusions on the cathode surface are selectively dissolved periodically resulting in more uniform deposit compared to DC electrodeposition process. In PRC electrodeposition of NiW, the tungsten atoms are the species that are removed selectively from the deposited NiW resulting in reduced content of the induced deposited tungsten. Deposits of NiW with improved surface morphology, corrosion resistance could be produced by optimizing pulse parameters including forward and backward current densities and pulse durations. [9, 23–25] Average current (I_A) and duty cycle (ý) are two important parameters in PRC method and are respectively determined by equations (1) and (2):

$$I_A = I(F).T(F) - I(R).T(R)/T(F)+T(R) \quad (1)$$

$$ý = T(F)/T(F)+T(R) \quad (2)$$

where I(F) is the forward (cathodic) current density, I(R) is the backward (anodic) current density, T(F) is the forward (cathodic) pulse duration and T(R) is the backward (anodic) pulse duration. [9]

6.3.1 Optimization of the brightener/grain refiner concentration using hull cell

Non–uniform electrodeposition process produces unevenly deposit across the surface of substrate. The ability to control the coating uniformity is the key to successful application of this technology. Various factors may cause non–uniform deposition. Examples are electrodeposition bath configuration, anode size and its location and configuration with respect to substrate, operating bath temperature, agitation mode of electrodeposition solution, distance

between anode and substrate (cathode), complexity in the shape of substrate being electrodeposited, etc. These parameters can cause variation of the current density distribution throughout the surface of substrate resulting in non–uniform coating. In order to characterize and improve the current density distribution throughout the substrate surface, initial electrodeposition experiments were performed inside a hull cell. In these experiments, various concentrations of propargyl–oxo–propane-2,3–dihydroxy ($g.L^{-1}$) were added into the electrodeposition electrolyte and the surface coverage of the deposit was examined by bare eye across the surface of brass panel. It was found that at concentration of about 1 $g.L^{-1}$, the surface coverage of the deposit was maximum.

6.3.2 Morphology and chemical composition of NiW and NiW–SiC coatings

A uniform and crack–free coating with the thickness of ~18 µm was observed in surface and cross–section SEM images of DC–NiW coatings (Figure 6.1a) deposited at current density of 40 $mA.cm^{-2}$. EDS spectra and mapping from the surface of DC coated brass substrate suggest that Ni (65.3 wt%) and W (34.7 wt%) are the main elements present in the coatings and were homogeneously distributed across the coating. As well, all PRC–NiW coated samples were very smooth and crack–free throughout the surface of the coating (Fig 6.1b). Furthermore, EDS mapping and line scan analysis from PRC–NiW coated substrates suggest that Ni, W, Cu and Zn are the main elements present in the coating (Figure 6.1b). The presence of a low quantity of Cu and Zn in the coating composition related to the diffusion of Cu and Zn from brass substrate during electrodeposition. A uniform distribution of approximately 14 µm PRC–deposited NiW coating was also observed on PRC–NiW coated substrates (Fig 6.1b).

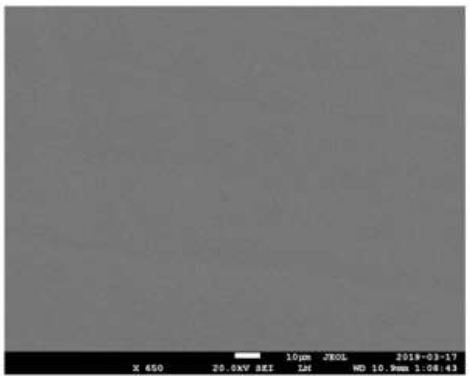

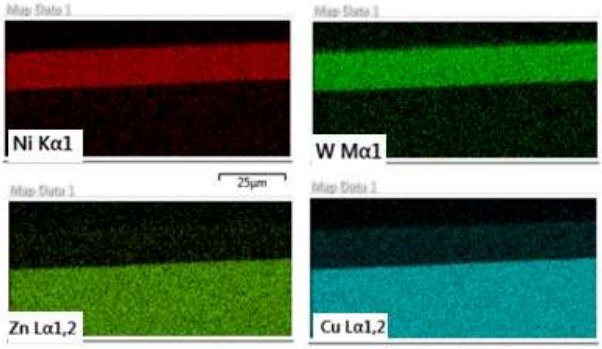
Ni Kα1
W Mα1
25μm
Zn Lα1,2
Cu Lα1,2

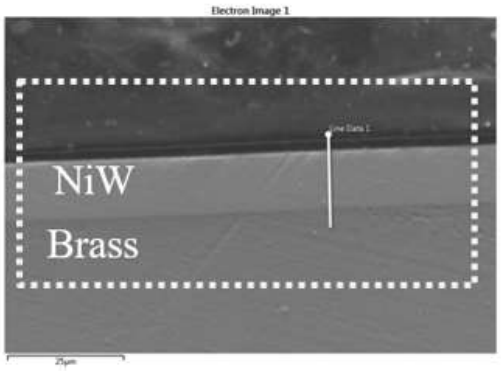
Electron Image 1
NiW
Brass

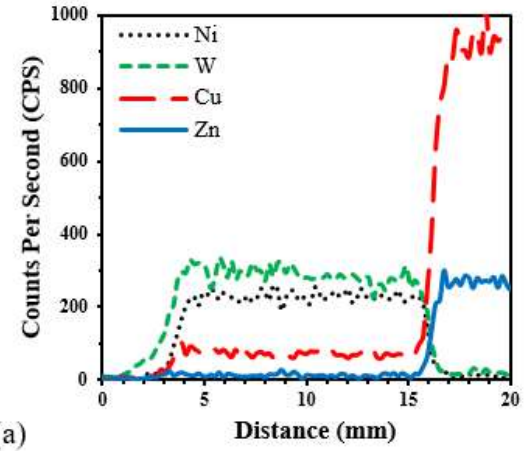
Ni
W
Cu
Zn
Counts Per Second (CPS)
Distance (mm)

(a)

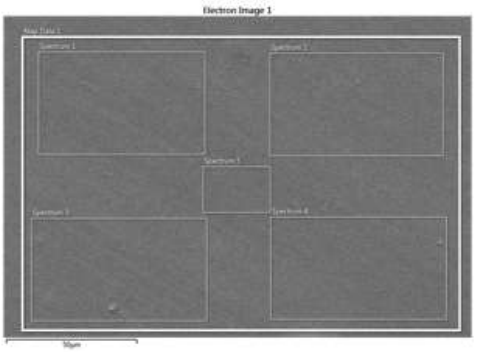
Electron Image 1

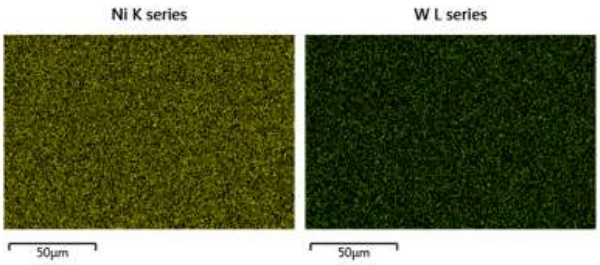
Ni K series
W L series
50μm
50μm

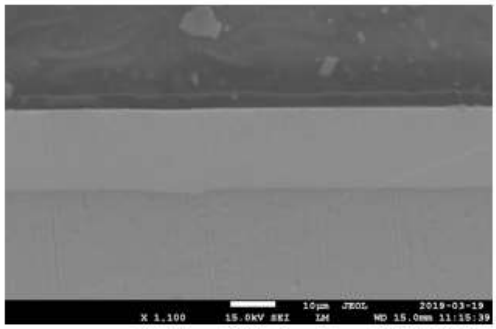

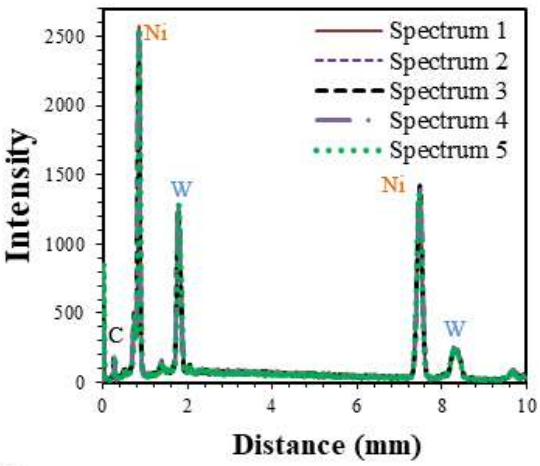
Spectrum 1
Spectrum 2
Spectrum 3
Spectrum 4
Spectrum 5
Ni
W
C
Intensity
Distance (mm)

(b)

Figure 6.1 SEM micrographs (surface and cross section), EDS spectra and mapping of DC–NiW (a) and PRC–NiW (b).

Figures 6.2a and 6.3 display SEM micrographs and EDS analysis of the DC and PRC deposited NiW samples reinforced with SiC (20 $g.L^{-1}$). As we can see, SiC particles in the samples prepared using PRC waveform were embedded within the NiW matrix, while in the case of DC–NiW–SiC, they were mainly deposited on the surface of the coatings. Similar effect has also been reported in few PRC electrodeposition coatings and explained by dissolved protrusions of the coatings by anode pulse current. [26–28]

SEM micrographs and EDS spectra of discrete locations on PRC–NiW–SiC substrates revealed the positive influence on its co–deposited content in the coating from 36.6 wt% to 52.8 wt% when we increased the SiC concentration from 20 to 40 $g.L^{-1}$ in electrolyte. Similarly, Zhang et al. [26] observed higher SiC content in Ni–B/SiC trapped in coatings upon increasing SiC concentration (up to 12.5 $g.L^{-1}$) in the electrodeposition bath. Ni and W contents for PRC–NiW–SiC (20 $g.L^{-1}$) were 40.1 and 23.3 wt% and for PRC–NiW–SiC (40 $g.L^{-1}$) were 35.8 and 11.4 wt% respectively.

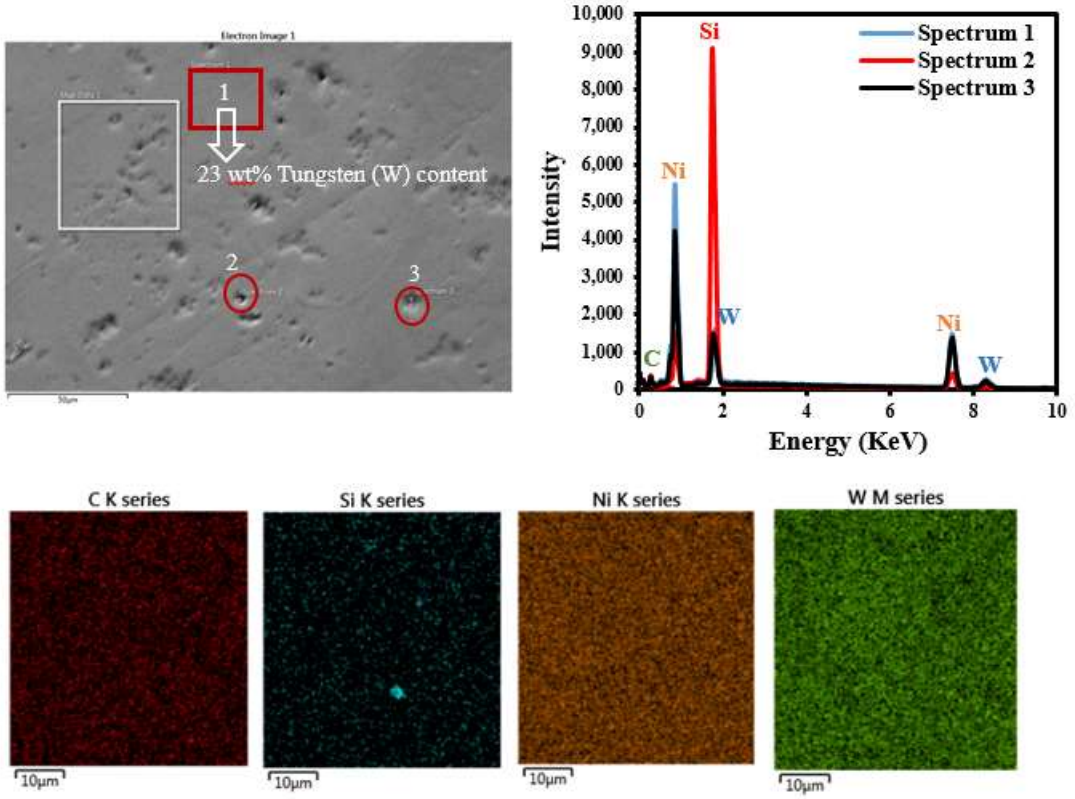
Electron Image 1
1
23 wt% Tungsten (W) content
2
3
50µm
Intensity
Energy (KeV)
Spectrum 1
Spectrum 2
Spectrum 3
Si
Ni
W
C
C K series
Si K series
Ni K series
W M series
10µm

(a)

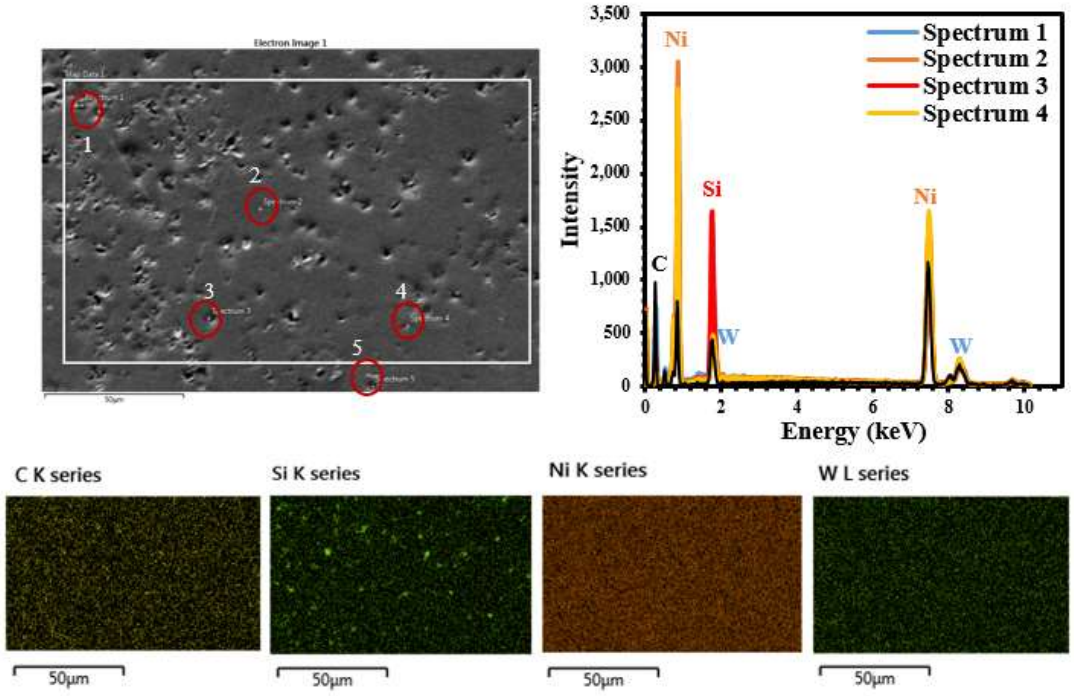
Electron Image 1
1
2
3
4
5
Intensity
Energy (keV)
Spectrum 1
Spectrum 2
Spectrum 3
Spectrum 4
Ni
Si
C
W
C K series
Si K series
Ni K series
W L series
50µm

(b)

Figure 6.2 (a) SEM micrographs taken from the surface PRC–NiW–SiC composite, EDS spectra taken from five different locations on the surface and EDS mapping. Concentration of SiC in electrolyte was 20 $g.L^{-1}$. (b) SEM micrographs taken from the surface of PRC electrodeposited NiW–SiC composite, EDS spectra taken from five different locations on the surface and EDS mapping. Duration of plating was 30 min and concentration of SiC in electrolyte was 40 $g.L^{-1}$.

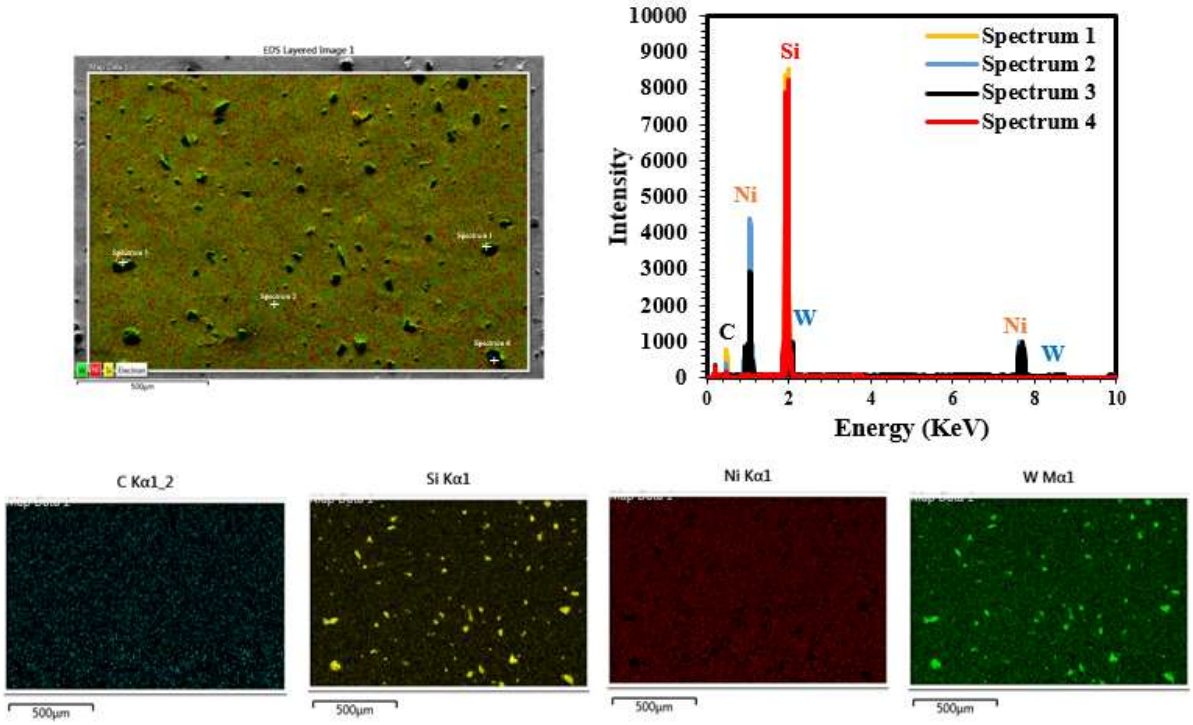

Figure 6.3 SEM micrograph, EDS spectra and EDS mapping from the surface of DC electrodeposited NiW–SiC; Concentration of SiC in electrolyte was 20 $g.L^{-1}$. Duration of plating was 30 min; the applied current density was 40 $mA.cm^{-2}$.

6.3.3 Corrosion behavior of DC and PRC deposited coatings

Potentiodynamic polarization graphs of the electrodeposited DC–Ni, PRC–Ni, DC–NiW, PRC–NiW, DC–NiW–SiC, and PRC–NiW–SiC are shown in Figure 6.4. The parameters of corrosion behavior of these materials such as their potential (E_{corr}) and corrosion current density (I_{corr})

extracted from the polarization graphs in Figure 6.4 are shown in Table 6.3. As it can be seen, the corrosion resistance improves in the following order for the various deposits:

DC–Ni < PRC–Ni < DC–NiW < DC–NiW–SiC < PRC–NiW < PRC–NiW–SiC

The sharp increase in anodic current density with increasing potential is associated with the pitting corrosion that can be seen for the samples named, respectively, DC–Ni, PRC–Ni, DC–NiW, DC–NiW–SiC, and PRC–NiW. For these coatings, no passive region was established before pitting. However, for PRC–NiW–SiC, a passive region between the potential of -0.5 and 0.1 V was observed. This could be explained by the higher corrosion resistance and stability of the coating in the corrosive liquid. Moreover, at higher positive potentials, for all coatings, one or more passivity breakdown occurs, leading to a sudden increase of the anodic current density. At the break down potential, the surface's passive film either breaks down locally, or it dissolves rapidly which will result in the failure of the coating system. This could be attributed to non–stability of the passive film when exposed to the corrosive liquid at higher positive potentials.

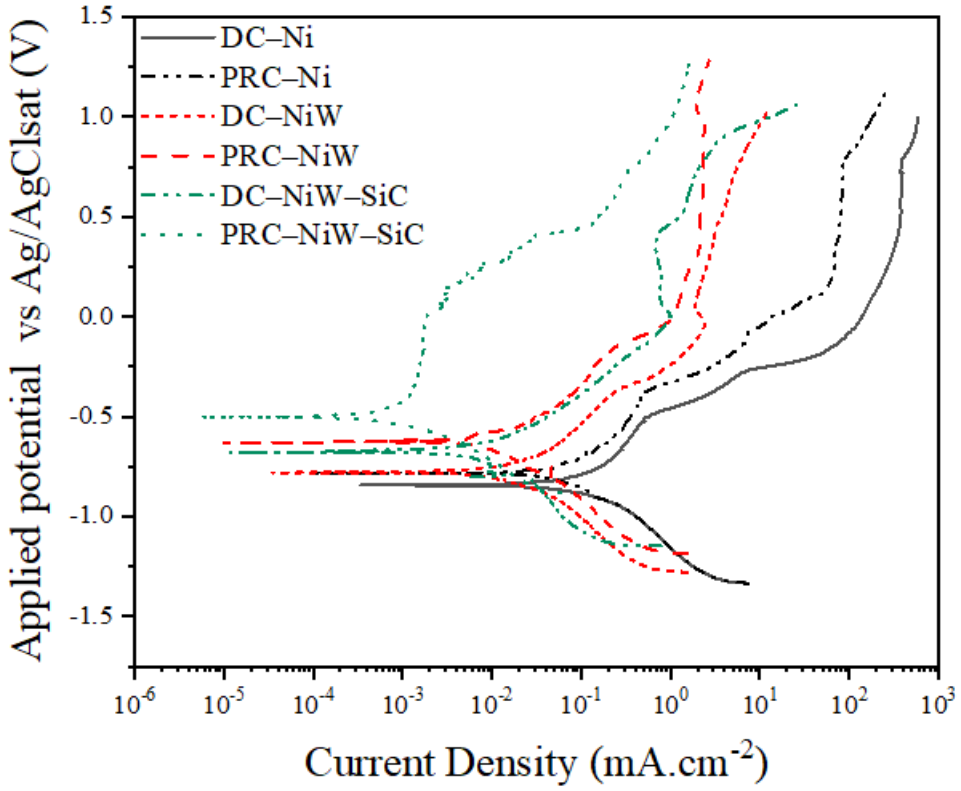

Figure 6.4 Potentiodynamic polarization (PD) of DC–Ni, PRC–Ni, DC–NiW, PRC–NiW, DC–NiW–SiC, and PRC–NiW–SiC.

Table 5.3 Corrosion potential and current density values extracted from potentiodynamic polarization graph.

Name of coatings	**Corrosion potential (V)**	**Current density (mA. cm^{-2})**
DC–Ni	-0.85	1.11×10^{-1}
PRC–Ni	-0.82	5.65×10^{-2}
DC–NiW	-0.79	1.76×10^{-2}
PRC–NiW	-0.64	5.89×10^{-3}
DC–NiW–SiC	-0.67	6.84×10^{-3}
PRC–NiW–SiC	-0.50	1.162×10^{-3}

Following the PP tests, the 3M insulating tapes that were exposing 1 cm^2 circular area of the coated samples were removed from DC electrodeposited DC–Ni, DC–NiW, DC–NiW–SiC, and PRC–NiW–SiC specimens and optical micrographs were taken from the surface of the specimens. Optical micrographs (Figure 6.5) were taken from the surface of specimens after performing PP tests. As it can be seen, the DC–Ni and PRC–Ni deposits were completely corroded and pulled off the surface. A significant discoloration was observed on the surface of DC–NiW, whereas the surface of PRC–NiW and PRC–NiW–SiC showed significantly slight damage. The surface of PRC–NiW–SiC deposit was also remained almost unchanged after the PP test. The optical micrographs in Figure 6.5 are correlated to the PP test results as demonstrated in Figure 6.4. As it was shown in the PP test results, DC deposited coatings exhibited more negative corrosion potential and higher corrosion current density compared to PRC deposited coatings. Furthermore, presence of SiC in the coatings shifted the corrosion potential to more positive values and corrosion current density to more small values (Table 5.3). This indicates that samples reinforced with SiC and electrodeposited with PRC methods exhibit better corrosion resistance.

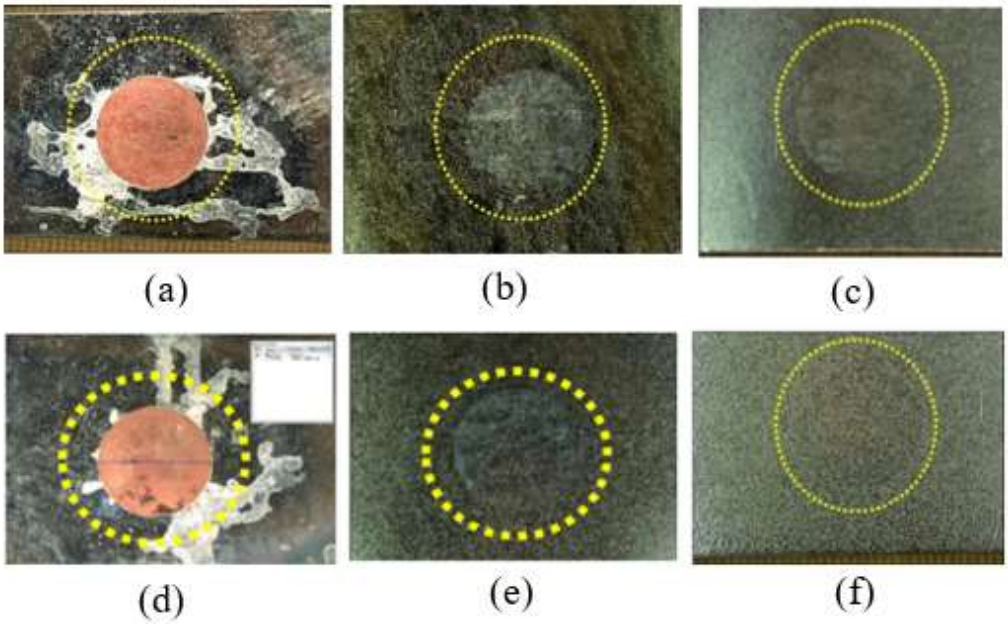

Figure 6.5 Optical micrographs taken from the exposed area of various deposits after potentiodynamic polarization of the deposits in artificial sea salt solution. The masking tape was removed prior to taking optical micrographs from the surface of the samples; (a) DC–Ni, (b) DC–NiW, (c) DC–NiW–SiC, (d) PRC–Ni, (e) PRC–NiW, and (f) PRC–NiW–SiC.

The influence of SiC content in the electrodeposition bath on corrosion resistance of PRC deposited NiW–SiC was investigated. Figure 6.6 displays the pp test taken from the surface of PRC–NiW–SiC electrodeposited from the bath containing 20 $g.L^{-1}$ and 40 $g.L^{-1}$ SiC. The corrosion potential (E_{corr}) and corrosion current density (I_{corr}) extracted from the polarization graphs in Figure 6.6 are displayed in Table 6.4. As it can be observed, the corrosion resistance improves with increase of SiC content in the electrodeposition bath. The increase of the corrosion potentials and decrease in the corrosion current density at higher SiC content in the coating was probably due to semiconducting properties of SiC and, hence, less tendency for formation of galvanic cells in NiW matrix.

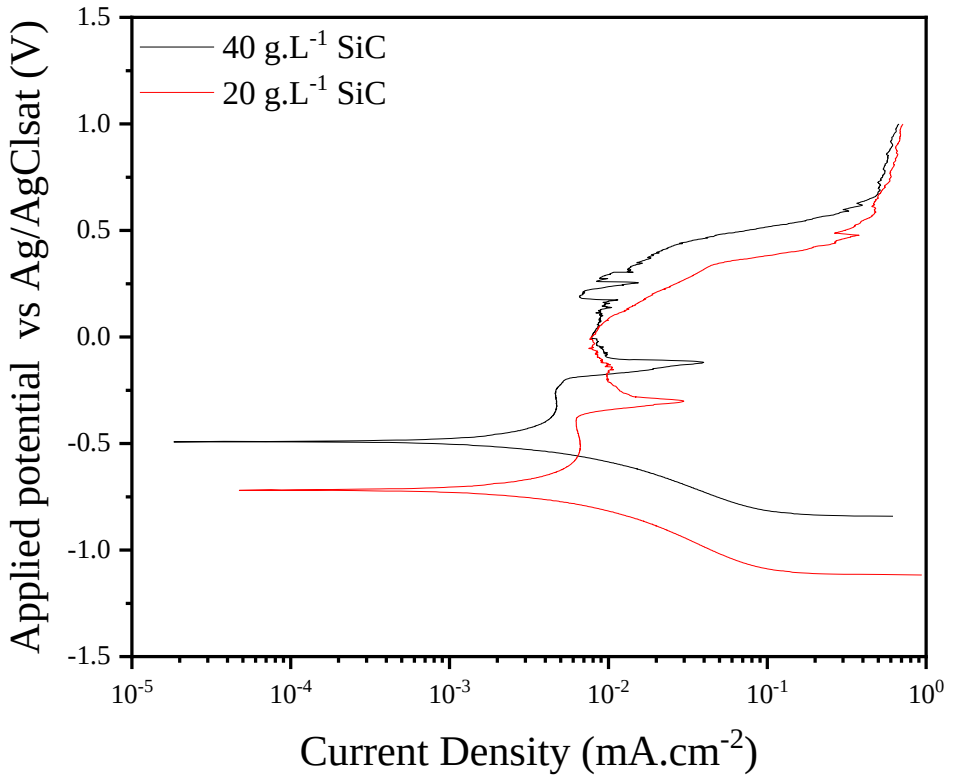

Figure 6.6 Influence of SiC concentration (20 $g.L^{-1}$ and 40 $g.L^{-1}$) in the bath on the potentiodynamic polarization (pp) curves of PRC–NiW–SiC.

Table 6.4 Corrosion potential and current density values extracted from potentiodynamic polarization graph.

Name of coatings	**Corrosion potential (V)**	**Current density (mA. cm^{-2})**
PRC–NiW–SiC (20 $g.L^{-1}$)	-0.71	7.3×10^{-3}
PRC–NiW–SiC (40 $g.L^{-1}$)	-0.49	4.5×10^{-3}

6.3.4 TOF–SIMS surface analysis

TOF–SIMS was applied to analyze corrosion behavior of DC and PRC deposited coatings (Ni, NiW and NiW–SiC) on brass substrates through examination of corrosion products after PP test at various ranges of 0–50 m/z, 50–90 m/z and 90–180 m/z.

In the first set, TOF–SIMS spectra (Figures 5.7 (a), 5.7 (b), and 5.7 (c)) were taken in the range of 0–50 m/z for positive and negative ions from the surfaces of DC–Ni, DC–NiW, and DC–NiW–SiC specimens, respectively. Various hydrocarbon contamination from exposure to the environment were observed on the surface of all specimens, e.g. C+ (m/z=12), COH^+ (m/z=29), CH_2OH^+ (m/z=31). The hydrocarbons are most likely adsorbed on the surfaces during sample preparation, when they were dried and transferred to the spectrometer. In addition to hydrocarbons, additional peak of Na^+ (23 m/z) was present on DC–NiW–SiC before PP test, which indicates the presence of alkali earth metal on the surface and is most likely due to surface contamination from the electrolytes. However, alkali earth metals such as sodium and potassium are often observed in SIMS analyses due to their low ionization energies.

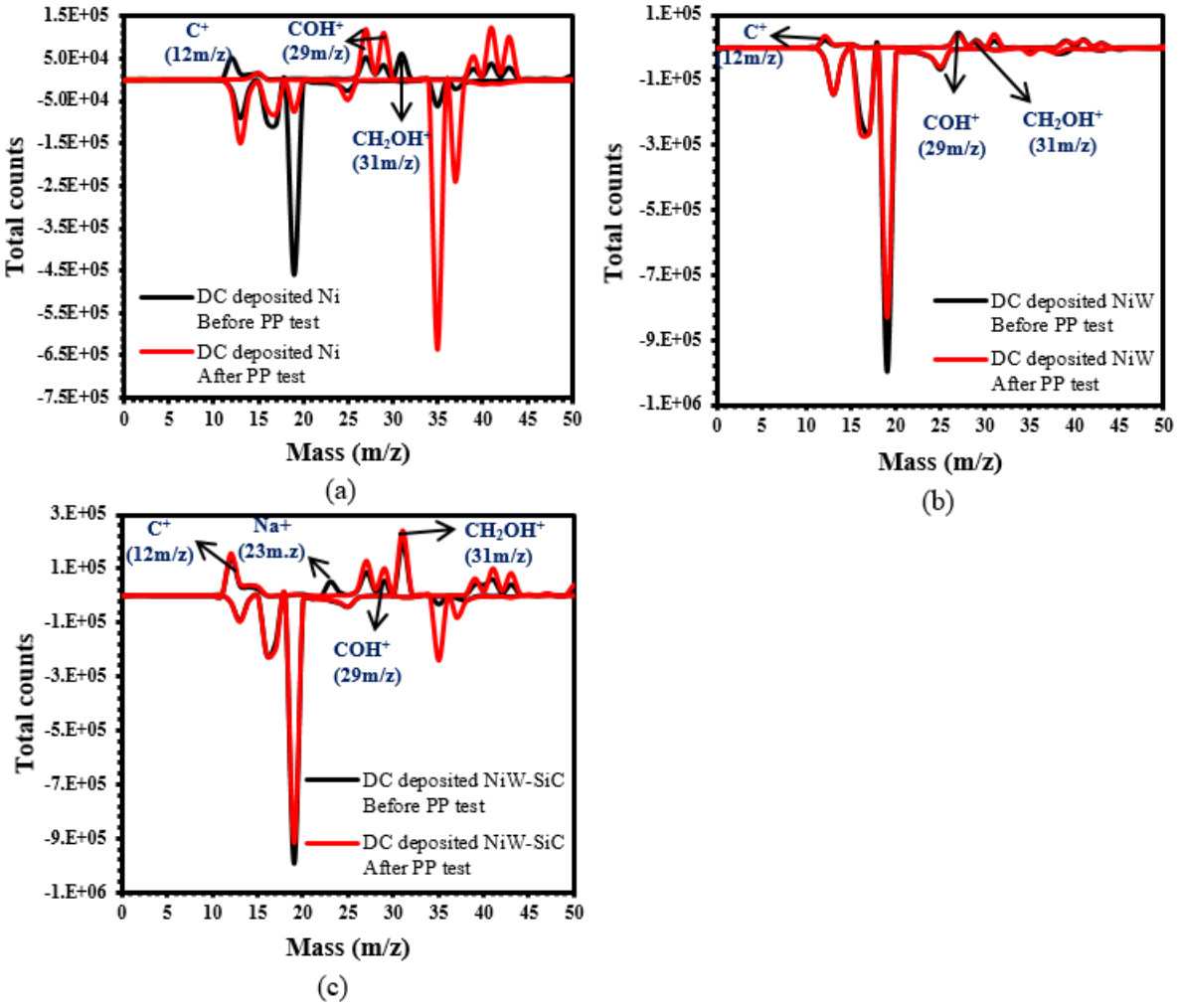

Figure 6.7 (a) TOF–SIMS (0–50 m/z) spectra taken from the deposits before and after potentiodynamic corrosion test for DC–Ni. (b) TOF–SIMS (0–50 m/z) spectra taken from the

deposits before and after potentiodynamic corrosion test for DC–NiW. (c) TOF–SIMS (0–50 m/z.

In the second set, TOF–SIMS spectra (Figures 6.8 a, 6.8b, and 6.8c) was taken in the range of 50–90 m/z for positive and negative ions from the surfaces of DC–Ni, DC–NiW, DC–NiW–SiC specimens, respectively. In DC–Ni, after PP test, nickel ions peaks were disappeared in the positive range of spectra, while the peaks related to brass substrate (i.e. Cu and Zn) were observed (Figure 6.8a). The same observation was realized in optical micrograph taken from the surface of the DC–Ni sample after corrosion test which was shown earlier (Figure 6.5 (a)), i.e. the nickel layer was completely removed after the PP test and the surface of brass substrate was exposed. For DC–NiW (Figure 6.8b), Ni layer was not completely removed after the PP test and no exposure of substrate was realized (i.e., no peaks related to Cu and Zn were observed) after the PP test. Similar observations were realized for the DC–NiW–SiC deposit. However, in the latter deposit, new positively charged silicon oxide based species were observed. These new species more likely were related to oxidation of silicon carbide during the PP test. The oxide form of silicon species might be responsible for further surface passivation and the observed improvement in corrosion resistance of the DC–NiW–SiC composite compared to DC–NiW deposit which could be as a result of SiC acting as a physical barrier against formation and propagation of corrosion pits. This presence of SiC oxidized species on the metal surface may also reduce the surface area of the metal which is more sensitive to corrosion. [29–30]

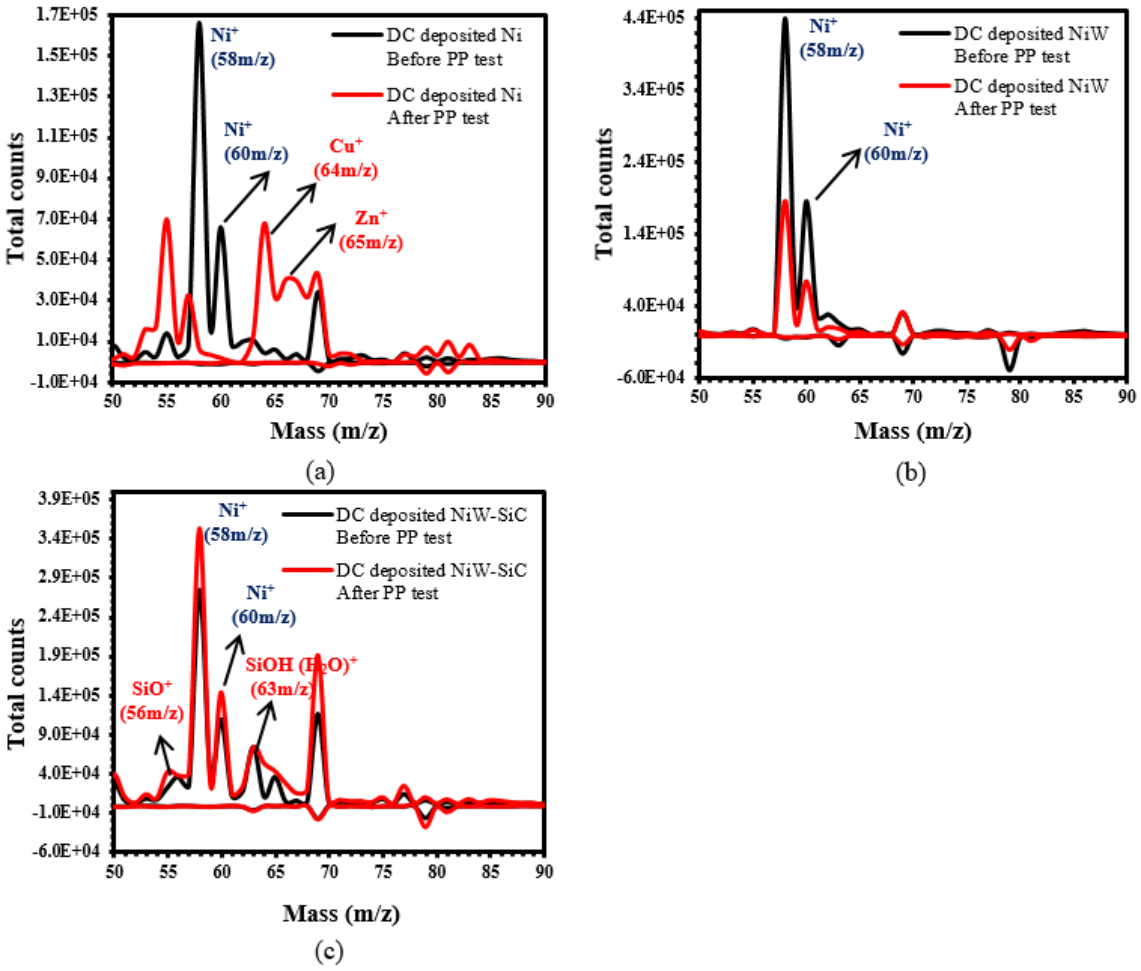

Figure 6.8 (a) TOF–SIMS (50–90 m/z) Spectra taken DC–Ni before and after potentiodynamic corrosion test. (b) TOF–SIMS (50–90 m/z) Spectra taken DC–NiW before and after potentiodynamic corrosion test. (c) TOF–SIMS (50–90 m/z) Spectra taken DC–NiW–SiC before and after potentiodynamic corrosion test.

In the third set, TOF–SIMS spectra (Figures 6.9a, 6.9b and 6.9c) was taken in the range of 180–290 m/z for as results of analysis of positive and negative ions from the surfaces of DC–Ni, DC–NiW, and DC–NiW–SiC specimens, respectively. As expected, no peaks related to tungsten species were observed in Figure 6.9a due to the fact that the DC deposited Ni did not have any tungsten. Figures 6.9b and 6.9c show the peaks related to tungsten containing species. As it can be seen, both deposits (DC–NiW and DC–NiW–SiC) display various oxide forms of tungsten within the deposits. According to Figures 6.9b and 6.9c, DC–NiW contains larger amounts of tungsten oxide with lower oxidation states compared to DC–NiW–SiC composite.

Presence of highly stable forms of tungsten oxides in the coating such as WO_3 could further improve passivity and increase the induction time for pit initiation, whereas lower oxidation forms of tungsten oxide such as WO and WO_2 are not considered stable protective oxides. This is attributed to insolubility of WO_3 when interacted with water. [31] It is known that the range of the m/z values of the TOF–SIMS characterization has an important role on the species which can be detected before and after corrosion. The TOF–SIMS method in a m/z range above 180 m/z is usually the most useful for detailed analysis of surfaces before and after corrosion. At lower m/z range, TOF–SIMS spectra are sometimes dominated by signals arising from hydrocarbon contaminants masking the underlying chemical species.

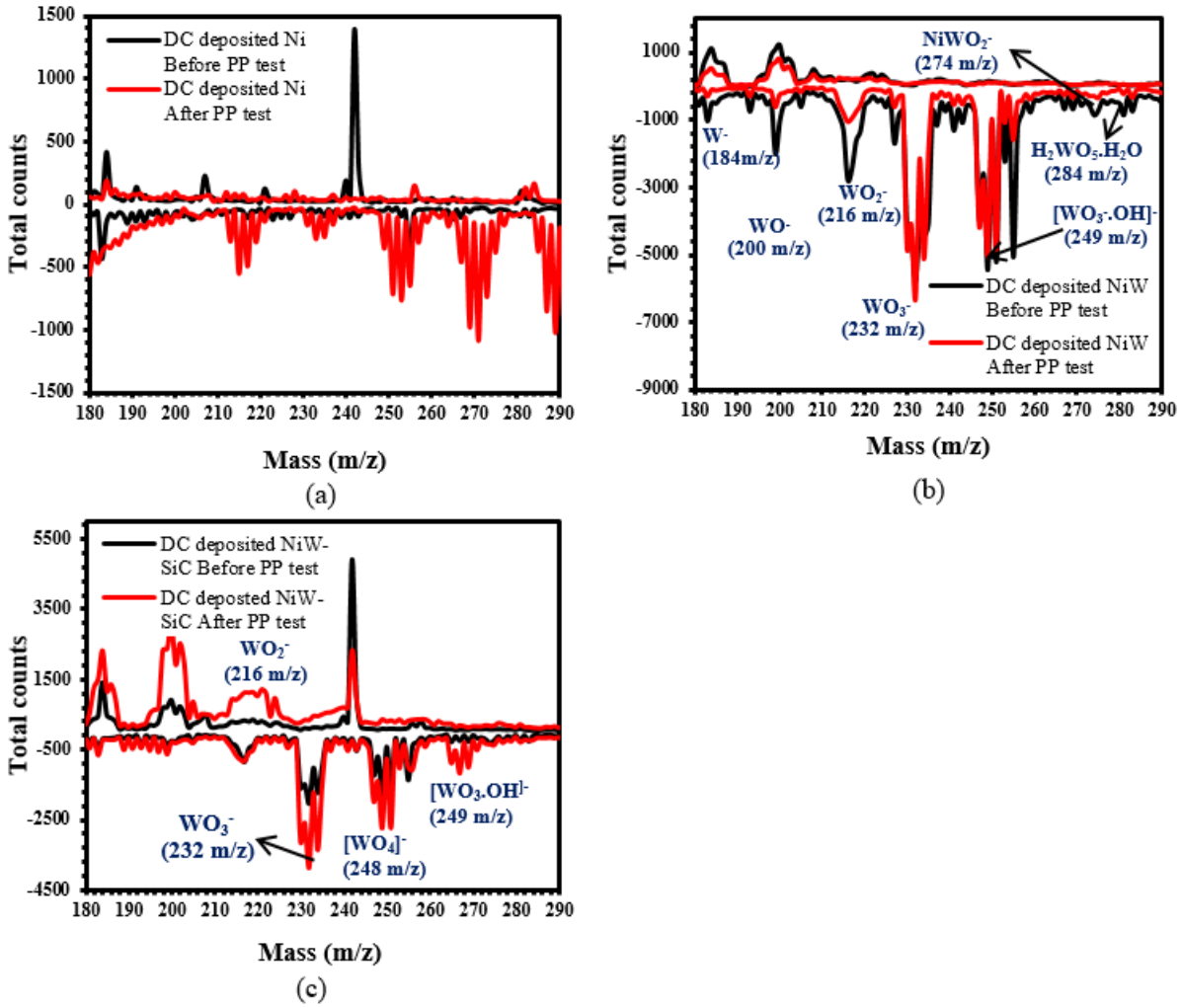

Figure 6.9 (a) TOF–SIMS (180–290 m/z) Spectra taken from DC–Ni before and after potentiodynamic corrosion test. (b) TOF–SIMS (180–290 m/z) Spectra taken from DC–NiW before and after potentiodynamic corrosion test. (c) TOF–SIMS (180–290 m/z) Spectra taken from DC–NiW–SiC.

Accordingly, in the fourth set of experiments, TOF–SIMS spectra (Figures 6.10a, 6.10b, and 6.10c) was taken in the range of 0–50 m/z, 50–90 m/z, and 180–290 m/z for positive and negative ions from the surface of PRC–NiW–SiC specimen, respectively. Comparing Figures 6.7c and 6.10a shows that in the range of 0–50 m/z, both DC and PRC electrodeposited NiW–SiC demonstrated carbon and alkali based (Na^+) contaminants at 12 m/z, 23 m/z, 29 m/z and 31 m/z. However, in the case of PRC–NiW–SiC, additional peak of $SiC(H)^+$ is seen which is possibly due to entrapment and oxidation of SiC within the tungsten oxide layers during each reverse pulse. SiC compounds could act as physical barriers to protect the coating from further corrosion.

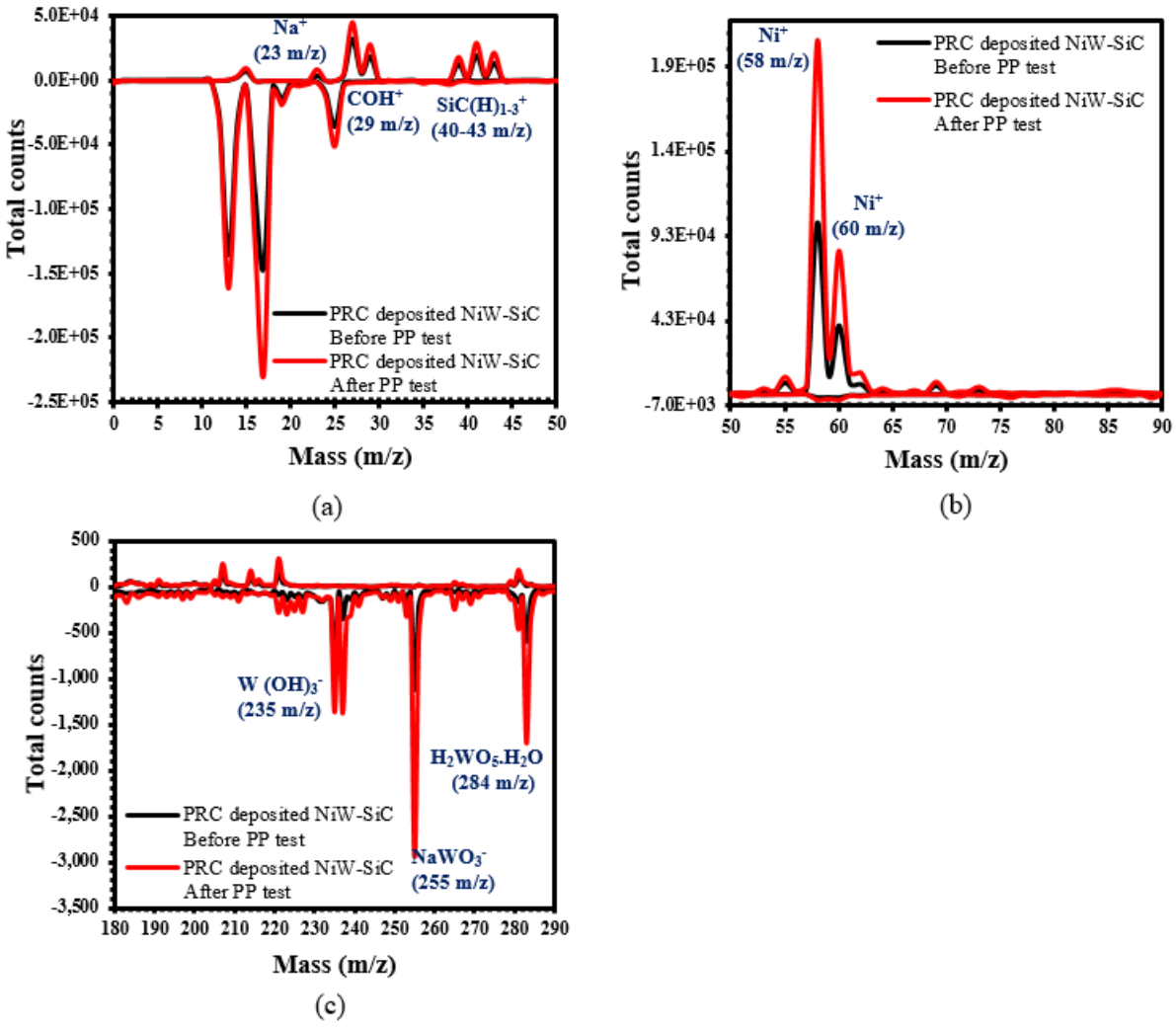

Figure 6.10 (a) TOF–SIMS spectra (0–50 m/z) from the surface of PRC–NiW–SiC deposit before and after PP test. (b) TOF–SIMS spectra (50–90 m/z) from the surface of PRC–NiW–

SiC deposit before and after PP test. (c) TOF–SIMS spectra (180–290 m/z) from the surface of PRC–NiW–SiC deposit before and after PP.

It was also observed that, in PRC deposited NiW–SiC, brass substrate was not exposed after the PP tests since no peaks of Cu and Zn is seen. Comparing of Figures 5.9c and 5.10c also demonstrates that the majority of tungsten containing species was based on the higher oxidation states of tungsten in the case of PRC–NiW–SiC. The latter observation may explain improved corrosion performance of PRC–NiW–SiC compared to DC–NiW–SiC. The utilization of the PRC based method produces higher oxidation state of tungsten oxide than using the DC method. Therefore, PRC–NiW–SiC sample resists more to corrosion than DC–NiW–SiC sample.

6.3.5 XPS analysis

XPS spectra was acquired from three different locations on the surfaces of PRC deposited Ni, NiW, and NiW–SiC coatings to measure the average atomic composition (%) and element valence state of all the samples before and after the PP test. Ni, Cu, O, and C elements are clearly observed in the XPS spectra of Ni (Figure 6.11a). The high resolution XPS spectra of the Ni, O, and C regions are given in Figures 6.11 (b–d). As seen from Figure 6.11b, two major peaks at around 852.43 eV and 869.77 eV were assigned to Ni 2p3/2 and Ni 2p1/2, and their corresponding satellite/shoulder peaks are located at 855 eV and 873.34 eV which agrees with reported values of NiOOH and Ni_2O_3. [32–39] Figure 6.15c depicts the O1s spectrum that was deconvoluted into three peaks at 529.37 eV, 531.09 eV, 532 eV, respectively. The peak at 529.37 eV is attributed to Ni–O and the peaks at 531.09 eV and 532 eV were resulted from the Ni^{3+}species (NiOOH) and Ni^{+2} species (Ni $(OH)_2$ respectively [32–38]. Figure 6.15d exhibits the C1s XPS spectra that decomposed into five peaks. The fitted peaks at 284.1 eV, 284.5 eV, 285.4 eV, 286 eV, and 288.45 eV correspond to the C–C, C=C, C–H, C–O, C=O, and O–C=O, respectively which are derived from the corresponding organic additives such as brightener, citrate, and carbon contamination during the electrodeposition process. [32–38]

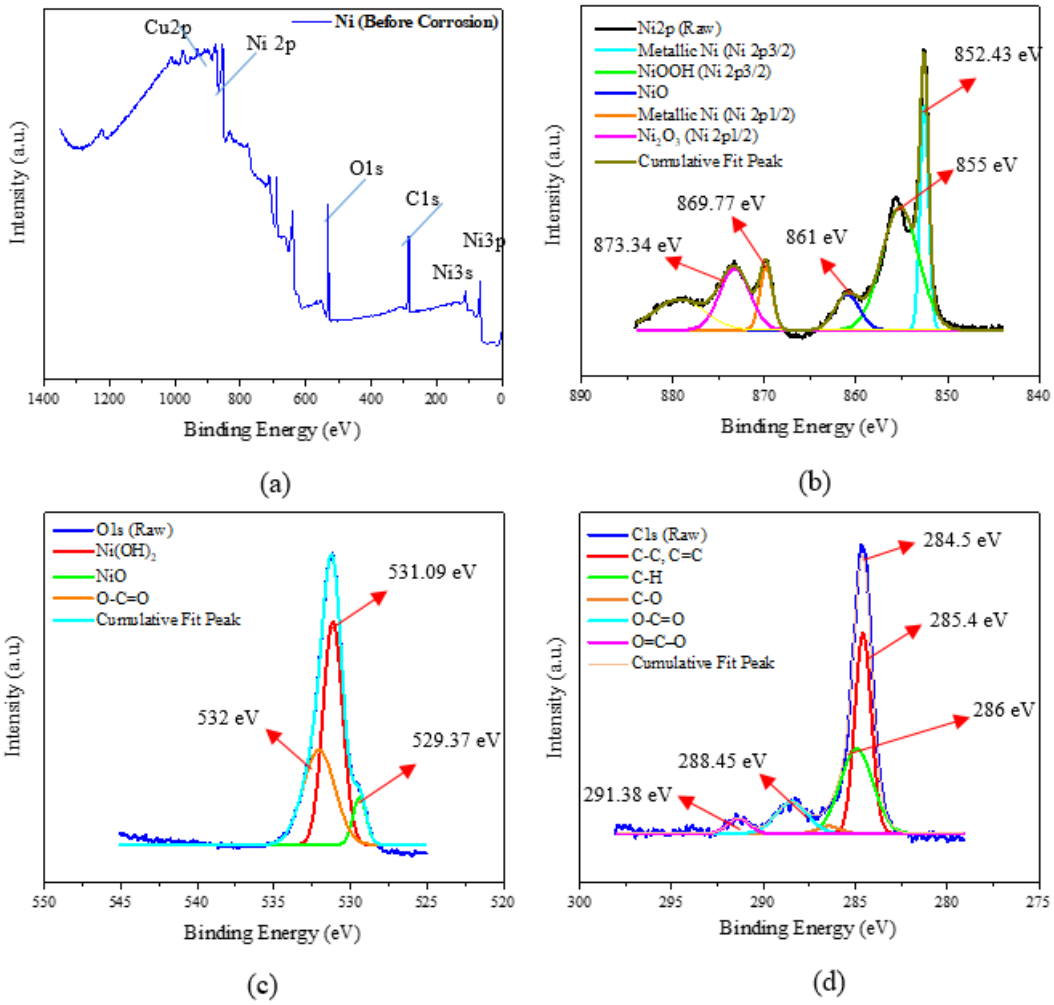

Figure 6.11 XPS spectra (A) for Ni and XPS regions of Ni2p (B), O1s (C) and C1s (D).

Figure 6.12 displays the XPS surface scans of PRC electrodeposited Ni on brass substrate after the PP test. Ni 2p spectrum of Ni film exhibits metallic Ni peaks at 852.61eV and 869.708 eV, and Ni oxide peaks (NiO) at 858 eV, 871.05 eV, and 874.74 eV. It was observed that after the PP test, the intensity of metallic nickel peaks became smaller, while the intensity of NiOOH and NiO became stronger (Figure 6.11). The same observation was realized through eye examination, i.e. the nickel layer was removed after the PP test and the surface of substrate was exposed. Figure 6.12c displays the O1s spectrum of Ni. It was noticed that the intensity of NiO peak was stronger after the pp test. This is an indication that the surface contains more NiO after passivation. A summary of the quantitative results of the chemical elements of PRC–Ni coatings before and after the pp test expressed as atomic percentage are displayed in Table 6.5. It is observed that the atomic concentrations of the Ni2p elements decreased from 13.76 at% to

2.086 at% after the corrosion test and Cu2p atomic percentage also increased from 0.913 at% to 2.163 at%. As well, the XPS spectra obtained from the surface of the samples reveal the largest amounts of oxygen and carbon. The coatings also contain fluorine and sulfur which is due to co–deposition of fluorine–containing surfactant and sodium saccharine used in preparation of the electrodeposition bath. Phosphorous, chloride, and nitrogen contaminations are also detected on the coating surface before and after the pp tests.

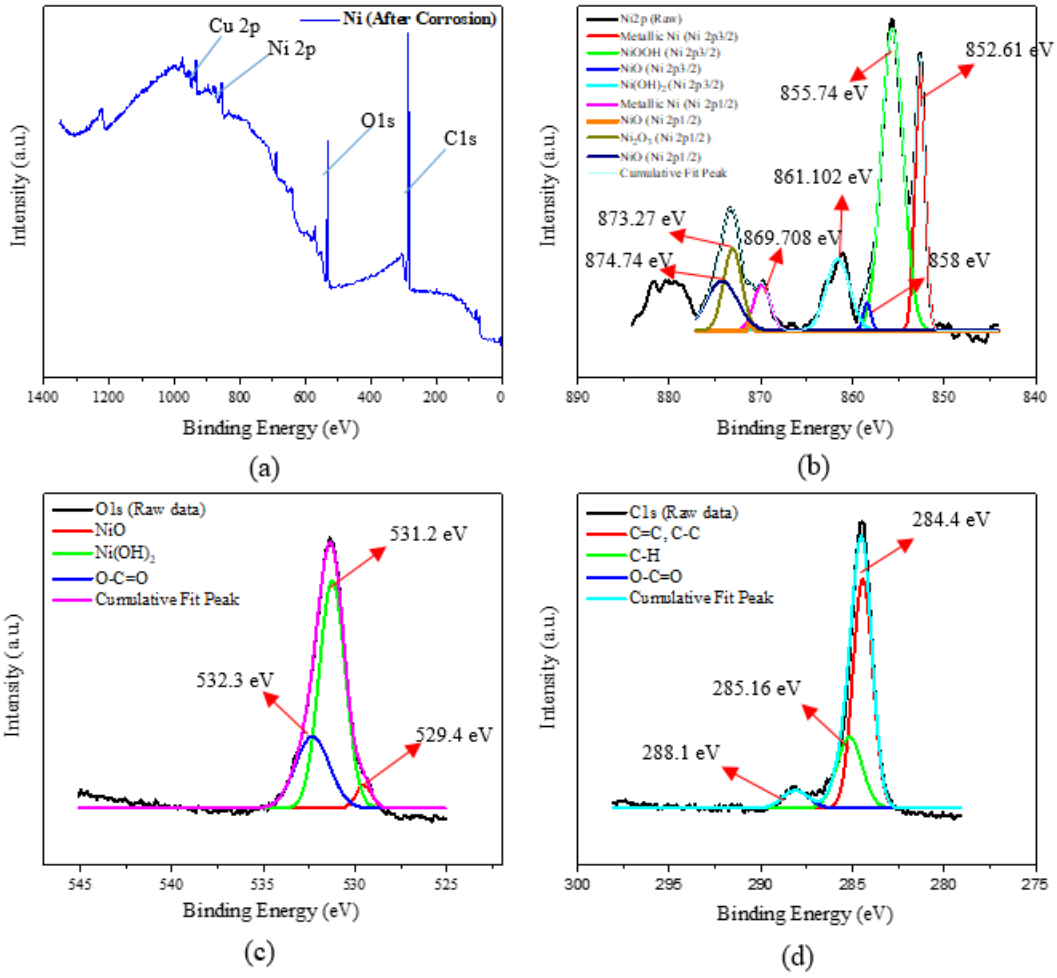

Figure 6.12 XPS spectra (A) for Ni after the pp test and XPS regions of Ni2p (B), O1s (C) and C1s (D).

Figure 6.13 displays the Ni2p, O1s, C1s, and W4f XPS profiles of PRC deposited NiW coating. The XPS analysis suggests that the surface of the coating contains mostly Ni, W, O, and C elements. There was also no Cu peak was observed on the NiW XPS spectra which

demonstrates no visible inter diffusion of Cu from the substrate through electrodeposited NiW coating.

The Ni 2p spectra exhibits Ni 2p3/2 and Ni 2p1/2 spectrum doublet, centered at about 852.59 eV and 869.57 eV, with the corresponding shake–up satellite at 855.67 eV and 873.37 eV. The O1s spectra presented in Figure 6.13c suggested presence of major peak at 531.3 eV corresponding to Ni $(OH)_2$, a peak at 530.4 eV and 532.9 eV corresponding to WO_3 and SiO_2. [39–46] The peak at 529.6 eV corresponds to Ni peak which is negligible since Ni presents mostly in metallic state. It is also well known that the majority of samples after being exposed to ambient air have a detectable quantity of carbon contamination (~ 2 nm thick) as shown in Figure 6.13d. C1s XPS spectrum for contamination typically contains C–C, O–C=O, and C–O–C components. As displayed in Figure 6.13e, XPS profiles of W4f have an asymmetric peak shape for tungsten metal. In this Figure, the W4f7/2 and W4f5/2 exist in both oxide (WO_3 at 35.408 eV and 37.63 eV) and metallic state (W^0 at 31.54 eV and 33.76 eV). Tungsten is extremely resistant to corrosion and forms a protective oxide (WO_3) when exposed to atmosphere. WO_3 has been reported as the most stable phase at room temperature.

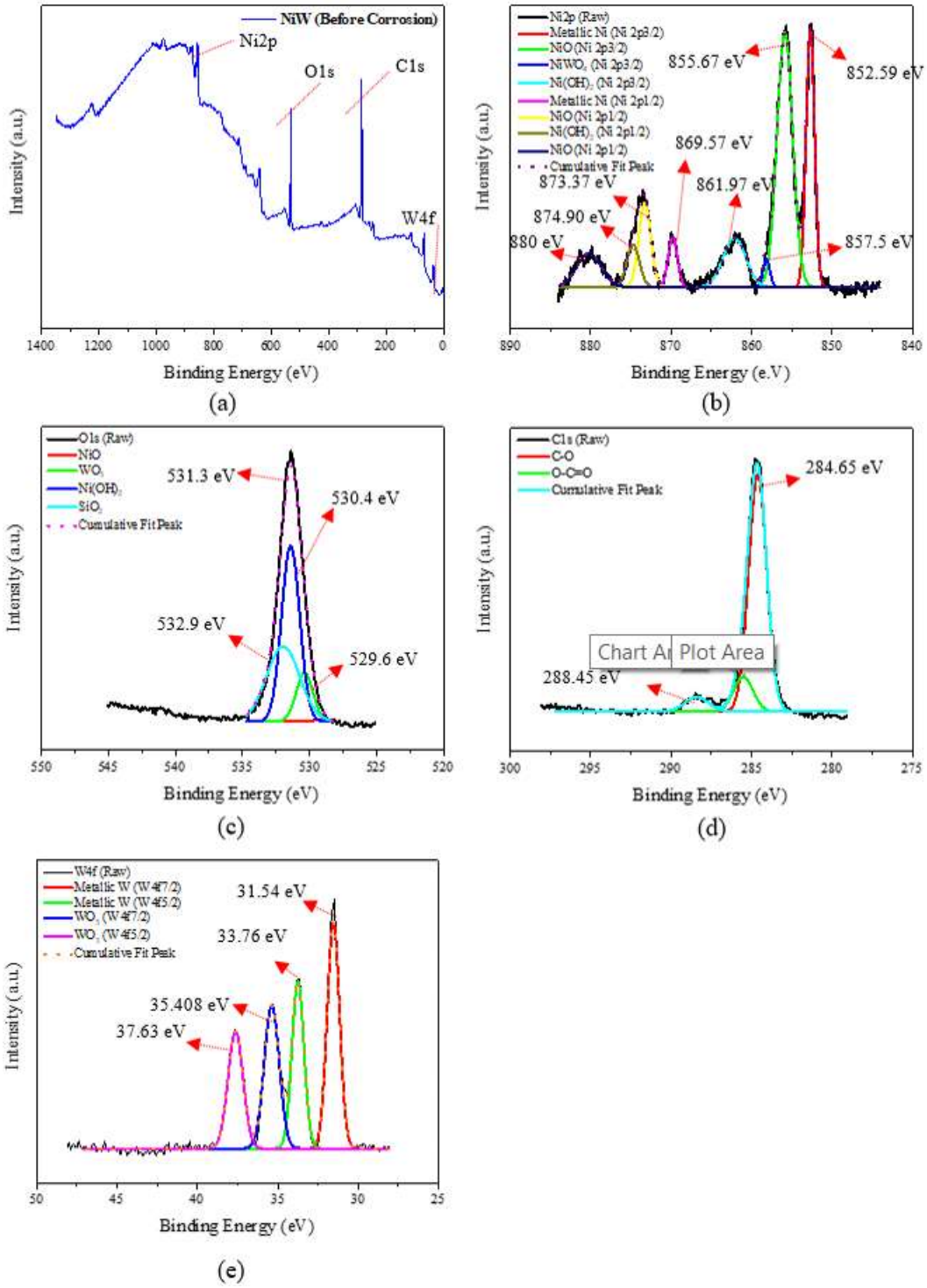

Figure 6.13 XPS spectra (A) for NiW and XPS regions of Ni2p (B), O1s (C), C1s (D), and W4f (E).

PP test was performed on the surface of PRC deposited NiW. XPS spectra for NiW and XPS regions of Ni2p, O1s, C1s, and W4f are shown in Figure 6.14 (a–e). It was found that after the

pp test, the intensity of Ni peak at 852.59 eV and 869.57 eV became very negligible or completely disappeared. However, other peaks of $NiWO_4$, Ni $(OH)_2$, and NiO became stronger and more intense after the pp test. It can be understood that Ni has been oxidized after the pp test and new phases have been formed. The W4f spectra displays a W4f7/2 and W4f5/2 for metals centered at 31.46 eV and 33.58 eV, and also displays a W4f5/2 for oxides centered at 35.27 and 37.42 eV, respectively. Comparing the XPS results of NiW coating before the corrosion test, the intensity of W peaks at 31.46 eV and 33.58 eV in W4f spectra were much higher compared to the W4f spectra of NiW after the corrosion test. This suggests oxidation of tungsten during the pp test. A summary of the quantitative results of PRC deposited NiW coatings before and after the pp test expressed as atomic percentage is displayed in Table 4.6. It is observed that the atomic concentrations of the Ni2p decreased from 7.16 at% to 2.29 at%. As well, the XPS spectra obtained from the surface of the NiW coated samples reveal the largest amounts of oxygen and carbon. Presence of fluorine on the surface of the coating can be associated with co–deposition of fluorine–containing surfactant used in preparation of the electrodeposition bath. Magnesium and calcium contaminations are also detected on the coating surface after the pp test which can be attributed to presence of calcium and magnesium in the seawater solution.

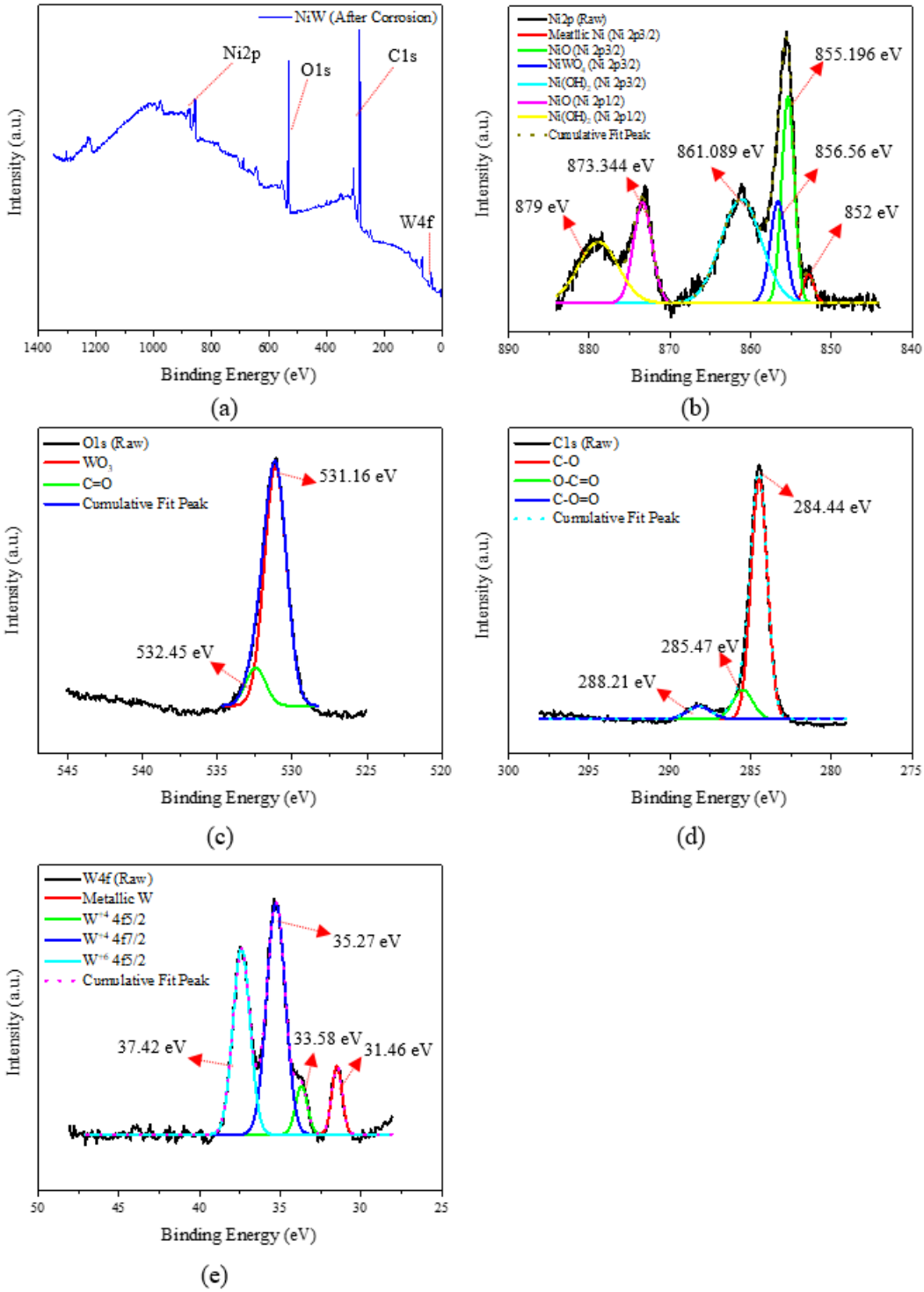

Figure 6.14 XPS spectra (A) for NiW after the PP test and XPS regions of Ni2p (B), O1s (C), C1s (D), and W4f (E).

Figure 6.15 displays the Ni2p, O1s, C1s, W4f, and Si2p XPS profiles of PRC deposited NiW–40 g.L^{-1} SiC coating. The XPS analysis suggests that the surface of the coating contains mostly

Ni, W, O, C, and Si elements. The Ni 2p spectra exhibits Ni 2p3/2 and Ni 2p1/2 spectrum doublet, centered at about 852.52 eV and 869.98 eV, with the corresponding shake–up satellite at 855.53 eV and 873.61 eV (Figure 6.15a).

Comparing the XPS results of NiW–SiC with the NiW before the pp test, the intensity of Ni peak at 852.52 eV was lower in NiW–SiC compared to the intensity of Ni peak in NiW. This is due to presence of SiC, acting as physical barrier against nucleation of Ni grains.

XPS spectra from the surface of NiW–SiC also confirmed the formation of $NiWO_4$ and SiO_2 barrier layers (Figures 6.15b and 6.15f) which can enhance the corrosion resistance of the coating and is in the confirmation with TOF–SIMS results. The formation of $NiWO_4$ and SiO_2 barrier layers might be due to the following reactions: [47–49]

$$Ni^{2+} + WO_4^{2-} \rightarrow NiWO_4 \quad (1)$$

$$SiC + 4H_2O \rightarrow SiO_2 + 8H^+ + CO_2 + 8e^- \quad (2)$$

It was observed from the W4f profile of NiW–SiC, peak intensity at 33.62 eV which is assigned to metallic W (Figure 6.15e) was also lower compared to the intensity of W peak in W4f spectra of NiW before the pp test (Figure 6.14). This demonstrates that reinforcement of NiW with SiC affected the W content of the coating. The XPS spectra from the Si2p region in sample is shown in Figure 6.19f. Deconvolution of Si2p spectra displays two main components corresponding to Si (Si 2p1/2) at 99.74 eV and SiO at 101.09 eV. The oxy phases might have formed on the surface of the coating as it was exposed to the atmosphere. C1s XPS spectra (Figure 6.15d) was also decomposed into four peaks. The fitted peaks at 282.04 eV, 284.56 eV, 285.90 eV, and 288.13 eV correspond to the SiC, C–C, C–O and O–C=O, respectively. They are derived from the corresponding organic additive such as brightener, citrate and carbon contamination during the electrodeposition process.

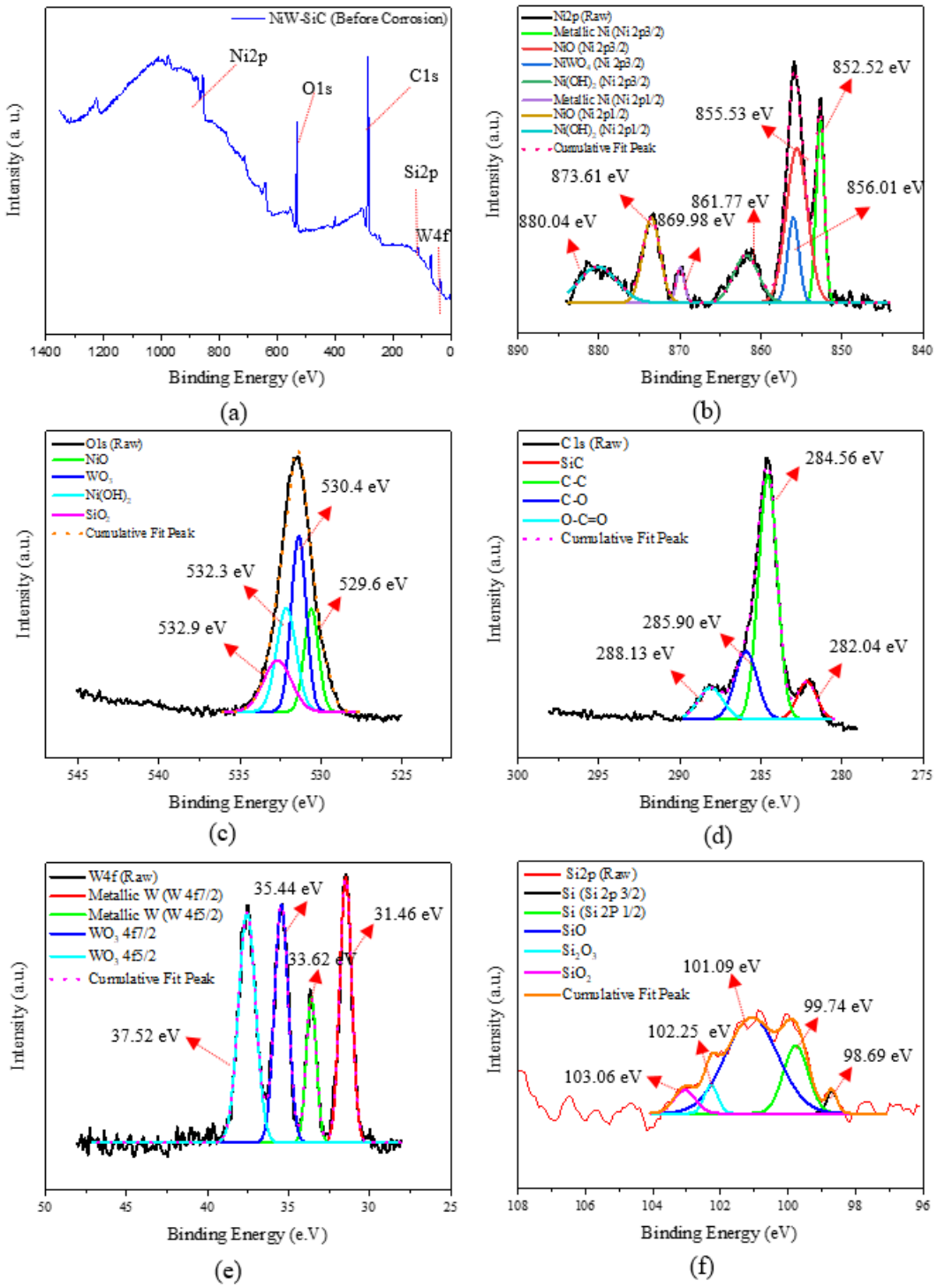

Figure 6.15 XPS spectra (A) for NiW–SiC and XPS regions of Ni2p (B), O1s (C), C1s (D), W4f (E), and Si2p (F).

PP test was performed on the surface of PRC deposited NiW–SiC. XPS spectra taken from the surface of NiW–SiC and XPS regions of Ni2p, O1s, C1s, and W4f are shown in Figures 5.16

(a–e). It was found that after the pp test, the metallic Ni peaks observed at 852.52 eV, 869.98 eV in Ni2p region of NiW–SiC XPS spectra (Figure 6.16b) were completely disappeared after the pp test. However, after the pp test, other peaks of NiO and $Ni(OH)_2$ became more intense. This was attributed to oxidation of Ni and formation of new phases. As well, in O1s spectra, NiO peak at 529.6 eV and WO_3 peak at 530.4 eV which were noticeable in O1s spectra of NiW–SiC before the pp test were also diminished after the pp test.

The W4f spectra displays a W4f7/2 and W4f5/2 for metals centered at 31.46 eV and 33.58 eV, and also displays a W4f5/2 for oxides centered at 35.27 and 37.42 eV, respectively. Comparing the XPS results of NiW–SiC coating before the corrosion test, the intensity of W peaks at 31.46 eV and 33.58 eV in W4f spectra were much higher compared to the W4f spectra of NiW–SiC after the corrosion test. This suggests the oxidation of tungsten during the pp test. A summary of the quantitative results of PRC deposited NiW–SiC coatings before and after the pp test expressed as atomic percentage is shown in Table 5.7. No significant difference in atomic concentrations of the Ni2p before and after the pp test was observed. Increase of the si2p after the corrosion test from 0.96 at% to 5.17 at% could be related to corrosion and removal of NiW layer on the surface and exposure of the trapped SiC particles within NiW to the surface of the coating. Significant amounts of oxygen and carbon on the surface can be seen, since XPS is so surface sensitive. As well, samples contained fluorine which is due to co–deposition of fluorine–containing surfactant used in preparation of the electrodeposition bath. Magnesium, calcium, and Zn contaminations are also detected on the coating surface after the pp test which can be attributed to presence of calcium and magnesium in the seawater solution.

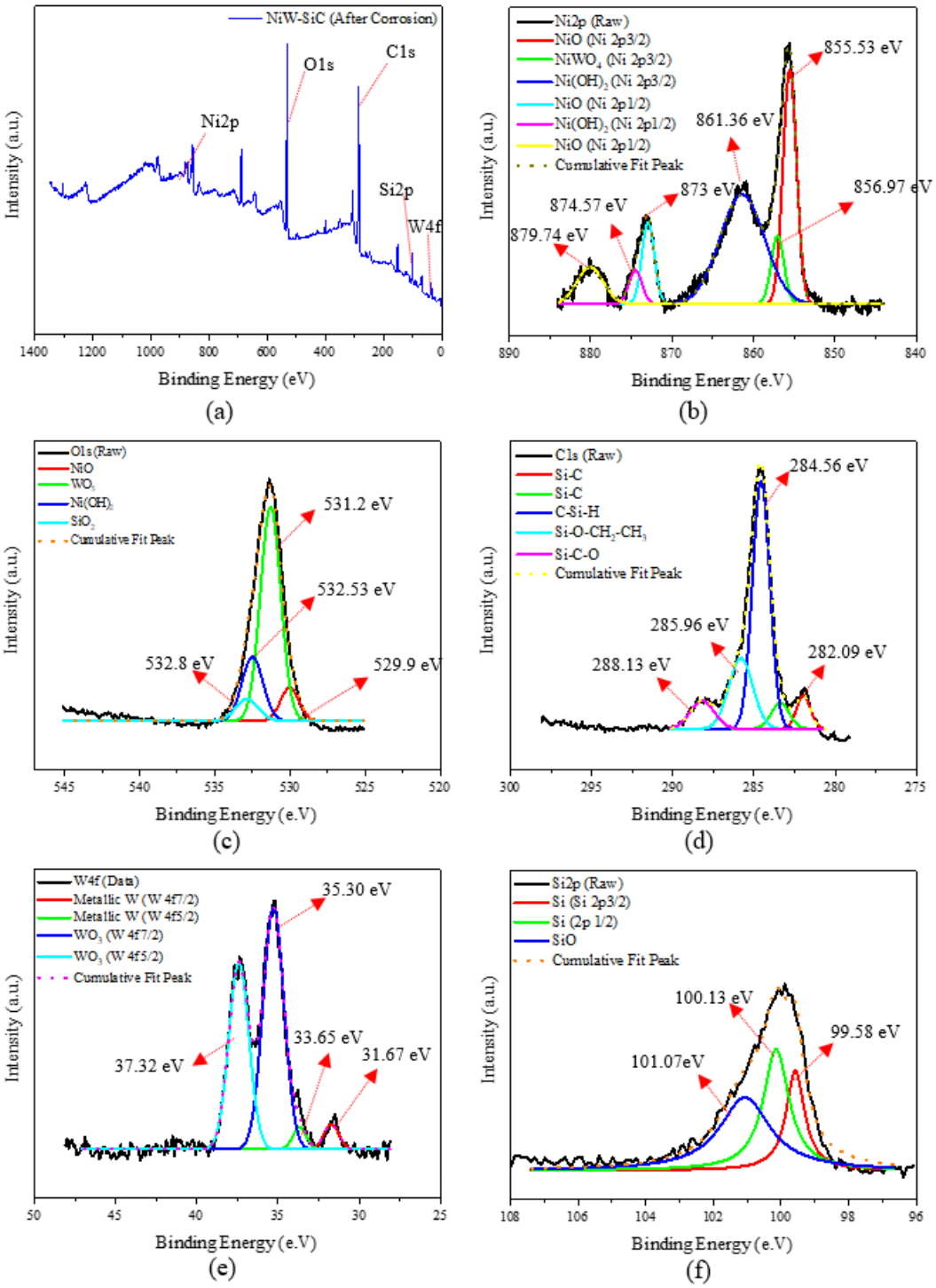

Figure 6.16 XPS spectra (A) for NiW–SiC after the pp test and XPS regions of Ni2p (B), O1s (C), C1s (D), W4f (E), and Si2p (F).

Table 6.5 Average atomic composition of PRC–Ni from three locations before and after the pp test.

Elements	**Atom concentration (at%)**	
	PRC–Ni (before the pp test)	PRC–Ni (after the pp test)
Ni2p	13.76	2.086
Cu2p	0.913	2.163
O1s	29.333	18.033
C1s	42.216	73.033
F1s	12.56	2.966
P2p	1.053	———
S2p	0.156	———
Cl2p	———	0.653
N1s	———	1.056

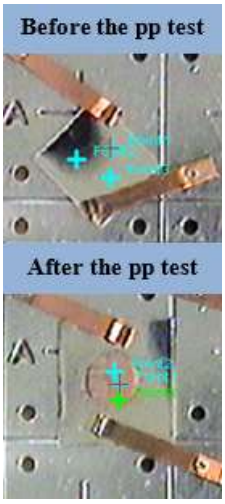

Table 6.6 Atomic composition of PRC–NiW deposited brass substrates before and after the pp test.

Elements	**Atom concentration (at%)**	
	PRC–NiW (before the pp test)	PRC–NiW (before the pp test)
Ni2p	7.16	2.29
O1s	24.17	18.93
C1s	62.11	73.48
F1s	3.05	1.14
W4f	1.84	0.35
N1s	1.64	1.58
Mg1s	———	1.36
Ca2p	———	0.85

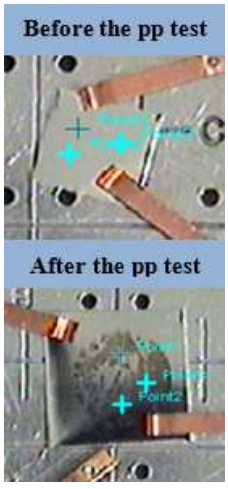

Table 6.7 Atomic composition of PRC–NiW–SiC deposited brass substrates before and after the pp test

Elements	**Atom concentration (at%)**	
	PRC–NiW–SiC (before the pp test)	PRC–NiW–SiC (after the pp test)
Ni2p	3.46	4.48
O1s	21.48	25.91
C1s	66.14	54.85
F1s	2.03	5.83
W4f	1.39	0.76
N1s	4.52	1.18
Si2p	0.96	5.15
Mg1s	———	0.99
Ca2p	———	0.81

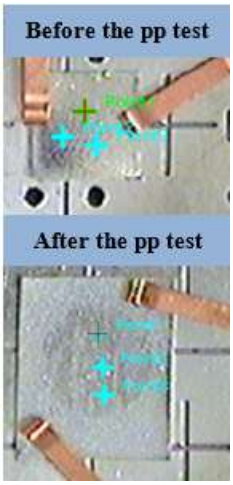

6.3.6 XRD results (Effect of heat treatment on crystallite sizes of PRC deposited Ni, NiW, and NiW–SiC)

Figure 6.17 displays the XRD spectra from the surfaces of as–deposited and heat–treated DC and PRC electrodeposited Ni on brass substrate at 350^{o}C and 500^{o}C. The diffraction peaks of DC and PRC deposited Ni were assigned to the Cu (111), Ni (111), Cu (200), Ni (200), Cu (220), Ni (220), Cu, (311), and Ni (311) planes, respectively. This indicated that PRC–Ni had a polycrystalline structure and intensity of the peaks and average crystallite size as displayed in Table 6.8 increases from 223 Å up to 1684 Å for DC and 197 Å up to 1210 Å for PRC with rising the annealing temperature. This was attributed to increase in crystallinity of the coating and hence increase in number of the crystallites. It is also noteworthy to mention that the presence of Cu peaks for DC and PRC coated samples were due to corrosion of the coatings and exposure of the substrates to the surface which is in agreement with optical micrographs, XPS, and TOF–SIMS results. The crystallites size (D) of the coatings were calculated (Table 6.8) from the broadening of the (111) peaks using Scherrer equation. [49–51]

$$D = K\lambda/\beta\cos\theta \qquad (3)$$

Where D is the crystallite size (nm), K is the Scherrer constant (0.9), λ is the wavelength of the x–ray source (Cu Kα source, 0.15406 nm), β is the FWHM (radians), and θ is the peak position (radians).

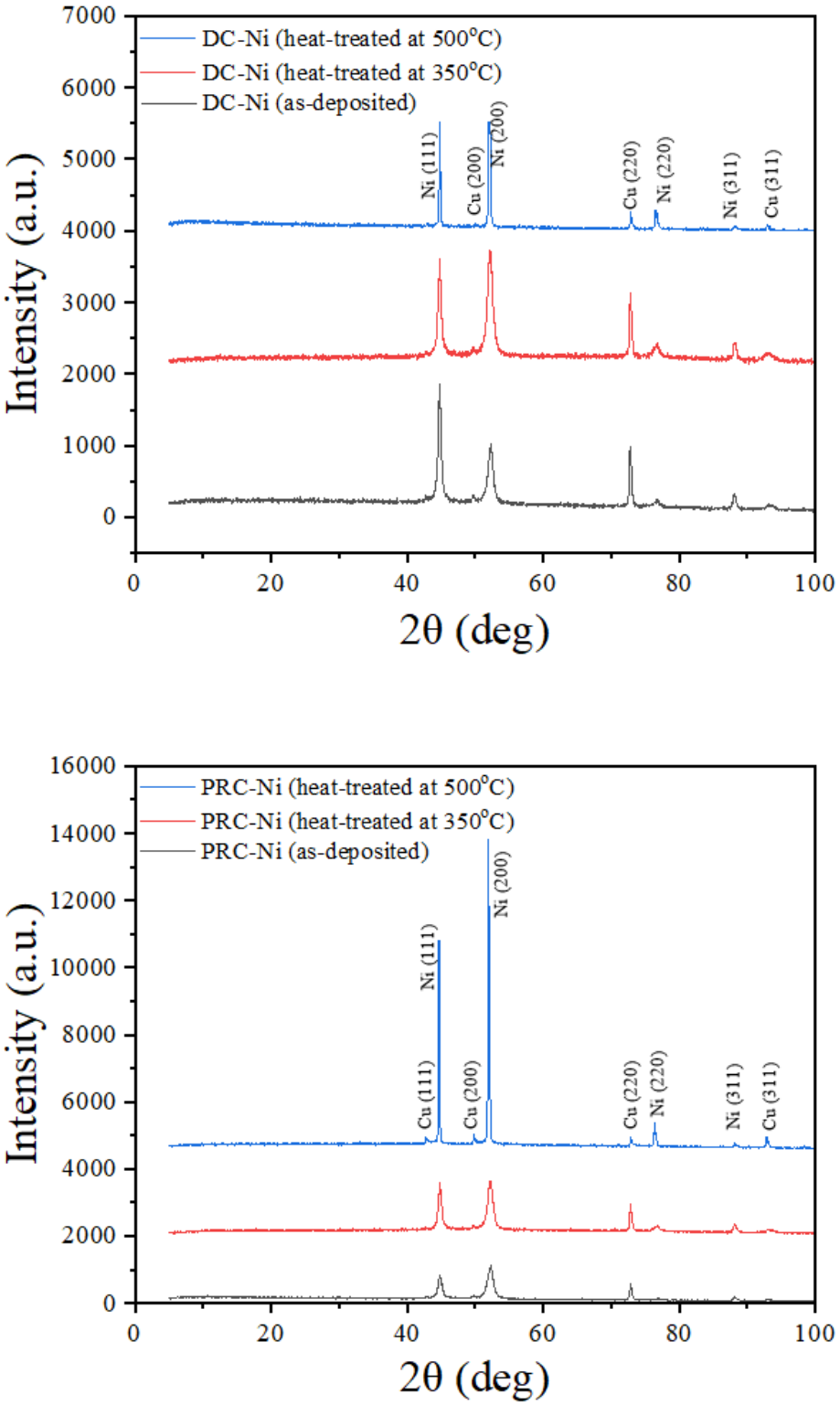

Figure 6.17 XRD spectra from the surfaces of DC and PRC electrodeposited Ni (as–deposited and heat–treated at 350°C and 500°C).

Figure 6.18 displays the XRD spectra from the surfaces of as–deposited and annealed DC and PRC deposited NiW at 350ºC and 500ºC. It was noticed that after heat treatment at 500ºC, in the case of PRC–NiW, the intensity of the Ni (111) and Ni (220) was increased and additional peaks of Ni (200) and Ni (311) was formed, while in the case of DC–NiW, the intensity of the Ni (220) and Ni (311) was diminished. As shown in Figure 6.18, the peaks of W were not observed in the XRD spectra of PRC–Ni, indicating that the crystal lattice of Ni was partly replaced by W atoms and formed a single phase solid solutions (W in Ni) with face centered cubic (F.C.C) crystal structure. Addition of the alloying element (W) in Ni, also resulted in the broadening of the lattice peaks and reduction in crystallite size due to decrease of Ni content and distortion of the phase structure. [49–51] Furthermore, the average crystallite size increased with increase of the temperature. The results of the average grain size before and after annealing at 350ºC and 500ºC are presented in Table 6.8.

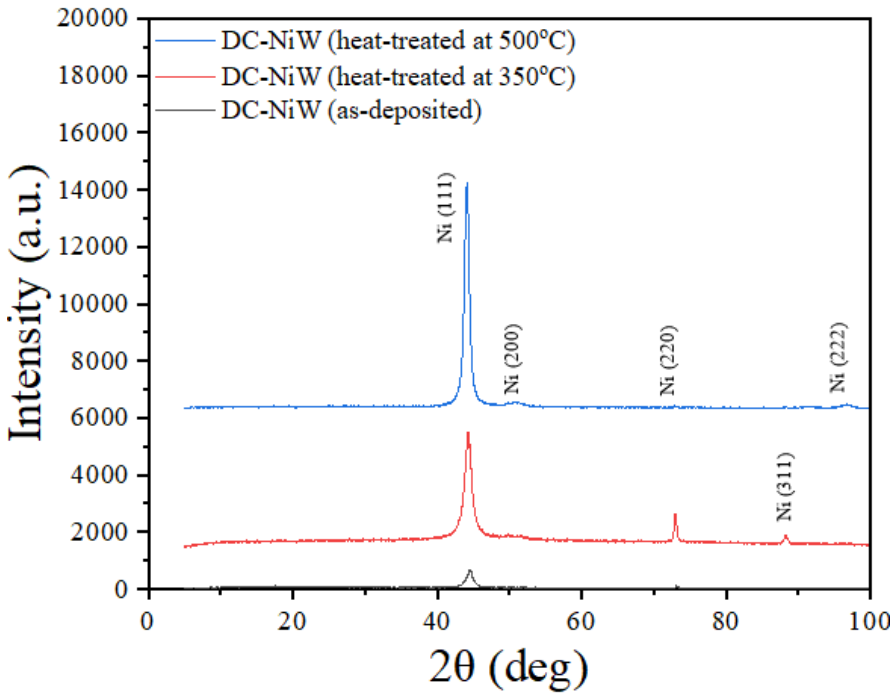

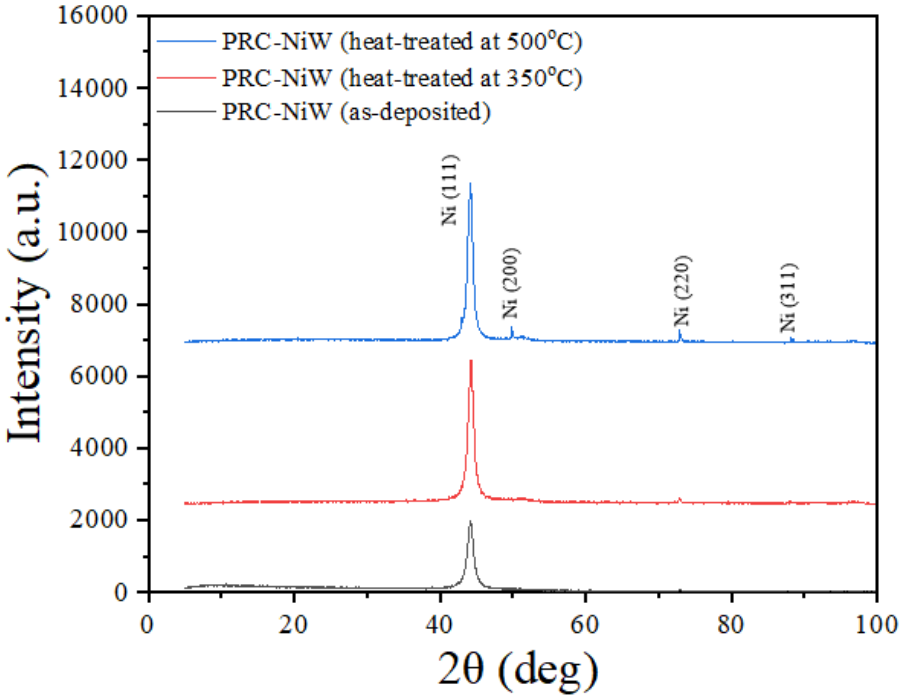

Figure 6.18 XRD spectra from the surface of DC and PRC electrodeposited NiW (as–deposited and heat–treated at 350°C and 500°C).

Figure 6.19 displays the XRD spectra from the surface of as–deposited and annealed PRC deposited NiW–SiC at 350°C and 500°C. As presented in Table 5.8, incorporation of SiC in the Ni (W) matrix resulted in decrease of the crystallite size compared to NiW due to refinement of the microstructure and encouraged nucleation overgrowth of Nickel due to presence of SiC. [52] It was also observed that in XRD spectrums of DC and PRC deposited NiW–SiC (Figure 6.19), the intensity of Ni (111) peak increases and additional peak of SiC (220) was formed with the rise of the anealing temperature. However, some peaks of SiC (101) and SiC (200) were disapeared after anealing at 500°C. Furthermore, the influence of anealing temperature on average crystallite size was investigated. It was found that increase of the anealing temperature upto 500°C in DC–NiW–SiC increased the average cristallite size form 100 Å to 124 Å. In PRC–NiW–SiC, the average grain size increased from 92 Å to 100 Å by annealing at 350°C and further increase of the annealing temperature up to 500°C did not have any effect on the average grain size of the Ni. As shown in Table 6.8, coatings produced using PRC deposition method exhibit finer grain size in comparison with DC deposited coatings. High instantaneous current density during PRC deposition results in increase of the

overpotential which promotes the nucleation rate and produces coatings with finer grain structure and higher compaction degree. [52–53]

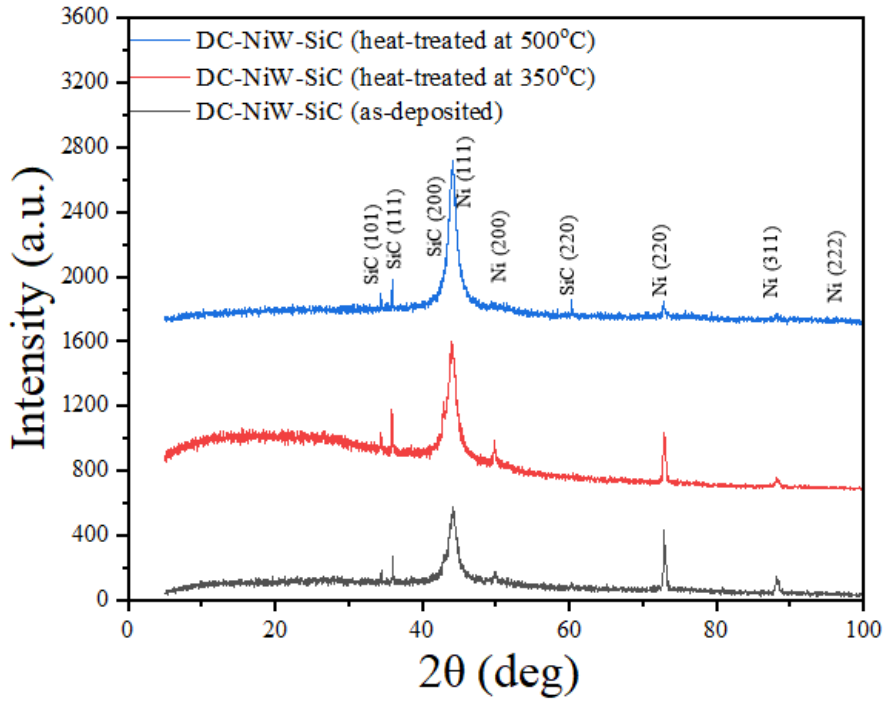

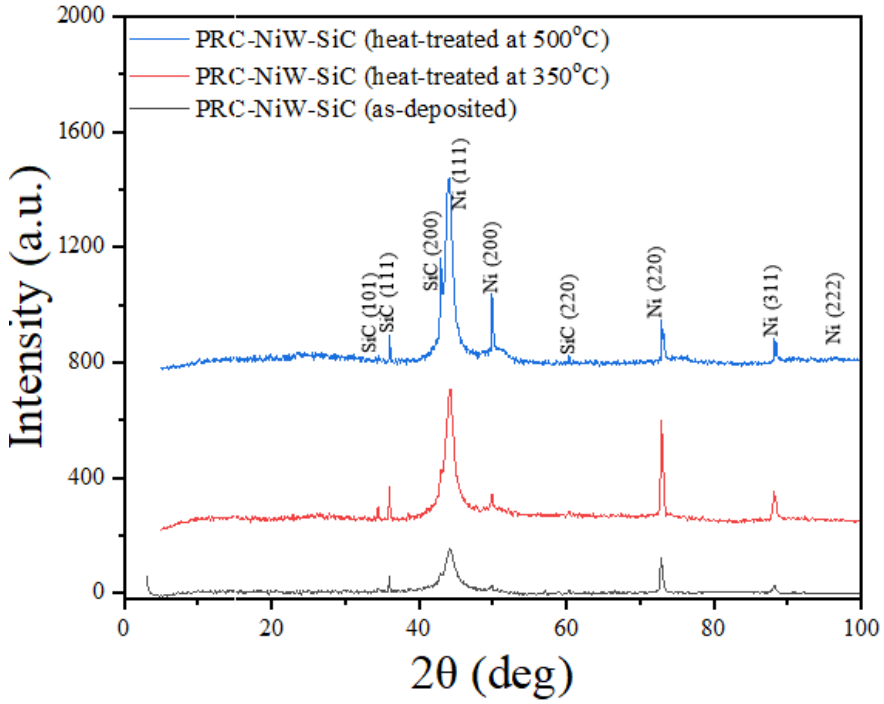

Figure 6.19 XRD spectra from the surface of DC and PRC electrodeposited NiW–SiC (as–deposited and heat–treated at 350^{o}C and 500^{o}C).

Table 6.8 Crystallite sizes of DC and PRC deposited Ni, NiW, and NiW–SiC

Coatings	**Peak position of (111) [°2Th]**	**FWHM [°2Th]**	**Crystallite size [Å]**
DC–Ni (as–deposited)	44.744	0.393	223
DC–Ni (heat–treated at 350^{o}C)	44.757	0.354	248
DC–Ni (heat–treated at 500^{o}C)	44.733	0.059	1684
PRC–Ni (as–deposited)	44.712	0.443	197
PRC–Ni (heat–treated at 350^{o}C)	44.810	0.315	280
PRC–Ni (heat–treated at 500^{o}C)	44.651	0.079	1210
DC–NiW (as–deposited)	44.600	0.551	158
DC–NiW (heat–treated at 350^{o}C)	44.319	0.433	202
DC–NiW (heat–treated at 500^{o}C)	44.140	0.216	412
PRC–NiW (as–deposited)	44.220	0.630	138
PRC–NiW (heat–treated at 350^{o}C)	44.319	0.433	202
PRC–NiW (heat–treated at 500^{o}C)	44.130	0.386	222
DC–NiW–SiC (as–deposited)	44.235	0.865	100
DC–NiW–SiC (heat–treated at 350^{o}C)	44.052	0.787	110
DC–NiW–SiC (heat–treated at 500^{o}C)	44.124	0.70	124
PRC–NiW–SiC (as–deposited)	44.205	0.945	92
PRC–NiW–SiC (heat–treated at 350^{o}C)	44.236	0.866	100
PRC–NiW–SiC (heat–treated at 500^{o}C)	44.072	0.864	100

6.4. Conclusions

Various composite coatings of Ni, NiW and NiW–SiC were successfully fabricated on brass substrates by DC and PRC current electrodeposition. From the results of PP test, it can be concluded that the incorporation of SiC into the alloy matrix, significantly improved the corrosion resistance

of the coatings and NiW–SiC composites deposited by PRC waveform had the highest corrosion resistance among all other DC and PRC electrodeposited coatings. The improvement in corrosion resistance is attributed to the SiC particles acting as physical barriers to initiation and development of defects such as crevices, gaps and micron holes in the composite coatings. SiC particles were also evenly distributed in the alloy matrix and shifted the corrosion potential of the composite coatings to more positive values resulting in restriction of localized corrosion. It was also observed that, the coatings prepared using PRC, exhibited outstanding corrosion resistance when exposed to corrosive liquid compared to that of DC waveform.

Following the PP tests, the optical micrographs were taken from the corroded surfaces of the DC–Ni, DC–NiW, DC–NiW–SiC and PRC–NiW–SiC and it was found that DC–Ni deposit was completely corroded and pulled off the surface, whereas the surface of PRC–NiW–SiC showed significantly small discoloration. A slight damage was observed on the surface of DC–NiW–SiC deposit after the PP test.

TOFF–SIMS spectra taken from the surface of DC–NiW deposit showed that the Ni layer was not completely removed after the PP test and no exposure of substrate was realized (i.e., no peaks related to Cu and Zn are seen). Similar observations were noticed for the DC–NiW–SiC and PRC–NiW–SiC deposits. However, in the latter deposits, new positively charged species were observed. These new species were more likely related to oxidation of SiC during the PP test. The oxide form of silicon species might be responsible for further surface passivation and the observed improvement in corrosion resistance of the DC and PRC–NiW–SiC composites compared to DC–NiW deposit. As well, it was found that the majority of tungsten species on the sample surface exhibited the higher oxidation states of tungsten in the case of PRC electrodeposited NiW–SiC than in the case of DC–NiW–SiC. This explains the better corrosion performance of PRC deposited NiW–SiC compared to DC deposited NiW–SiC.

XPS spectra was taken from the surface of PRC deposited Ni, NiW, and NiW–SiC to measure the average atomic concentration (%) and element valence state of all coatings before and after the PP test. In Ni coating, Cu peak was observed and the intensity of metallic Ni peaks were smaller and atomic concentration of Ni2p was lower after the pp test. Similar observation was made in NiW coating. However, no Cu peak was observed on the NiW XPS spectra which demonstrates no visible inter diffusion of Cu from the substrate into the NiW coating or exposure of the substrate to the

surface of the coating. As well, in the PRC deposited NiW–SiC, no significant difference was observed in atomic concentrations of the Ni2p before and after the pp test. It was speculated that formation of $NiWO_4$ and SiO_2 barrier layers on the surface of NiW–SiC could be responsible for high corrosion performance of the coatings which is in agreement with TOF–SIMS results.

The XRD results obtained from the surfaces of the as–deposited and annealed DC and PRC electrodeposited Ni, NiW, and NiW–SiC at 350°C and 500°C also revealed that the intensity of the peaks and the average crystallite size increased with the annealing temperature up to 500°C. PRC deposited coatings revealed finer grain size compared to the coatings produced by DC method. As well, Incorporation of SiC in DC and PRC deposited NiW also reduced the crystallite size compared to DC and PRC deposited NiW by providing more nucleation sites and refining the microstructure. The smaller crystallite size promotes the number of nucleation sites and formation of compact and well–adherent passive films with a lower defect density due to a higher amount of active surface atoms. This can enhance the resistance to chloride ion adsorption on the surface of the coating and remarkably improve the anti–corrosion and wear performance of the coatings.

6.5. References

[1] D. Jones, and P. Amy, "A thermodynamic interpretation of microbiologically influenced corrosion," vol. 58, no. 8, p. 638-645, 2002.

[2] F. Presuel-Moreno, M. A. Jakab, N. Tailleart, M. Goldman, and J. R. Scully, "Corrosion-resistant metallic coatings," vol. 11, no. 10, p. 14-23, 2008.

[3] S. Siebert, W. Theisen, and H. Hill, "Korrosionsbeständige Metall-Matrix-Composite," vol. 65, no. 4, p. 201-208, 2010.

[4] M. Q. Argañaraz, S. Ribotta, M. Folquer, L. Gassa, G. Benítez, M. Vela, and R. Salvarezza "Ni–W coatings electrodeposited on carbon steel: Chemical composition, mechanical properties and corrosion resistance," vol. 56, no. 17, p. 5898-5903, 2011.

[5] M. Hosseini, M. Abdolmaleki, and J. Ghahremani, "Investigation of corrosion resistance of electrodeposited Ni–W/SiC composite coatings," vol. 49, no. 4, p. 247-253, 2014.

[6] L. Elias, and A.C. Hegde, "Electrodeposition of laminar coatings of Ni–W alloy and their corrosion behaviour," vol. 283, p. 61-69, 2015.

[7] Y. Yao, S. Yao, and L. Zhang, "Corrosion behavior of Ni–W/SiC nanocomposite coating in NaCl solution," vol. 13, no. 04, p. 489-494, 2006.

[8] M. H. Allahyarzadeh, M. Aliofkhazraei, A.S. Rouhaghdam, V. Torabinejad, H. Alimadadi, and A. Ashrafi, "Electrodeposition mechanism and corrosion behavior of multilayer nanocrystalline nickel-tungsten alloy," vol. 258, p. 883-899, 2017, 883.

[9] M. Chandrasekar, and M. Pushpavanam, "Pulse and pulse reverse plating—Conceptual, advantages and applications," vol. 53, no. 8, p. 3313-3322, 2008.

[10] S. Singh, M. Sribalaji, N. P. Wasekar, S. Joshi, G. Sundararajan, R. Singh, and A. K. Keshri, "Microstructural, phase evolution and corrosion properties of silicon carbide reinforced pulse electrodeposited nickel–tungsten composite coatings," vol. 364, p. 264-272, 2016.

[11] Y. Yao, S. Yao, L. Zhang, and H. Wang, "Electrodeposition and mechanical and corrosion resistance properties of Ni–W/SiC nanocomposite coatings," vol. 61, no. 1, p. 67-70, 2007.

[12] E. Sheha, and H. S. Refai, "Water scavenger as effective electrolyte additive and hybrid binder-free organic/inorganic cathode for Mg battery applications," vol. 372, p. 137883, 2021.

[13] A. Chianpairot, G. Lothongkum, C.A. Schuh, and Y. Boonyongmaneerat, "Corrosion of nanocrystalline Ni–W alloys in alkaline and acidic 3.5 wt.% NaCl solutions," vol. 53, no. 3, p. 1066-1071, 2011.

[14] M. Q. Argañaraz, S. Ribotta, M. Folquer, L. Gassa, G. Benítez, M. Vela, and R. Salvarezza "Ni–W coatings electrodeposited on carbon steel: Chemical composition, mechanical properties and corrosion resistance," vol. 56, no. 17, p. 5898-5903, 2011.

[15] N. Shakibi Nia, J. Creus, X. Feaugas, and C. Savall, "Influence of metallurgical parameters on the electrochemical behavior of electrodeposited Ni and Ni–W nanocrystalline alloys," vol. 370, p. 149-159, 2016.

[16] D. Yin, C. J. Marvel, F. Y. Cui, R. P. Vinci, and M. P. Harmer, "Microstructure and fracture toughness of electrodeposited Ni-21 at.% W alloy thick films," vol. 143, p. 272-280, 2018.

[17] B. Li, W. Zhang, W. Zhang, and Y. Huan, "Preparation of Ni-W/SiC nanocomposite coatings by electrochemical deposition," vol. 702, p. 38-50, 2017.

[18] R. Juškėnas, I. Valsiūnas, V. Pakštas, A. Selskis, V. Jasulaitienė, V. Karpavičienė, and V. Kapočius, "XRD, XPS and AFM studies of the unknown phase formed on the surface during electrodeposition of Ni–W alloy," vol. 253, no. 3, p. 1435-1442, 2006.

[19] N. J. Vickers, "Animal communication: when i'm calling you, will you answer too," vol. 27, no. 14, p. R713-R715, 2017.

[20] O. A. Rahman, N. P. Wasekar, G. Sundararajan, and A. K. Keshri, "Experimental investigation of grain boundaries misorientations and nano twinning induced strengthening on addition of silicon carbide in pulse electrodeposited nickel tungsten composite coating," vol. 116, p. 1-7, 2016.

[22] Z. Mohammadpour, and H. R. Zare, "Improving the Corrosion Resistance of the Nickel–Tungsten Alloy by Optimization of the Electroplating Conditions," vol. 73, no. 4, p. 937-944, 2020, 937.

[23] P. Leisner, C. Zanella, I. Belov, C. Edström, G. Sandulache, and W. Hansal, "Control of silver throwing power by pulse reverse electroplating," vol. 95, no. 1, p. 25-30, 2017.

[24] S. Mohajeri, A. Dolati, and M. Ghorbani, "The influence of pulse plating parameters on the electrocodeposition of Ni-TiO_2 nanocomposite single layer and multilayer structures on copper

substrates," vol. 262, p. 173-183, 2015.

[25] T. Frade, V. Bouzon, A. Gomes, and M. I. da Silva Pereira, "Pulsed-reverse current electrodeposition of Zn and Zn-TiO_2 nanocomposite films," vol. 204, no. 21-22, p. 3592-3598, 2010.

[26] U. Pramod Kumar, T. Liang, C. J. Kennady, R. Nandha Kumar, and J. Prabhu, "Influence of Positional Isomeric Spacers of Naphthalene Derivatives on Ni–W Alloy Electrodeposition: Electrochemical and Microstructural Properties," vol. 5, no. 7, p. 3376-3388, 2020.

[27] L. Orlovskaja, N. Periene, M. Kurtinaitiene, and S. Surviliene, "Ni–SiC composite plated under a modulated current," vol. 111, no. 2-3, p. 234-239, 1999.

[28] F. Wang, S. Arai, and M. Endo, "Preparation of nickel–carbon nanofiber composites by a pulse-reverse electrodeposition process," vol. 7, no. 7, p. 674-678, 2005.

[29] H. Zakaria, "Microstructural and corrosion behavior of Al/SiC metal matrix composites," vol. 5, no. 3, p. 831-838, 2014.

[30] T. Rabizadeh, and S. R. Allahkaram, "Corrosion resistance enhancement of Ni–P electroless coatings by incorporation of nano-SiO_2 particles," vol. 32, no. 1, p. 133-138, 2011.

[31] J. Chen, and J. K. Wu, "The improved passivation of iron induced by additions of tungsten," vol. 30, no. 1, p. 53-58, 1990.

[32] Z. Bai, and B. Zhang, "Fabrication of superhydrophobic reduced-graphene oxide/nickel coating with mechanical durability, self-cleaning and anticorrosion performance," vol. 2, no. 2, p. 151-158, 2020.

[33] D. Fa, B. Yu, and Y. Miao, "Synthesis of ultra-long nanowires of nickel phosphate by a template-free hydrothermal method for electrocatalytic oxidation of glucose," vol. 564, p. 31-38, 2019.

[34] A. P. Grosvenor, M. C. Biesinger, R. S. C. Smart, and N. S. McIntyre, "New interpretations of XPS spectra of nickel metal and oxides," vol. 600, no. 9, p. 1771-1779, 2006.

[35] W. Huang, S. Ding, Y. Chen, W. Hao, X. Lai, J. Peng, J. Tu, Y. Cao, and X. Li, "3D NiO hollow sphere/reduced graphene oxide composite for high-performance glucose biosensor," vol. 7, no. 1, p. 1-11, 2017.

[36]] Y. Koshtyal, D. Nazarov, I. Ezhov, I. Mitrofanov, A. Kim, A. Rymyantsev, O. Lyutakov, A. Popovich, and M. Maximov, "Atomic layer deposition of nio to produce active material for thin-film lithium-ion batteries," vol. 9, no. 5, p. 301, 2019.

[37] H. Li, F. Musharavati, E. Zalenezhad, X. Chen, K. N. Hui, and K. S. Hui, "Electrodeposited NiCo layered double hydroxides on titanium carbide as a binder-free electrode for supercapacitors," vol. 261, p. 178-187, 2018/01/20/ 2018. [En ligne]. Disponible: https://www.sciencedirect.com/science/article/pii/S0013468617327135

[38] P. Salunkhe, M. A. AV, and D. Kekuda, "Investigation on tailoring physical properties of Nickel Oxide thin films grown by dc magnetron sputtering," vol. 7, no. 1, p. 016427, 2020.

[39] G. Cui, J. Wang, H. Fan, X. Sun, Y. Jiang, S. Wang, D. Liu, and J. Gui, "Towards understanding the microstructures and hydrocracking performance of sulfided Ni–W catalysts: Effect of metal loading," vol. 92, no. 12, p. 2320-2327, 2011, 2320.

[40] S. Green, A. Kuzmin, J. Purans, C. G. Granqvist, and G. A. Niklasson, "Structure and composition of sputter-deposited nickel-tungsten oxide films," vol. 519, no. 7, p. 2062-2066, 2011.

[42] R. Kukushkin, P. Yeletsky, C. Grassin, B. H. Chen, O. Bulavchenko, A. Saraev, and V. Yakovlev, "Deoxygenation of esters over sulfur-free Ni–W/Al_2O_3 catalysts for production of biofuel components," vol. 396, p. 125202, 2020.

[43] P. Lammel, L. D. Rafailovic, M. Kolb, K. Pohl, A. H. Whitehead, G. Grundmeier, and B. Gollas, "Analysis of rain erosion resistance of electroplated nickel–tungsten alloy coatings," vol. 206, no. 8-9, p. 2545-2551, 2012.

[44] N. P. Wasekar, N. Hebalkar, A. Jyothirmayi, B. Lavakumar, M. Ramakrishna, and G. Sundararajan, "Influence of pulse parameters on the mechanical properties and electrochemical corrosion behavior of electrodeposited Ni-W alloy coatings with high tungsten content," vol. 165, p. 108409, 2020.

[45] A. Andrews, M. Herrmann, M. Sephton, C. Machio, and A. Michaelis, "Electrochemical corrosion of solid and liquid phase sintered silicon carbide in acidic and alkaline environments," vol. 27, no. 5, p. 2127-2135, 2007, 2127.

[46] H. Farsi, and S. A. Hosseini, "The electrochemical behaviors of methylene blue on the surface of nanostructured $NiWO_4$ prepared by coprecipitation method," vol. 17, no. 7, p. 2079-2086, 2013.

[47] L. Niu, Z. Li, Y. Xu, J. Sun, W. Hong, X. Liu, J. Wang, and S. Yang, "Simple synthesis of amorphous $NiWO_4$ nanostructure and its application as a novel cathode material for asymmetric supercapacitors," vol. 5, no. 16, p. 8044-8052, 2013.

[48] Ahadian, E. Nouri, M. Ranjbar, and A. Dolati, "Diffusion and segregation of substrate copper in electrodeposited Ni–Fe thin films," vol. 443, no. 1-2, p. 81-86, 2007.

[49] S. Mbugua Nyambura, M. Kang, J. Zhu, Y. Liu, Y. Zhang, and N. J. Ndiithi, "Synthesis and characterization of Ni–W/Cr_2O_3 nanocomposite coatings using electrochemical deposition technique," vol. 9, no. 12, p. 815, 2019.

[50] K. Sriraman, "Ganesh Sundara Raman S, Seshadri SK. Synthesis and evaluation of hardness and sliding wear resistance of electrodeposited nanocrystalline Ni–W alloys," vol. 418, p. 303-311, 2006.

[51] S. Pinate, and C. Zanella, "Wear behavior of Ni-based composite coatings with dual nano-SiC: graphite powder mix," vol. 10, no. 11, p. 1060, 2020.

[52] T. Borkar, and S. P. Harimkar, "Effect of electrodeposition conditions and reinforcement content on microstructure and tribological properties of nickel composite coatings," vol. 205, no. 17-18, p. 4124-4134, 2011, 4124.

[53] M. Chandrasekar, and M. Pushpavanam, "Pulse and pulse reverse plating—Conceptual, advantages and applications," vol. 53, no. 8, p. 3313-3322, 2008.

[54] A. Rashidi, and A. Amadeh, "The effect of current density on the grain size of electrodeposited nanocrystalline nickel coatings," vol. 202, no. 16, p. 3772-3776, 2008.

CHAPTER 7 ARTICLE 2: PITTING CORROSION AND MECHANICAL PROPERTIES OF DIRECT CURRENT AND PULSED REVERSE CURRENT ELECTRODEPOSITED NICKEL–TUNGSTEN COATINGS

Authors: Mina Dadvand, Oumarou Savadogo

Article published: Journal of New Materials for Electrochemical System, 10 June 2022
DOI: https://doi.org/10.14447/jnmes.v25i2.a06

Abstract

The electrochemical corrosion and mechanical properties of direct current and pulsed reverse current electrodeposited nickel and nickel–tungsten were investigated by using cyclic polarization measurement and nano–indentation techniques. Direct and pulsed reverse current electrodeposited nickel–tungsten coatings revealed a significant higher resistance to pitting corrosion when compared to direct and pulsed reverse current deposited nickel. Furthermore, pulsed reverse current electrodeposited nickel–tungsten displayed the most noble corrosion potential and higher corrosion resistance compared to direct current electrodeposited nickel–tungsten. This was attributed to the more nano–crystalline structure of the pulsed–reverse current deposited coatings when compared to that of the direct current electrodeposited nickel–tungsten. The average modulus for both direct and pulsed reverse current deposited nickel–tungsten were found to be similar but the average hardness of direct current deposited nickel–tungsten was slightly higher than that of pulsed reverse current deposited nickel–tungsten. This was attributed to the higher tungsten content in the direct current deposited nickel–tungsten coating (35 wt.%) compared to the pulsed reverse current deposited nickel–tungsten (25 wt.%) and is supported by our energy dispersive x–ray spectroscopy results.

Keywords: Nickel–tungsten coating, direct current, pulsed reverse current, electrodeposition, cyclic polarization.

7.1 Introduction

Electrochemical deposition methods have been widely used to produce various coatings of nickel (Ni) alloys such as nickel–tungsten (NiW) in various engineering applications due to their simplicity and affordability [1]. In recent years, pulsed reverse current (PRC) electrodeposition method has gained considerable interest owing to its unique mechanical and corrosion properties. PRC technique has unique ability to produce coatings with greater uniformity, and finer grain size than the coatings obtained by using direct current (DC).

It has been also reported that deposits with high tungsten content produced by means of PRC are superior with respect to being crack–free with lower defects compared to those produced by DC with the same tungsten content. Formation of residual tensile stress as a result of hydrogen evolution over the cathode was reported as the main cause for cracking of DC deposited NiW with high tungsten content, whereas in PRC technique, the reverse or anodic current consumes evolved hydrogen through its re–oxidation on the surface of cathode [1–3].

In general, electrodeposited NiW coatings have demonstrated high hardness and high wear resistance. Therefore, improving their corrosion performance in various environments is in high interest. It is also imperative to investigate their corrosion behavior as well as corrosion mechanism and correlate them with their microstructures [1–6]. There are a limited number of published articles about electrochemical investigation on corrosion behavior of electrodeposited NiW alloys [7–12] Majority of such studies are on investigation of general corrosion behavior of NiW alloys and their composites using potentiodynamic polarization technique in various corrosive environments and there is also not much information available regarding their pitting behavior [7–8, 13–17]. For example, Sriraman et al. [7] studied the influence of the tungsten content of the coatings on the corrosion resistance of the Ni–W and Ni–W–Fe alloys in 3.5 wt. % NaCl and sulfuric acid solution using polarization and electrochemical impedance spectroscopy techniques. They found that Ni–W with 7.54 at.%. tungsten and Ni–W–Fe with 9.20 at.% tungsten had the highest corrosion resistance.

Yao et al. [13] investigated the general corrosion behavior of NiW–SiC composite by using anodic polarization and electrochemical impedance spectroscopy (EIS) techniques. They reported that the inclusion of SiC nano–particulates into the NiW alloy matrix increased the general corrosion resistance. The enhancement of corrosion resistance was explained by physical barrier behavior of the SiC particles to the corrosion process. Hosseini et al. [14] reported the corrosion characteristics

of DC electrodeposited NiW–SiC composite coatings by using mass loss and electrochemical measurements, including open circuit potential, electrochemical impedance spectroscopy and potentiodynamic polarization in a 3.5 wt. % NaCl solution. The results showed that the addition of SiC particle to the deposition bath of NiW significantly increased the corrosion resistance. To the best of our knowledge, no research has been reported to investigate the pitting corrosion behavior of pulsed reverse (PRC) electrodeposited nanostructure NiW and to compare them with those of electrodeposited by DC current waveform.

Pitting corrosion is a localized form of corrosion that occurs through localized acceleration of dissolution of the material. The formation of passive films on many engineering metallic materials reduces the corrosion rate substantially [4–5]. However, the passive films can be broken locally resulting in accelerated dissolution of the underneath metal. The tendency of materials towards the localized corrosion in a corrosive environment can be evaluated by using cyclic polarization (CPP) technique. During the cyclic polarization test, the applied potential to the specimen is swept linearly in anodic direction [4–6].The direction of the sweep is then reversed (cathodic) once the measured current density approaches a certain value. The formation and the size of a hysteresis represent the pitting formation and the tendency of the specimen towards the pitting, respectively. In CPP technique, pitting or breakdown potential (Ep or Eb), protection or re–passivation potential (Eprot or Erep), passivation current density (ip), anodic to cathodic transition potential, hysteresis, and anodic nose or active–passive transition potential can be used to evaluate the corrosion behavior of materials [4–5]. Pitting, re–passivation, and anodic to cathodic transition potentials are based on the difference in corrosion potential (Ecorr). In fact, the most important parameters for investigating of pitting resistance are the relative locations of pitting and protection potentials to corrosion potential.

In this work, we report for the first time on the pitting corrosion behavior of DC and PRC electrodeposited Ni and NiW coatings using cyclic polarization as well as their mechanical properties by nano–indentation technique.

7.2 Material and methods

7.2.1 Electrolyte components

The Ni electrodeposition electrolyte was composed of nickel sulfate ($NiSO_4.6H_2O$) as a source of nickel ions, citric acid as complexing agent, o– benzoic sulfimide (sodium saccharin, $C_7H_5NO_3S$) as stress reducer, propargyl–oxopropane– 2,3–dihydroxy as a grain refiner and brightener, and DuPont Capstone fluorosurfactant FS–63 as a wetting agent. The NiW electrodeposition bath was prepared by adding sodium tungstate dehydrate ($Na_2WO_4.2H_2O$) as a source of tungstate ions into Ni electrodeposition bath. The composition and operating conditions used for electrodeposition condition of NiW is summarized in Table 7.1.

In this formulation, citric acid is used as a complexing agent to form complexes with both tungstate (WO_4^{2-}) and nickel (Ni^{2+}) ions to prevent direct reaction between nickel and tungstate ions. Such direct reaction could result in the formation of an insoluble nickel tungstate compound in the plating bath [18–19]. Sodium saccharin was used as a stress removal agent to reduce the accumulated stress within the electrodeposited coating. [20]

We used propargyl–oxo–propane-2, 3–dihydroxy as a grain refiner and brightening agent to produce uniform deposit with mirror–finish surface. This compound increases the active nucleation sites on the electrode surface leading to the refinement of the grain size of the nickel [21]. Finally we used, Capstone fluoro–surfactant FS–63 (DuPont) as a wetting agent to facilitate separation of adsorbed hydrogen gas bubbles covering the electrode surface during the electrodeposition process. [22]

7.2.2 Substrate preparation

The surface of brass substrates was degreased, activated and rinsed prior to electrodeposition process. Substrates were immersed into 50 $g.L^{-1}$ alkaline soap solution (TEC1001; Technic Inc.) at temperature of about 50°C for approximately 1 min followed by rinsing with deionized (DI) water. The substrate was then activated by immersing into dilute sulfuric acid (10% v/v) at room temperature for about 10 sec followed by rinsing with DI water. In order to determine the cleanliness of the substrate, water break test was performed. In this testing protocol, the substrate was gently rinsed

with deionized water following the final rinse step. The substrate was considered clean if the water completely wets the surface.

7.2.3 Electrodeposition bath setup

The electrodeposition setup was composed of an electrodeposition tank containing electrolyte, a pump (Flo King Filter System Inc.) to provide adequate agitation, an anode made of platinized titanium mesh, a cathode made of brass as a substrate being electrodeposited, and a pulsed reverse plating power supply. The electrodeposition bath was placed inside a water circulating bath operating at 60°C temperature. A typical composition of the electrochemical bath for the electrodeposition of NiW is displayed in Table 7.1.

Table 7.1 Electrodeposition electrolyte ingredients and experimental parameters

Chemical Compound	**Concentration**
Nickel sulfate	29.5–30 ($g.L^{-1}$)
Sodium tungstate	58–60 ($g.L^{-1}$)
Citric acid	63–67 ($g.L^{-1}$)
Ammonia	58 ($ml.L^{-1}$)
Sulfuric acid	As needed
Propargyl–oxo propane-2,3– dihydroxy	0.9–1 ($g.L^{-1}$)
DuPontTM Capstone® Fluoro–surfactant FS– 63	1.8-2 ($g.L^{-1}$)
Sodium saccharin	0.5–1 ($g.L^{-1}$)
Polyethyleneimine branched, Mn~600 by GPC	0.5 ($g.L^{-1}$)
Experimental parameters	
pH	7.8–8.0
Temperature	58–61 °C
Time	30 min

Figure 7.1 represents the general schematic diagram of electrodeposition setup used for electrodeposition. A pulse reverse power supply (Model pe8005, Plating Electronic GmbH,

Germany) was used to apply direct current (DC) and pulse reverse current (PRC) waveforms to electrodeposition bath. DC–Ni and DC–NiW coatings were electrodeposited by applying of DC waveform (0.14 $A.cm^{-2}$ for duration of 30 min) from Ni and NiW baths, respectively. Whereas, PRC–Ni, and PRC–NiW coatings were electrodeposited by applying of PRC waveform (forward current density of 0.15 $A.cm^{-2}$ for 16 ms and reverse current density of 0.11 $A.cm^{-2}$ for 9 ms) from Ni, and NiW baths, respectively.

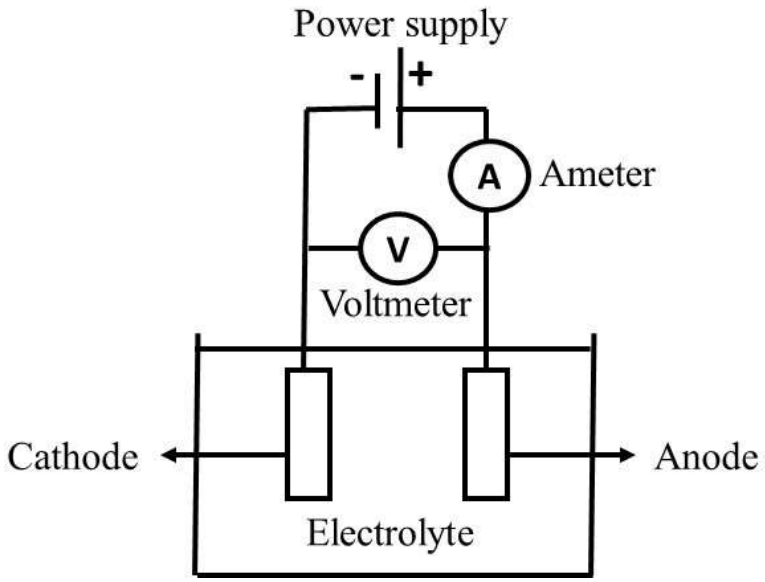

Figure 7.1 Electrodeposition bath setup.

7.2.4 Characterization of deposits

The grain size and surface morphology of the deposits were characterized by energy scanning transmission electron microscopy (STEM, Hitachi Model HT7700) and scanning electron microscopy (SEM, Joel 7600 TFE), respectively.

The hardness and elastic modulus were evaluated by using a nano–indenter (Nanomechanics, Inc) with a conical diamond indenter tip (90 degrees, 5 µm radius spherical end). The pre–test parameters are displayed in Table 7.2. The nano–indentation technique is commonly used for the measurement of mechanical properties of the coating such as hardness and elastic modulus. In a typical nano–indentation, load and displacement are recorded as the indenter is pressed into the surface of the

testing material under a fixed load. The response of interest is the load–displacement curve which is often called the P–h curve. [23–25]

Table 7.2 Pre–test parameters for nano–indentation

Parameters	**Value**
Target load (mN)	200
Target depth (nm)	5000
Poisson's Ratio of Sample	0.3
Target Indentation Strain Rate (s^{-1}) Target Frequency (Hz) Surface Approach Velocity ($nm.s^{-1}$) Hold Maximum Load Time (s)	0.2 100 100 1

In Nano–indentation process, target load **s**pecifies the load at which the indentation test will terminate. This value also determines the load at which the average results will be reported. Poisson's ratio of the sample was used in calculating the elastic modulus from indentation data. Target Indentation Strain Rate method attempts to maintain a constant indentation strain rate during loading and this value sets that strain rate. The loading algorithm of a constant indentation strain rate test follows a constant $\frac{dp/dt}{P}$, where *P* is load and *t* is time. The result is an exponential load rate. This is an important loading condition for strain rate sensitive materials. In order to obtain reliable statistics, 100 indents on various locations for each specimen were performed. [26–28]

Potentiostat (Princeton Applied Research Potentiostat/Galvanostat Model 273A) was used for studying of pitting corrosion behaviors of the deposits. The potentiostat was equipped with CorrWare software enabling to apply potential scans remotely through the software. The Cyclic potentiodynamic polarization (CPP) scans were performed from -0.6 to 1.0 V in forward scan at room temperature and 5 $mV.s^{-1}$ scan rate and from 1.0 to -1.0 V in reversed scan with 5 $mV.s^{-1}$ scan rate. For all the CPP experiments, silver/silver sulfate electrode and graphite rod were used as reference and counter electrodes, respectively. The surface of the specimen was covered with an

insulating 3M tape to expose 1 cm^2 of the surface to corrosive liquid (artificial sea water). The composition of the artificial sea water is summarized in Table 7.3.

Table 7.3 Electrodeposition electrolyte ingredients and experimental parameters

Ingredients	**Concentration wt.%**
NaCl	58.49
Na_2SO_4	9.75
$CaCl_2$	2.765
KCl	1.645
$NaHCO_3$	0.477
KBr	0.238
H_3BO_3	0.071
$SrCl_2.6H_2O$	0.095
NaF	0.007
$MgCl_2$	26.46

7.3 Results and discussion

7.3.1 Cyclic potentiodynamic polarization (CPP)

The cylic potentiondynamic polarization (CPP) curve of the DC electrodeposited Ni is shown is Figure 7.2. As it can be seen, during the anodic polarization scan, the potential scanning begins from the corrosion potential (E_{corr}). The rapid increase in current density before approaching the oxygen evolution potential can be due to the following factors: 1) formation of metastable pitting within the pore at the passive potential due to local dissolution of the active regions; 2) existence of defects on the surface of passive layer that can cause instability of the passivation film throughout the passive region. These defects are active and can propagate resulting in the increase of the current density; 3) breakdown of the passive layer and occurrence of pitting corrosion in the presence of corrosive ions [29–31].These values of the current density can be also related to their corresponding

potential values. The potential in which this sudden increase in current density occurs is named as pitting corrosion (E_p), breakdown or rupture potential. In other words, pitting potential is the minimum potential at which the material tends to the pitting corrosion. Above the pitting potential, new pits will initiate and develop. Pitting corrosion resistance (R_p) can be calculated from $R_p = |E_{corr} - E_p|/d_i$, where di is the corresponding variation of the current density. After increasing the current density at pitting potential, the direction of potential scanning is reversed. During the reversed scan, the current density is higher than the current density in the forward scan resulting in positive hysteresis which is indicative of pitting corrosion. Re–passivation or protection potential is the potential at intersection between reversed and forward polarization curves. At this potential, the anodic current density decreases to the smallest value on the reversed scan. This is in agreement with the results published elsewhere. [4, 29–31]

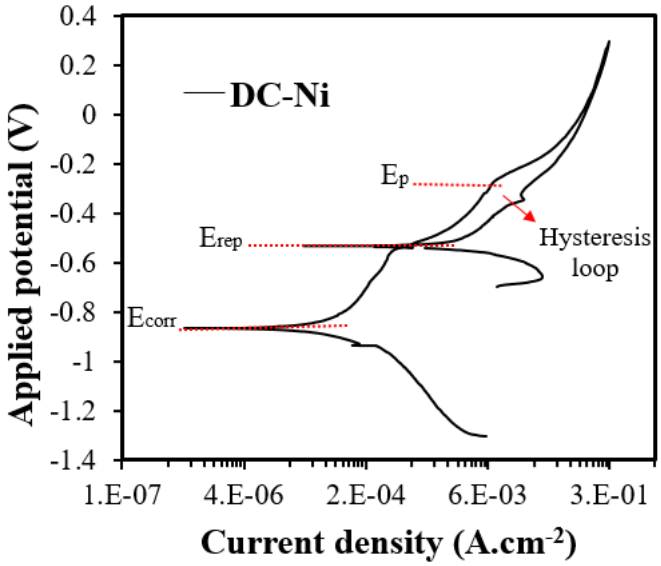

Figure 7.2 Cyclic potentiodynamic polarization (CPP) curves of Direct Current (DC) electrodeposited Ni.

The CPP curves of DC–Ni, PRC–Ni, DC–NiW, and PRC–NiW are shown in Figure 7.3, respectively. The curves of the DC and PRC electrodeposited Ni samples (Figure 7.3a) display a relatively large positive hysteresis compared to those of the DC and PRC deposited NiW (Figure

7.3b). The difference between E_p and E_{rep} for Ni deposit is larger compared to that NiW. In other words, the deposited NiW displays higher pitting resistance (almost no pitting) than Ni deposit.

This conclusion is supported by the following explanation of difference between the value of the pitting (E_p) potential and that of the protection or repassivation potential (E_{rep}). At the protection or repassivation potential, the growth of pits is stopped. The size of hysteresis is indicative of the degree of pitting corrosion and it is determined by the difference between pitting potential and protection potential (E_p–E_{rep}). At the potential between E_p and E_{rep}, only old pits propagate and there is no nucleation of new pits. The relative location of re–passivation potential (E_{rep}) with respect to corrosion potential (E_{corr}) determines the resistance of the material to localized or pitting corrosion. In other words, if E_{rep} is nobler than E_{corr}, the propagation of active pits is reduced or stopped and at potentials region between E_{rep} and E_{corr}, the passive layer is stable and pits will not initiate or grow. As well, in this region (perfect passivity region) crack initiation and propagation will not occur. [17]

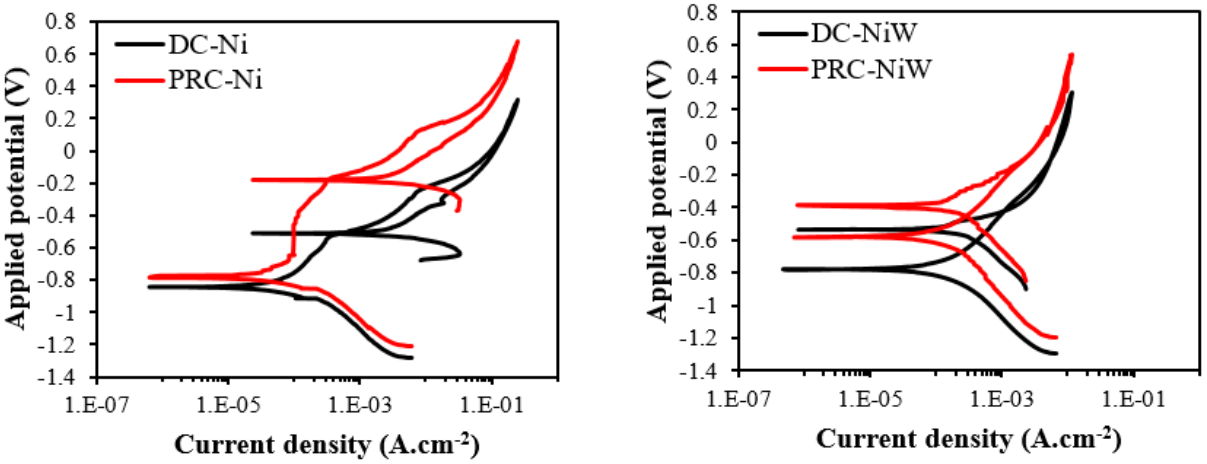

Figure 7.3 (a) CPP of electrodeposited DC–Ni and PRC–Ni (b) CPP of electrodeposited DC–NiW and PRC–NiW.

The corrosion potential values for DC–Ni, PRC–Ni, DC–NiW, and PRC–NiW extracted from Figures 7.3 (a) and 7.3 (b) are displayed in Figure 7.4. As it can be seen, PRC–NiW demonstrated the more noble corrosion potential. It was speculated that the difference in grain structures of DC–NiW and PRC–NiW resulting from the applied current waveforms (DC and PRC) were mainly

responsible for different corrosion behaviors. Ghavidel et al. [32] investigated the pitting corrosion behavior of nano and microcrystalline Ni coatings deposited by direct and pulse current (PC) waveforms. They found that nano–crystalline coatings possessed higher breakdown potential than that of microcrystalline coating.

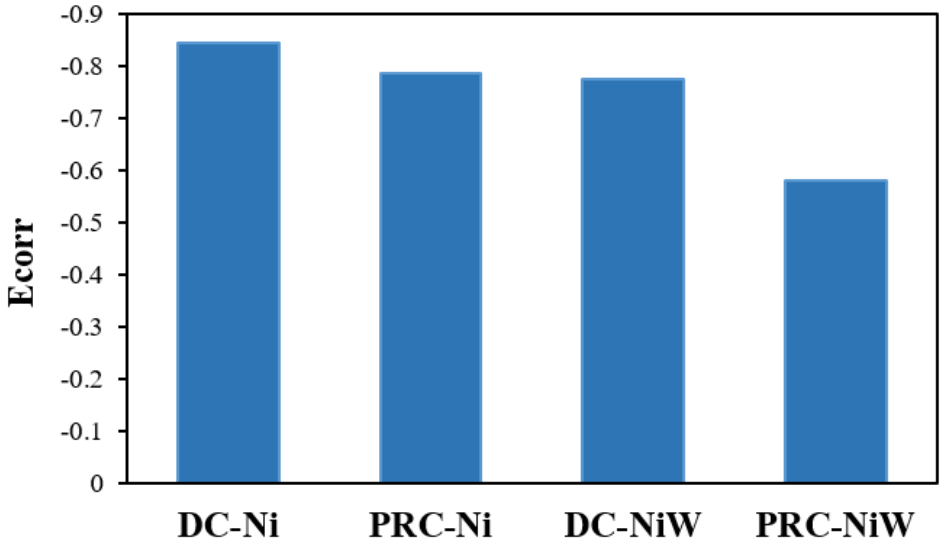

Figure 7.4 Comparison of DC–Ni, PRC–Ni, DC–NiW and, PRC–NiW coatings with respect to their corrosion potential.

7.3.2 STEM analysis

STEM observations were conducted on DC–NiW and PRC–NiW electrodeposited samples to examine the crystalline and/or amorphous structure of NiW coatings deposited on brass substrates. The samples for STEM analysis were thinned to <50 nm in thickness by FIB lift–out procedure to enable the analyzing beam of electrons to pass through the samples. The grains at region adjacent to brass substrate (Figures 7.5a and 7.6a) exhibit preferentially oriented nano–twinned structure while all the grains in other region further from the substrate such as middle section of the coating (Figures 7.5b and 7.6b), appear to be amorphous. In this region, numerous sub–domains are also visible which display various types of mass–thickness contrast (resulting from increased/decreased W content) or diffraction contrast. Different magnifications from middle section of the coatings are displayed in Figures 7.5c, 7.5d, 7.6c, and 7.6d.

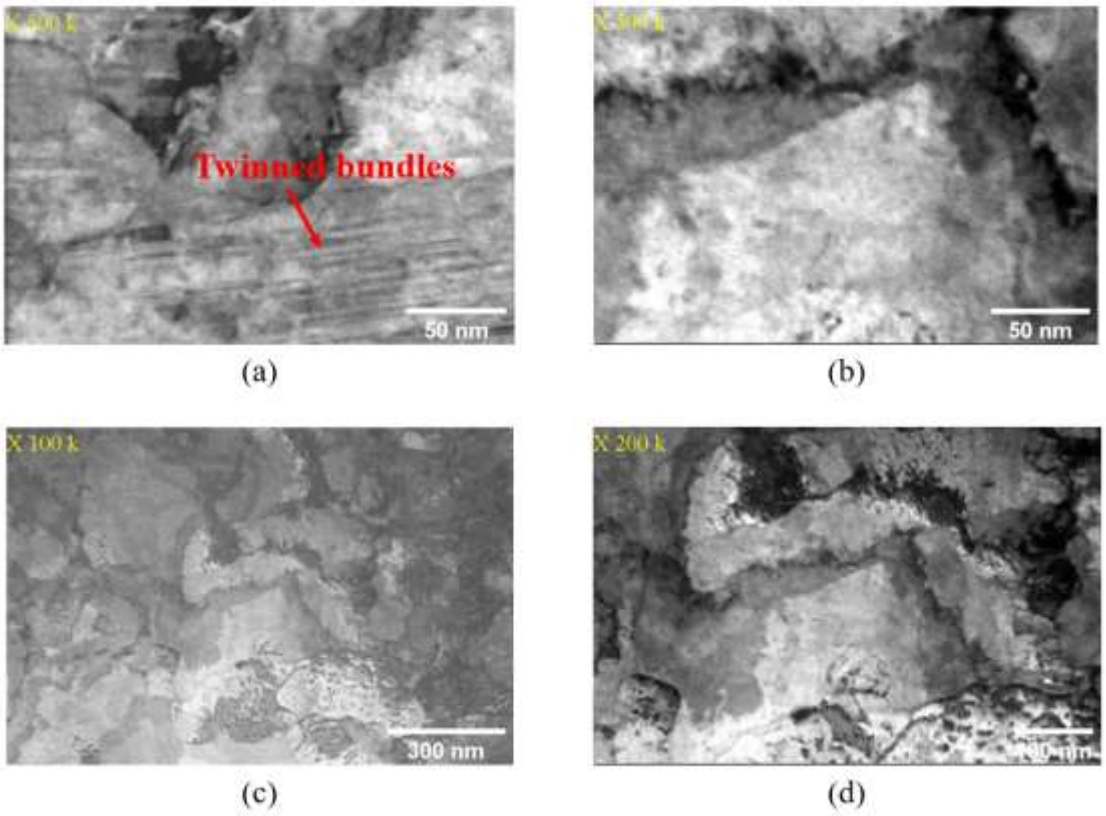

Figure 7.5 BF–STEM micrographs of DC electrodeposited NiW; (a) the field of view is close to the substrate; (b) the field of view is near the middle section of the deposit; (c) and (d) different magnification images from deposit.

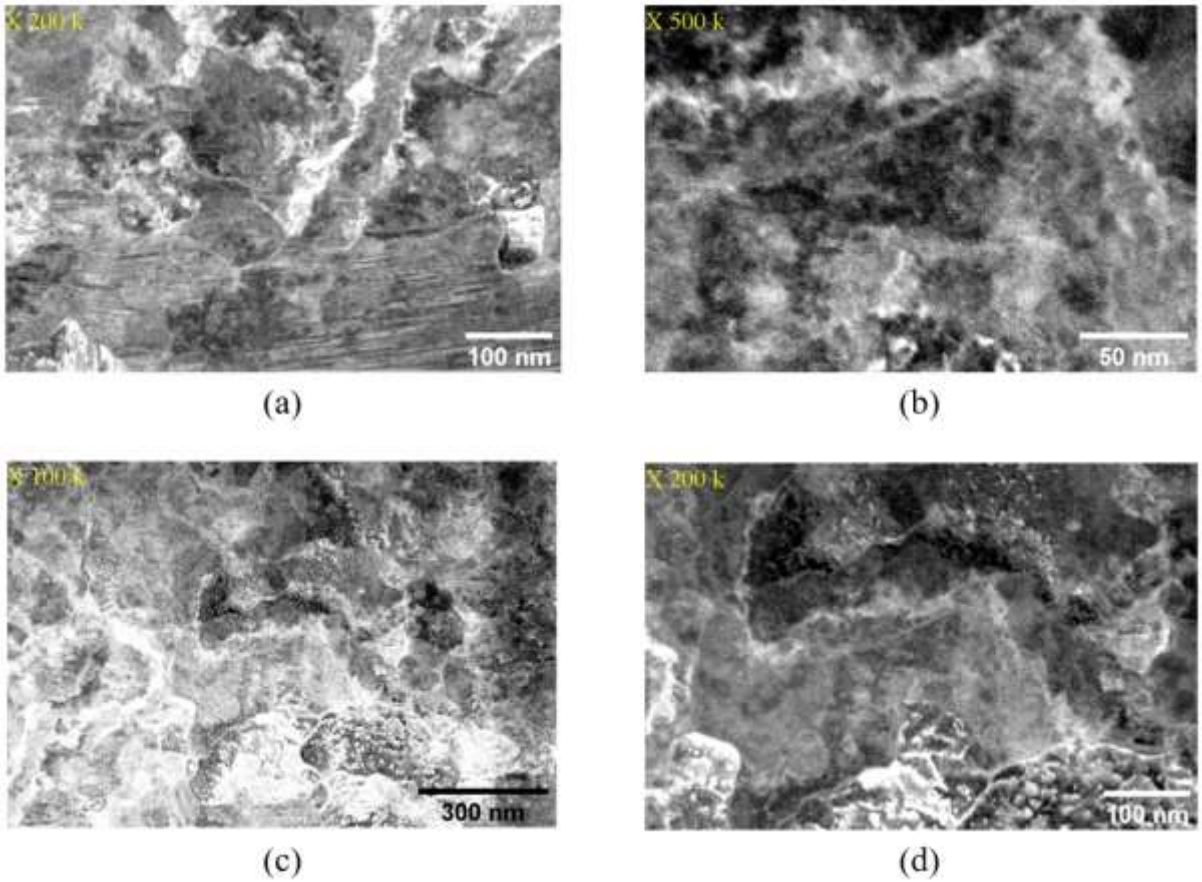

Figure 7.6 DF–STEM micrographs of DC electrodeposited NiW; (a) the field of view is close to the substrate; (b) the field of view is further from the substrate; (c) and (d) images with different magnifications.

BF and DF STEM images of PRC–NiW are displayed in Figure 7.7. Although BF–STEM has higher contrast than DF–STEM, DF–STEM provides better view from too small or out of view crystalline structures. Densely packed coherent nano–twins can be clearly seen throughout the deposits in DF–STEM image (Figures 7.7c and 7.7d).

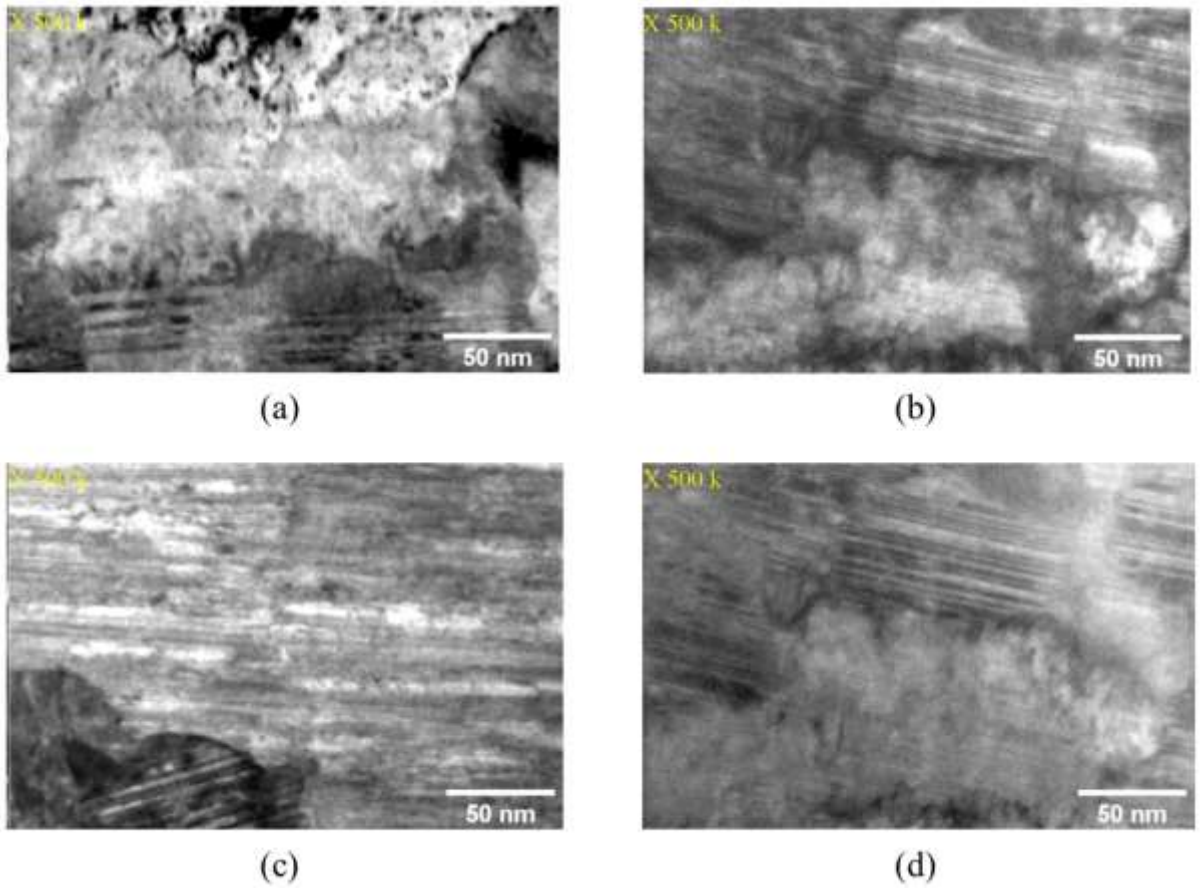

Figure 7.7 (a) and (b) BF–STEM of PRC electrodeposited NiW; (c) and (d) DF–STEM of PRC electrodeposited NiW.

To investigate the influence of DC and PRC electrodeposition on microstructure of NiW coating, the BF–STEM images were taken from the DC (Figures 7.8a, 7.8b, and 7.8c) and PRC–NiW (Figures 7.8d, 7.8e, and 7.8f) at different locations of adjacent to the substrate, smaller than 100 nm and greater than 500 nm from the substrate. It was noticed that, in the case of DC–NiW, only few twinned grains are visible at regions close to the substrate. However, in the case of PRC–NiW, preferentially orientated twinned grains are visible at different locations of PRC–NiW deposit which could be the possible reason for high pitting resistance of the PRC deposited coatings compared to DC electrodeposited ones. As well, some amorphous regions are still visible in locations smaller than 100nm and greater than 500 nm from the substrate. It was reported that high pitting corrosion resistant of coatings with smaller grain size were attributed to the reduced absorption of chloride

ions on the surface of the coating, which prevented the incorporation of chloride ions into the passive film. Recent studied have also shown that, nano–twins promote the formation of thin and compact passive film that improves the corrosion resistance of the coating. [33–34]

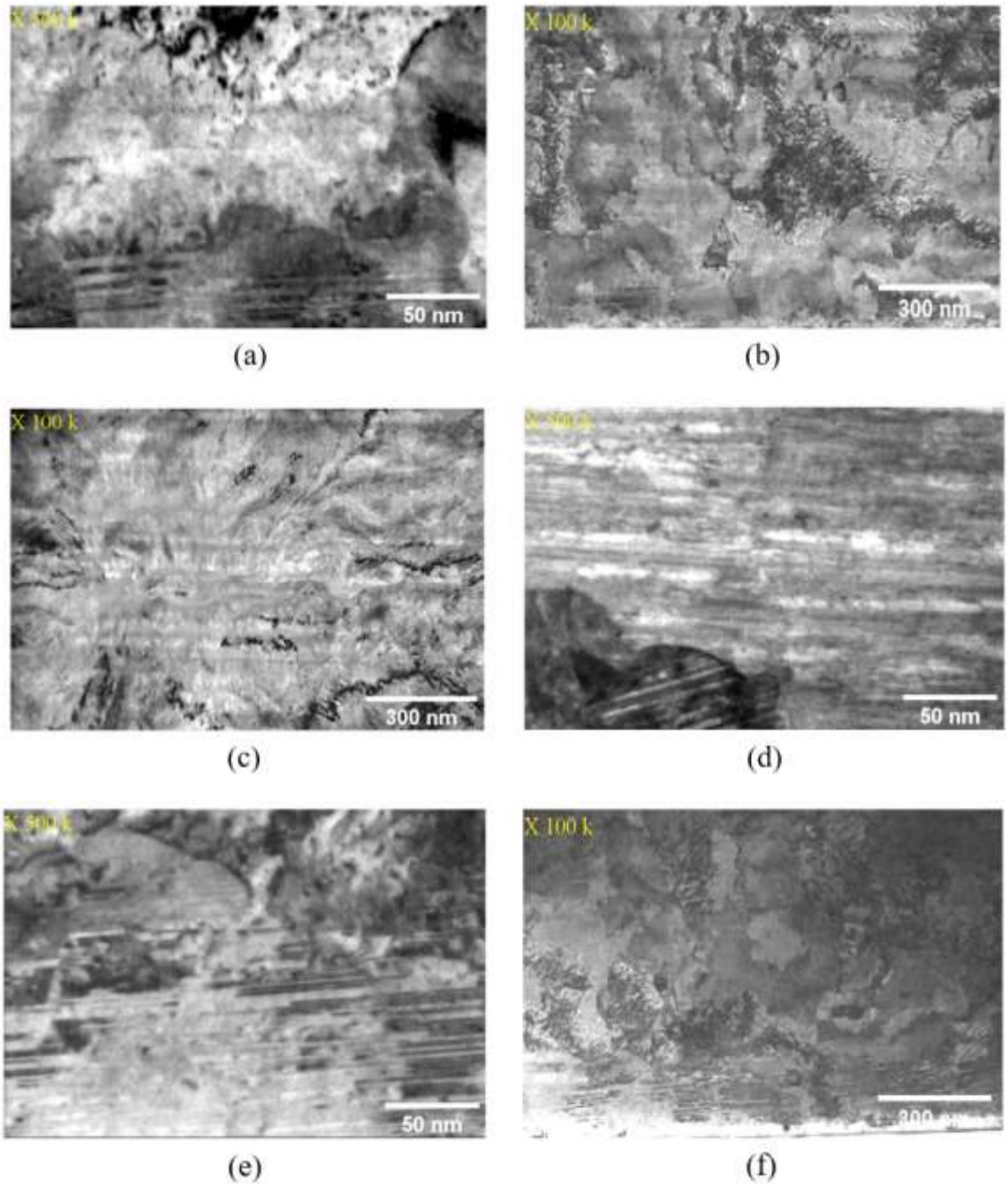

Figure 7.8 BF–STEM comparison of DC and PRC electrodeposited NiW; (a), (b), and (c) are related to DC electrodeposition; (d), (e), and (f) are related to PRC electrodeposition.

7.3.3 SEM and EDS analysis

A uniform and defect–free coating was observed in surface and cross–section of SEM micrographs of DC–NiW and PRC–NiW (Figures 7.9a and 7.9b). Furthermore, EDS from different locations of DC and PRC–NiW coated substrates suggest that Ni and W are the main elements present in the coatings (Figure 7.9c).

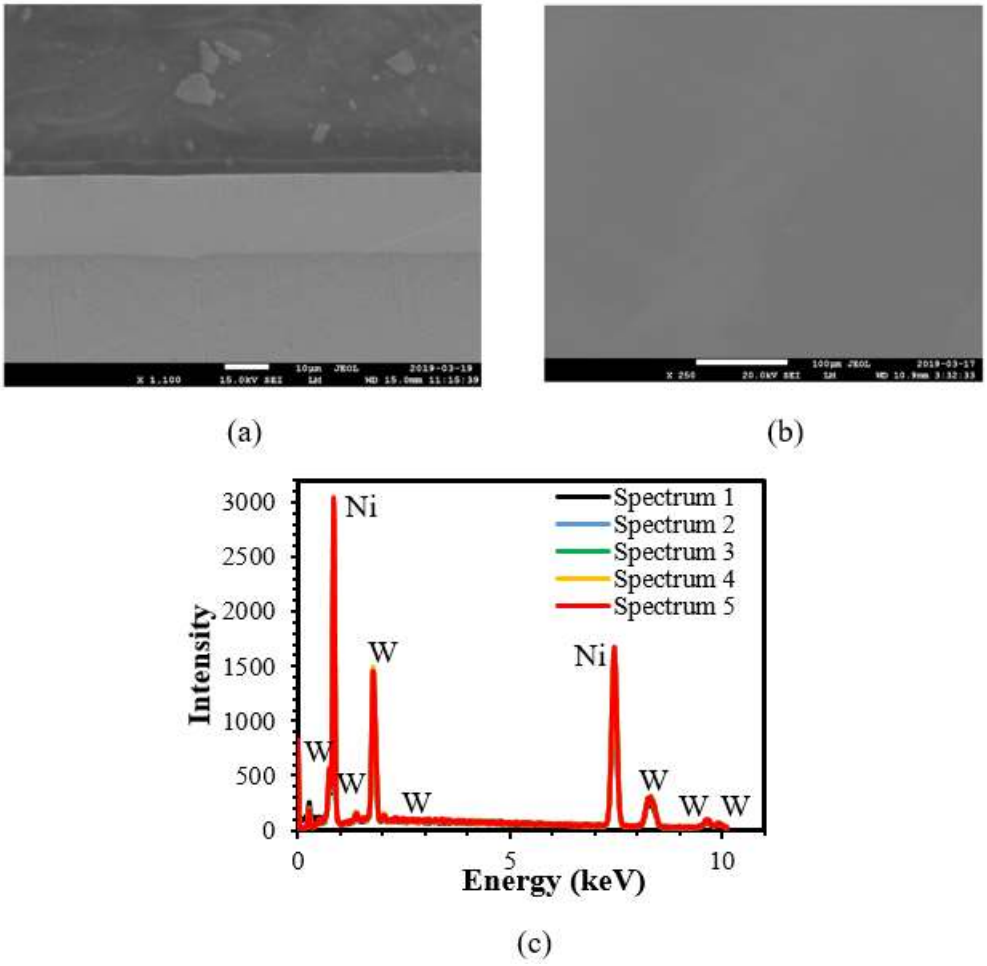

Figure 7.9 SEM micrographs from (a) cross section of DC–NiW, (b) surface of DC–NiW electrodeposited on brass substrate, and (c) EDS spectra from surface of DC–NiW.

Similar to DC–NiW coatings, PRC–NiW coated samples were very smooth and crack–free throughout the surface and across the coatings (Figure 7.10).

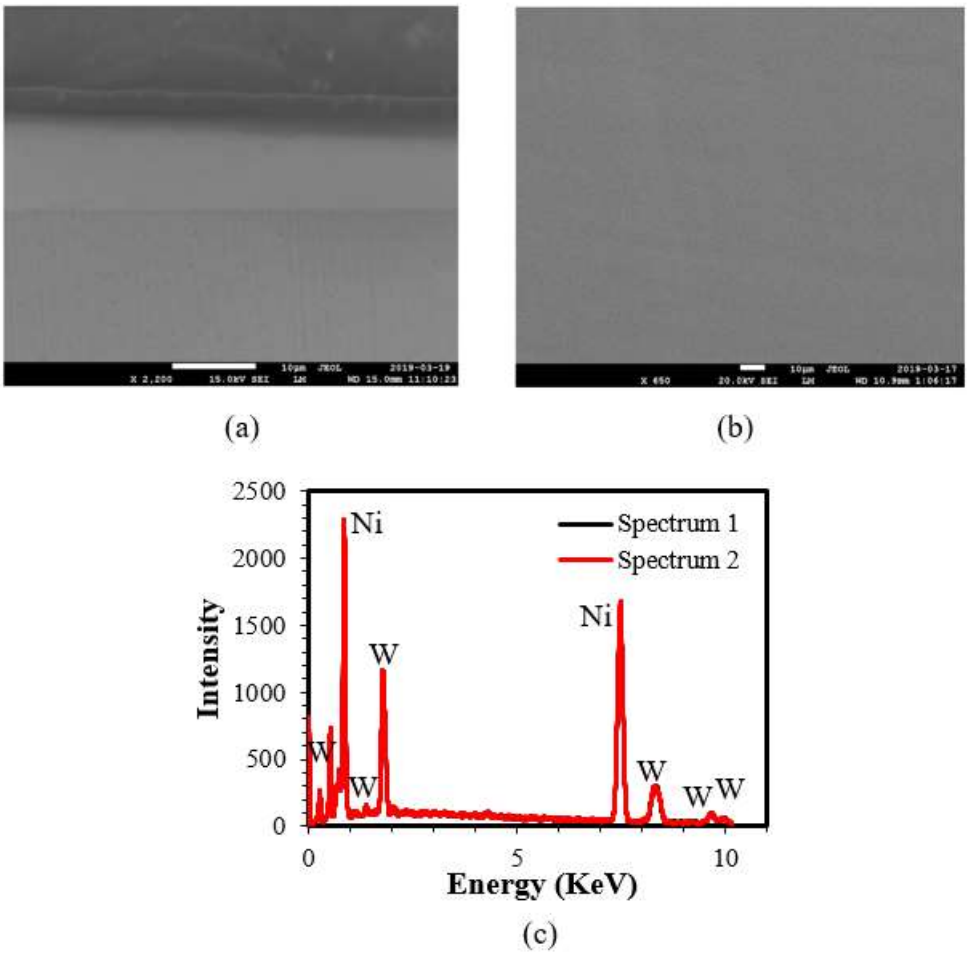

Figure 7.10 SEM micrographs from (a) cross section of PRC–NiW, (b) surface of PRC–NiW electrodeposited on brass substrate, and (c) EDS spectra from surface of PRC–NiW.

7.3.4 Mechanical properties

7.3.4.1 Nano–hardness results

Nanoindentation provided information on mechanical properties by calculation from indenter load and displacement. The first information on mechanical properties was obtained from a simple load–unload test, which provided a general idea and basic characteristics such as hardness and elastic modulus and also informed about irreversible processes. Load–displacement (depth) curves for DC–NiW, PRC–NiW, and brass substrate are shown in Figure 7.11, respectively. They display typical load–depth curves of indentation into elastic–plastic materials. The curve for brass substrate was

typical for a soft elastoplastic material, whereas those of DC–NiW and PRC–NiW were more typical of hard elastoplastic materials. Also, neither of the displayed curves display any cracks formation during loading, no phase transformation during unloading and no delamination of the indented coatings from brass substrate.

In general, the indentation response of a coating material is influenced by the properties of the coating. Therefore, to minimize the effect of the substrate, the indentation depth should be confined to less than 10% of the coating thickness. However, this 10% rule is not always reliable, especially if there is a large elastic mismatch between the film and the substrate and if the films are too thin that makes it difficult to obtain accurate results for very shallow indentations. [35–36]

The hardness and elastic modulus of brass substrate, DC–NiW and PRC–NiW coatings were evaluated by nano–indentation test from the load–displacement curves using the standard analysis procedure proposed by Oliver and Pharr [37].

Hardness (H) was calculated from:

$$H = \frac{Pmax}{A}$$

Elastic modulus was calculated as follows:

$$E = \frac{S\sqrt{\pi}}{2\beta\sqrt{A}}$$

where P_{max} is the maximum load applied during nano–indentation, A is the contact surface area, β is a geometrical constant of the indenter, and S is the stiffness of contact and is the defined as the slope of the curve upon unloading.

The hardness values calculated from load–depth curves for each material (i.e., Brass substrate, DC–NiW, and PRC–NiW) are demonstrated in Figure 7.12. As it can be seen, the average hardness of DC–NiW was slightly higher than that of PRC–NiW. This is expected since the content of co–deposited tungsten during pulse reverse electrodeposition step is reduced from 35 wt.% W down to about 25 wt.% W. The tungsten content of the electrodeposited layers was measured by using EDS.

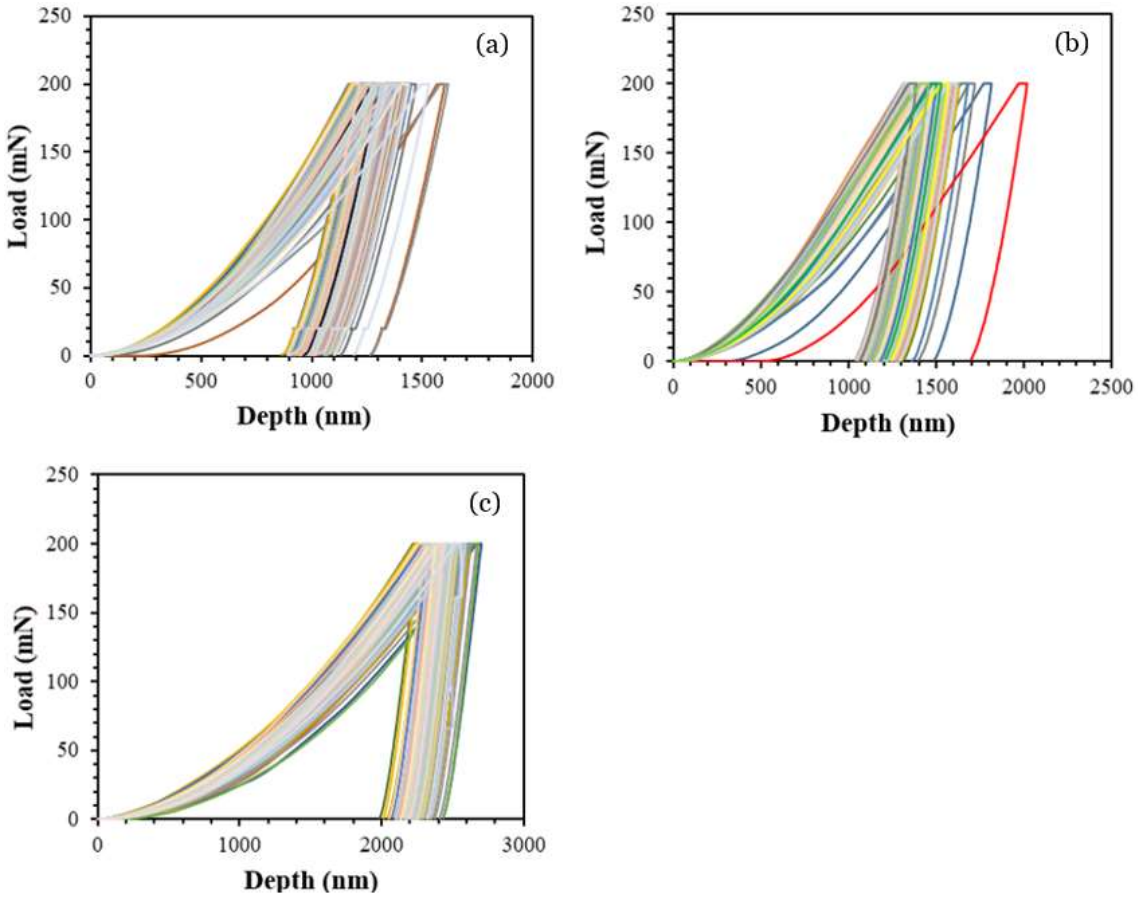

Figure 7.11 Load vs. depth profiles for (a) DC–NiW deposited on brass substrate, (b) PRC–NiW deposited on brass substrate, and (c) Brass substrate.

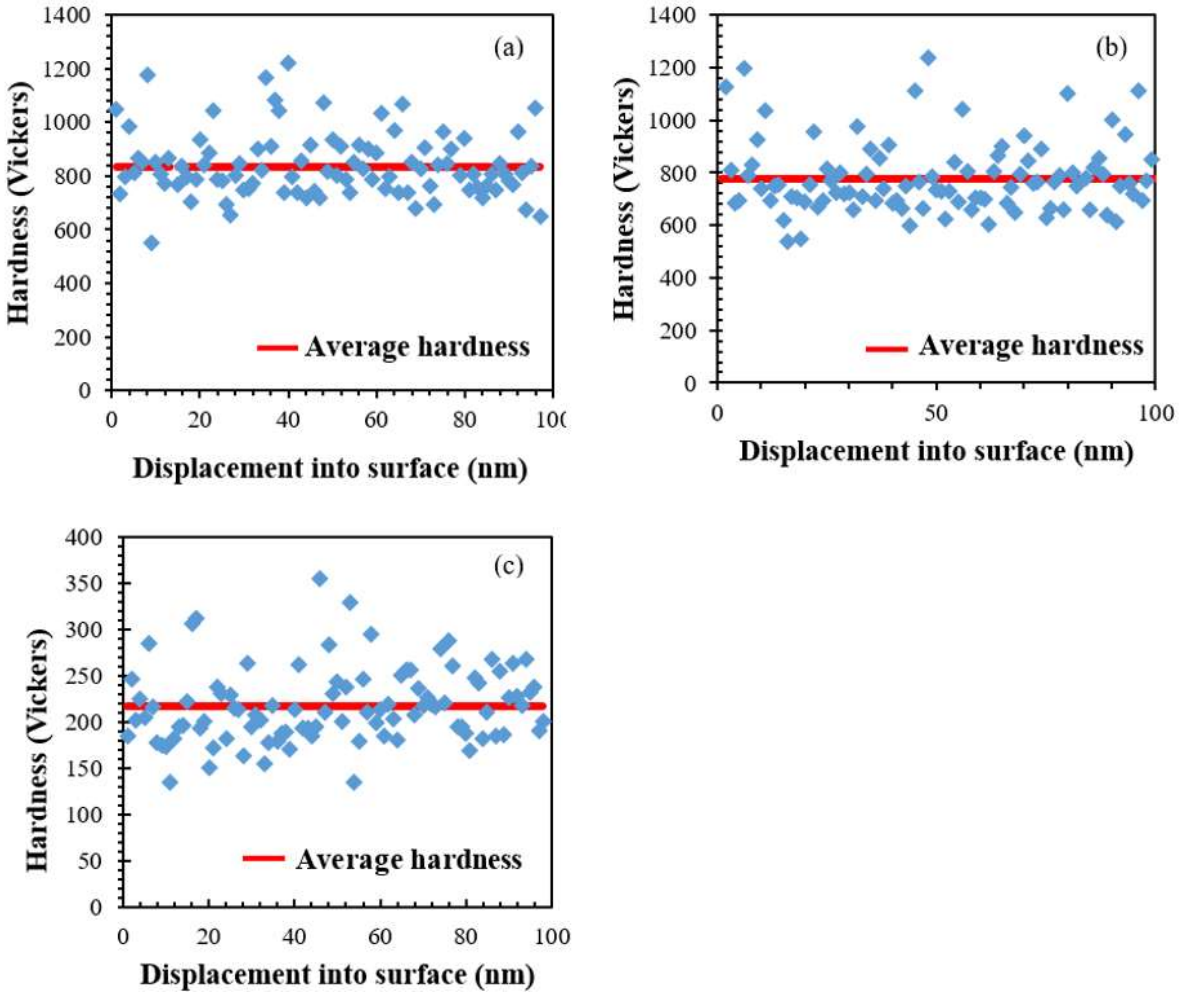

Figure 7.12 Nano–hardness measurements at various locations on (a) DC–NiW electrodeposited on brass substrate, (b) PRC–NiW electrodeposited on brass substrate, and (c) brass substrate.

7.3.4.2 Elastic–modulus results

The variation of the modulus on the applied load for DC–NiW, PRC–NiW, and brass substrate was investigated (Figure 7.13). From these figures, there is no significant effect of the rate of the loading on the modulus for DC–NiW and PRC–NiW based coatings. The average modulus values for 100 measurements at different location on each sample was reported in Figure 7.14. We may conclude that the average modulus for both DC–NiW and PRC–NiW is approximately independent of loading rate. The current mode (DC or pulse reverse) of electrodeposition of NiW has no significant effect on the modulus of the electrodeposited sample.

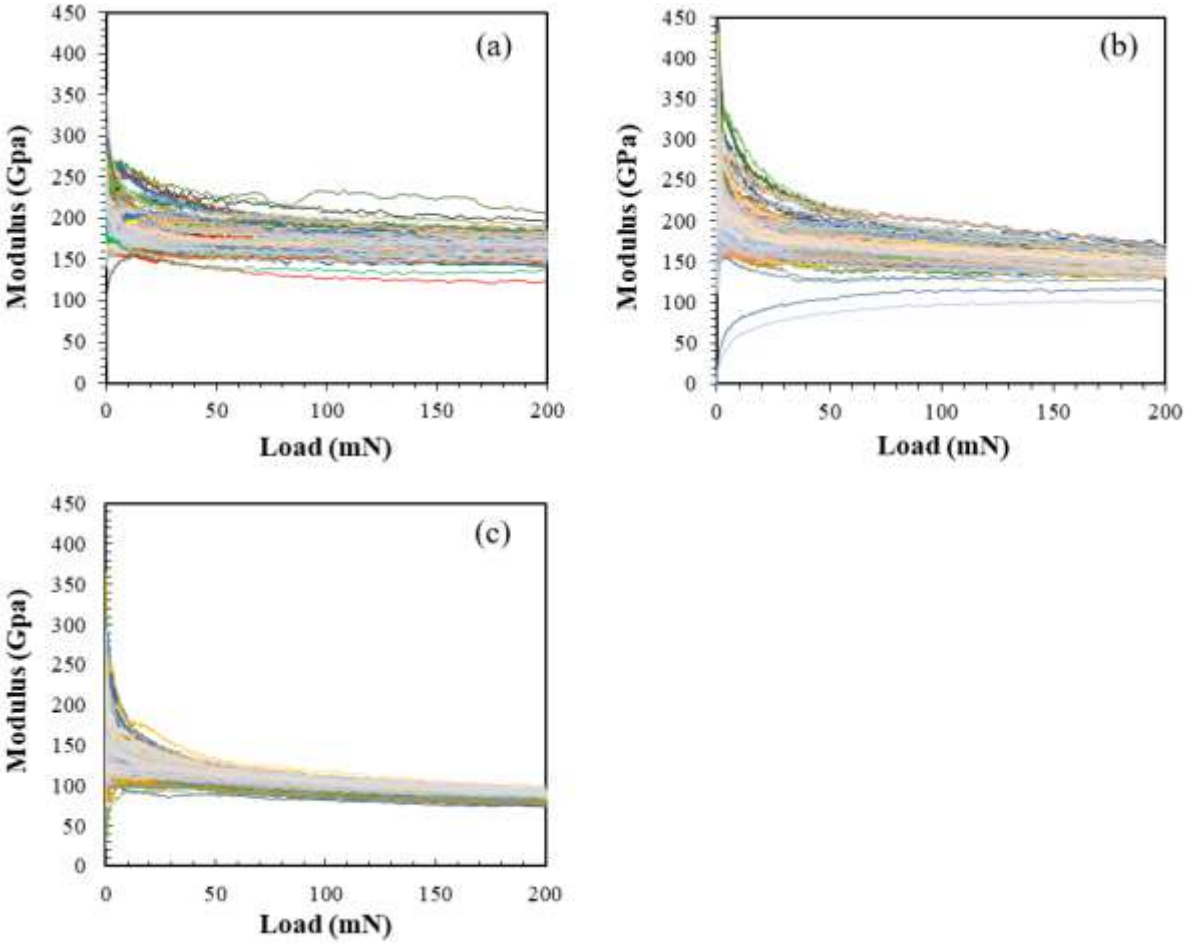

Figure 7.13 Modulus vs. load profiles for (a) DC–NiW deposited on brass substrate, (b) PRC–NiW deposited on brass substrate, and (c) Brass substrate.

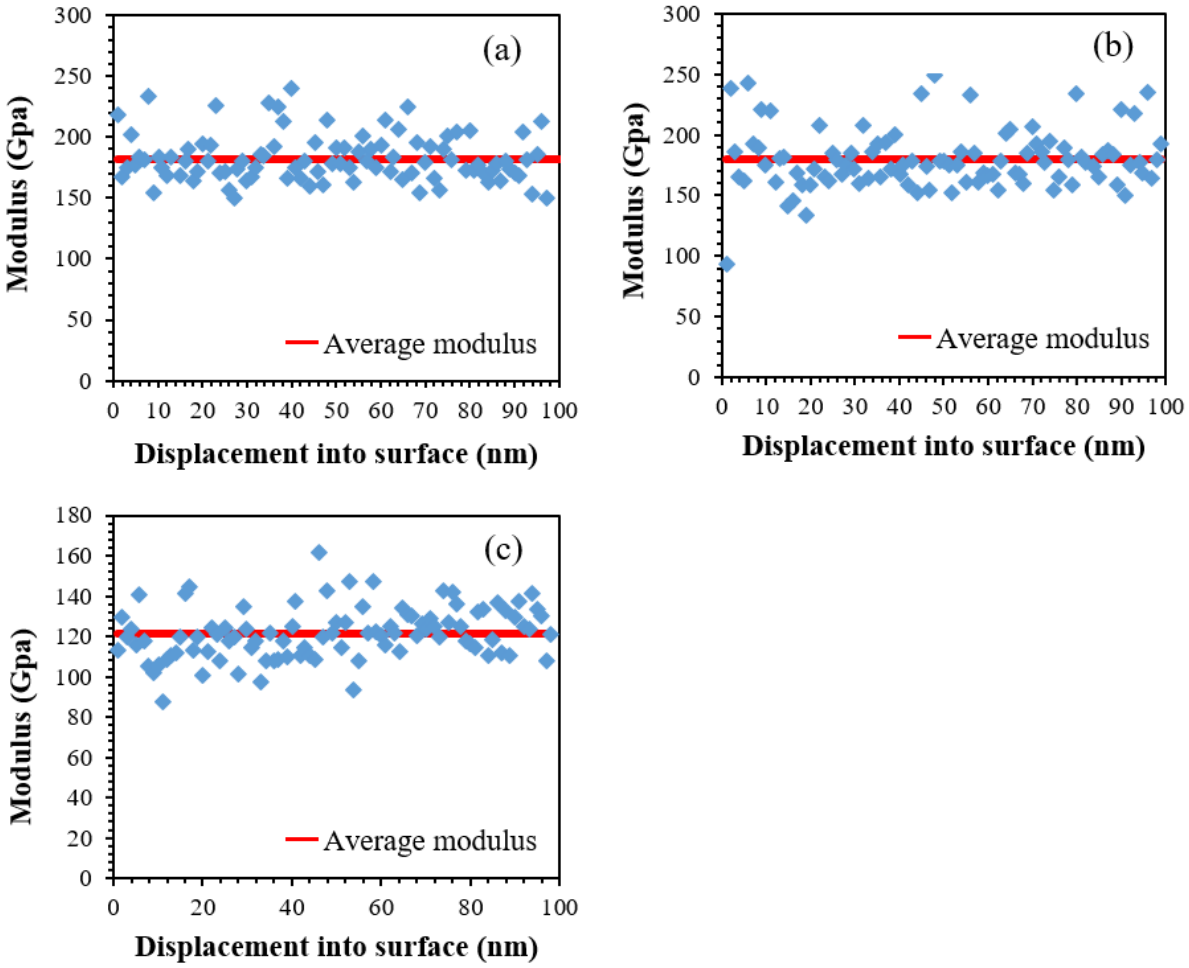

Figure 7.14 Modulus measurements at various locations on (a) DC–NiW electrodeposited on brass substrate, (b) PRC–NiW electrodeposited on brass substrate, and (c) Brass substrate.

7.4 Conclusion

The corrosion potential obtained from CPP graphs for DC–Ni, DC–NiW, PRC–Ni, and PRC–NiW were increased towards less anodically active (i.e. nobler) region as follows: DC–Ni < DC–NiW < PRC–Ni < PRC–NiW. As well, CPP graphs showed that the difference between E_p and E_{rep} for DC and PRC–Ni deposit was larger compared to DC and PRC–NiW. In other words, the NiW displayed higher pitting resistance compared to Ni deposit.

It was speculated that the difference in grain structures of DC–NiW and PRC–NiW resulting from the applied current waveforms (DC and PRC) were mainly responsible for different corrosion

behaviors. The pulse reverse current waveform produced grains in nanometer sizes whereas the deposits formed by applying DC displayed amorphous structure.

The influence of the current waveform (DC and PRC) on nano–hardness and elastic modulus of NiW coating was also investigated. The average hardness of DC–NiW was slightly higher than that of PRC–NiW. However, the elastic modulus of the both coatings was approximately similar with increase of the loading rate.

7.5 References

[1] Z. Mahidashti, M. Aliofkhazraei, and N. Lotfi, "Review of nickel-based electrodeposited tribo-coatings," vol. 71, no. 2, p. 257-295, 2018.

[2] M. Allahyarzadeh, M. Aliofkhazraei, A. SabourRouhaghdam, V. Torabinejad, H. Alimadadi, and A. Ashrafi., "Electrodeposition mechanism and corrosion behavior of multilayer nanocrystalline nickel-tungsten alloy," vol. 258, p. 883-899, 2017.

[3] S. Esmailzadeh, M. Aliofkhazraei, and H. Sarlak, "Interpretation of Cyclic Potentiodynamic Polarization Test Results for Study of Corrosion Behavior of Metals: A Review," vol. 54, no. 5, p. 976-989, 2018, 976.

[4] Q. Sun, and K. Chen, "Inflection of backward sweep of cyclic polarization curve: Pit transition potential Eptp," vol. 69, no. 12, p. 1729-1740, 2018, 1729.

[5] G. Frankel, "Pitting corrosion of metals: a review of the critical factors," vol. 145, no. 6, p. 2186, 1998.

[6] N. P. Wasekar, N. Hebalkar, A. Jyothirmayi, B. Lavakumar, M. Ramakrishna, and G. Sundararajan, "Influence of pulse parameters on the mechanical properties and electrochemical corrosion behavior of electrodeposited Ni-W alloy coatings with high tungsten content," vol. 165, p. 108409, 2020.

[7] K. R. Sriraman, S. Ganesh Sundara Raman, and S. K. Seshadri, "Corrosion behaviour of electrodeposited nanocrystalline Ni–W and Ni–Fe–W alloys," vol. 460-461, p. 39-45, 2007, 39.

[8] H. Alimadadi, M. Ahmadi, M. Aliofkhazraei, and S.R. Younesi, "Corrosion properties of electrodeposited nanocrystalline and amorphous patterned Ni–W alloy," vol. 30, no. 4, p. 1356-1361, 2009.

[9] F.Z. Yang, Y.F. Guo, L. Huang, S.K. Xu, and S.M. Zhou, "Electrodeposition, structure and corrosion resistance of nanocrystalline Ni-W alloy," vol. 22, no. 3, p. 228-231, 2004.

[10] L. Elias, and A.C. Hegde, "Electrodeposition of laminar coatings of Ni–W alloy and their corrosion behaviour," vol. 283, p. 61-69, 2015.

[11] P. Indyka, E. Beltowska-Lehman, L. Tarkowski, A. Bigos, E. García-Lecina, "Structure characterization of nanocrystalline NiW alloys obtained by electrodeposition," vol. 590, p. 75–79, 2014.

[12] Y. Yao, S. Yao, and L. Zhang, "Corrosion behavior of Ni–W/SiC nanocomposite coating in NaCl solution," vol. 13, no. 04, p. 489-494, 2006.

[13] M. Hosseini, M. Abdolmaleki, and J. Ghahremani, "Investigation of corrosion resistance of electrodeposited Ni–W/SiC composite coatings," vol. 49, no. 4, p. 247-253, 2014.

[14] M.G. Hosseini, H. Teymourinia, A. Farzaneh, and S. Khameneh-asl, "Evaluation of corrosion, mechanical and structural properties of new Ni–W–PCTFE nanocomposite coating," vol. 298, p. 114-120, 2016.

[15] C. N. Panagopoulos, G. D. Plainakis, and D. A. Lagaris, "Nanocrystalline Ni–W coatings on copper," vol. 176, no. 6, p. 477-479, 2011, 477.

[16] P. de Lima-Neto, A.N. Correia, R.A.C. Santana, R.P. Colares, E.B. Barros, P.N.S. Casciano, and G.L. Vaz, "Morphological, structural, microhardness and electrochemical characterisations of electrodeposited Cr and Ni–W coatings," vol. 55, no. 6, p. 2078-2086, 2010.

[17] M. V. N. Vamsi, N. P. Wasekar et G. Sundararajan, "Sliding wear of as-deposited and heat-treated nanocrystalline nickel-tungsten alloy coatings," vol. 412-413, p. 136-143, 2018, 136.

[18] N. P. Wasekar, S. M. Latha, M. Ramakrishna, D. S. Rao, and G. Sundararajan, "Pulsed electrodeposition and mechanical properties of Ni-W/SiC nano-composite coatings," vol. 112, p. 140-150, 2016, 140.

[19] Z. Mohammadpour, and H. R. Zare, "Improving the Corrosion Resistance of the Nickel–Tungsten Alloy by Optimization of the Electroplating Conditions," vol. 73, no. 4, p. 937-944, 2020, 937.

[20] Y. Wang, M. Yu, H. Luo, Q. Qiao, Z. Xiao, Y. Zhao, L. Zhao, H. Sun, Z. Xu, K. Matsugi, and J. Yu, "Effect of Saccharin on the Structure and Properties of Electrodeposition NiWP Alloy Coatings," vol. 25, no. 10, p. 4402-4407, 2016, 4402.

[21] J. C. Cameron, "Acetylenic compositions and nickel plating baths containing same," éd: Google Patents, 1983.

[22] https://www.chemours.com/en/–/media/files/capstone/capstone–surfactants–brochure.pdf

[23] C. A. Schuh, "Nanoindentation studies of materials," vol. 9, no. 5, p. 32-40, 2006.

[24] V. Kushch, S. Dub, and P. Litvin, "Determination of the young modulus from elastic section of the Berkovich indenter loading curve," vol. 29, no. 4, p. 228-234, 2007.

[25] S. Bull, "Nanoindentation of coatings," vol. 38, no. 24, p. R393, 2005.

[26] G. Guillonneau, G. Kermouche, S. Bec, and J. L. Loubet, "Determination of mechanical properties by nanoindentation independently of indentation depth measurement," vol. 27, no. 19, p. 2551–2560, 2012, 2551.

[27] S. Basu, A. Moseson, and M. W. Barsoum, "On the determination of spherical nanoindentation stress–strain curves," vol. 21, no. 10, p. 2628-2637, 2006.

[28] D. J. Shuman, A. L. M. Costa, and M. S. Andrade, "Calculating the elastic modulus from nanoindentation and microindentation reload curves," vol. 58, no. 4, p. 380-389, 2007, 380.

[29] Y. Shi, B. Yang, and P. Liaw, "Corrosion-Resistant High-Entropy Alloys: A Review," vol. 7, no. 2, 2017, 43.

[30] L. Feng, Y. Y. Ren, Y. h. Zhang, S. Wang, and L. Li, "Direct correlations among the grain size, texture, and indentation behavior of nanocrystalline nickel coatings," vol. 9, no. 2, p. 188, 2019.

[31] C. Dong, H. Luo, K. Xiao, X. Li, and Y. Cheng, "In situ characterization of pitting corrosion of stainless steel by a scanning electrochemical microscopy," vol. 21, no. 3, p. 406-410, 2012.

[32] M. Zamanzad-Ghavidel, K. Raeissi, and A. Saatchi, "The effect of surface morphology on pitting corrosion resistance of Ni nanocrystalline coatings," vol. 63, no. 21, p. 1807-1809, 2009.

[33] L. Liu, Y. Li, and F. Wang, "Influence of grain size on the corrosion behavior of a Ni-based superalloy nanocrystalline coating in NaCl acidic solution," vol. 53, no. 5, p. 2453-2462, 2008.

[34] A. Tiamiyu, U. Eduok, J. Szpunar, and A. Odeshi, "Corrosion behavior of metastable AISI 321 austenitic stainless steel: Investigating the effect of grain size and prior plastic deformation on its degradation pattern in saline media," vol. 9, no. 1, p. 1-18, 2019.

[35] H. Li, and J. J. Vlassak, "Determining the elastic modulus and hardness of an ultra-thin film on a substrate using nanoindentation," vol. 24, no. 3, p. 1114-1126, 2009.

[36] Abadias, G, Chason, E, Keckes, J, Sebastiani, M, Thompson, GB, Barthel, E, Doll, GL, Murray, CE, Stoessel, CH, and Martinu, L, "Review Article: Stress in thin films and coatings: Current status, challenges, and prospects," vol. 36, no. 2, 2018, 020801.

[37] S. Kossman, T. Coorevits, A. Iost, and D. Chicot, "A new approach of the Oliver and Pharr model to fit the unloading curve from instrumented indentation testing," vol. 32, no. 12, p. 2230-2240, 2017.

CHAPTER 8 ARTICLE 3: EFFECT OF PULSE REVERSE CURRENT WAVEFORM ON TRIBOLOGICAL AND MECHANICAL PROPERTIES OF ELECTRODEPOSITED NICKEL–TUNGSTEN ALLOYS ON BRASS SUBSTRATE

Authors: Mina Dadvand, Oumarou Savadogo

Article published: Journal of Tribology – Materials, Surfaces & Interfaces, 23 June 2022
DOI: https://doi.org/10.1080/17515831.2022.2075649

Abstract

The precise control of tungsten content of electrodeposited nickel–tungsten (NiW) on brass substrate was achieved by applying a well–designed pulse reverse current waveform. A crack–free, uniform and, mirror–like finish surface was obtained by using a novel derivative of propargyl compound, propargyl–oxopropane–2,3–dihydroxy, as a brightener and grain refiner into the electrodeposition bath. This study indicates that the electrodeposited nickel–tungsten alloys with an optimum tungsten content (32 wt%) possesses outstanding mechanical and, wear performance, also with very low friction of coefficient of 0.2.

Keywords: Nickel–tungsten coating, pulsed reverse current electrodeposition, direct current electrodeposition, friction coefficient, mechanical and wear properties.

8.1 Introduction

In automobile, electronic, energy, marine and construction–based applications, brass is mainly used due to its low cost, machinability, high thermal and electrical conductivity. However, brass is very susceptible to wear and corrosion especially in moist environments producing toxic

corrosion products which can become a health hazard to biological systems. On the other hand, the low mechanical strength of the brass substrate can lead to short life–span of devices resulting in energy and economical losses. This has been a challenge for both academic and industrial research. [1–4] Therefore, various barrier coatings were developed to improve the mechanical and corrosion performance of brass. Although nickel (Ni) and cobalt have health related concerns and they can cause allergic reactions in some people, they are in industrial use for various applications especially nickel and its alloys since there are no alternative options among elements in periodic table. However, among all electroplated Ni alloys, nickel–tungsten (NiW) coatings are in great deal of interests due to their excellent corrosion and wear resistance, high hardness, and enhanced ductility. Moreover, NiW electrolytes used in this research activity has only 30 $g.L^{-1}$ Nickel sulfate hexahydrate (equivalent to 6.7 $g.L^{-1}$ Ni) which is considered low concentrated Ni based solution. [5–10] Various techniques such as vacuum–based methods, physical and chemical vapor deposition, and electrodeposition have been used to produce NiW coatings. The main advantages of using electrodeposition method are simplicity and low cost [9–16]. In recent years, electrodeposited NiW coatings have been reported to have better wear and corrosion performance compared to other electrodeposited coatings such as conventional hard chromium [12, 17]. The influences of the addition of various additives into NiW bath electrolyte have been investigated and it has been reported the addition of such additives can alter the texture, uniformity, and properties of the electrodeposited NiW significantly. As well, the type and characteristics of the applied current pulse waveform can have significant impact on the microstructure, uniformity, as well as properties of the deposited NiW alloy. [18–21]

Wu and et al. investigated the influence of brightener, 2–butyne–1, 4–diol on plating process and structures of NiW electrodeposit. The resultant coatings were fully bright and smooth. However, the addition of 2–butyne–1, 4–diol into electrodeposition bath, resulted in gradual decrease of W content followed by rapid drop of current efficiency with increase of its concentration. [19]

The applied current waveform can be either direct current (DC), pulse current (PC), or pulse reverse current (PRC) [17, 22]. During the DC electrodeposition process, the negatively charged layer formed around the cathode charges to a certain thickness preventing the approach of ions towards the substrate, whereas in PC electrodeposition process, this layer is discharged periodically during the T_{OFF}. The discharge of the layer allows the ions pass through the layer and approaches the substrate. The locations in electrodeposition bath with higher current density are depleted from the ions faster than the locations with lower current densities. The

OFF–time of the pulse allows the ions to migrate towards the depleted areas. Therefore, ions with more uniform distribution will be available for reduction during the T_{ON}. [14, 17, 21–23]

In PC method, the three independent parameters (i.e. T_{OFF}, T_{ON}, and I_p) can be varied to obtain a deposit with desired properties. In PC method, the duty cycle (γ) is described as the percentage of total time of a cycle [17, 24]:

$$\text{Duty cycle} = \frac{TON}{TON+TOFF} = T_{ON} \times f \qquad (1)$$

Where f is frequency or the reciprocal of the cycle duration (T):

$$f = \frac{1}{TON+TOFF} = \frac{1}{T} \qquad (2)$$

The deposition rate of the PC and DC will be the same if the average applied current density (I_A) in PC is equivalent to the applied current density in DC electrodeposition process. The average applied current density in PC is described by equation (3):

$$I_A = I_P \times \gamma \qquad (3)$$

In PRC method, the applied current is interrupted and a reversed current is introduced into the electrodeposition cycle for a certain duration. The diffusion layer is replenished in similar to PC process. As well, the protrusions on the surface selectively are dissolved during the reverse resulting in more uniform deposit. The introduction of PRC waveform with high frequency may reduce or eliminate the use of additives in electrodeposition bath chemistry. Some of these additives may have negative impact on ductility and electrical conductivity of electrodeposited material.

It should be stated that there are two notable parameters in PRC process: average current and duty cycle. Average current density (I^*_A) is described by the following equation [18, 24]:

$$I^*_A = \frac{I(f) \times t(f) - I(r) \times t(r)}{t(f) + t(r)} \qquad (4$$

Where I(f) is the forward current density, I(r) is the reversed current density, t(f) is the duration of forward pulse, and t(r) is the duration of the reversed pulse. The duty cycle in PRC electrodeposition is calculated by the following equation [24–25]:

$$Y^* = \frac{t(f)}{t(f)+t(r)} \qquad (5)$$

Although PRC electrodeposition process has lower current efficiency compared to PC method, PRC electrodeposition process has gained a great deal of interest in obtaining of better control on composition and the microstructure of deposited materials. The PRC changes the concentration of ions by adsorption and desorption at the interface of cathode and electrolyte. Deposition and dissolution occur during the cathodic and anodic cycle, respectively. Therefore, the composition, microstructure and properties of the deposited material are altered. [24–25] In comparison with DC and PC, the PRC method provides better control on the composition and the properties of the electrodeposited materials and produces coatings with higher hardness, wear resistance, more compact surfaces and finer grain size. [24–25]

In this work, NiW coating with outstanding mechanical, wear performance, and very low coefficient of friction was produced by the precise control of the tungsten (W) content of the deposit through applying a well–designed PRC waveform and using a novel derivative of propargyl compound as a grain refiner and brightener into the deposition bath.

8.2 Methodology

8.2.1 Electrolyte components

The electrodeposition electrolyte was composed of nickel sulfate ($NiSO_4.6H_2O$) as a source of nickel ions, citric acid as complexing agent, sodium tungstate dehydrate ($Na_2WO_4.2H_2O$) as a source of tungstate ions, *o*–Benzoic sulfimide (sodium saccharin, $C_7H_5NO_3S$) as stress reducer,

propargyl–oxopropane–2,3–dihydroxy as a grain refiner and brightener, and DuPont Capstone Fluorosurfactant F–63 as a wetting agent. Table 8.1 displays the ingredients of the bath chemistry as well as the optimized experimental parameters to obtain uniform and defect–free NiW coating with desired mechanical and tribological performance.

In this formulation, citric acid is used to form stable complexes with tungstate (WO_2^{+4}) and nickel (Ni^{2+}) ions to prevent direct interaction between nickel and tungstate ions. Such direct interaction would result in irreversible precipitation of non–soluble nickel tungstate compound in electrodeposition bath solution [26, 27]. Sodium saccharin was used as a stress removal agent to reduce the internal stress within the electrodeposited coating materials. [28] We used propargyl–oxo–propane–2, 3–dihydroxy as a brightener and grain refiner. This compound is a specific type of propargyl derivative containing a carbon–carbon triple bond (i.e. –C≡C–H) at the end of its molecular chain which has a tendency to deposit preferentially at high current density areas on the substrate such as sharp areas during electrodeposition to control the nickel ion diffusion towards the cathode. Therefore, a uniform and crack–free deposit with mirror like finish surface was obtained. This organic compound can also enhance the nucleation sites for initiating the first stages of the metal deposition process on the surface of substrate leading to the decrease in grain size of the nickel. Unlike other brighteners such as sodium citrate–sulfonic acid used in Ni electrodeposition or Thiourea, this propargyl based brightener does not contain sulfur compound. Co–deposition of sulfur with Ni could deteriorate the corrosion properties of the coating [29]. Finally, Capstone fluoro–surfactant FS–63 (DuPont) was selected as a wetting agent to release the hydrogen gas bubbles from the substrate surface. FS–63 (DuPont) is a low foaming type anionic fluoro–surfactant which is soluble in water and provides low surface tensions. [31]

Table 8.1 Electrodeposition bath ingredients and optimized experimental parameters

Name of chemicals	**Concentration**
Nickel sulfate	29.5–30 ($g.L^{-1}$)
Sodium tungstate	58–60 ($g.L^{-1}$)
Citric acid	63–67 ($g.L^{-1}$)
Ammonia	58 ($ml.L^{-1}$)
Sulfuric acid	As needed
Propargyl–oxo–propane–2,3–dihydroxy (POPDH)	0.9–1 ($g.L^{-1}$)
DuPont™ Capstone® Fluoro–surfactant FS–63	1.8–2 ($g.L^{-1}$)
Sodium saccharin	0.5–1 ($g.L^{-1}$)
Experimental parameters	
pH	7.8–8.0
Temperature	58–61 °C
Duration of electrodeposition	30 min

8.2.2 Substrate preparation

The surface of brass substrate was degreased, activated, and rinsed prior to electrodeposition process. Substrate was immersed into 50 $g.L^{-1}$ alkaline soap solution (TEC1001; Technic Inc.) at temperature of about 50°C for approximately 1 min followed by rinsing with deionized (DI) water. The substrate was then activated by immersing into dilute sulfuric acid (10% v/v) at room temperature for about 10 sec followed by rinsing with DI water. Water break test was performed to determine the cleanliness of the substrate. In this testing protocol, the substrate was gently rinsed with deionized water following the final rinse step. The substrate was considered clean if the water completely wets the surface.

8.2.3 Electrodeposition setup

A schematic diagram of an electrodeposition setup is displayed in Figure 8.1. The electrodeposition setup was composed of an electrodeposition tank containing electrolyte, a pump (Flo King Filter System Inc.) to provide adequate agitation, an anode made of platinized titanium mesh, a cathode made of brass as a substrate being electrodeposited, and a reversed

pulse plating power supply. The electrodeposition bath was placed inside a water circulating bath operating at 60^{o}C temperature. An immersion heater connected to temperature controller was used to keep the solution temperature at optimized value. A filter pump (Flo King Filter System Inc.) connected to polypropylene filter was used to provide adequate agitation and to keep the solution free of particulates during the deposition. Platinized titanium mesh was used as anode.

Hull cell (Figure 8.2) equipped with heater, thermostat air agitation and air pump was used to perform the initial electrodeposition experiments to characterize and improve the current density distribution throughout the substrate surface. A brass substrate was used as cathode and a platinized titanium mesh sheet was used as anode.

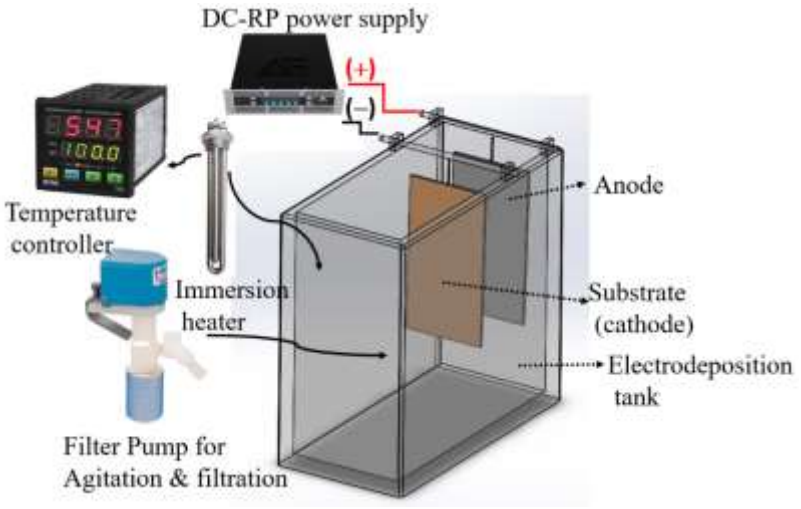

Figure 8.1 Schematic diagram of electrodeposition setup.

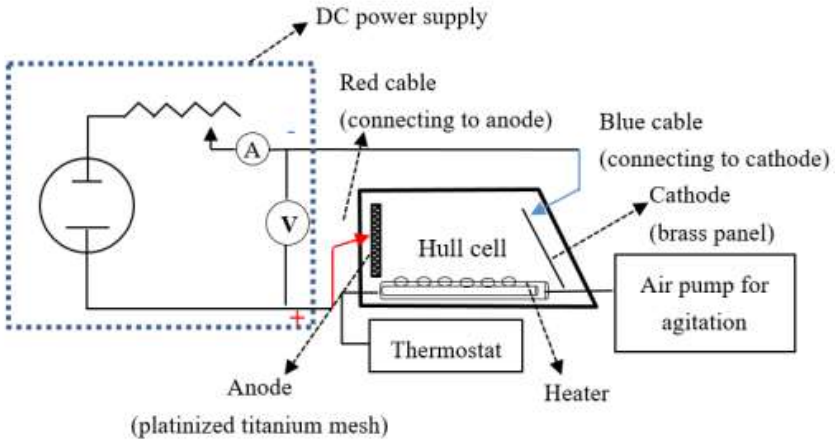

Figure 8.2 Schematic diagram of hull cell equipped with thermostat and air agitation.

8.2.4 Optimization of PRC waveform

The PRC current waveform was designed with regards to its forwards and backward current densities and pulse durations. Figure 8.3 displays the schematic diagram of the applied PRC waveform.

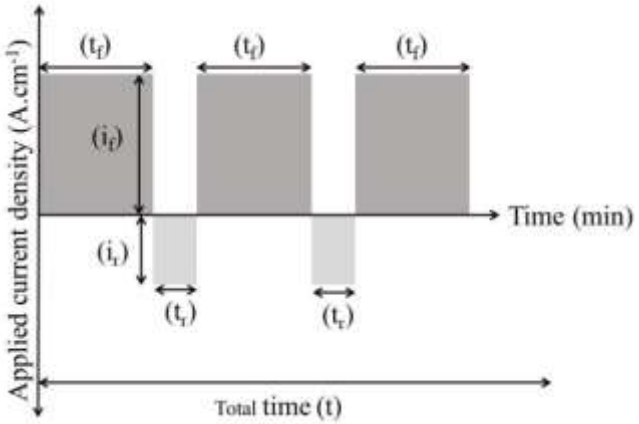

Figure 8.3 Reverse pulse waveform; i_f = 0.15 A.cm^{-2}; i_r = 0.11 A.cm^{-2}; t_f = 16 ms; t_r = 9 ms; and total time = 30 min. i_f = forward current density; i_r = reverse current density; t_f = forward pulse duration; t_r = reverse pulse duration.

8.2.5 Characterization of deposits

The tungsten content, grain structure and surface morphology of the deposits were characterized by energy–dispersive X–ray spectroscopy (EDS), transmission electron microscopy (TEM, Jeol JEM–2100F) and scanning electron microscopy (SEM, Joel 7600 TFE), respectively. A Gallium Focused Ion Beam (Ga–FIB, Hitachi FB–2000A) was also used to extract from the NiW coated samples, the thin lamellae (~100 nm) that were observed with the TEM.

The hardness of the coatings was evaluated by using a nano–indenter (Nanomechanics, Inc) with a conical diamond indenter tip (90 degrees, 5 µm radius spherical end). Pin–on–disk tests (Rtec Instruments) were performed to evaluate the wear resistance and measure the coefficient of friction. The tests were performed under dry air conditions and ambient temperature.

Spherical AISI 52100 steel balls with a diameter of 1.6 mm were used for the pin specimen. The coefficients of friction were measured according to ASTM Standard G99–05 (2010). The sliding velocity and the sliding distance were 100 mm/s and 1000 m, respectively. For all of the experiments, the applied load was 2 N. The coefficients of friction were continuously recorded with respect to the sliding distance. Each friction experiment was repeated six times and the average results were reported. The volume of the worn tracks was measured using a 3D profilometer (Bruker ContourX–100). The wear constant increases with increasing wear volume, which is the volume of removed material.

8.3 Results and discussion

8.3.1 Influence of experimental parameters on W content of DC– and PRC–NiW

The effect of applied current density on the W content of the DC electrodeposited NiW coatings was investigated (Figure 8.4). It was noticed that, varying the current density from 0.02 to 0.1 A.cm^{-2} did not significantly affect the tungsten content of the DC electrodeposited NiW coating. This study was important in order to make sure that the substrate with complex shape that may experience varying applied current density during the DC electrodeposition process, will have similar tungsten content throughout the deposit.

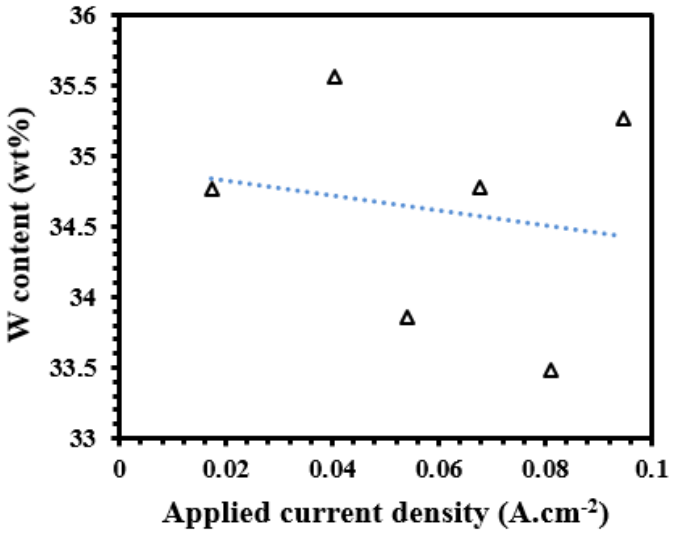

Figure 8.4 Effect of applied current density on W content of DC–NiW.

On the other hand, the content of the tungsten in PRC electrodeposited NiW coating was decreased upon increasing the current density and duration of the reversed portion of the applied PRC waveform (Figure 8.5). In general, the increase in tungsten content of electrodeposited NiW decreases the grain size due to the segregation of tungsten atoms to the nickel grain boundaries in order to stabilize the grain structure. During the forward portion of the applied PRC waveform, the specimen acts as cathode resulting in electrochemical reduction of nickel–citrate–tungstate complex and deposition of NiW. During the reversed portion of the applied PRC current waveform, the specimen acts as anode resulting in oxidation of tungsten followed by dissolving back into the solution hence preferential removing of tungsten atoms from the deposit. Therefore, the increase in pulse duration and its current density during the reversed portion results in the decrease in tungsten content of the deposit. Similar observations have been reported in literature [14, 23, 31] for other electrodeposition bath chemistries of NiW that are different from our newly formulated chemistry with respect to grain refiner, stress reducer as well as the PRC waveform characteristics.

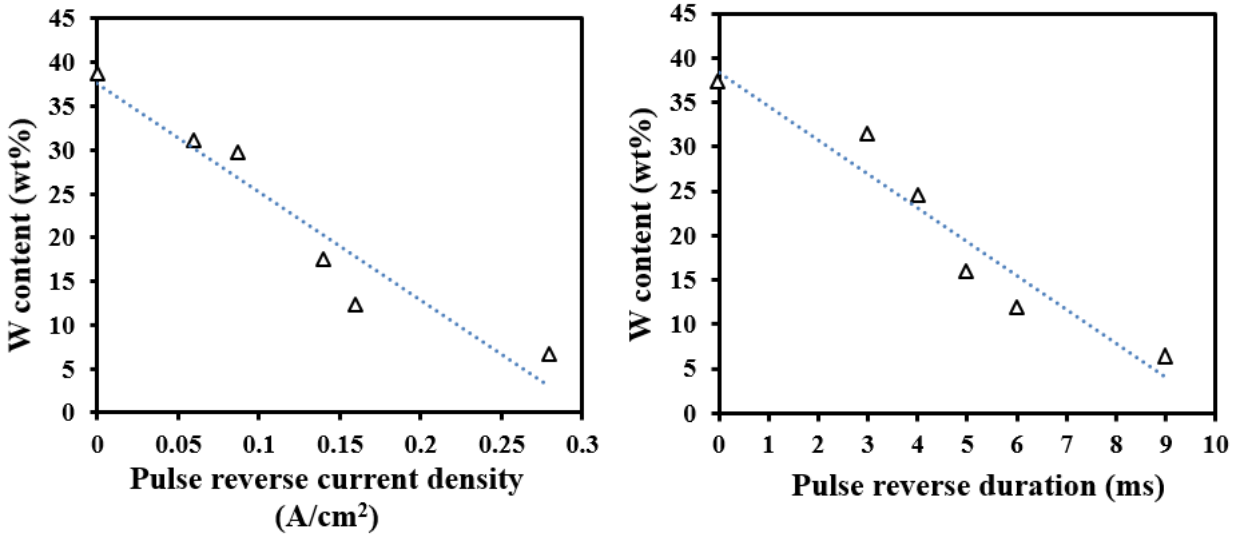

Figure 8.5 Effect of reversed pulse current density on W content of PRC–NiW.

Another important parameter that greatly influence the W content of the deposit is the electrodeposition bath temperature. As demonstrated in Figure 8.6, the tungsten content in deposit reached to 40 wt% at 85^{o}C, almost 2.5 times higher than when the operating bath was kept at 45^{o}C. As a matter of fact, increase of bath temperature, increases the movement of

particles in the solution towards the cathode surface and more tungsten species will be co–deposited with Nickel.

It was also noticed that, the increase of bath temperature up to 60^{o}C resulted in obtaining brighter deposits due to increase of the current efficiency. However, at temperature greater than 60°C a quick degradation of the electroplating bath was observed leading to less bright coatings containing pores. This was possibly due to the fast growth of the grains at elevated temperatures, leading to decrease of the nucleation rate on the surface of the substrate and creating less bright, lower quality coating. Therefore the optimal bath temperature to maintain the stability of the deposition bath and to obtain pores–free bright deposit was 60^{o}C.

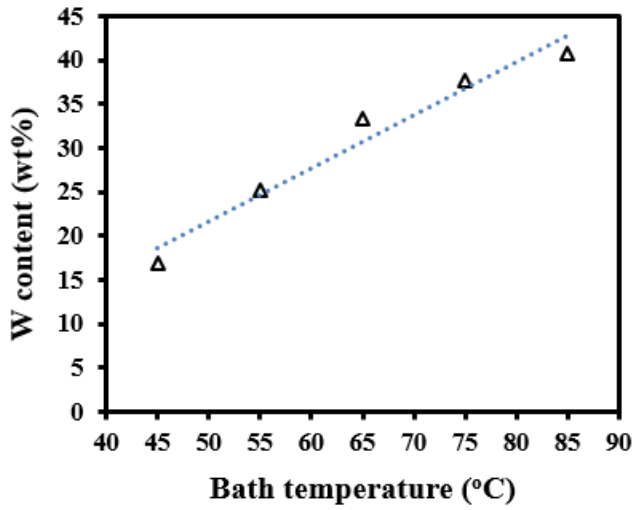

Figure 8.6 Effect of bath temperature on W content of PRC–NiW.

8.3.2 Effect of W content on the hardness, and wear rate of PRC–NiW

Ni by itself has limitations in applications where properties such as thermal stability, corrosion resistance, mechanical strength, hardness, and wear resistance are needed. Obvious alternative options to pure Ni is to use Ni alloys since their properties can be adjusted through various combinations of Ni and other metallic components such as formation of NiW alloys [32]. NiW alloys can improve hardness and wear resistance of pure Ni significantly. Tungsten itself has unusual properties such as highest melting point (3410^{o}C), highest tensile strength (410 Kg/mm^{2}) and Vickers hardness of 3430 MPa (compared to Ni 638 MPa). Tungsten can render its properties to its alloys with Ni [32–34]. The amount of improvements in the hardness and

wear resistance properties of NiW alloys mainly depend on the chemical composition of plating electrolyte as well as operating conditions such as temperature, applied current density, etc [33]. Transmission electron microscopy (TEM) studies reported in literature showed that only solid solution of tungsten in nickel existed in NiW (7–12 at%W) alloy which is in agreements with NiW phase diagram [33, 34]. The influence of W content of the PRC electrodeposited NiW on the hardness, and wear rate of the deposit was investigated (Figure 8.8). As it was displayed, the increase in W content, increased the hardness and wear resistance of the deposit. This is possibly due to the decrease of the grain size with the increase in W content which could be explained by the segregation of the W atoms to grain boundaries of nickel matrix. In this work, with increase of the tungsten content up to 35 wt%, hardness reached to 10 GPa and then suddenly decreased. However, the wear rate still decreases beyond the tungsten content of 35 wt%. Therefore, optimal W content to obtain the highest hardness and wear resistance was estimated 35 wt% which beyond this amount, the coating performance deteriorates. As defined by Hall–Petch principle, there is a relationship between hardness and grain size and according to this principle, metals and alloys coatings with finer grain size display significant increase in hardness and strength compared to coarser–grained coatings. However, there is an inverse Hall–Petch relation below a critical grain size which the hardness decreases and is due to grain softening which occurs below a certain critical grain size. The increase of hardness by decrease of the grain size up to critical grain size, could be explained by presence of larger volume of grain boundaries in finer grain coatings which could effectively hinder the dislocation motion by providing strong barriers for dislocation transmission from one grain to the next [35]. Giga and et al. investigated the inverse Hall–Petch relationship in electrodeposited nano–crystalline NiW coatings with grain sizes of 20, 12, 8 and 5 nm through tensile testing. They observed the inverse Hall–Petch relation below 8 nm of grain size [36]. Furthermore, another report on NiW electrodeposits by Srirman and et al. indicated that, NiW alloys electrodeposited at 75^{o}C followed direct Hall–Petch relation, while NiW alloys electrodeposited at 85^{o}C displayed an inverse Hall–Petch relation below a grain size of 15 nm. [37]

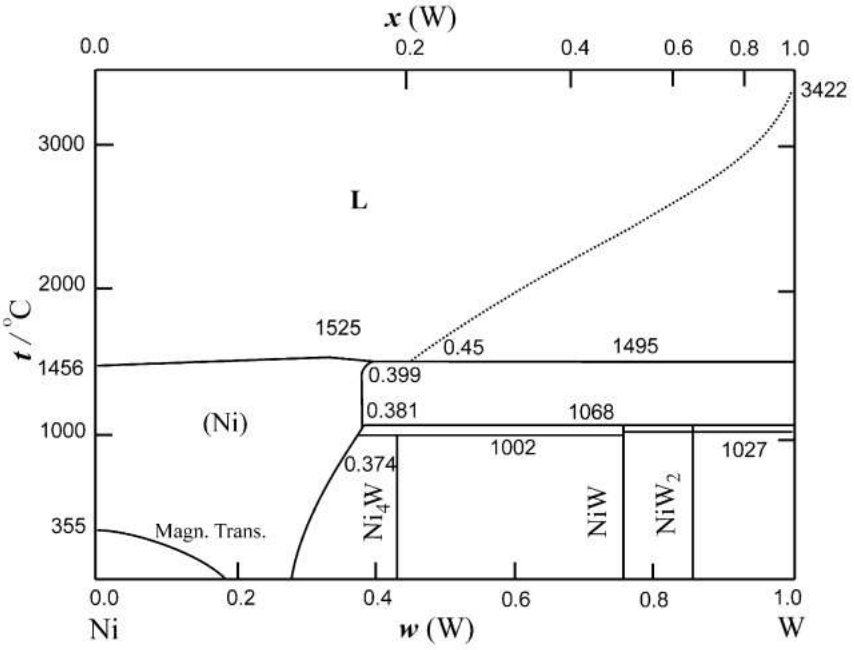

Figure 8.7 NiW phase diagram. [25]

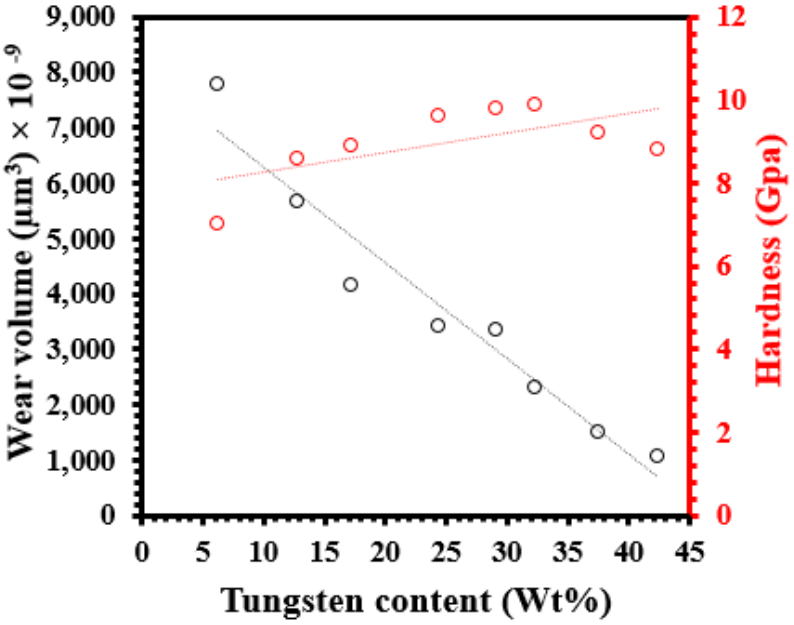

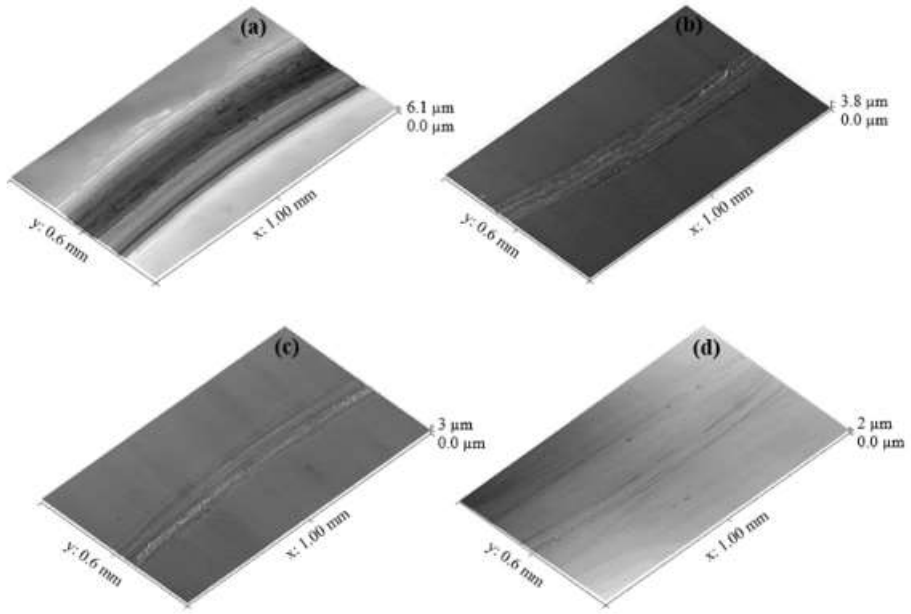

Figure 8.8 Effect of W content on hardness and wear volume and wear profiles related to the coatings with tungsten contents of 5 (a), 25 (b), 33 (c), and 43 (d) wt%.

8.3.3 Influence of current waveform on coefficient of friction

Figure 8.9 displays the variation in the average coefficient of friction for DC–NiW and PRC–NiW electrodeposited materials on brass substrate. As it can be seen, the PRC–NiW demonstrated a lower coefficient of friction (0.2) compared to the DC–NiW deposit (0.5). The low friction coefficient of the PRC–NiW coating can be attributed to the formation of stable tungsten oxide layer during the reverse pulse on the coating surface which will effectively reduce the contact between the sliding surfaces.

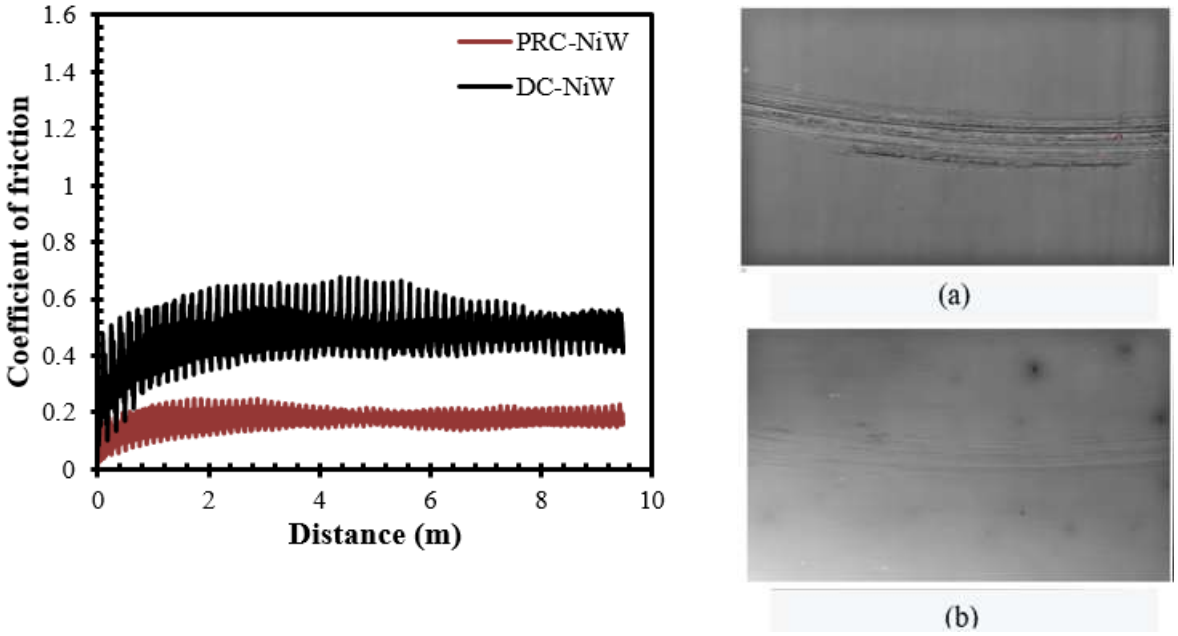

Figure 8.9 Coefficient of friction and partial wear scars for the DC–NiW (a) and PRC–NiW (b) electrodeposited on the brass substrate at room temperature.

8.3.4 SEM/EDS results

To examine any possible defects and delamination at the surface and interface of DC electrodeposited NiW, the SEM micrographs were taken from the surface (Figure 8.10a) and cross–section of DC–NiW and brass substrate (Figure 8.10b). As it is displayed, the coating is smooth throughout the surface and across the coating and no delamination can be observed. Similar to DC–NiW coatings, PRC–NiW coated sample was smooth and crack–free on the surface (Figures 8.11a, 8.11b, and 8.11c) and cross–section of the substrate–coating system (Figure 8.12a).

A uniform distribution of approximately 18 μm DC–deposited NiW and 6 μm PRC–deposited NiW coating was also observed on DC and PRC–NiW coated substrates (Figures 8.10b and 8.12a). Furthermore, EDS from different locations on the surface of DC and PRC–NiW suggest that Ni and W are the main elements present in the coatings (Figures 8.10c and 8.11d) and the reported contents for DC–NiW were 64.3% and 35.7% and for PRC–NiW were reported 66% and 34% accordingly. EDS mappings (Figures 8.10d and 8.11e) and EDS line scan (Figure 8.12c) from the surface and cross–section of the coating and brass substrate also revealed that the coatings were homogeneous and uniform. Other than tungsten content, surface morphology

of the coatings can also have a significant influence on the lifespan and performance of the coating in terms of contact stress, friction and wear.

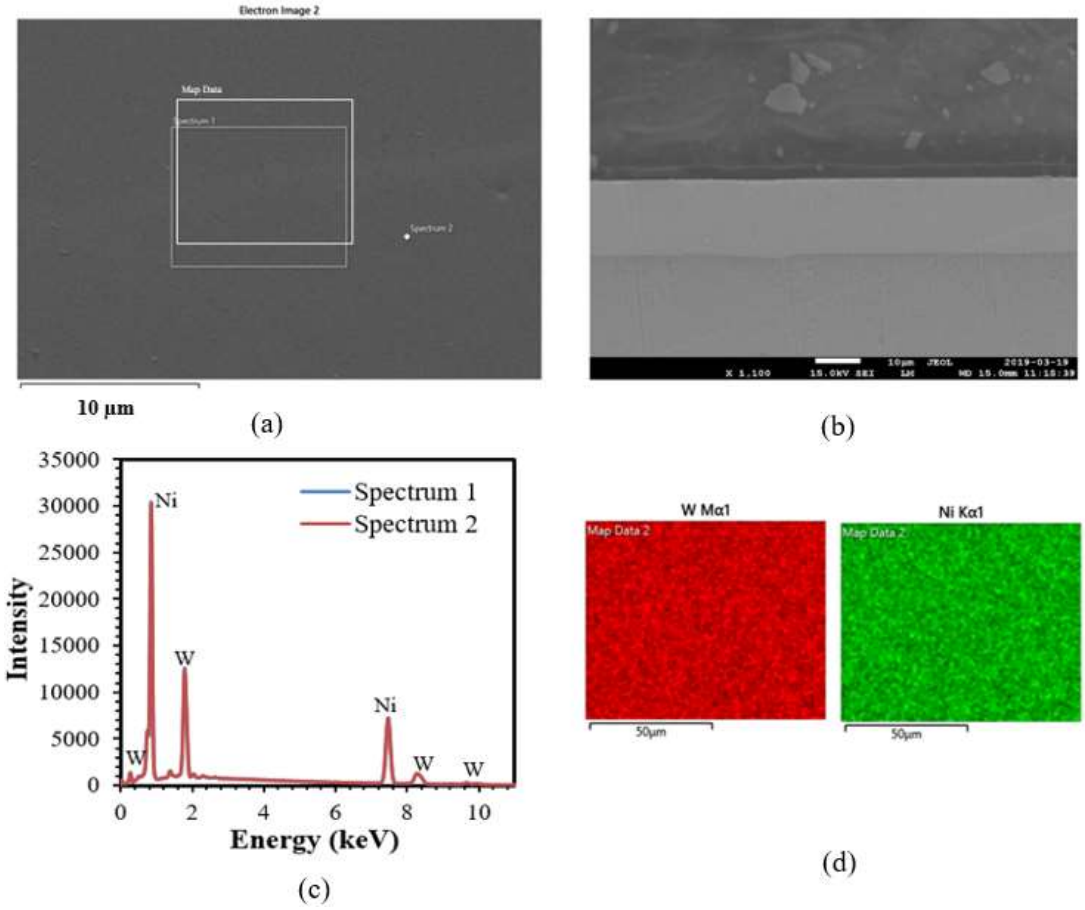

Figure 8.10 SEM micrograph (a), EDS spectra (b), and X–ray mapping (c) taken from the surface of NiW coating.

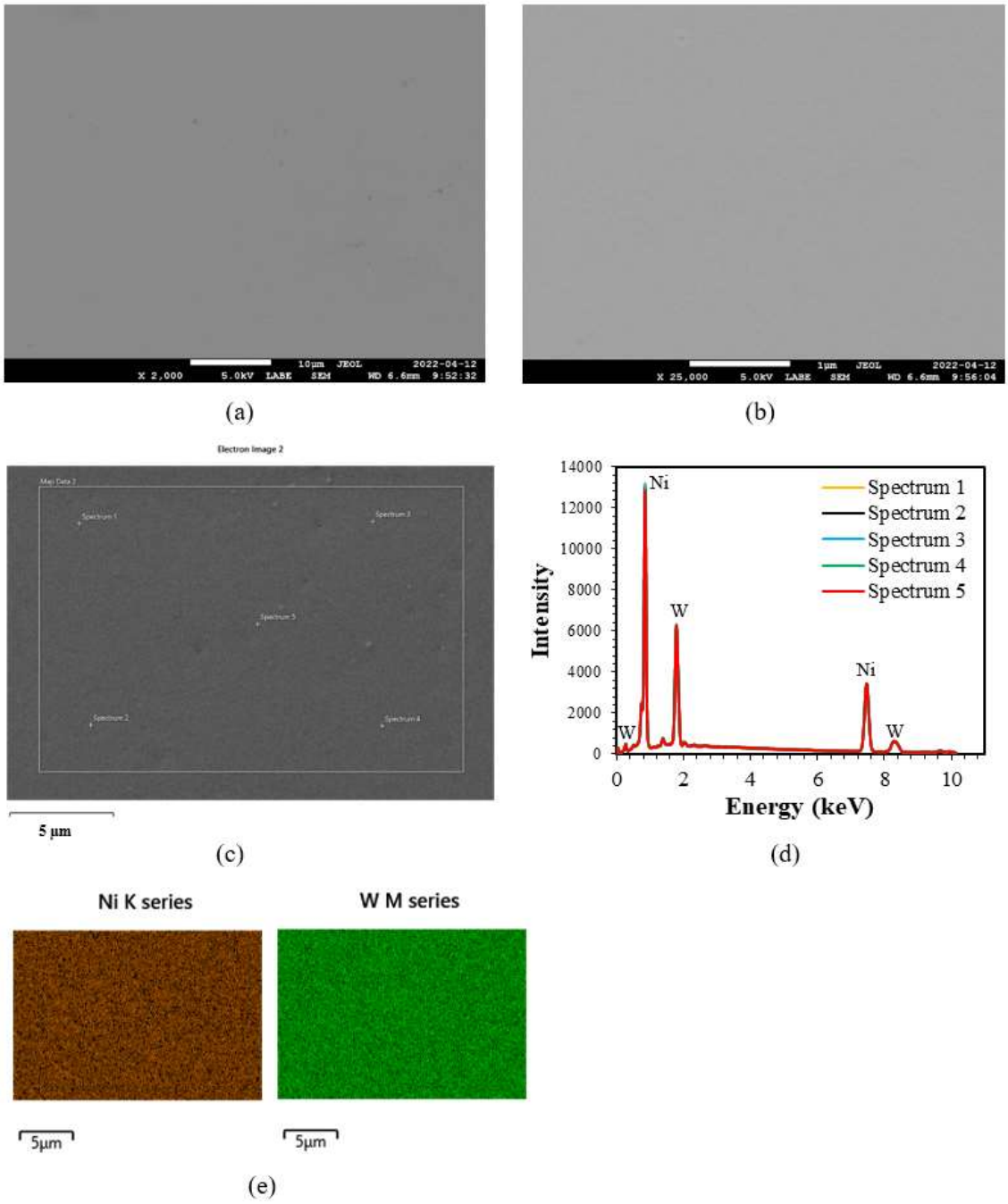

Figure 8.11 SEM micrograph (a, b, c), EDS spectra (d), and EDS mapping (e) of the elemental components from the surface of PRC–NiW deposit.

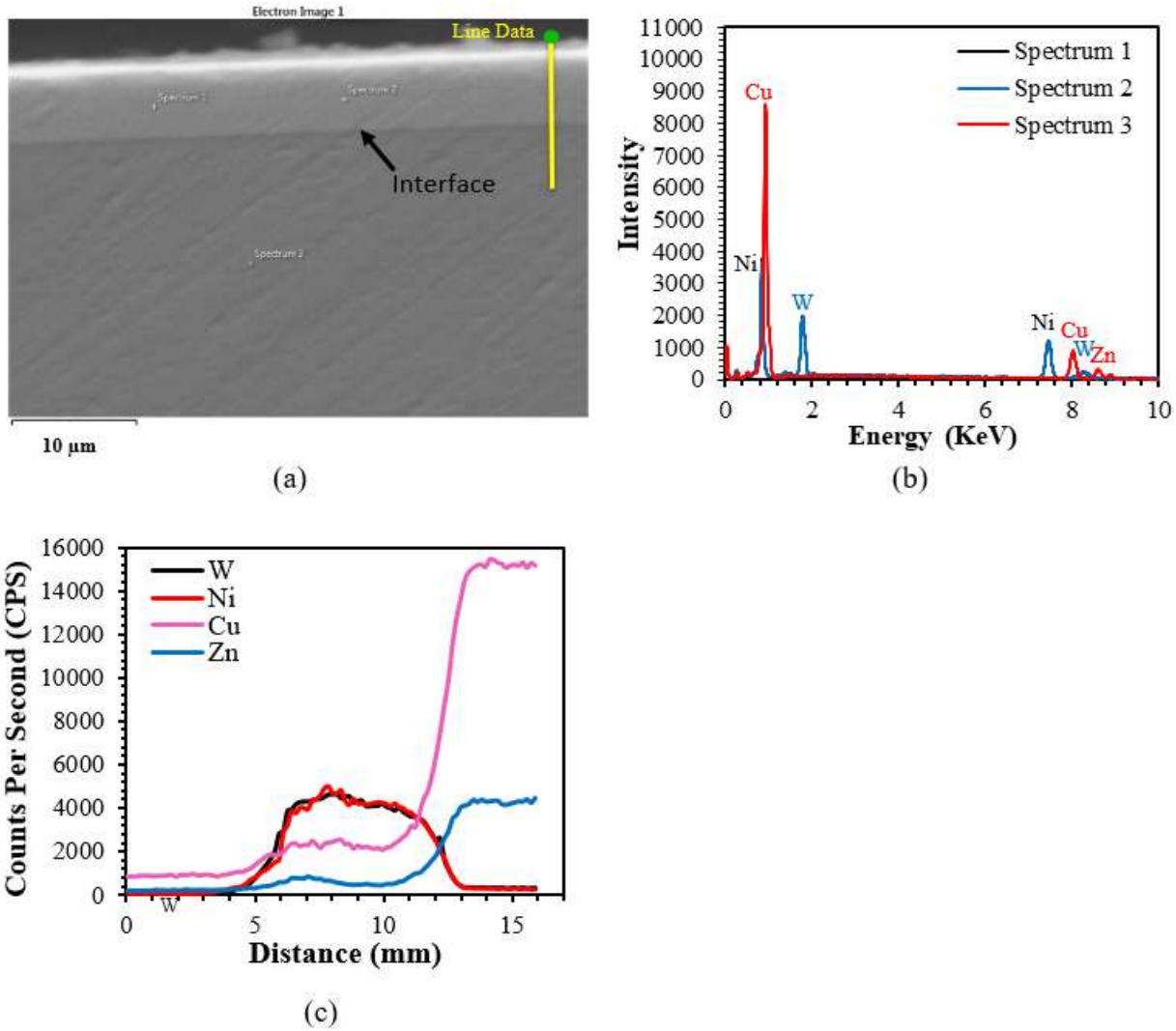

Figure 8.12 SEM micrograph (a), EDS spectra (b) of the elemental components, and line scan (c) from across the PRC–NiW deposit on brass substrate.

8.3.5 TEM analysis

Bright–field (BF) TEM observations were carried out on the surface of DC and PRC electrodeposited NiW samples (Figure 8.13) to examine the crystalline and/or amorphous structure of the coatings. The samples for TEM analysis were thinned to a thickness of ~100 nm by FIB lift–out method to enable the electron beam to pass through the samples. The Sample coated by DC method displayed a dominant amorphous phase structure, while the samples coated by PRC method exhibited mostly crystalline structure. Figures 8.13d, 8.13e, and 8.13f revealed plenty of nanotwin bundles with average inter–plane distance of 0.65 nm formed

across the surface of PRC–NiW coating. However few nano–twin bundles with average inter–plane distance of 0.4 nm can be observed on the surface of DC–NiW coating (Figures 8.13a, 8.13b, and 8.13c). Presence of nanotwins in the coating can greatly enhance the tribological performance of the coatings by acting as strong dislocation barriers. Figure 8.13c is the HR–TEM image showing the presence of two nanograins (grain I and grain II), that are oriented in different directions. In between two nanograins, there is an existence of amorphous region.

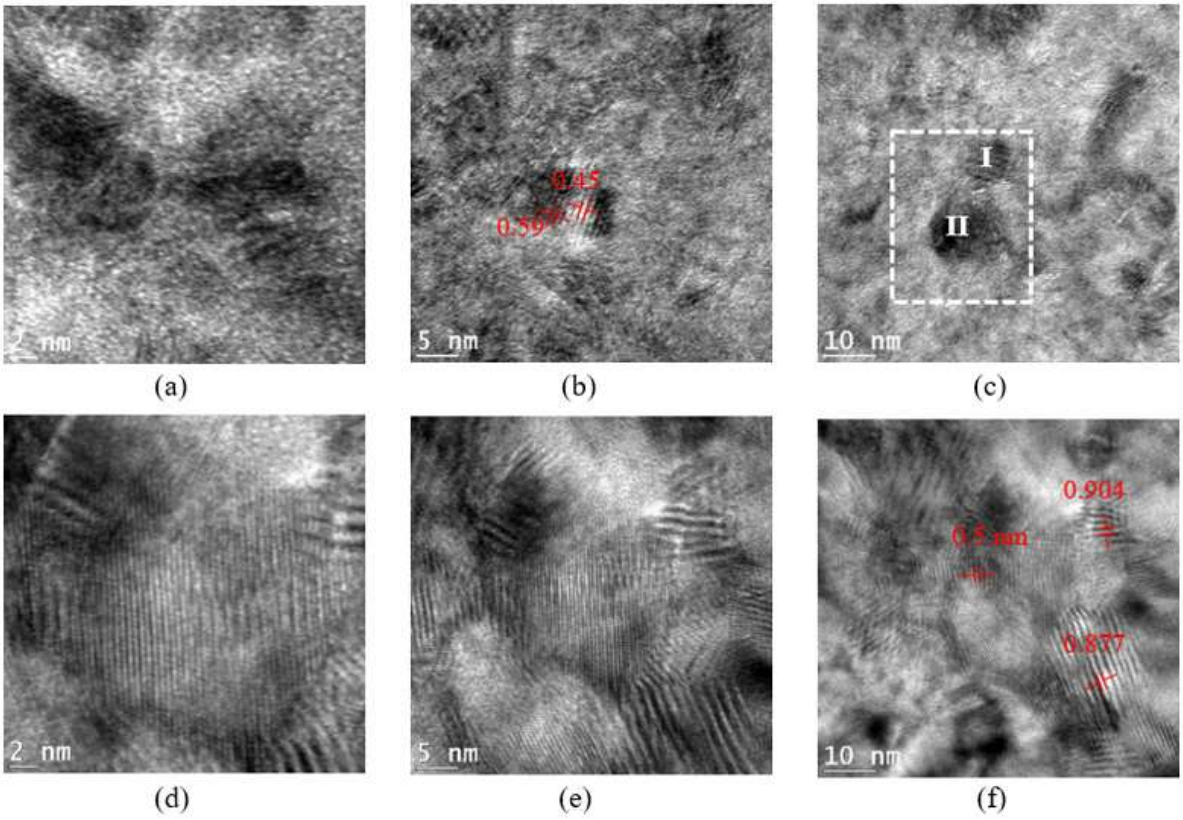

Figure 8.13 BF–TEM images of DC (a, b, c) and PRC–NiW (d, e, f) at different resolutions.

Figure 8.14 displays the selected area electron diffraction (SAED) pattern of DC and PRC–NiW coatings, respectively. DC–NiW reveals a halo feature suggesting the presence of dominant amorphous phase, while the PRC–NiW exhibits the consecutive and continuous rings, which is a typical characteristic of polycrystalline structure. The radius of these circular rings represents the interplanar spacings between the atoms. The value of miller indices or the phase structure of the coatings can be obtained by comparing the interplanar spacings with the standard values found in JCPDS data cards. According to the standard values, the major constituent phase is FCC Ni which are randomly oriented throughout the surface of the coatings.

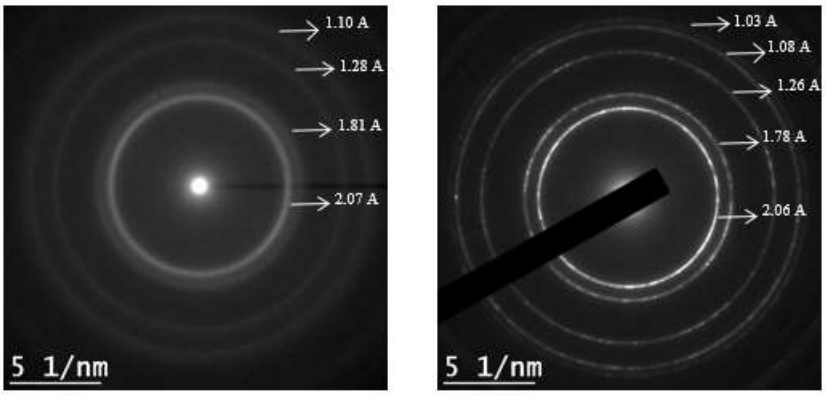

(a) (b)

Figure 8.14 SAED patterns from DC (a) and PRC (b) electrodeposited NiW.

8.4 Conclusion

NiW deposit was fabricated by using PRC electrodeposition process through applying a unique pulsed reverse current waveform on the electrodeposition bath chemistry containing specially selected ingredients. It was found that the tungsten content of the PRC–NiW deposit decreased with the increase in current density and duration of the reversed portion of the applied pulsed reverse current waveform. As well, the increase in bath temperature, increased the W content of the electrodeposited material. It was also found that the increase in tungsten content resulted in the increase in hardness and wear resistance of the PRC–NiW deposit. The increase in hardness and wear resistance was attributed to decrease of grain size due to segregation of the tungsten atoms to grain boundaries of nickel matrix. It was also revealed that, the PRC–NiW possessed a lower coefficient of friction compared to the DC–NiW deposit. According to BF–TEM results, plenty of nanotwin bundles were formed across the surface of PRC–NiW coating. However few nano–twin bundles were observed on the surface of DC–NiW coating. Nanotwins can effectively hinder the dislocation motion, and therefore enhance the tribological performance of the coatings.

8.5 References

[1] E. Feyzullahoğlu, A. Zeren, and M. Zeren, "Tribological behaviour of tin-based materials and brass in oil lubricated conditions," vol. 29, no. 3, p. 714-720, 2008.

[2] C. Liu, X. Huang, R. Xu, Y. Mai, L. Zhang, and X. Jie, "Microstructure and Properties of Nanocrystalline Ni-Mo Coatings Prepared by Ultrasound-Assisted Pulse Electrodeposition," vol. 30, no. 4, p. 2514-2525, 2021.

[3] I. Dinaharan, S. Karpagarajan, R. Palanivel, and J. D. Raja Selvam, "Microstructure and sliding wear behavior of fly ash reinforced dual phase brass surface composites synthesized through friction stir processing," vol. 263, 2021, 124430.

[4] X. Wang, C. C. Chou, J. W. Lee, R. Wu, H. Y. Chang, and Y. Ding, "Preparation and investigation of diamond-incorporated copper coatings on a brass substrate by composite electrodeposition," vol. 386, p. 125508, 2020.

[5] Y. Zhang, S. Zhang, Y. He, H. Li, T. He, Y. Fan, and H. Zhang, "Mechanical properties and corrosion resistance of pulse electrodeposited Ni-B/B_4C composite coatings," vol. 421, p. 127458, 2021.

[6] M.S. Safavi, M. Tanhaei, M.F. Ahmadipour, R. Ghaffari Adli, S. Mahdavi, and F.C. Walsh, "Electrodeposited Ni-Co alloy-particle composite coatings: a comprehensive review," vol. 382, p. 125153, 2020.

[7] O. Fayyaz, A. Bahgat Radwan, M.H. Sliem, A.M. Abdullah, A. Hasan, R.A. Shakoor, "Investigating the Properties of Electrodeposited of Ni-P-ZrC Nanocomposite Coatings," vol. 6, no. 49, p. 33310-33324, 2021.

[8] A. Bigos, M. Wolowicz, M. Janusz–Skuza, Z. Starowicz, M.J. Szczerba, R. Bogucki, and E. Beltowska–Lehman, "Citrate-based baths for electrodeposition of nanocrystalline nickel coatings with enhanced hardness," vol. 850, 2021, 156857.

[9] S. Shaik, and A. Basu, "Effect of multiple dissimilar nanoparticles in Ni–W alloy matrix composite coating and evaluation of surface-mechanical, corrosion, and hydrophobic properties," vol. 278, p. 125585, 2022.

[10] M.P.Q. Argañaraz, S.B. Ribotta, M.E. Folquer, E. Zelaya, C. Llorente, J.M. Ramallo–López, G. Benítez, A. Rubert, L.M. Gassa, M.E. Vela, and R.C. Salvarezza, "The chemistry and structure of nickel–tungsten coatings obtained by pulse galvanostatic electrodeposition," vol. 72, p. 87-93, 2012, 87.

[11] L. Elias, and A.C. Hegde, "Electrodeposition of laminar coatings of Ni–W alloy and their corrosion behaviour," vol. 283, p. 61-69, 2015.

[12] M.G. Hosseini, M. Abdolmaleki, and J. Ghahremani, "Investigation of corrosion resistance of electrodeposited NiW/SiC composite coatings," vol. 49, p. 247–253, 2013, 247.

[13] R. Juškėnas, I. Valsiūnas, V. Pakštas, A. Selskis, V. Jasulaitienė, V. Karpavičienė, and V. Kapočius, "XRD, XPS and AFM studies of the unknown phase formed on the surface during electrodeposition of Ni–W alloy," vol. 253, no. 3, p. 1435-1442, 2006.

[14] N. P. Wasekar, S. M. Latha, M. Ramakrishna, D. S. Rao, and G. Sundararajan, "Pulsed electrodeposition and mechanical properties of Ni-W/SiC nano-composite coatings," vol. 112, p. 140-150, 2016, 140.

[15] Y. Yao, S. Yao, L. Zhang, and H. Wang, "Electrodeposition and mechanical and corrosion resistance properties of Ni–W/SiC nanocomposite coatings," vol. 61, no. 1, p. 67-70, 2007.

[16] D. Yin, C.J. Marvel, F.Y. Cui, R.P. Vinci, and M.P. Harmer, "Microstructure and fracture toughness of electrodeposited Ni-21 at.% W alloy thick films," vol. 143, p. 272-280, 2018.

[17] M.H. Allahyarzadeh, M. Aliofkhazraei, A.R. Rezvanian, V. Torabinejad, and A.R. Sabour Rouhaghdam, "Ni-W electrodeposited coatings: characterization, properties and applications," vol. 307, p. 978-1010, 2016.

[18] I. Matsui, Y. Takigawa, T. Uesugi, and K. Higashi, "Effect of additives on tensile properties of bulk nanocrystalline Ni–W alloys electrodeposited from a sulfamate bath," vol. 99, p. 65-67, 2013.

[19] Y. Wu, D. Chang, D. Kim, and S. Kwon, "Effects of 2-butyne-1, 4-diol on structures and morphologies of electroplating Ni–W alloy," vol. 162, no. 2-3, p. 269-275, 2003.

[20] P. C. Huang, C. C. Chou, H. T. Wang, C. H. Cheng, K. H. Hou, and M. D. Ger, "Tribocorrosion study of electrodeposited Ni W alloy/BN(h) composited coatings for piston rings," vol. 436, 2022, 128289.

[21] M. Vamsi, N. P. Wasekar, and G. Sundararajan, "Influence of heat treatment on microstructure and mechanical properties of pulse electrodeposited Ni-W alloy coatings," vol. 319, p. 403-414, 2017.

[22] N. Shakibi Nia, J. Creus, X. Feaugas, and C. Savall, "Influence of metallurgical parameters on the electrochemical behavior of electrodeposited Ni and Ni–W nanocrystalline alloys," vol. 370, p. 149-159, 2016.

[23] N. P. Wasekar, and G. Sundararajan, "Sliding wear behavior of electrodeposited Ni–W alloy and hard chrome coatings," vol. 342, p. 340-348, 2015.

[24] N.S. Mbugua, M. Kang, Y. Zhang, N.J. Ndiithi, and V.B. G, L. Yao, "Electrochemical deposition of Ni, NiCo alloy and NiCo–ceramic composite coatings—A critical review," vol. 13, no. 16, p. 3475, 2020.

[25] M. Chandrasekar, and M. Pushpavanam, "Pulse and pulse reverse plating—Conceptual, advantages and applications," vol. 53, no. 8, p. 3313-3322, 2008.

[26] Z. Mohammadpour, and H. R. Zare, "Improving the Corrosion Resistance of the Nickel–Tungsten Alloy by Optimization of the Electroplating Conditions," vol. 73, no. 4, p. 937-944, 2020, 937.

[27] N. P. Wasekar, S. M. Latha, M. Ramakrishna, D. S. Rao, and G. Sundararajan, "Pulsed electrodeposition and mechanical properties of Ni-W/SiC nano-composite coatings," vol. 112, p. 140-150, 2016, 140.

[28] Y. Wang, M. Yu, H. Luo, Q. Qiao, Z. Xiao, Y. Zhao, L. Zhao, H. Sun, Z. Xu, and K. Matsugi, "Effect of Saccharin on the Structure and Properties of Electrodeposition NiWP Alloy Coatings," vol. 25, no. 10, p. 4402-4407, 2016, 4402.

[29] M.D. Obradović, G.Ž. Bošnjakov, R.M. Stevanović, M.D. Maksimović, and A.R. Despić, "Pulse and direct current plating of Ni–W alloys from ammonia–citrate electrolyte," vol. 200, no. 14-15, p. 4201-4207, 2006.

[30] https://www.chemours.com/en/–/media/files/capstone/capstone–surfactantsbrochure.pdf

[31] O. A. Rahman, N. P. Wasekar, G. Sundararajan, and A. K. Keshri, "Experimental investigation of grain boundaries misorientations and nano twinning induced strengthening on addition of silicon carbide in pulse electrodeposited nickel tungsten composite coating," vol. 116, p. 1-7, 2016.

[32] L. Namburi, "Electrodeposition of NiW alloys into deep recesses," 2001.

[33] M.H. Allahyarzadeh, M. Aliofkhazraei, A.R. Rezvanian, V. Torabinejad, and A.R. Sabour Rouhaghdam, "Ni-W electrodeposited coatings: Characterization, properties and applications," vol. 307, p. 978-1010, 2016, 978.

[34] Handbook, Vol. 3: Alloy Phase Diagrams, ASM International, Materials Park, OH, USA, DOI, 1992 2.48.

[35] H.S. Maharana, and K. Mondal, "Manifestation of Hall–Petch breakdown in nanocrystalline electrodeposited Ni-MoS_2 coating and its structure dependent wear resistance behavior," vol. 410, 2021, 126950.

[36] A. Giga, Y. Kimoto, Y. Takigawa, and K. Higashi, "Demonstration of an inverse Hall–Petch relationship in electrodeposited nanocrystalline Ni–W alloys through tensile testing," vol. 55, no. 2, p. 143-146, 2006.

[37] K. R. Sriraman, S. Ganesh Sundara Raman, and S. K. Seshadri, "Synthesis and evaluation of hardness and sliding wear resistance of electrodeposited nanocrystalline Ni–W alloys," vol. 418, no. 1-2, p. 303-311, 2006, 303.

CHAPTER 9 ARTICLE 4: EFFECT OF HBN ON CORROSION AND WEAR PERFORMANCES OF DC ELECTRODEPOSITED NIW AND NIW–SIC ON BRASS SUBSTRATES

Authors: Mina Dadvand, Oumarou Savadogo

Article published: Journal of Coatings, 18 July 2022

DOI: https://doi.org/10.3390/coatings12071011

Abstract

Crack–free and uniform NiW coatings and their composite coatings filled with ceramic particles such as SiC and hBN were deposited on brass substrates by applying direct current (DC) waveforms. Among all coatings, NiW–SiC–hBN coatings displayed the noblest corrosion potential (-0.49 V) and lowest current density (4.36 $\times 10^{-6}$ A.cm^{-2}). It also seems that addition of hBN and SiC ceramic particles to NiW matrix significantly enhanced the wear resistance of the NiW coatings. However, NiW–hBN exhibited the lowest wear volume (48.84 $\times 10^{3}$ µm^{3}) and the friction coefficient of 0.1 due to ultra–low friction coefficient of hBN particles.

Keywords: Nickel–tungsten coating, pulsed reverse current electrodeposition, direct current electrodeposition, friction coefficient, corrosion, and wear resistance.

9.1 Introduction

Brass has been used in a wide variety of demanding applications such as aerospace, automotive, electronics, construction, marine, and many others. This material has low cost, good

machinability, high electrical, and thermal conductivity. However, it is very susceptible to corrosion and wear after exposure to humid environment at any pH including marine medium producing harmful corrosion products that can have adverse effect on the biological systems. The low mechanical strength of the brass can also negatively influence the performance, shorten the lifespan of equipment resulting in expensive downtime, extra maintenance, power and economical losses [1–4]. Therefore, an attempt has been made to develop various barrier coatings to enhance the mechanical, wear and corrosion performance of brass.

Recently, development of solid lubricant coatings has been the major topic of interest in fabrication of corrosion and wear resistant coatings for various industries. Among various solid lubricants, hexagonal–boron nitride (hBN) has attracted significant attention from researchers due to its chemical inert properties and its ultra–low coefficient of friction. The anisotropic structure of hBN consisting of covalently bonded boron and nitrogen intra–layers stacked together by weak interlayer van der Waals forces provides efficient inter–layer sliding and long wear life [5–7]. The schematic structure of hBN is displayed in Figure 9.1. [8]

Recently, metal matrix composites (MMCs) with superior performance, have shown a great potential in aerospace, automotive, military, and electronic applications. In these materials, the properties of a metallic matrix are modified through incorporating of a different material type (second phase). Electrodeposition is one of the most important techniques for producing MMC. During this process, insoluble particles are dispersed in the plating electrolyte and tapped in the growing metal layer in order to form a composite coating. Nickel, copper, gold, and silver are commonly used as the continuous metallic phase. The dispersed phase can be hard oxides such as alumina (Al_2O_3), titanium oxide (TiO_2) and silicon dioxide (SiO_2), carbides such as tungsten carbide (WC), boron carbide (B_4C) and silicon carbide (SiC), diamond or polymers such as polytetrafluoroethylene (PTFE) and polyethylene terephthalate (PET) [9–14]. Nickel–boron nitride (Ni–BN) composites have become increasingly attractive for various industrial applications due to their high hardness and wear performance. [15–18] Electrodeposition of nickel–boron nitride (Ni–hBN) composites was reported. It was found that Microhardness and wear resistance of the composites were impacted by the content of the co–deposited boron nitride particles [14]. Gyawali et al. [19] reported successful fabrication of Ni–hBN composite coating by using pulse electrodeposition technique. They investigated grain structure as well as corrosion behavior of the deposit in 3.5 wt% NaCl solution. They found that the coatings had smooth surface compared to pure Ni coating and had mixed orientations of crystallite unlike

pure Ni. As well, they found that the addition of hBN particles within Ni matrix improved corrosion performance of the coating in 3.5 wt% NaCl solution. [19]

The properties of eletrodeposited Ni–based composites can be further improved through alloying with other transition metals such as tungsten (W). [20–25] Sangeetha et al. [26] reported DC and pulse electrodeposition of NiW–hBN composites on mild steel. They investigated corrosion and tribological performances of the composites. They reported uniform surface finish, higher microhardness, and excellent corrosion performance of pulse electrodeposited composites compared to DC electrodeposits [26]. Li et al. [27] investigated pulse electrodeposition of functionally graded NiW–hBN nano–composite coatings where the amount of co–deposited hBN particles varied along the coating thickness. They found that the wear resistance, corrosion resistance and microhardness of coatings were improved substantially compared to that of non–graded NiW–hBN coatings.

In another study, NiW–hBN nano–composite coatings were fabricated by using DC electrodeposition method. Morphology, phase structure, roughness, grain size, wear resistance and corrosion resistance of deposited composites were investigated. It was found that the increase of co–deposited hBN increases corrosion resistance. This was attributed to grain refinement and porosity reduction due to the fact that the hBN particles could perform as nucleation sites hence preventing crystal growth. It was also reported that, the wear resistance and hardness increased with the increase of hBN content to a certain level in composites. [28]

To the best of our knowledge, there is no research activities reported on electrodeposition of NiW–SiC–hBN composites and investigation on their microstructure and properties.

In this paper, the influence of hBN on wear performance and corrosion resistance of DC deposited NiW and NiW–SiC was investigated. It was found that the addition of hBN to NiW matrix enhanced the wear resistance significantly due to high lubricity of hBN. Also, addition of SiC to NiW–hBN improved corrosion resistance significantly by shifting of corrosion potential to more positive values and lowering the corrosion current density.

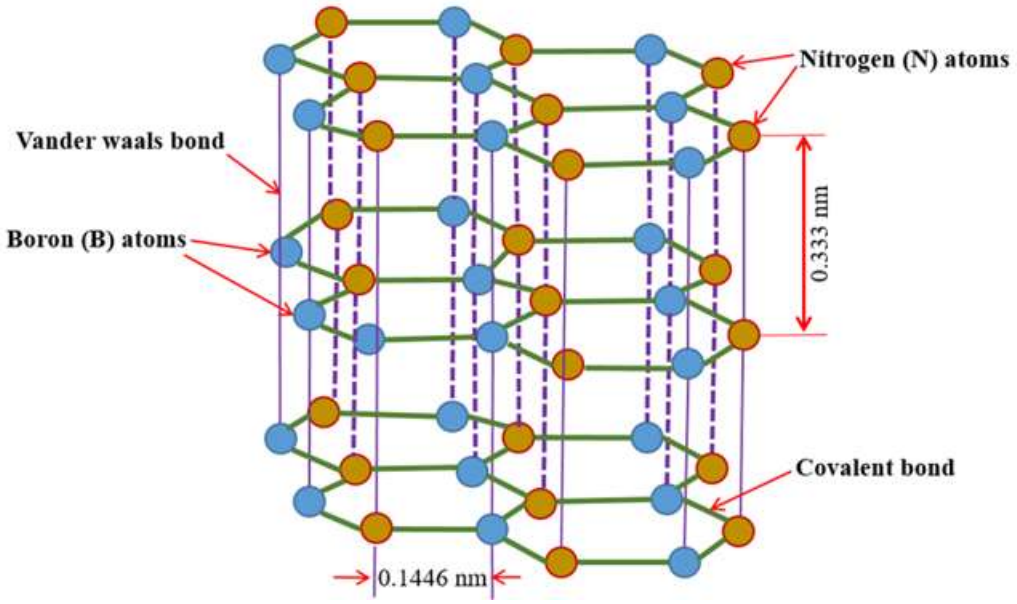

Figure 9.1 Crystal structure representation of the hexagonal boron nitride (hBN).

9.2 Methodology

9.2.1 Electrolyte components and substrate preparation

The substrates used for plating were made of brass (65% Cu, remaining Zn) having dimension of 2.5×1.5 cm^2. The surface of substrate was degreased through immersion into 50 $g.L^{-1}$ alkaline soap solution (TEC1001; Technic Inc, Cranston, RI, USA) at 50 (± 5^oC) for ~ 1 min followed by rinsing with deionized (DI) water. The cleaned substrate was then sensitized by immersing into dilute sulfuric acid (10% v/v) at room temperature for ~ 10 sec followed by rinsing with DI water. Electrodeposition process was accomplished in electroplating bath containing nickel sulfate ($NiSO_4.6H_2O$) as a source of nickel ions, citric acid as a complexing agent [25, 26], sodium tungstate dehydrate ($Na_2WO_4.2H_2O$) as a source of tungstate ions, *o*–Benzoic sulfimide (sodium saccharin, $C_7H_5NO_3S$) as stress reducer to reduce the internal stress within the electrodeposited coating materials [27], propargyl–oxopropane–2,3–dihydroxy as a grain refiner and brightener, and DuPont Capstone Fluorosurfactant F–63 as a wetting agent. Bath electrolyte composition and optimized operating conditions are summarized in Table 9.1.

Finally, NiW–SiC, NiW–hBN, and NiW–hBN–SiC baths were made by adding hBN (20 g·L^{-1}), SiC particles (20 g·L^{-1}) and a dispersant agent such as polyethyleneimine branched, Mn~600 by GPC (0.5 g·L^{-1}) as dispersing agent. SiC and hBN particles are transported to the electrodesurface through the diffusion layer by convective–diffusion and then are adsorbed onto thegrowing surface. The adsorbed particles get physically entrapped into the metallic matrixwithout forming any molecular bonding only if their residence time is large relative to theburial time. Burial time is inversely proportional to the rate of metal electrodeposition andproportional to the particle size. Larger particles require longer time to be engulfed in the depositing metal. [28, 29]

Table 9.1 Electrodeposition bath ingredients and optimized experimental parameters.

Name of Chemicals	**Concentration**
Nickel sulfate	29.5–30 (g.L^{-1})
Sodium tungstate	58–60 (g.L^{-1})
Citric acid	63–67 (g.L^{-1})
Ammonia	58 (ml.L^{-1})
Sulfuric acid	as needed
Propargyl–oxo–propane–2,3–dihydroxy (POPDH)	0.9–1 (g.L^{-1})
DuPont™ Capstone® Fluoro–surfactant FS–63	1.8–2 (g.L^{-1})
Sodium saccharin	0.5–1 (g.L^{-1})
Experimental Parameters	
pH	7.8–8.0
Temperature	58–61 °C
Duration of electrodeposition	30 min
Applied current density	0.14 A.cm^{-2}

9.2.2 Electrodeposition setup

The electrodeposition bath setup is displayed in Figure 9.2. The electrodeposition setup was composed of an electrodeposition tank containing electrolyte, a pump (Flo King Filter System Inc. Longwood, FL, USA) to provide adequate agitation, two anodes made of stainless steel mesh, a cathode made of brass as a substrate being electrodeposited, and a reversed pulse

plating power supply (Model pe8005, Plating Electronic GmbH, Sexau, Berlin, Germany). The electrodeposition bath was placed inside a water circulating bath operating at 60^{o}C temperature. A water circulating bath with temperature controller was used to keep the solution temperature at optimized value. A filter pump (Flo King Filter System Inc.) connected to polypropylene filter was used to provide adequate agitation and to keep the solution free of particulates during the deposition. Platinized titanium mesh was used as anode.

Figure 9.3 displays the Hull cell setup equipped with heater, thermostat, and air pump. Hull cell was used to perform the initial electrodeposition tests and to optimize the conditions of the electrodeposition. A platinized titanium mesh was used as anode and brass substrate was used as cathode.

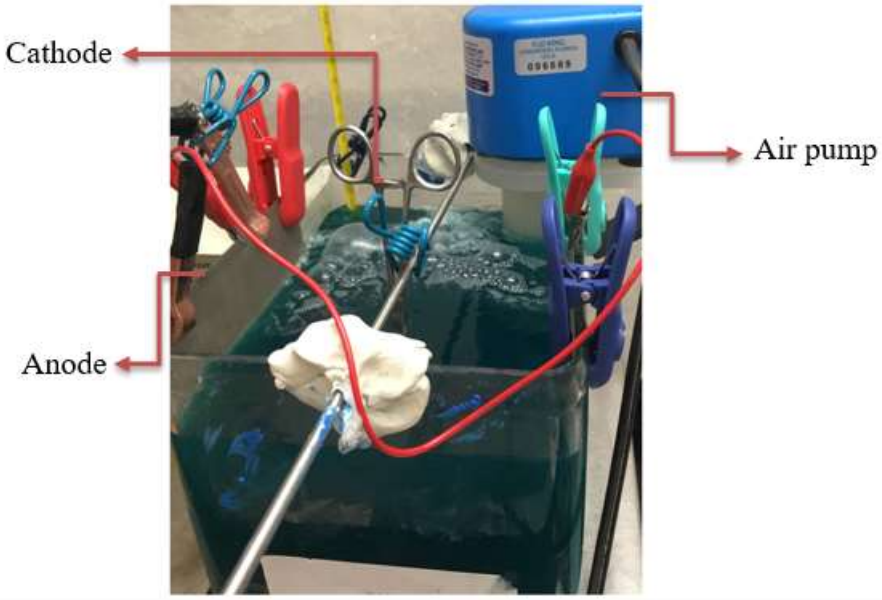

Figure 9.1. Image of the electrodeposition bath setup.

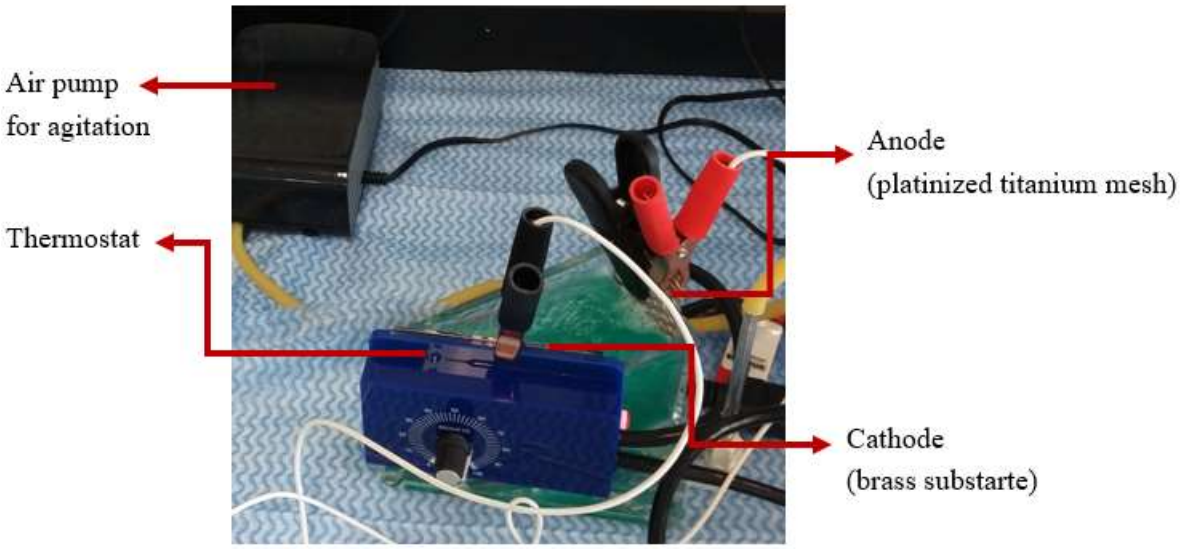

Figure 9.2 Image of the Hull cell setup equipped with thermostat and air pump.

9.2.3 Characterization of deposits

Surface morphology and elemental composition of the deposits were characterized by using scanning electron microscopy and energy dispersive spectroscopy (SEM–EDS, Joel 7600 TFE, JEOL Ltd, Akishima, Tokyo, Japan) with an acceleration voltage of 20 kV. The observations of surfaces were performed without any specific sample preparation. Grain size analysis were also performed using X–ray diffraction (XRD, Bruker D8 Advance, Bruker AXS, Madison, WI, USA) with Cu–Kα radiation (λ= 0.154 nm) and transmission electron microscopy (TEM, Jeol JEM–2100F, JEOL Ltd, Akishima, Tokyo, Japan) at 200 kV, respectively. The samples were thinned to the thickness of ~100 nm using a Gallium Focused Ion Beam (Ga–FIB, Hitachi FB–2000A, Hitachi High–Tech Kyushu Corporation, Tegama, Omuta–shi, Fukuoka, Japan) at 30 kV. Various electrochemical corrosion tests including potentiodynamic polarization (PP) and cyclic potentiodynamic polarization (CPP) tests were performed to evaluate the corrosion performance of the deposits. The potentiostat was operated by a PC equipped with corrosion software (CorrWare) enabling the test parameters to be set and the experiments to be conducted. Potentiodynamic polarization (PP) measurements were performed in the potential range of -0.6 to 1.0 V vs. Ecorr at room temperature and scan rate of 5 $mV \cdot s^{-1}$. Similarly, cyclic potentiodynamic polarization (CPP) scans were performed in the potential range of -0.6 to 1.0 V in forward direction and from 1.0 to -1.0 V in reversed direction at room temperature and 5 $mV \cdot s^{-1}$ scan rate. For all the PP and CPP experiments, graphite rod was employed as reference

electrode and silver/silver sulfate was used as reference electrode. The coated specimens were sealed with an insulating adhesive tape and 1 cm^2 of the surface was exposed to artificial sea water. The composition of the artificial seawater is displayed in Table 9.2.

Table 9.2 Composition of artificial seawater

Ingredients	Concentration (wt%)
NaCl	58.49
Na_2SO_4	9.75
$CaCl_2$	2.765
KCl	1.645
$NaHCO_3$	0.477
KBr	0.238
H_3BO_3	0.071
$SrCl_2.6H_2O$	0.095
NaF	0.007
$MgCl_2$	26.46

Wear tests were performed using a custom–built pin–on–disk wear testing machine under dry air conditions and room temperature. The pin specimens were spherical with a diameter of 1.6 mm and were made of steel (AISI). ASTM G99–05 (2010) was used as a standard to conduct the tests. The applied load was 1 N for all the experiments and the sliding speed and the number of revolutions were 100 $mm \cdot s^{-1}$ and 3500, respectively. The friction experiments were continuously recorded and repeated three times with regard to the sliding distance. Profilometer (Bruker Dektak XT, Bruker Corporation, Billerica, MA, USA) was used to measure the volume of the worn tracks.

9.3 Results and discussion

9.3.1 SEM/EDS analysis

The SEM images were taken from the surface of NiW electrodeposited on brass substrate (Figure 9.4a). The micrograph shows that the coating surface is smooth and free of any cracks or defects. This can have a great influence on the durability and on the performance of the coating in terms of corrosion since such surface can greatly prevent the penetration of corrosive agents from reaching the substrate. EDS spectra and X–ray mapping (Figure 9.4 b,c) were also taken from different locations of the DC–deposited NiW. Accordingly, Ni (~65.9 wt%) and W

(~34.1 wt%) were the main elements of the coatings (Figure 9.4b) and were distributed uniformly across the coating surface (Figure 9.4c). The homogeneous microstructure and elemental distributions can remarkably improve the corrosion and wear performance of the coating. SEM micrographs (Figure 9.5a) were taken from the surfaces of the DC–deposited NiW–SiC to examine any possible defects at the surface of coatings. No defect or delamination was observed on the surface of the coatings and SiC particles with average size of 60 μm were uniformly distributed across the surface. Furthermore, EDS spectra and X–ray mapping (Figure 9.5 b,c) taken from various locations on the surface suggest that the elemental composition of the coatings Ni (~45.6 wt%), W (~20.7 wt%), Si (~32.5 wt%), and C (~1.2 wt%) were uniformly distributed throughout the surface. Surface roughness of the coatings can have a remarkable influence on the longevity and performance of the coatingin terms of contact stress, friction, and wear. Higher surface roughness may result in a lower contact area and lower adhesion between contact surfaces, minimizing the friction and adhesive wear. [30, 31]

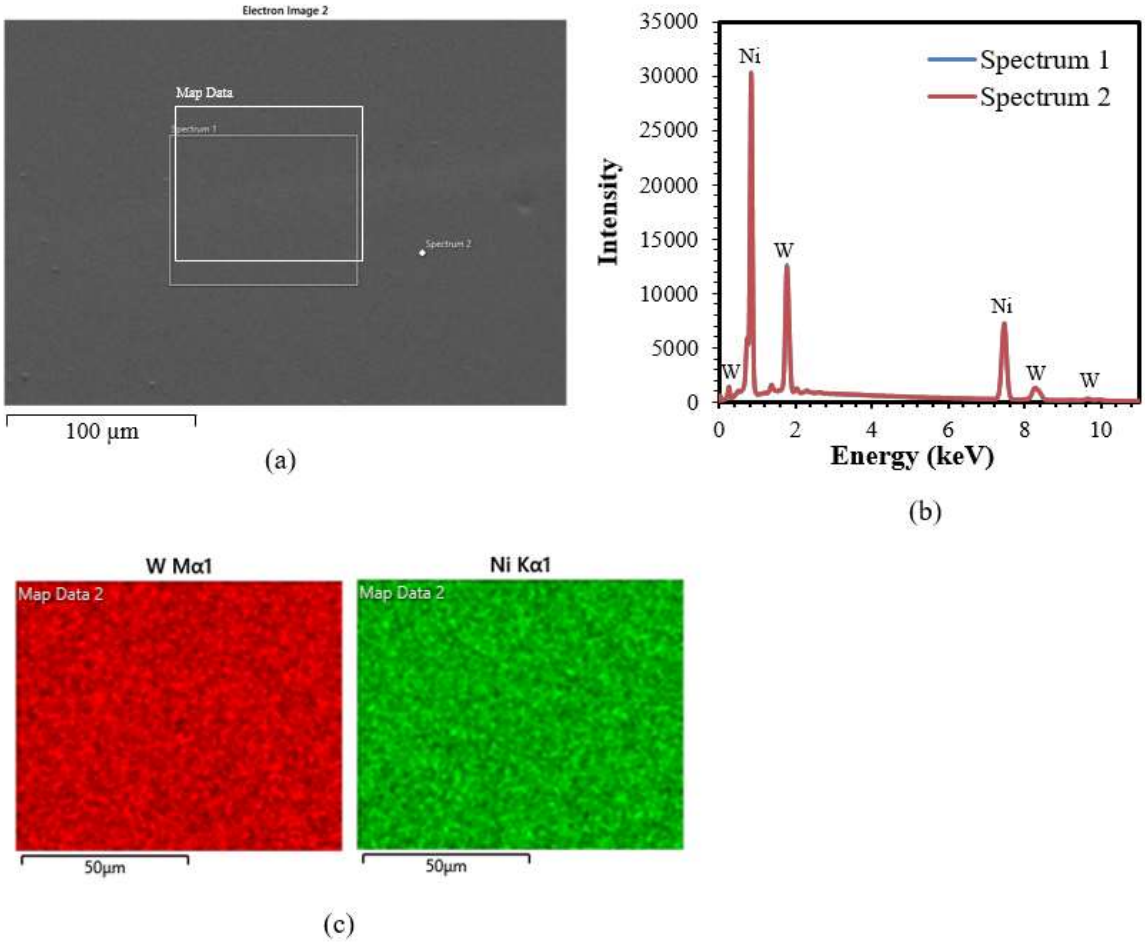

Figure 9.3 SEM micrograph (a), EDS spectra (b), and X–ray mapping (c) taken from the surface of the NiW coating; EDS spectra and EDS map of the area are highlighted with white rectangles in the SEM image.

.

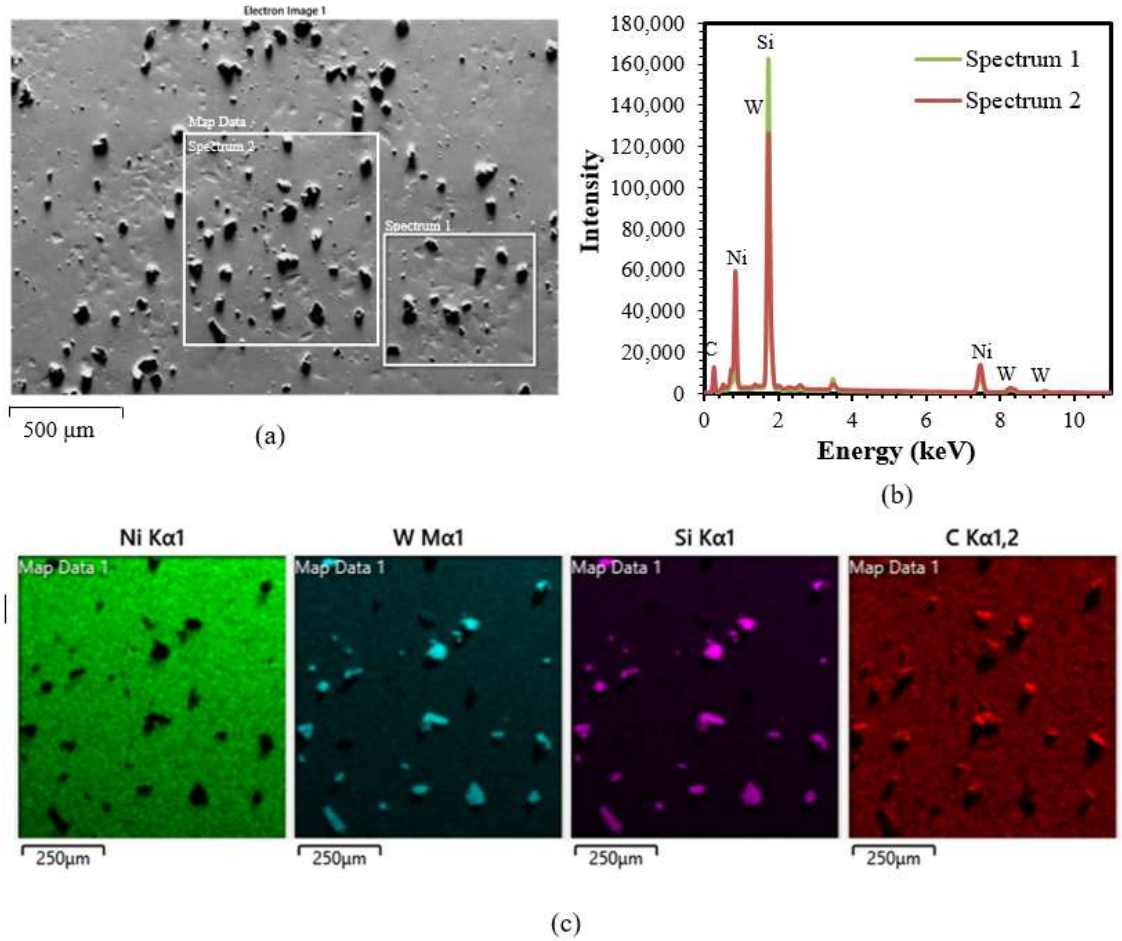

Figure 9.4 SEM micrograph (a), EDS spectra (b), and X–ray mapping (c) taken from the surface of the NiW–SiC coating; EDS spectra and EDS map of the area are highlighted with white rectangles in the SEM image.

SEM micrograph (Figure 9.6a) was taken from the surfaces of the DC–deposited NiW–hBN. No crack or delamination was observed on the surface of the coating and hBN particles with average size of 44µm were uniformly distributed across the surface. Furthermore, EDS spectra and X–ray mapping (Figure 9.6 b,c) taken from various locations on the surface suggest that

the elemental composition of the coatings Ni (~66.2 wt%), W (~24.2 wt%), B(~8.5 wt%), and N (~1.1 wt%) were homogeneously distributed throughout the surface.

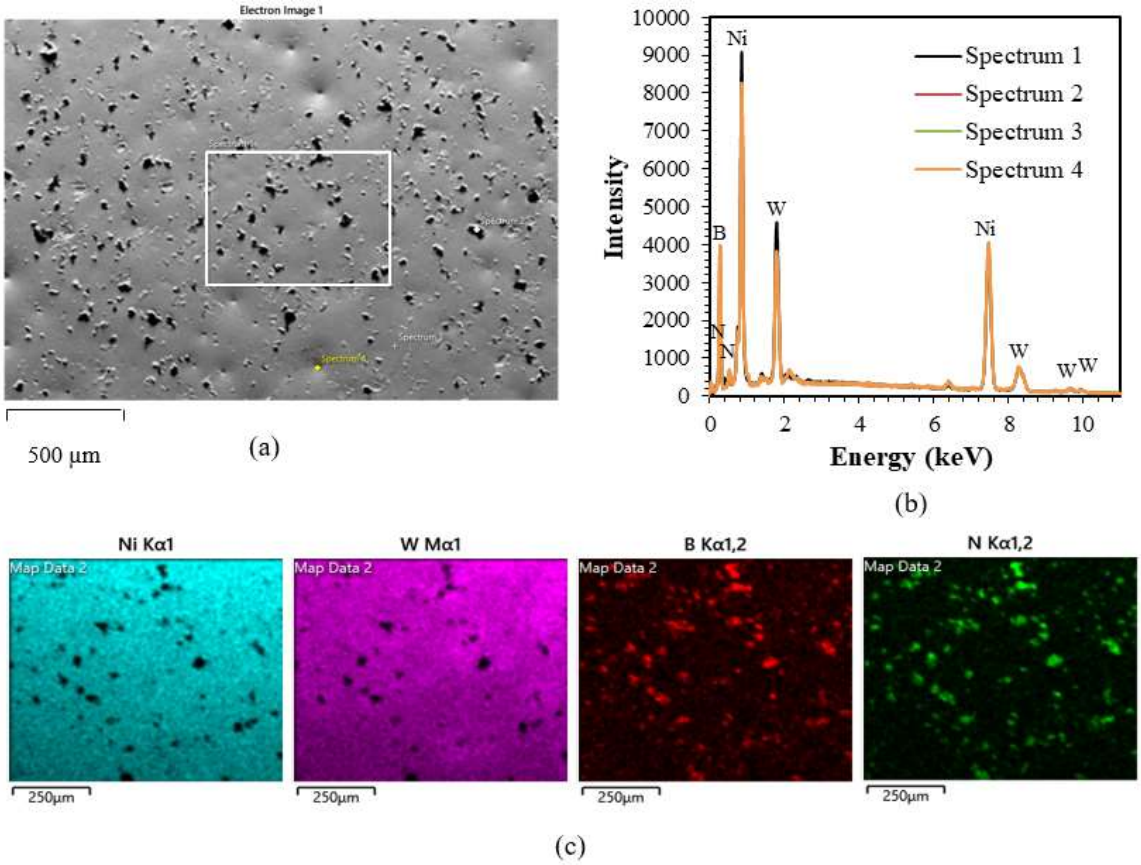

Figure 9.5 SEM micrograph (a), EDS spectra (b), and X–ray mapping (c) taken from the surface of the NiW–hBN coating; EDS map of the area is highlighted with a white rectangle in the SEM image.

SEM micrograph, EDS spectra, and X–ray mapping (Figure 9.7) were taken from the surfaces of the electrodeposited NiW–SiC–hBN. The coating surface was crack–free without any delamination and coating elements were homogeneously distributed across the surface. As well, EDS spectra and X–ray mapping results suggest that the elemental composition ofthe coatings Ni (~69.6 wt%), W (~9.3 wt%), Si (~8.6 wt%), C (~5.1 wt%), B (~5.8 wt%), and N (~1.1 wt%) were homogeneously distributed throughout the surface.

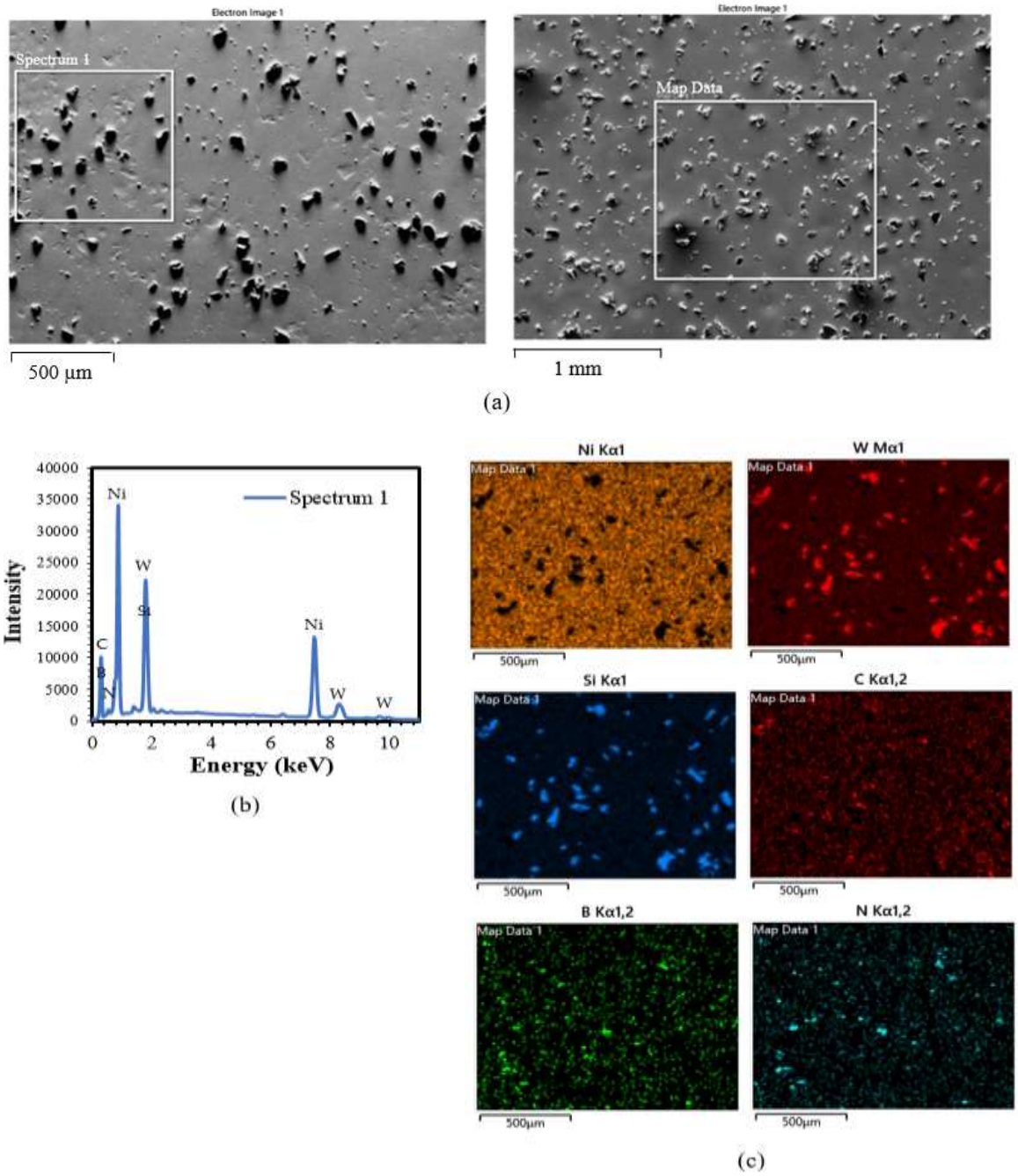

Figure 9.6 SEM micrograph (a), EDS spectra (b), and X–ray mapping (c) taken from the surface of the NiW–SiC–hBN coating; EDS spectra and EDS map of the area are highlighted with white rectangles in the SEM images

9.3.2 Potentiodynamic polarization of DC electrodeposited NiW, NiW–hBN, and NiW–hBN–SiC

Potentiodynamic polarization (PP) tests (Figure 9.8) were performed on the surface of various DC–deposited NiW, NiW–hBN, and NiW–hBN–SiC composites. The intersecting point of the anodic and cathodic polarization curves (Ecorr) showed a significant shift toward the nobler values from -0.92 VAg/AgCl to -0.49 VAg/AgCl and lower current density values were obtained with the addition of SiC, hBN, and mixture of SiC and hBN, respectively (Table 8.3).

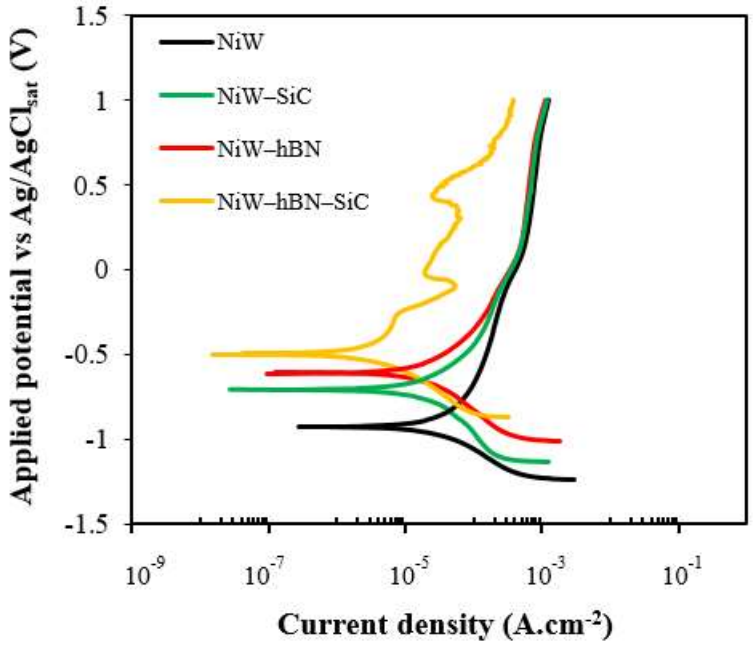

Figure 9.7 Potentiodynamic polarization of DC electrodeposited NiW, NiW–SiC, NiW–hBN, and NiW–hBN–SiC performed at room temperature (~25 °C) and pH of ~8.

Table 9.3 Corrosion potential and current density values extracted from potentiodynamic polarization graph.

Name of Coatings	**Corrosion Potential (V)**	**Current Density ($A \cdot cm^{-2}$)**
NiW	-0.92	2.38×10^{-5}
NiW–SiC	-0.70	2.04×10^{-5}
NiW–hBN	-0.60	2×1^{-5}
NiW–hBN–SiC	-0.49	4.3×10^{-6}

The increase in corrosion potential of NiW towards positive values with the addition of SiC could be attributed to uniform distribution of SiC particles within the NiW, surface oxidation of SiC particles or presence of SiO_2 in the interplanar layers of individual SiC [32, 33]. As well, formation of double layer of $NiWO_4$ and SiO_2 on coating surface when exposed to corrosive media. These protective layers will act as physical barriers to initiation and propagation of cracks or defect corrosion and thus hinder the matrix dissolution. Similar observations were reported by Yao and et al, Jin and et al, Li and et al. [22–24]

The formation of $NiWO_4$ and SiO_2 barrier layers might be attributed to the following reactions [34–36]:

$$Ni^{2+} + WO_4^{2-} \rightarrow NiWO_4 \quad (1)$$

$$SiC + 4H_2O \rightarrow SiO_2 + 8H^+ + CO_2 + 8e^- \quad (2)$$

The formations of $NiWO_4$, SiO_2 and CO_2 are supported by the zone of stabilities of m potential vs pH diagrams of Ni–H_2O, W–H_2O, Si–H_2O and C–H_2O at 25°C. [37]

Moreover, the corrosion resistance enhancement in NiW with the addition of hBN could be explained by its chemical inertness due to its wide band gap (Eg~5.15 eV) [38] and strong in–plane covalent bond, preventing corrosive ion diffusion to the surface of the electrode.

The results are in agreement with those reported by Sangeetha and et al. [26]. They found that the inclusion of hBN nanoparticles within in the NiW matrix could decrease the cracking, porosity, and pinholes of the coating, improving the shielding effect.

Further improvement of corrosion performance in NiW by incorporating a mixture of SiC and hBN could be related to taking advantage of the properties of both ceramic particles for example combination of chemical inertness of hBN together with the formation of protective layers of $NiWO_4$ and SiO_2. Similar to hBN, SiC is also a wide band gap semiconductor (Eg~3.26 eV). [39]

According to potentiodynamic polarization (PP) graphs, NiW–SiC–hBN coatings displayed active–passive transitions, and relatively small passive regions were observed that could be attributed to slightly defective passive films. Presence of active–passive transitions in the anodic curve indicates that the time used to scan the potential range where passivation is expected to occur is much longer than the natural timescale required to obtain the passive film. If the material does not go under active–passive transition, it would corrode at much higher rate in the corrosive environment. Formation of a passive layer offers a great protection against the ionic and electronic diffusions and lowers the corrosion rate of the metal. It also has self–repairing ability after the rupture. The performance of passive layer in corrosive media is affected by many factors, such as pH, temperature, and dissolved oxygen content. [40–43]

9.3.3 Cyclic polarization of DC electrodeposited NiW, NiW–hBN, and NiW–hBN–SiC

Figure 9.9 displays the CPP graphs for DC electrodeposited NiW, NiW–SiC, NiW–hBN, and NiW–hBN–SiC coatings. In the anodic polarization scan, the potential scanning begins from the corrosion potential (E_{corr}). A rapid rise in anodic current density at the potential below the potential of oxygen evolution can be due to: (1) Local dissolution of passive films and formation of metastable pits in the presence of aggressive Cl^- ions; (2) presence and propagation of active defects on the surface of passive layer. The potential at which current density increases sharply is called critical pitting potential, pitting potential, rupture potential, or breakdown potential [44–46]. In order to investigate the materials' response to the pitting corrosion, the scanning direction of the potential was changed at the pitting potential from positive values toward the negative values. It can be observed that DC–deposited NiW exhibits a zero hysteresis loop, while NiW–hBN, NiW–SiC, and NiW–hBN–SiC indicate negative hysteresis loop, depicting repassivation of pits. In fact, reverse anodic curve is shifted to lower current densities in contrast to the forward anodic scan. This indicates the uniform corrosion and reconstruction of the damaged passive layer at higher potentials. As well, the corrosion potential for the

electrodeposited NiW–hBN and NiW–hBN–SiC appeared to be similar and nobler compared to NiW and NiW–SiC coatings due to hBN's chemical inertness. As it is seen in Figure 9.9, all deposits displayed anodic to cathodic transition potential. During the reversal scan, the rapid decrease in corrosion current density at anodic nose or active–passive transition potential was observed at more positive potentials compared to Ecorr. Therefore, the potential of the corroded region is nobler than the un–corroded area. This behavior is usually characteristics of materials that are susceptible to passivation or the materials that are not susceptible to pitting corrosion. [40–43]

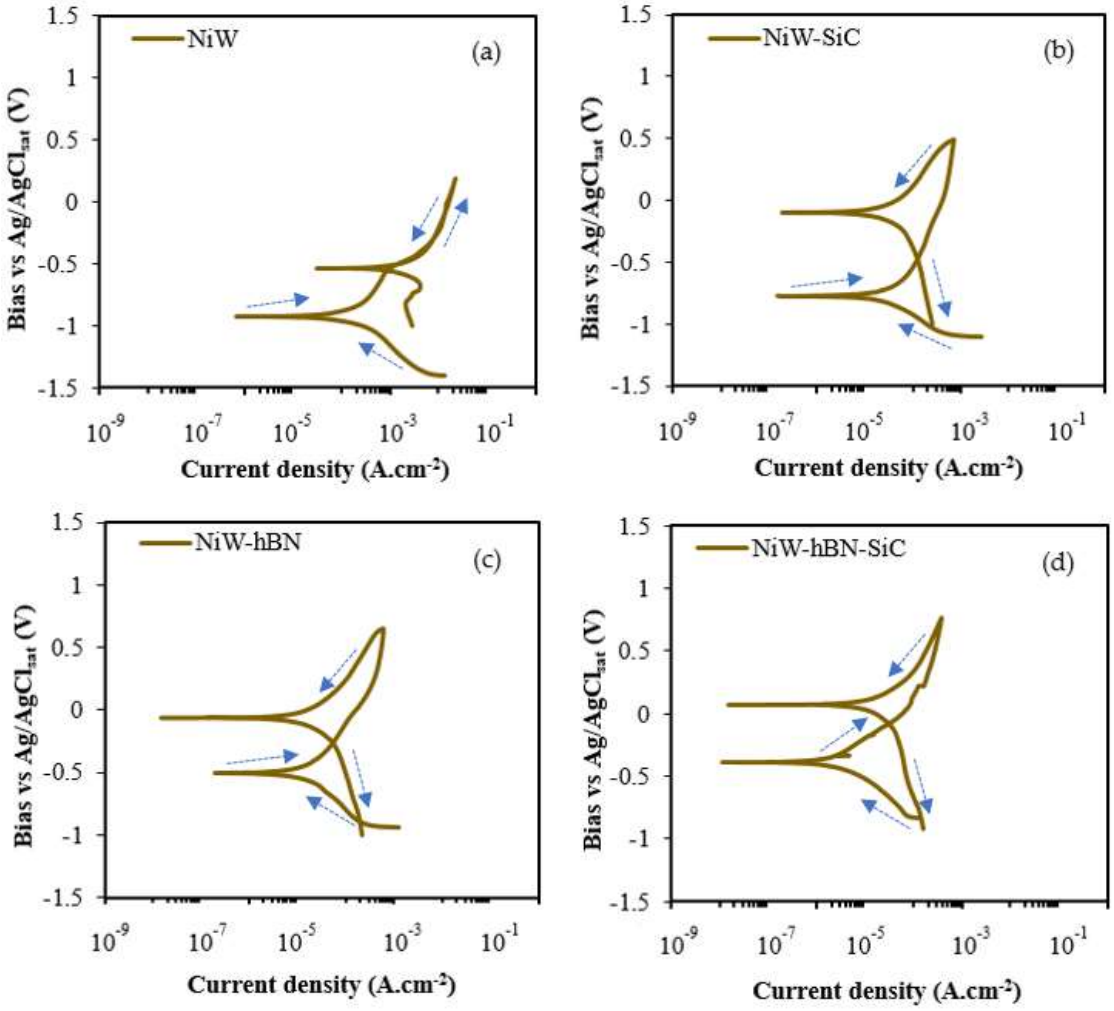

Figure 9.8 CPP of DC electrodeposited NiW, NiW–hBN, and NiW–hBN–SiC.

9.3.4 Tribological analysis

Figure 9.10 displays the variation in the average coefficient of friction for DC deposited Ni, NiW, NiW–hBN, and NiW–hBN–SiC electrodeposited materials on brass substrate using pin–on–disc wear testing equipment. As it can be seen, the DC–NiW–hBN demonstrated a lower coefficient of friction (0.04) compared to the DC–NiW–hBN–SiC (0.15), DC–NiW–SiC (0.4), and DC–NiW deposits (0.6). This is attributed to the ultra–low coefficient and anisotropic structure of h–BN consisting of covalently bonded boron and nitrogen intra–layers stacked together by weak interlayer van der Waals forces providing efficient inter–layer sliding effect. As well, presence of SiC particles in the NiW matrix will effectively reduce the contact between the sliding surfaces due to formation of stable SiO_2. Figure 9.11 displays the wear volume rate of each coating after the friction test.

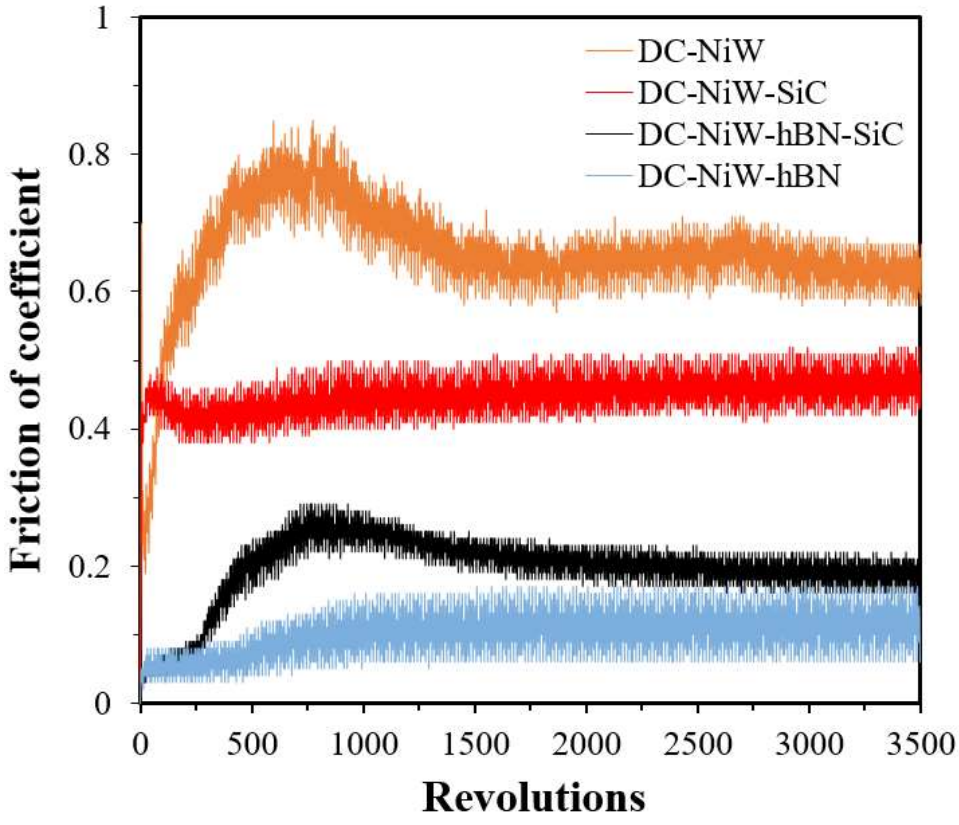

Figure 9.9 Coefficient of friction for the respective DC electrodeposited of NiW, NiW–SiC, NiW–hBN, and NiW–hBN–SiC electrodeposited from an optimized electrolyte on the brass substrate for3500 revolutions at room temperature and normal applied load of 1 N.

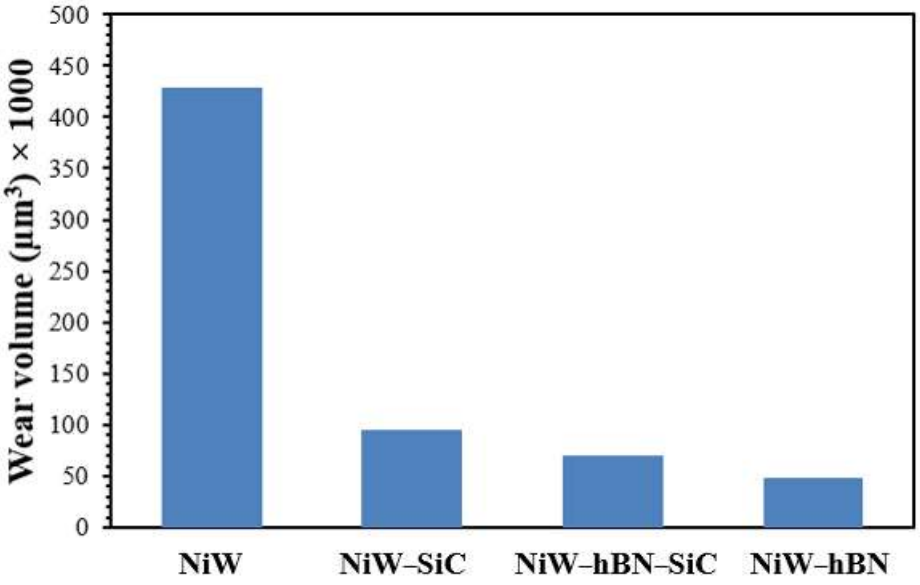

Figure 9.10 Wear volume for the respective DC electrodeposited coatings of NiW, NiW–SiC, NiW–hBN, and NiW–hBN–SiC.

9.3.5 XRD analysis (Influence of Annealing on Crystallite Sizes of DC Electrodeposited NiW, NiW–hBN, and NiW–hBN–SiC)

Curves (a), (b) and (c) of Figure 9.12 display, respectively, the XRD patterns obtained from the surfaces of as–deposited and heat–treated NiW, NiW–hBN, and NiW–SiC–hBN at 350 and 500◦C on brass substrates. No significant differences were found between the XRD patterns of heat–treated and as–deposited coatings. However, crystallite size and peak intensity of the as–deposited coatings were lower than those of the annealed coatings. The increase in peak intensity and crystallite size as a function of annealing temperature can be attributed to FCC crystal grain growth, phase transformation from amorphous type to crystalline structure, and reduction in internal micro–strains. The crystal grain growth, phase transformation from crystalline to amorphous structure, and reduction in internal micro–strains.

The crystallites size (D) of the coatings were calculated (Table 9.4) from the broadening of the (111) peaks using Scherrer equation. [47]

$$D = K\lambda/\beta\cos\theta \qquad (1)$$

Where D is the crystallite size (nm), K is the Scherrer constant (0.9), λ is the wavelength of the x–ray source (0.15406 nm), β is the FWHM (radians), and θ is the peak position (radians).

Table 8.4 Crystallite sizes of DC–deposited NiW, NiW–hBN, and NiW–hBN–SiC.

Coatings	**Peak Position of (111) [°2Th]**	**FWHM [°2Th]**	**Crystallite Size [Å]**
DC–NiW (as–deposited)	43.931	0.720	120
DC–NiW (heat–treated at 350 °C)	44.011	0.673	129
DC–NiW (heat–treated at 500 °C)	44.213	0.413	212
DC–NiW–hBN (as–deposited)	44.226	1.260	68
DC–NiW–hBN (heat–treated at 350 °C)	44.056	1.102	78
DC–NiW–hBN (heat–treated at 500 °C)	43.851	0.336	261
DC–NiW–hBN–SiC (as–deposited)	43.940	0.960	90
DC–NiW–hBN–SiC (heat–treated at 350 °C)	43.949	0.630	138
DC–NiW–hBN–SiC (heat–treated at 500 °C)	43.772	0.528	165

As we can see in Figure 9.12b, the diffraction peaks of DC–deposited NiW–hBN were assigned to the Ni (111), Ni (200), Ni (220), Ni (311), Ni (222), hBN (002), hBN (100), hBN (101), and hBN (004) planes, respectively. The intensity of the peaks and average crystallite size as displayed in Table 9.4 increases from 68 Å up to 261 Å with rising the annealing temperature. This was attributed to an increase in crystallinity of the coating and hence increase in number of the crystallites with the increase of the temperature.

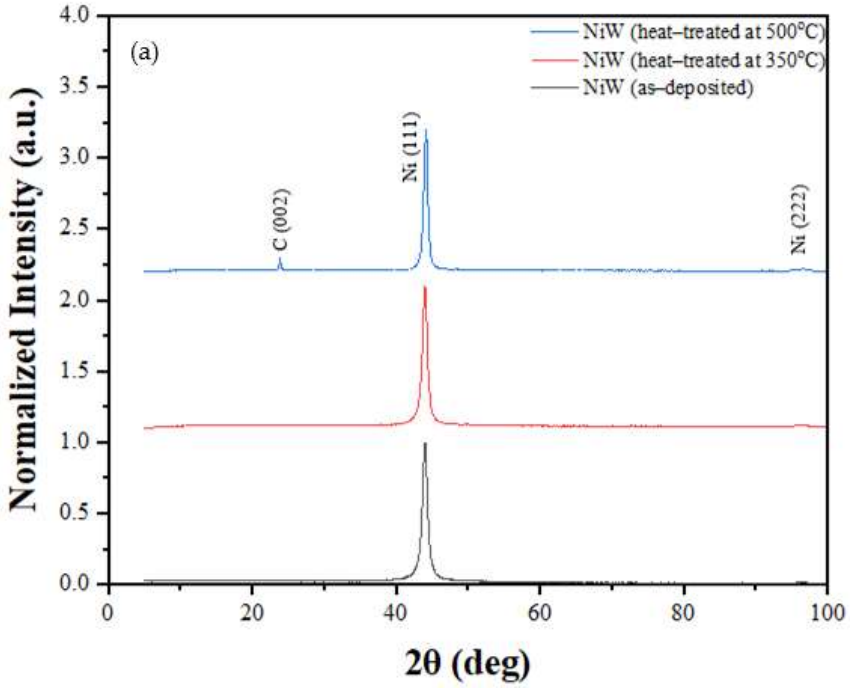
(a)
NiW (heat–treated at 500°C)
NiW (heat–treated at 350°C)
NiW (as–deposited)
C (002)
Ni (111)
Ni (222)
Normalized Intensity (a.u.)
2θ (deg)
0.0
0.5
1.0
1.5
2.0
2.5
3.0
3.5
4.0
0
20
40
60
80
100

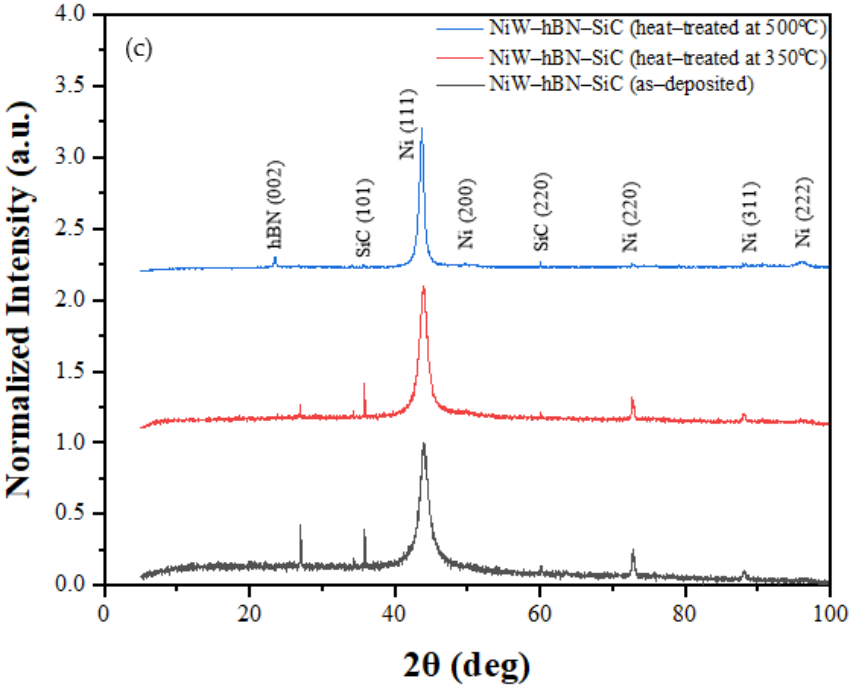
(c)
NiW–hBN–SiC (heat–treated at 500°C)
NiW–hBN–SiC (heat–treated at 350°C)
NiW–hBN–SiC (as–deposited)
hBN (002)
SiC (101)
Ni (111)
Ni (200)
SiC (220)
Ni (220)
Ni (311)
Ni (222)
Normalized Intensity (a.u.)
2θ (deg)
0.0
0.5
1.0
1.5
2.0
2.5
3.0
3.5
4.0
0
20
40
60
80
100

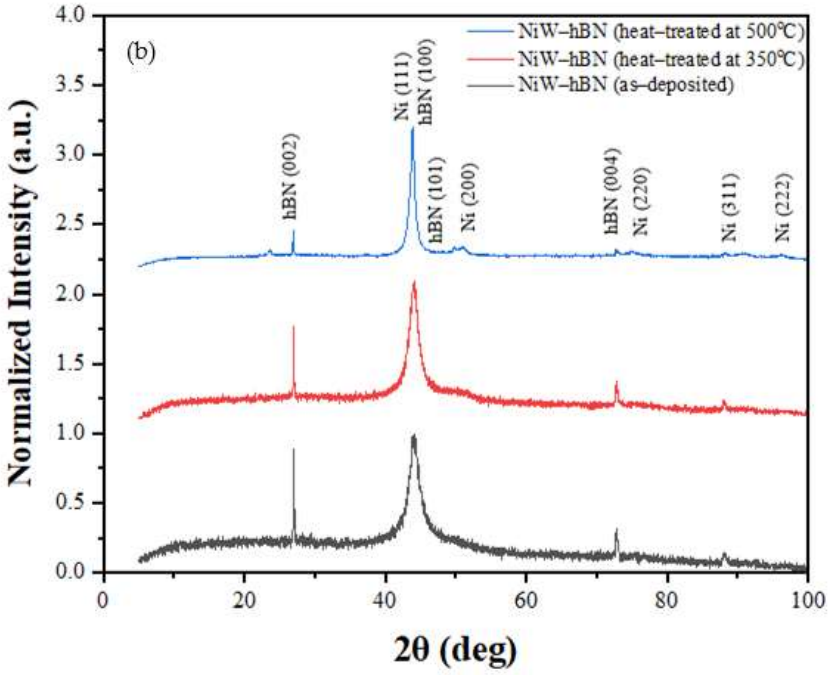

Figure 9.11 XRD spectra from the surface of, respectively, as–deposited, heat–treated at 350 °C and heat treated at 500°C of DC electrodeposits: NiW(a), NiW–hBN (b), and NiW–hBN–SiC (c).

It was noticed that the intensity of the Ni (111) was increased and additional peak of hBN (101) and Ni (200) were formed after heat treatment at 500^{o}C. Furthermore, the average crystallite size increased with increase of the temperature. The results of the average grain size before and after annealing at 350^{o}C and 500^{o}C are presented in Table 9.4. Similar results are obtained from Figure 9.2c which shows the XRD spectra from the surface of as–deposited and annealed electrodeposited NiW–hBN–SiC at 350 and 500 ◦C.

As presented in Table 9.4, incorporation of SiC and hBN in the DC electrodeposited NiW matrix resulted in a decrease in the crystallite size compared to DC–NiW due to micro–strain, lattice distortion of the Ni (W) matrix and grain refinement effect of SiC and hBN particles. The smaller grain size promotes the formation of highly dense and stable passive films with a lower defect density due to a higher amount of active surface atoms. This can repel the adsorption of chloride ions on the surface of the coating and remarkably improves the pitting corrosion and wear performance of the coatings. [48–51]

It was also observed that intensity of Ni (111), Ni (200) were higher with the increase of the annealing temperature. However, some peaks of SiC (101) disappeared after annealing at

500 °C which could be attributed to the decomposition of SiC at high temperatures. Furthermore, the influence of annealing temperature on average crystallite size was investigated. It was found that the average grain size increased from 90 to 165 Å by increase of the annealing temperature from 350 °C up to 500 °C.

9.3.6 TEM Analysis

Crystal structure of the DC–electrodeposited NiW, NiW–SiC, NiW–hBN, and NiW–hBN–SiC samples was investigated by TEM at 200 kV in bright–field (BF) imaging mode (Figure 9.13). TEM samples were cut at the thickness of ~100 nm by focused ion beam (FIB) at normal operating parameters to allow the electron beam to transmit through the ultra–thin samples to form an image. The DC–NiW sample presented mainly a dominant amorphous phase structure, while the DC–deposited NiW–SiC, NiW–hBN, and NiW–hBN–SiC samples exhibited mostly crystalline structure with high crystallographic texture. Figure 9.13 (d–l) revealed plenty of nanotwin bundles for DC electrodeposited NiW–SiC, NiW–hBN, and NiW–hBN–SiC with an average inter–plane distances of 0.63, 0.53, and 0.43 nm formed throughout the surface of the samples. However, DC–NiW coating (Figure 9.13 (a–c)) displayed only few nano–scale twin bundles with average inter–plane distance of 0.47 nm. Nanograins and nanotwins in the coatings can remarkably improve the mechanical, tribological, as well as corrosion properties of coatings by serving as strong dislocation barriers, altering the microstructure, and semiconducting response of the passive film [52, 53]. Figure 9.13b is the high resolution TEM (HRTEM) image revealing the presence of two nanograins with different orientations (marked in dotted box). In between two nanograins, there is a presence of amorphous structure.

Figure 9.14 shows the selected area of the electron diffraction (SAED) pattern of DC–electrodeposited NiW, NiW–SiC, NiW–hBN, and NiW–hBN–SiC coatings, respectively. DC–NiW reveals diffused ring patterns suggesting the existence of dominant amorphous phase, while the DC electrodeposited NiW–hBN and NiW–hBN–SiC exhibit the noncontinuous rings, which is indicative of a crystalline structure with preferred orientation in the microstructure. The interplanar spacings between the atoms can be calculated by measuring the radius of these circular rings. The value of miller indices (hkl) or the phase structure of the materials can be obtained by comparing the estimated values of interplanar spacings derived from SAED rings with the standard values available from JCPDS data cards. According to these values, the primary constituent phase is FCC Ni with random grain orientation. Therefore, the diffraction

pattern analysis from Tem confirms the XRD results.

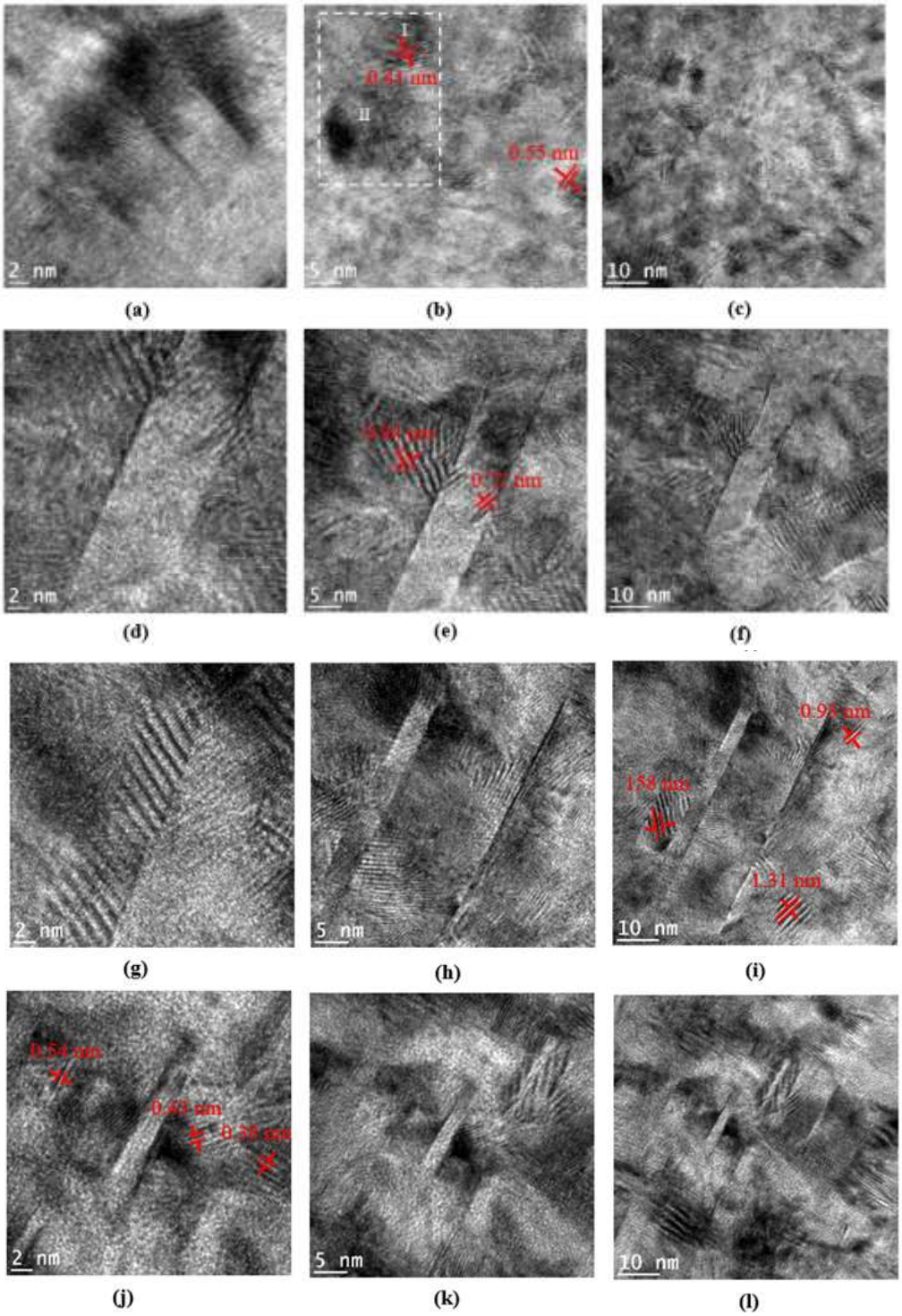

Figure 9.12 BF–TEM images of DC–electrodeposited NiW (a–c); NiW–SiC (d–f); NiW–hBN (g–i), and NiW–hBN–SiC (j–l) at different resolutions.

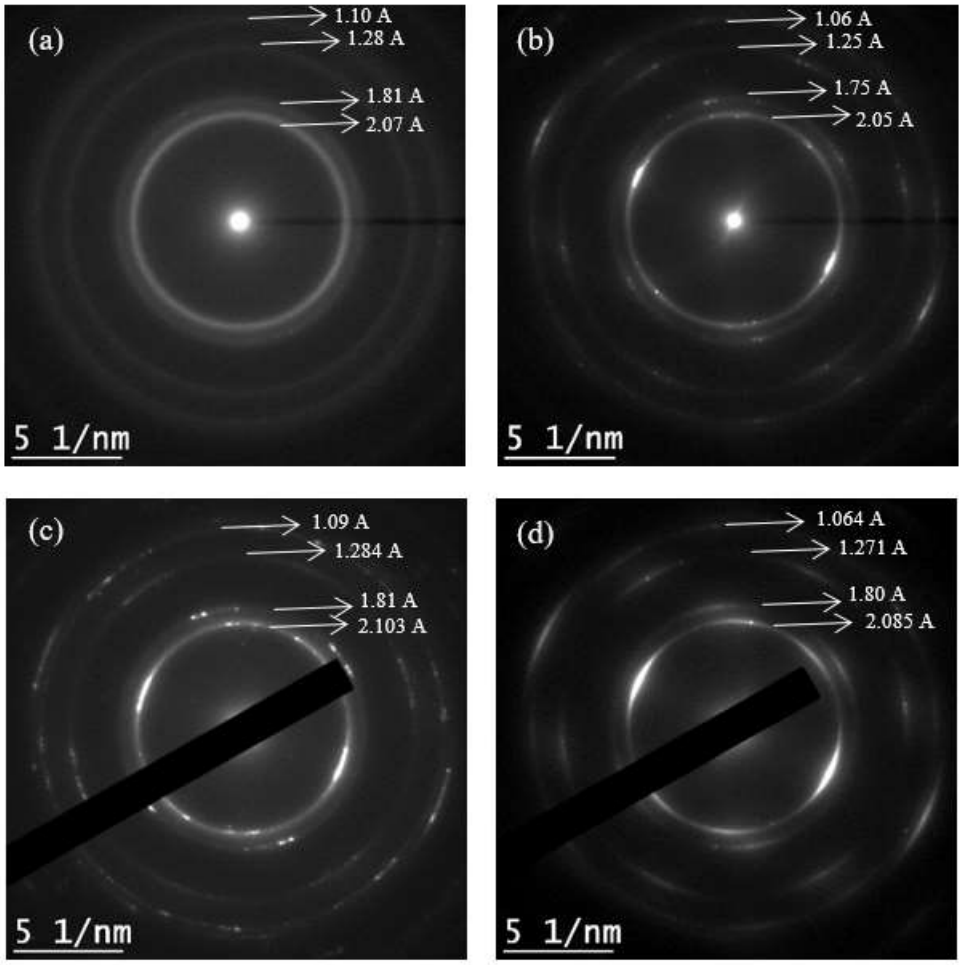

Figure 9.13 SAED patterns from DC–deposited NiW (a); NiW–SiC (b); NiW–hBN (c); NiW–hBN–SiC (d).

9.4 Conclusion

In this research work, NiW filled with hBN and SiC nanocomposite coatings were successfully fabricated via DC electrodeposition and their morphological features, grain structure, electrochemical and wear properties of the coatings were investigated, and the following results were obtained:

- Inclusion of wide band gap semiconductors particles such as hBN and SiC within NiW is shown to enhance the corrosion and wear performance of electrodeposited NiW coatings by altering the morphological features, composition, grain structure, and surface properties of the coatings.

- The coatings were uniform, compact without defects or any cracks. Elemental distribution map also confirmed that the SiC and hBN particles were homogeneously distributed within the NiW matrix.
- Incorporation of hBN and SiC ceramic particles within the NiW matrix enhanced the corrosion performance of the NiW coating. Several sets of experiments were performed to investigate the corrosion performance of the NiW coatings reinforced with hBN and SiC ceramic particles. It was observed that that reinforcement of hBN within NiW and NiW–SiC significantly improved the corrosion performance of the coating and NiW–SiC–hBN exhibited the highest corrosion performance compared to DC–deposited NiW, NiW–SiC, and NiW–hBN. According to potentiodynamic polarization test results, the corrosion resistance improves in the following for deposits.

NiW < NiW–SiC < NiW–hBN < NiW–SiC–hBN

- According to wear performance results, NiW–hBN demonstrated the lowest wear rate and coefficient of friction (0.04) compared to NiW–SiC–hBN (0.15), DC–NiW–SiC (0.4), and DC–NiW deposits (0.6).
- The XRD results obtained from the surfaces of the as–deposited and annealed DC–deposited NiW, NiW–hBN, and NiW–SiC–hBN at 350 and 500◦C also revealed that the intensity of the peaks and the average crystallite size increased with the annealing temperature up to 500 ◦C. Inclusion of hBN and SiC within NiW also reduced the grain size due to micro–strain and lattice distortion of the Ni (W) matrix.
- According to BF–TEM results, plenty of nanotwin bundles were formed across the surface of DC–deposited NiW–hBN and NiW–hBN–SiC coatings. However few nano–twin bundles were observed on the surface of DC–NiW coating. Nanotwins can effectively hinder the dislocation motion, and therefore enhance the tribological performance of the coatings.

8.5. References

[1] A. Kumar, G. Malik, R. Chandra, and R. Mulik, "Bluish emission of economical phosphor h-BN nanoparticle fabricated via mixing annealing route using non-toxic precursor," vol. 288, p. 121430, 05/01 2020.

[2] R. An-hua, "Effect of Current Density on the Properties of Ni–CeO_2 Composite Coatings prepared using Magnetic Field-Assisted Jet Electrodeposition," 2021, ArticleID:210658.

[3] S. Guo, L. Wang, Y. Jin, N. Piao, Z. Chen, G. Tian, J. Li, C. Zhao, and X. He, "A polymeric composite protective layer for stable Li metal anodes," vol. 7, no. 1, p. 21, Jun 15 2020. [En ligne]. Disponible: https://www.ncbi.nlm.nih.gov/pubmed/32542452

[4] J. Cao, L. Wang, X. He, M. Fang, J. Gao, J. Li, L. Deng, H. Chen, G. Tian, J. Wang, and S. Fan, "In situ prepared nano-crystalline TiO_2–poly (methyl methacrylate) hybrid enhanced composite polymer electrolyte for Li-ion batteries," vol. 1, no. 19, p. 5955-5961, 2013.

[5] Y. Yao, H. Dong, L. Jiao, N. Yu, and L. He, "Preparation and electrocatalytic property of PbO_2-CeO_2 nanocomposite electrodes by pulse reverse electrodeposition methods," vol. 163, no. 5, p. D179, 2016.

[6] Y. Bao, H.Y. Liu, Q. Liu, L.L. Gao, and C.Q. Zhang, "Mechanical states of repaired full-thickness defects of articular cartilage by tissue engineering under compression," communication présentée à Applied Mechanics and Materials, 2013, p. 658-661.

[7] L. Wang, S. Xing, H. Liu, C. Jiang, and V. Ji, "Improved wear properties of NiTi nanocomposite coating with tailored spatial microstructures by extra adding CeO_2 nanoparticles," vol. 399, p. 126119, 2020.

[8] E. Pompei, L. Magagnin, N. Lecis, and P.L. Cavallotti, "Electrodeposition of nickel–BN composite coatings," vol. 54, no. 9, p. 2571-2574, 2009.

[9] N. K. Shrestha, D. B. Hamal, and T. Saji, "Composite plating of Ni–P–Al_2O_3 in two steps and its anti-wear performance," vol. 183, no. 2-3, p. 247-253, 2004.

[10] M. Pushpavanam, and S. Natarajan, "Nickel-boron nitride electrocomposites," vol. 93, no. 6, p. 97-99, 1995.

[11] S. Teruyama, N. Shrestha, Y. Ito, M. Iwanaga, and T. Saji, "Plating of Ni/c-BN composite film in two steps," vol. 39, no. 8, p. 2941-2943, 2004.

[12] G. Gyawali, R. Adhikari, H.S. Kim, H.B. Cho, and S.W. Lee, "Effect of h-BN Nanosheets Codeposition on Electrochemical Corrosion Behavior of Electrodeposited Nickel Composite Coatings," vol. 2, no. 3, p. C7-C10, 2012, C7.

[13] L. Tarkowski, P. Indyka, and E. Bełtowska-Lehman, "XRD characterisation of composite Ni-based coatings prepared by electrodeposition," vol. 284, p. 40-43, 2012.

[14] N. Atanassov, K. Gencheva, and M. Bratoeva, "Properties of nickel-tungsten alloys electrodeposited from sulfamate electrolyte," vol. 84, no. 2, p. 67-74, 1997.

[15] L. Jinlong, W. Zhuqing, L. Tongxiang, K. Suzuki, M. Hideo, "Effect of tungsten on microstructures of annealed electrodeposited Ni-W alloy and its corrosion resistance," vol. 337, p. 516-524, 2018.

[16] O. Younes-Metzler, and E. Gileadi, "Electroplating of Ni/W Alloys," vol. 149, no. 2, 2002, C100.

[17] M. Klimenkov, A.S.M.A. Haseeb, and K. Bade, "Structural investigations on nanocrystalline Ni-W alloy films by transmission electron microscopy," Thin Solid Films, vol. 517, no. 24, p. 6593-6598, 2009. [En ligne].

Disponible: https://www.cheric.org/research/tech/periodicals/view.php?seq=1062420

[18] K. R. Sriraman, S. G. Sundara Raman, and S. K. Seshadri, "Synthesis and evaluation of hardness and sliding wear resistance of electrodeposited nanocrystalline Ni–Fe–W alloys," vol. 22, no. 1, p. 14-20, 2013, 14.

[19] S. Sangeetha, and G.P. Kalaignan, "Tribological and electrochemical corrosion behavior of N‰ W/BN (hexagonal) nano-composite coatings," vol. 41, p. 10415-10424, 2015.

[20] H. Li, Y. He, T. He, D. Qing, F. Luo, Y. Fan, and X. Chen, "Ni-W/BN(h) electrodeposited nanocomposite coating with functionally graded microstructure," vol. 704, p. 32-43, 2017, 32.

[21] B. Li, D. Li, T. Mei, W. Xia, and W. Zhang, "Fabrication and characterization of boron nitride reinforced Ni–W nanocomposite coating by electrodeposition," vol. 777, p. 1234-1244, 2019, 1234.

[22] P. Jin, C. Sun, Z. Zhang, C. Zhou, and T. Williams, "Fabrication of the Ni-W-SiC thin film by pulse electrodeposition," vol. 392, 2020, 125738.

[23] B. Li, W. Zhang, W. Zhang, and Y. Huan, "Preparation of Ni-W/SiC nanocomposite coatings by electrochemical deposition," vol. 702, p. 38-50, 2017, 38.

[24] Y. Yao, S. Yao, L. Zhang, and H. Wang, "Electrodeposition and mechanical and corrosion resistance properties of Ni–W/SiC nanocomposite coatings," vol. 61, no. 1, p. 67-70, 20.

CHAPTER 10 ARTICLE 5: SYNTHESIS AND CHARCTERIZATION OF NOVEL NIW–SIC–CEO_2 COMPOSITE COATING ON BRASS SUBSTRATE WITH ENHANCED CORROSION AND WEAR RESISTANCE

Authors: Mina Dadvand, Oumarou Savadogo

Article was accepted prior to revision: Journal of Surface Engineering, 3 August 2022

Abstract

Crack–free and uniform NiW composite coatings filled with ceramic particles such as SiC and CeO_2 were deposited on brass substrates by applying direct current (DC) and a well–designed pulse reverse current waveforms (PRC). PRC coatings displayed the noblest corrosion potential and lowest current density compared to DC electrodeposited coatings. Among all PRC coatings, PRC–NiW–SiC–CeO_2 demonstrated the highest corrosion resistance and the lowest current density. It also seems that addition of ceramic particles to NiW matrix enhanced the wear resistance of the coatings and the lowest wear volume of about (14.119×10^3 μm^3) and the friction coefficient of 0.25 were obtained due to the formation of the uniform, void free and packed structures with high content of SiC and CeO_2 particles in the deposit.

Keywords: Nickel–tungsten composite, pulsed reverse current electrodeposition, direct current electrodeposition, friction coefficient, corrosion, and wear resistance.

10.1 Introduction

In recent years, metal matrix composites (MMCs) with an excellent performance, have been widely used in aerospace, automotive, and electronics, applications. These materials are

prepared by adding various reinforcing phases [1–3]. Among MMCs, nickel–based alloys have been widely used in different industrial applications due to their outstanding performance and low cost [1]. Among various fabrication techniques, electrodeposition is one of the most common method of producing various metal matrix coatings [1–7]. The reinforcing phases (insoluble materials) are suspended in a conventional electrodeposition bath and co–deposited within the metal matrix during the electrodeposition process. These insoluble components can be in the form of powder, fiber or encapsulated particles. Electrodeposition of various Ni based composites have been reported in which one or more of various metallic oxides such as ZrO_2, Al_2O_3, TiO_2, MoO_2 and carbides such as SiC were added into Ni based electrodeposition baths [1–17]. Substantial improvements in material properties such as microhardness, wear, and corrosion resistance as a result of codeposition of reinforcements phase(s) into Ni matrix [18–19]. The degree of improvements in the properties depends on various factors such as the type and content of the reinforcements particles as well as their uniformity in distribution within the Ni based matrix, electrodeposition parameters such as operating temperature, agitation modes, applied current density, plating duration, and electrolyte formulation (i.e., type and concentration of ingredients). [1–20]

The addition of CeO_2 particles into Ni matrix could enhance hardness, wear– and oxidation resistance of the matrix [1, 4–6]. However, inclusion of CeO_2 within Ni matrix is required to be dispersed uniformly without agglomeration. Therefore, electrodeposition parameters including applied current density and operating temperature as well as plating electrolyte need to be well–designed and optimized [1, 7]. Zhou et al. [8] reported that well dispersion of CeO_2 in Ni matrix enhances mechanical, wear and corrosion properties of the Ni–CeO_2 coating compared to bare Ni. They attributed the enhancement to grain refining effect of CeO_2 on Ni matrix and formation of passivation layer on the surface. [8]

Extensive research works have been reported on electrodeposition of Ni–SiC composites and their applications as protective coatings in friction parts and combustion engines due to their improved properties compared to Ni pure metal deposits [21–30]. It was found that the size and the content of co–deposited SiC particles had significant influence on microstructure as well as corrosion behavior of electrodeposited Ni–SiC composites. [31]

The properties of eletrodeposited Ni–based composites can be further improved through alloying with other transition metals such as tungsten (W) [32]. NiW alloy was developed as one of the surface treatments to replace hard chromium coating for its excellent properties. Among various reinforcement particles, SiC was investigated extensively and applied for

various applications due to its enhanced properties such as high hardness, good corrosion resistance and excellent chemical stability [32–36]. The influence of the content of co–deposited SiC particles as well as electrodeposition parameters such as applied current density and agitation speed on the amount of co–deposited SiC particles within NiW matrix was reported. As well, Microhardness, corrosion and wear performance of NiW–SiC composites were investigated. [32]

To the best of our knowledge, there is no research activities reported on electrodeposition of NiW–CeO_2 and NiW–SiC–CeO_2 composites and investigation on their microstructure, corrosion, and tribological properties.

In this research work, NiW–SiC–CeO_2 deposit was fabricated by using DC and PRC process through applying a unique pulsed reverse current waveform on electrodeposition bath chemistry containing specially selected ingredients. It was found that the incorporating of CeO_2 and SiC ceramic particles within the NiW matrix enhanced the corrosion and tribological performance of the deposit and PRC–NiW–SiC–CeO_2 possessed superior corrosion and wear performance compared to the DC and PRC electrodeposited NiW and NiW–SiC coatings.

10.2 Methodology

10.2.1 Electrolyte components

Electrodeposition of Ni and NiW alloys were accomplished in electroplating bath containing source of metals to be plated, complexing agent (Citric acid), stress reducer (*o*–Benzoic sulfimide), brightener/grain refiner (propargyl –oxopropane –2,3 –dihydroxy), and wetting agent (DuPont™ Capstone® Fluorosurfactant F–63).

The NiW electrodeposition bath was prepared by adding a source of tungstate ions (sodium tungstate dehydrate) into the same electroplating bath that was used for Ni electrodeposition. NiW–SiC–CeO_2 bath was made by adding SiC and CeO_2 particles and a dispersant agent such as polyethyleneimine into NiW electrodeposition solution. Table 10.1 summarizes the ingredients plating electrolyte and optimized operating conditions to obtain uniform and defect–free NiW coating with desired mechanical and tribological performance.

Table 10.1 Electrodeposition bath ingredients and optimized experimental parameters

Name of chemicals	**Concentration**
Nickel sulfate	29.5–30 ($g.L^{-1}$)
Sodium tungstate	58–60 ($g.L^{-1}$)
Citric acid	63–67 ($g.L^{-1}$)
Ammonia	58 ($ml.L^{-1}$)
Sulfuric acid	As needed
Propargyl–oxo–propane–2,3–dihydroxy (POPDH)	0.9–1 ($g.L^{-1}$)
DuPont™ Capstone® Fluoro–surfactant FS–63	1.8–2 ($g.L^{-1}$)
Sodium saccharin	0.5–1 ($g.L^{-1}$)
Experimental parameters	
pH	7.8–8.0
Temperature	58–61 ºC
Duration of electrodeposition	30 min

The role of citric acid was to form stable complexes with tungstate (WO_2^{+4}) and nickel (Ni^{2+}) ions to prevent direct interaction between nickel and tungstate ions. Such direct interaction would result in irreversible precipitation of non–soluble nickel tungstate compound in electrodeposition bath solution [37–38]. Sodium saccharin was used as a stress removal agent to reduce the internal stress within the electrodeposited coating materials [39]. We used propargyl–oxo–propane–2, 3–dihydroxy as a brightener and grain refiner. This compound is a specific type of propargyl derivative containing a carbon–carbon triple bond (i.e. –C≡C–H) at the end of its molecular chain which has a tendency to deposit preferentially at high current density areas on the substrate such as sharp areas during electrodeposition to control the nickel ion diffusion towards the cathode. Therefore, a uniform and crack–free deposit with mirror like finish surface was obtained. This organic compound can also enhance the nucleation sites for initiating the first stages of the metal deposition process on the surface of substrate leading to the decrease in grain size of the nickel. Unlike other brighteners such as sodium citrate–sulfonic acid used in Ni electrodeposition or Thiourea, this propargyl based brightener does not contain sulfur compound. Co–deposition of sulfur with Ni could deteriorate the corrosion properties of the coating [40]. Finally, Capstone fluoro–surfactant FS–63 (DuPont) was selected as a wetting agent to release the hydrogen gas bubbles from the substrate surface. FS–63 (DuPont) is a low

foaming type anionic fluoro–surfactant which is soluble in water and provides low surface tensions. [41]

In these experiments, platinized titanium mesh sheet was used as anode and brass (68 wt% Cu, remaining Zn) having dimension of 2.5 × 1.5 cm^2 was used as substrate. The surface of substrate was pretreated before electroplating. The pretreatment was composed of six steps: i) degreasing by immersing into 50 $g.L^{-1}$ alkaline soap solution (TEC1001; Technic Inc.) at ~ 50°C for ~1 min; ii) rinsing with DI water for ~30 sec; iii) activation/sensitization by immersing into i dilute sulfuric acid (10% v/v) at room temperature for ~10 sec; iv) rinsing with DI water for ~30 sec.

A hull cell (Figure 10.1) setup equipped with heater, thermostat air agitation and air pump was used to characterize, optimize, and improve applied current density distribution throughout the substrate surface. A brass substrate was used as cathode and a platinized titanium mesh sheet was used as anode.

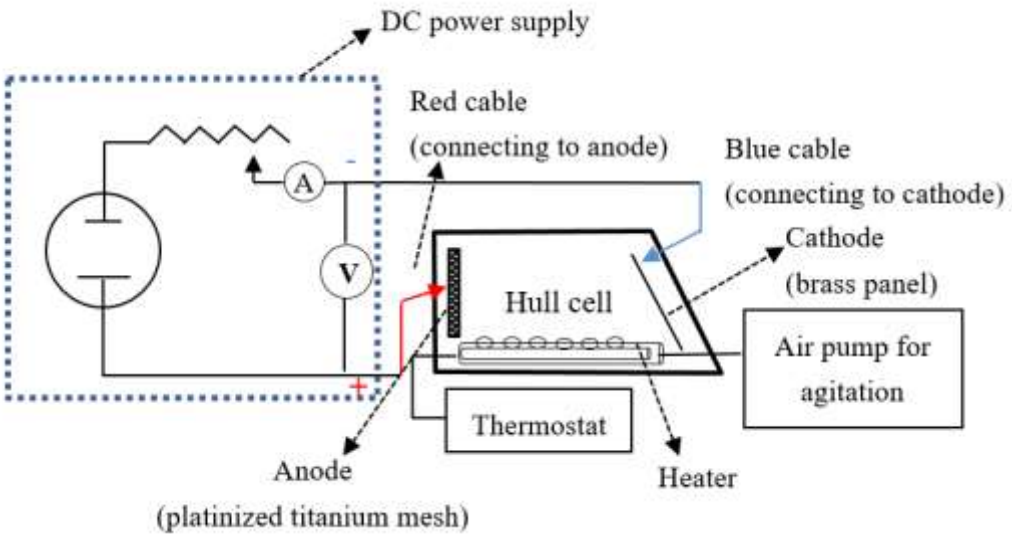

Figure 10.1 Schematic diagram of hull cell equipped with thermostat and air agitation.

The optimized reversed pulse waveform was composed of forward pulse current density of (I_f) of 0.15 $A.cm^{-2}$ with forward pulse duration (t_f) of 16 ms and reversed pulse current density (I_r) of 0.11 $A.cm^{-2}$ with reversed pulse duration (t_r) of 9 ms. The total plating duration for all experiment was 30 min.

10.2.2 Characterization of deposits

The elemental composition, grain size, and surface morphology of the deposits were characterized by energy dispersive spectroscopy (EDS), X–ray diffraction (XRD, Bruker D8 Advance), and scanning electron microscopy (SEM, Joel 7600 TFE), respectively.

Pin–on–disk (Custom–built) and Profilometer (Bruker Dektak XT) tests were performed to measure the coefficient of friction and volume of the worn tracks. The tests were performed under dry air conditions and ambient temperature. Spherical Al_2O_3 balls with a diameter of 4.7 mm were used for the pin specimen. The sliding velocity and the number of revolutions were 100 mm/s and 3500, respectively. For all the experiments, the applied load was 2 N. The coefficients of friction were continuously recorded with respect to the sliding distance. Each friction experiment was repeated three times and the average results were reported. Potentiostat (Princeton Applied Research Potentiostat/Galvanostat Model 273A) was used to investigate the corrosion behavior of the deposits. The potentiostat was equipped with CorrWare software enabling to apply potential scans remotely through the software. Potentiodynamic polarization (PP) scans were performed from -0.6 to 1.0 V vs. Ecorr at room temperature and 5 $mV.s^{-1}$ scan rate. For all the PP experiments, silver/silver sulfate electrode and graphite rod were used as reference and counter electrodes, respectively. The surface of the specimen was covered with an insulating 3M tape to expose 1 cm^2 of the surface to corrosive liquid (artificial sea water). Table 10.2 shows the composition of the artificial seawater.

Table 10.2 Composition of Artificial Sea Water

Ingredients	**Concentrations (wt%)**
NaCl	58.49
Na_2SO_4	9.75
$CaCl_2$	2.765
KCl	1.645
$NaHCO_3$	0.477
KBr	0.238
H_3BO_3	0.071
$SrCl_2.6H_2O$	0.095
NaF	0.007
$MgCl_2$	26.46

10.3 Results and discussion

10.3.1 Corrosion analysis

10.3.1.1 Cyclic potentiodynamic polarization (CPP)

Figure 10.2 displays the CPP graphs for DC and PRC electrodeposited Ni, NiW, and NiW–SiC–CeO_2 composite coatings. As it can be seen, NiW and composite coatings exhibit resistance to pitting corrosion. In fact, during the potential scan, when the forward curve coincides with the reverse curve, the hysteresis loop is not formed meaning that the localized corrosion does not occur. However, this does not prove any resistance to general corrosion. As well, the corrosion potential for the PRC plated NiW–SiC–CeO_2 appears to be nobler compared to other coatings.

As it can be seen from Figure 10.2, all deposits display anodic to cathodic transition potential. At anodic to cathodic transition potential, the anodic current density changes to the cathodic current density. At reverse scan, the rapid decrease in corrosion current density at anodic nose or active–passive transition potential occurs at nobler potentials compared to E_{corr}. This behavior is usually characteristics of materials that are susceptible to passivation and restore the damaged passivation layer or the materials that are not susceptible to pitting corrosion [42]. For these type of materials, the difference between the anodic to cathodic transition potential and Ecorr are used to determine the stability of the passivation layer. In fact, the stability of passivation layer is determined by the location of anodic to cathodic transition potential with respect to the E_{corr}. If the anodic to cathodic transition potential is nobler than Ecorr during the reverse scan, the passivation layer will be stable; whereas, if E_{corr} is nobler than the anodic to cathodic transition potential, the passivation film will be then unstable. [43]

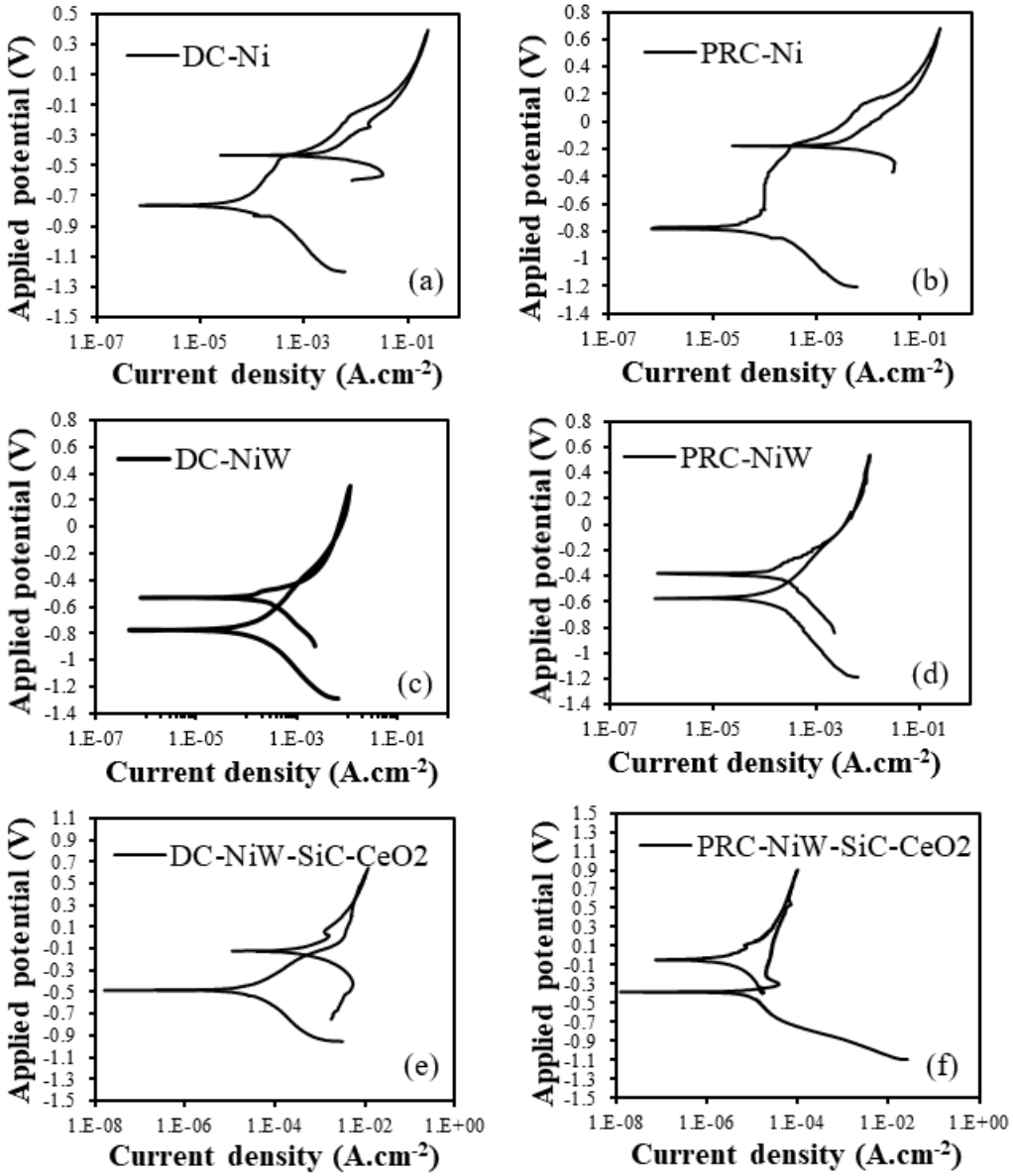

Figure 10.2 Cyclic potentiodynamic polarization (CPP) of (a) DC–Ni; (b) PRC–Ni; (c) DC–NiW; (d) PRC–NiW; (e) DC–NiW– SiC–CeO_2; and (f) PRC–NiW–SiC–CeO_2.

The corrosion potential values for DC and PRC deposited Ni, NiW, and NiW–SiC–CeO_2 extracted from Figure 10.2 are displayed in Figure 10.3. As it can be seen, PRC–NiW–SiC–CeO_2 demonstrated the more noble corrosion potential. It was also speculated that the difference in grain structures of coatings deposited by various current waveforms (DC and PRC), and outstanding corrosion properties of CeO_2, were mainly responsible for different corrosion behaviors.

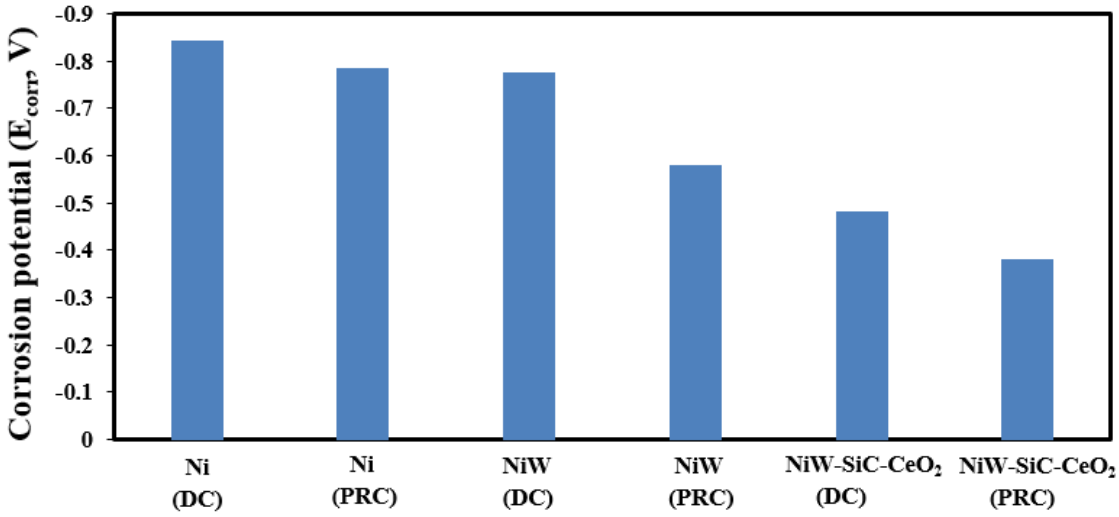

Figure 10.3 Comparison of DC–Ni, PRC–Ni, DC–NiW and, PRC–NiW coatings with respect to their corrosion potential.

10.3.1.2 Potentiodynamic polarization (PP)

Potentiodynamic polarization graphs of the electrodeposited DC–Ni, PRC–Ni, DC–NiW, PRC–NiW, DC–NiW–SiC–CeO_2, and PRC–NiW–SiC–CeO_2 are shown in Figure 10.4. The parameters of corrosion potential (Ecorr) and corrosion current density (I_{corr}) extracted from the polarization graphs in Figure 10.4 are demonstrated in Table 10.3 for all the deposits. As it can be seen, the corrosion resistance improves in the following order for deposits:

DC–Ni < PRC–Ni < DC–NiW < PRC–NiW < DC–NiW–SiC–CeO_2 < PRC–NiW–SiC–CeO_2.

Following the PP tests, the masking tapes were removed from DC and PRC electrodeposited Ni, NiW, and NiW–SiC–CeO_2 specimens and optical micrographs were taken from the surface of specimens. Figure 10.5a displays the schematic diagram of the specimen after masking the surface with tape and exposing 1 cm^2 unmasked surface area. Optical micrographs (Figure 10.5b) were taken from the surface of specimens after performing PP tests. As it can be seen, the DC and PRC Ni deposits were completely corroded and pulled off the surface, whereas the surface of DC and PRC PRC–NiW–SiC–CeO_2 displayed significantly small discoloration. There was a slight damage on the surface of DC and PRC NiW deposit after the PP test. The optical micrographs in Figure 10.5b are correlated to the PP test results as demonstrated in Figure 10.4.

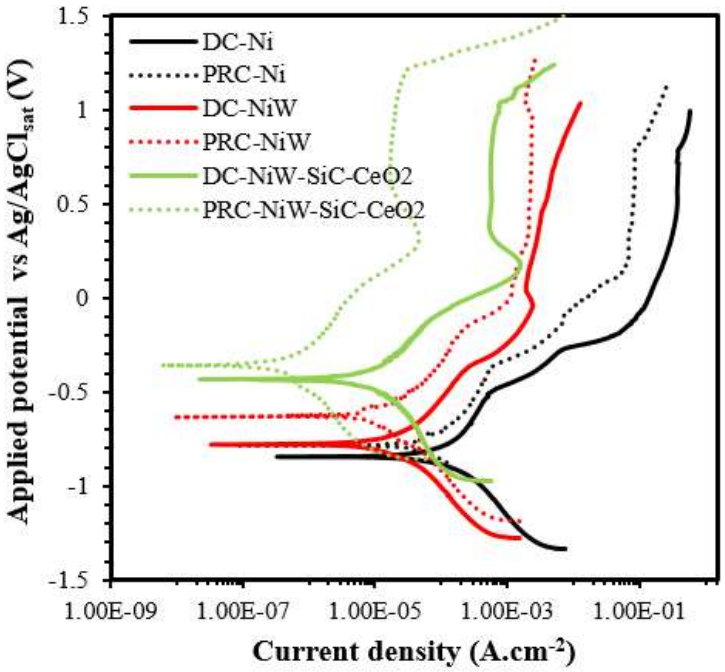

Figure 10.4 Potentiodynamic polarization (PP) of DC–Ni, PRC–Ni, DC–NiW, PRC–NiW, DC–NiW–SiC–CeO_2, and PRC–NiW–SiC–CeO_2.

Table 10.3 Corrosion potential and current density values extracted from potentiodynamic polarization graph.

Name of coatings	Corrosion potential (V)	Current density (A. cm^{-2})
DC–Ni	-0.85	8.05×10^{-5}
PRC–Ni	-0.79	6.21×10^{-5}
DC–NiW	-0.78	1.18×10^{-5}
PRC–NiW	-0.61	1.19×10^{-5}
DC–NiW–SiC–CeO_2	-0.48	1.02×10^{-5}
PRC–NiW–SiC–CeO_2	-0.40	5.34×10^{-7}

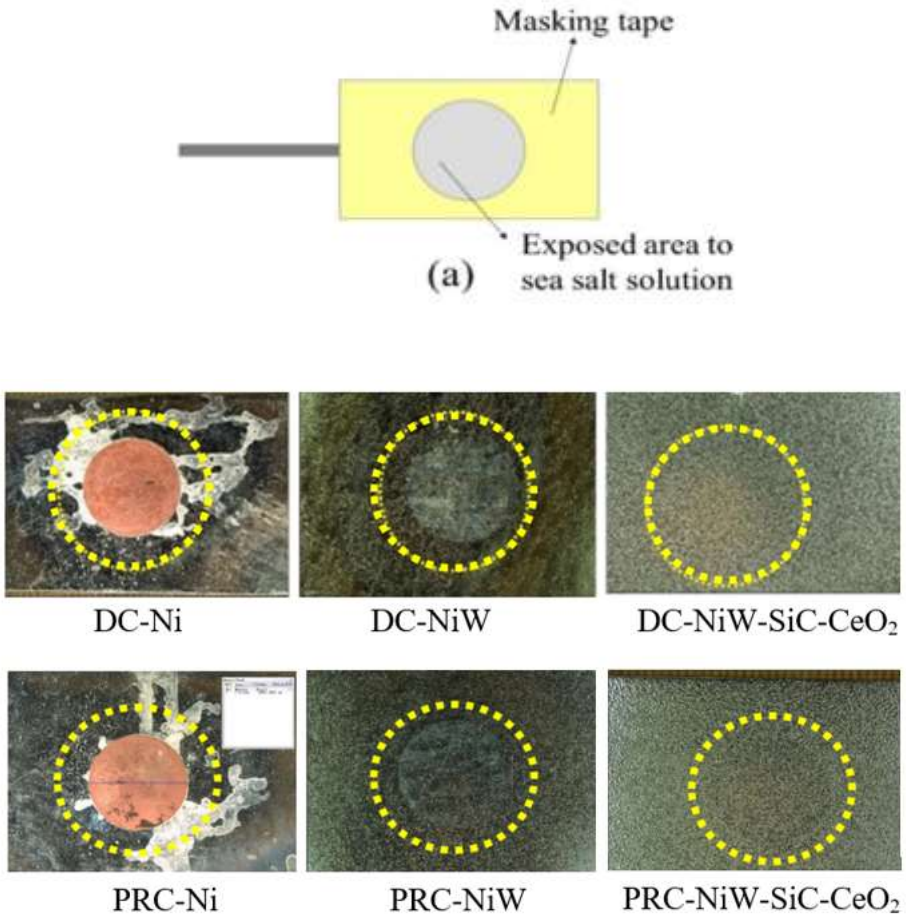

Figure 10.5 (a) schematic diagram of the specimen masked with 3M insulating tape with 1cm^2 exposed circular area; (b) Optical micrographs taken from the exposed area of various deposits after potentiodynamic polarization of the deposits in artificial sea salt solution;

10.3.2 SEM/EDS analysis

EDS spectra and map taken from different locations on the surface of the DC and PRC deposited NiW–CeO_2–SiC coatings suggest that Ni, W, Ce, O, Si, and C are the main elements present in the coatings (Figures 10.6 and 10.7). EDS mapping from the surface of the DC and PRC deposited coatings also revealed that the coatings were homogeneous and uniform which demonstrates that ceramic particles were successfully embedded into NiW alloy and evenly distributed in the coating, however it seems that the higher content of SiC and CeO_2 are embedded within NiW matric in PRC deposited coating than DC deposited sample.

NiW–CeO_2–SiC composite was DC and PRC electrodeposited from the NiW bath containing dispersed 20 g.L^{-1} CeO_2 and 20 g.L^{-1} SiC particles. The applied current density was 0.0405

A.cm^{-2} and the electrodeposition duration was 30 min for DC electrodeposition. In PRC, the forward current density of 0.15 A.cm^{-2}, reverse current density of 0.11 A.cm^{-2}, forward pulse duration of 16 ms, reverse pulse duration of 9 ms, and total time of 30 min were applied.

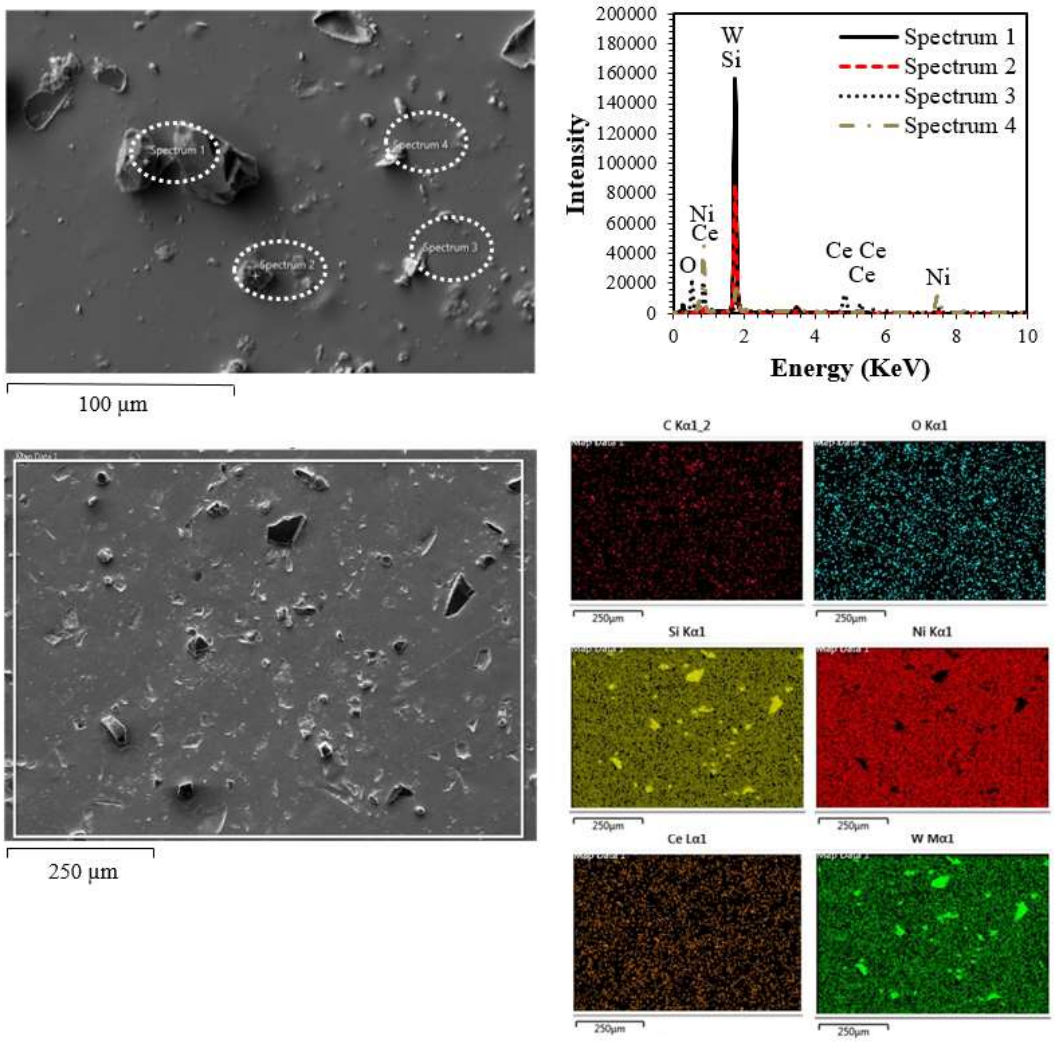

Figure 10.6 SEM micrograph and EDS mapping from the surface of electrodeposited DC–NiW–SiC–CeO_2 composite; The concentration of CeO_2 and SiC particles dispersed into the plating solution were 20 g.L^{-1} each and the duration of deposition was 30 min.

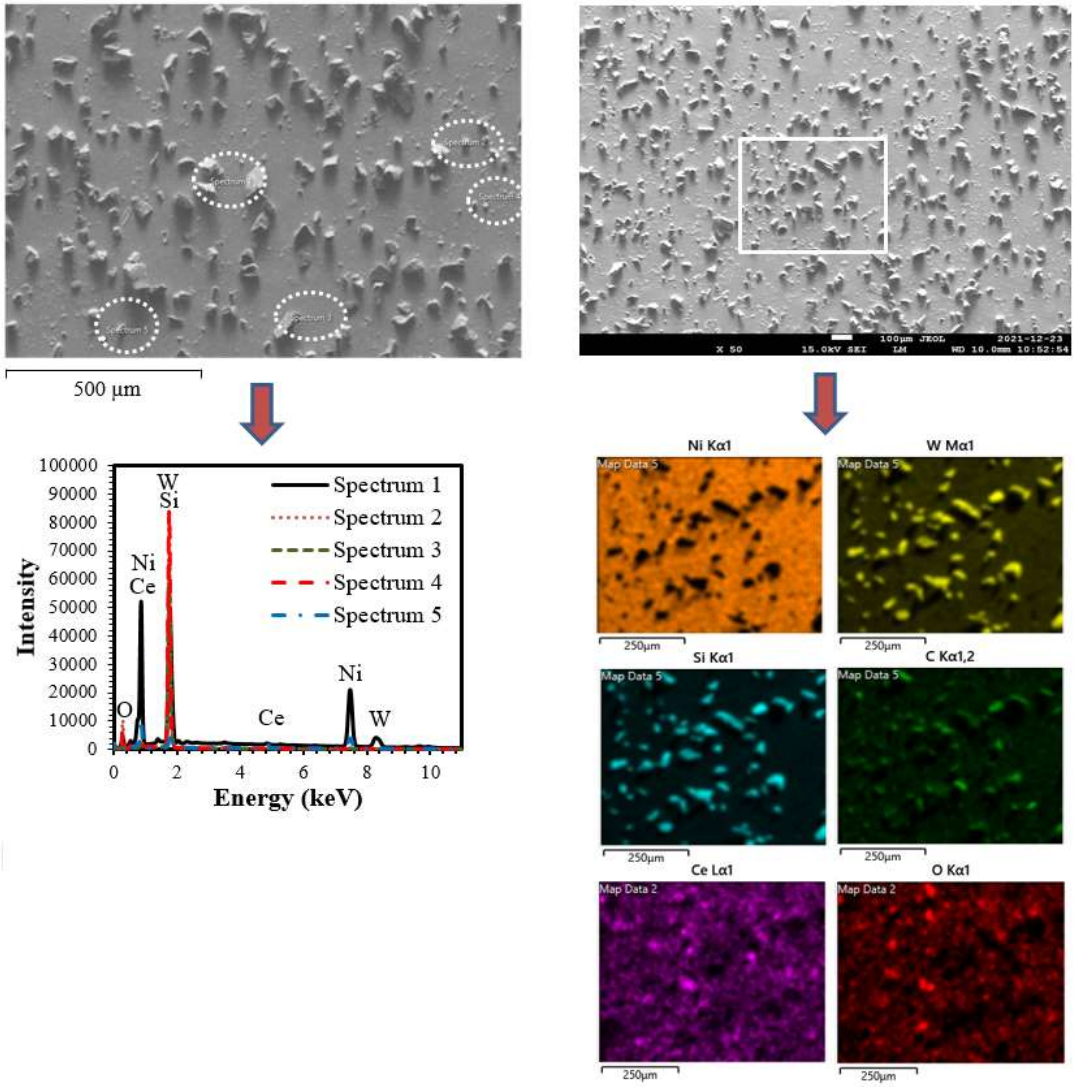

Figure 10.7 (a) EDS spectra and mapping taken from the surface of PRC–NiW–SiC–CeO_2 composite; concentration of SiC and CeO_2 in electrolyte was 20 $g.L^{-1}$; Current density: 0.0405 $A.cm^{-2}$; Duration of electrodeposition was 30 min.

EDS mapping results were collected from the cross–section of PRC coating as illustrated in Figure 10.8. The EDS–Mapping reveals uniform distribution of the CeO_2 and SiC particles in the whole cross–section area of the coating.

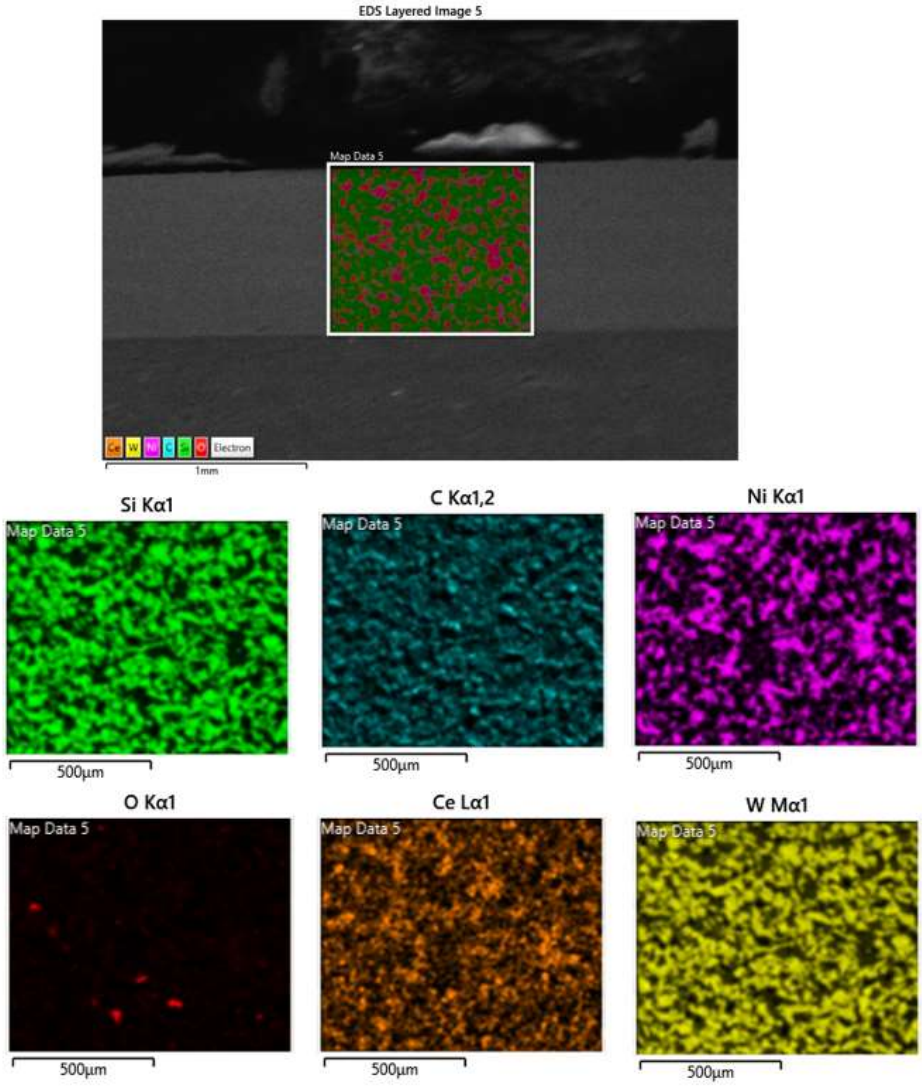

Figure 10.8 EDS mapping taken from the cross–section of PRC–NiW–SiC–CeO_2 composite; Reverse pulse waveform; I_f = 0.15 A.cm^{-2}; I_r = 0.11 A.cm^{-2}; t_f = 16 ms; t_r = 9 ms; and total time = 30 min. I_f = forward current density; I_r = reverse current density; t_f = forward pulse duration; t_r = reverse pulse duration.

10.3.3 Tribological analysis

Figure 10.9 displays the variation in the average coefficient of friction for DC and PRC deposited Ni, NiW, and NiW–SiC–CeO_2 electrodeposited materials on brass substrate using pin–on–disc wear testing equipment. As it can be seen, the DC and PRC–NiW–SiC–CeO_2 demonstrated a lower coefficient of friction (0.2) compared to the DC–NiW (0.1), PRC–NiW (0.4), DC–NiW deposits (0.5), DC–Ni (0.7), and PRC–Ni (0.6). The low friction coefficient of

the DC and PRC–NiW–SiC–CeO_2 coatings compared to the DC and PRC deposited Ni and NiW can be attributed to reduction of the contact between the Al_2O_3 ball and the coating. Ahmadiyeh et al. [45] also studied the corrosion and wear performance of pulse plated Ni–W–B/SiC composite coatings. They found that the main reason for improving the corrosion resiatnce and wear performance of the composite coating was attributed to the dense structure of the coating with higher amounts and uniform distribution of SiC particles.

The low friction coefficient of the DC and PRC deposited NiW compared to Ni could be associated with the solid solution strengthening mechanism by tungsten of nickel matrix. As well, the formation of stable nickel oxide and tungsten oxide layer during the reverse pulse on the coating surface will effectively reduce the contact between the sliding surfaces. Figure 10.10 displays the wear volume rate of each coating after the friction test.

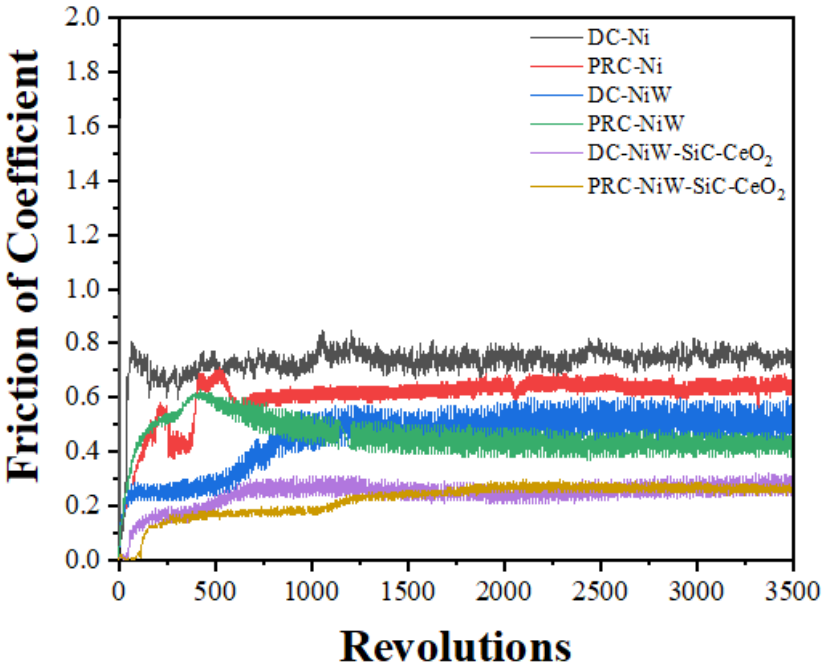

Figure 10.9 Coefficient of friction for the DC and PRC deposited Ni, NiW, NiW–SiC–CeO_2 electrodeposited from an optimized electrolyte on the brass substrate for 3500 revolutions at room temperature and normal applied load of 1 N.

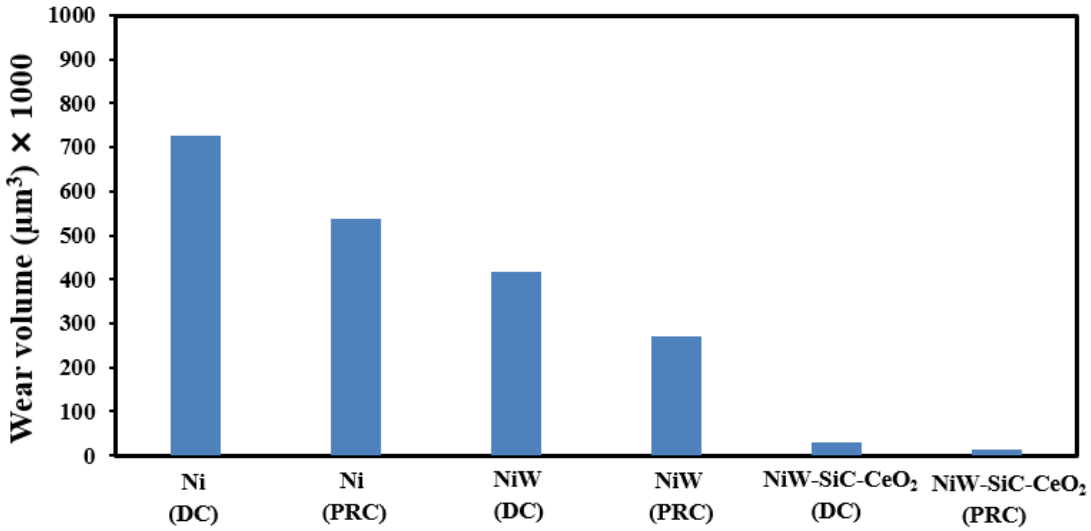

Figure 10.10 Wear volume for the DC and PRC deposited Ni, NiW, and NiW–SiC–CeO_2 electrodeposited coatings.

10.3.4 XRD analysis

XRD (Figure 10.11) patterns were taken from the surfaces of as–deposited and heat–treated DC and PRC electrodeposited NiW–SiC–CeO_2 at 350°C and 500°C on brass substrates. Coating produced by DC and PRC method contained the peaks of Ni (111), SiC (113), SiC (311), SiC (220), and CeO_2 (220). As well, some additional peaks of Ni (200), Ni (220), Ni (222), CeO_2 (111), and CeO_2 (200) were appeared on XRD pattern of the coating produced by PRC method. It was also observed that the peak intensity of the heat–treated DC and PRC deposited coatings were higher than that of the as–deposited coating, and hence the crystallite size increased with increase of the annealing temperature (Table 10.4) which was possibly attributed to FCC crystal grain growth, and reduction in internal micro–strains. Furthermore, the crystallite size of the coatings produced by PRC method were smaller than that of the coatings deposited by DC method. This was due to the grain refinement and promotion of the grain nucleation on the surface by applying the high instantaneous current density during the PRC electrodeposition. It is noteworthy to mention that, the coatings with refined grain structure tend to decrease the adsorption rate of chloride ions on the surface due to formation of highly compact, stable, and well–adherent passive films. This will significantly enhance the anti–corrosion and tribological performance of the coatings.

The crystallites size of the coatings were calculated (Table 10.4) from the broadening of the (111) peaks using Scherrer equation. [45–47]

$D = K\lambda/\beta\cos\theta$ (1)

Where D is the crystallite size (nm), K is the Scherrer constant (0.9), λ is the wavelength of the x–ray source (0.15406 nm), β is the FWHM (radians), and θ is the peak position (radians).

As it is displayed in Figure 10.11, no peaks of W can be observed in XRD spectra. This can be attributed to formation of single–phase solid solutions (W in Ni) with face–centered cubic (F.C.C) structure as a result of partial replacement of Ni by W atoms. Replacement of Ni by W atoms also resulted in broadening of the peaks and decrease in average crystallite size due to lattice distortion and decrease of the Ni content of the coating. [45–47]

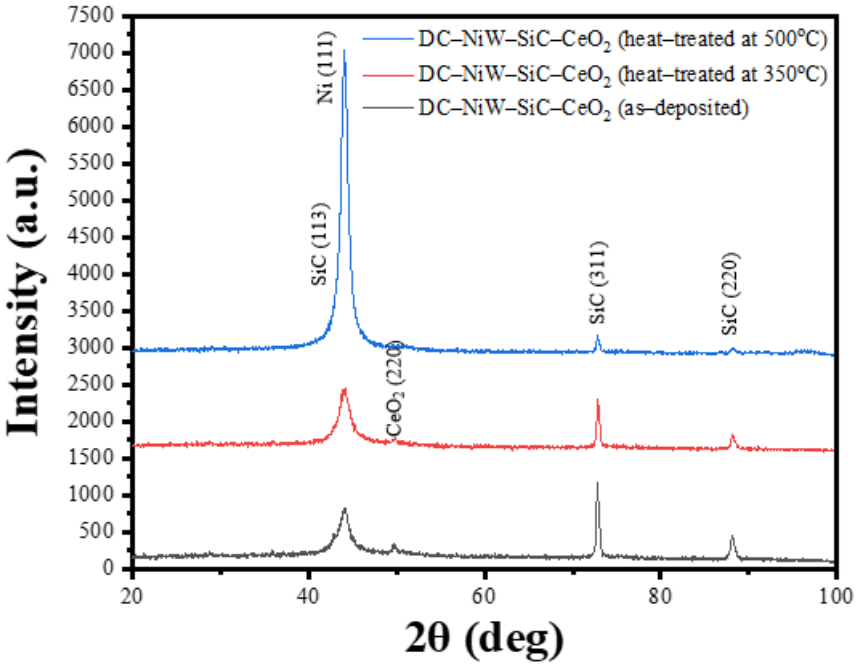

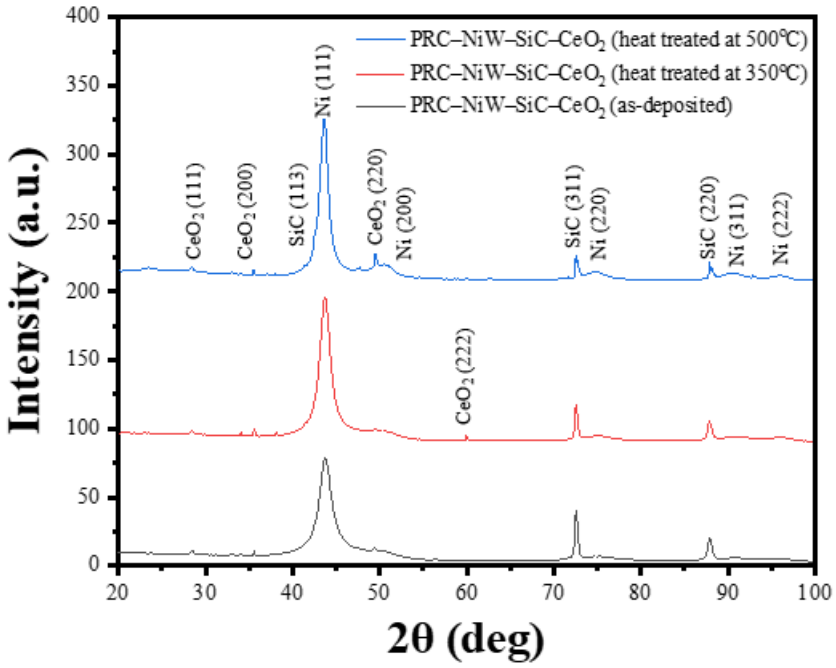

Figure 10.11 XRD spectra from the surface of DC and PRC electrodeposited NiW–SiC–CeO_2 (as–deposited and heat–treated at 350°C and 500°C).

Table 10.4 Crystallite sizes of DC and PRC deposited NiW–SiC–CeO_2

Name of coatings	**Peak position of (111) [°2Th]**	**FWHM [°2Th]**	**Crystallite size [Å]**
DC–NiW–SiC–CeO_2 (as–deposited)	44.121	0.709	122
DC–NiW–SiC–CeO_2 (heat–treated at 350°C)	43.890	0.709	122
DC–NiW–SiC–CeO_2 (heat–treated at 500°C)	44.100	0.433	202
PRC–NiW–SiC–CeO_2 (as–deposited)	43.746	1.578	53.7
PRC–NiW–SiC–CeO_2 (heat–treated at 350°C)	43.713	1.303	65

10.4. Conclusion

Incorporation of CeO_2 and SiC ceramic particles within the NiW matrix along with applying the PRC waveform to the electrodposition bath, enhanced the corrosion performance of the

NiW coating. Several sets of experiments were performed to investigate the corrosion performance of the NiW coatings reinforced with CeO_2 and SiC ceramic particles. It was observed that, the coatings prepared using PRC, exhibited outstanding corrosion resistance when exposed to corrosive liquid compared to that of DC waveform. It was also revealed that reinforcement of CeO_2 within NiW–SiC significantly improved the corrosion performance of the coating and PRC–NiW–SiC–CeO_2 exhibited the highest corrosion performance compared to DC deposited Ni, NiW, NiW–SiC, DC–NiW–SiC–CeO_2 and PRC deposited Ni, NiW, NiW–SiC. According to pp test results, the corrosion resistance improves in the following order for deposits:

DC–Ni < PRC–Ni < DC–NiW < PRC–NiW < DC–NiW–SiC–CeO_2 < PRC–NiW–SiC–CeO_2.

Following the PP tests, the optical micrographs were taken from the corroded surfaces of the DC–Ni, DC–NiW, DC–NiW–SiC–CeO_2 and PRC–Ni, PRC–NiW, PRC–NiW–SiC–CeO_2 and it was found that DC–Ni deposit was completely corroded and pulled off the surface, whereas the surface of DC and PRC–NiW showed significantly small discoloration. The surface of DC deposited NiW–SiC–CeO_2 and PRC deposited NiW–SiC–CeO_2 deposit were remained almost unaffected after the PP test.

The XRD results obtained from the surfaces of the as–deposited and annealed DC and PRC–NiW–SiC–CeO_2 at 350^{o}C and 500^{o}C also revealed that the intensity of the peaks and the average crystallite size increased with increase of the annealing temperature up to 500^{o}C. As well, coatings produced by PRC had finer crystallite size compared to those that were produced by DC method.

10.5. References

[1] R. An-hua, "Effect of Current Density on the Properties of Ni–CeO_2 Composite Coatings prepared using Magnetic Field-Assisted Jet Electrodeposition," 2021, ArticleID:210658.

[2] S. Guo, L. Wang, Y. Jin, N. Piao, Z. Chen, G. Tian, J. Li, C. Zhao, and X. He, "A polymeric composite protective layer for stable Li metal anodes," vol. 7, no. 1, p. 21, Jun 15 2020. [En ligne]. Disponible: https://www.ncbi.nlm.nih.gov/pubmed/32542452

[3] J. Cao, L. Wang, X. He, M. Fang, J. Gao, J. Li, L. Deng, H. Chen, G. Tian, J. Wang, and S. Fan, "In situ prepared nano-crystalline TiO_2–poly (methyl methacrylate) hybrid enhanced composite polymer electrolyte for Li-ion batteries," vol. 1, no. 19, p. 5955-5961, 2013.

[4] Y. Yao, H. Dong, L. Jiao, N. Yu, and L. He, "Preparation and electrocatalytic property of PbO_2-CeO_2 nanocomposite electrodes by pulse reverse electrodeposition methods," vol. 163, no. 5, p. D179, 2016.

[5] Y. Y. Xu, Y. J. Xue, F. Yang, C. Y. Liu, and J. S. Li, "Preparation of Ni-ZrO_2-CeO_2 Nanocomposite Coatings by Pulse Electrodeposition," communication présentée à Applied Mechanics and Materials, 2013, p. 174-178.

[6] L. Wang, S. Xing, H. Liu, C. Jiang, and V. Ji, "Improved wear properties of NiTi nanocomposite coating with tailored spatial microstructures by extra adding CeO_2 nanoparticles," vol. 399, p. 126119, 2020.

[7] S. Uhm, Y. Yi, and J. Lee, "Electrocatalytic activity of Pd–CeO_2 nanobundle in an alkaline ethanol oxidation," vol. 138, no. 1, p. 46-49, 2010.

[8] X. Zhou, and Y. Shen, "A comparative study of pure nickel and the Ni–CeO_2 nanocrystalline coatings: microstructural evolution, oxidation behavior, and thermodynamic stability," vol. 49, no. 10, p. 3755-3774, 2014.

[9] T. Chen, D. Liu, F. Wu, and H. Wang, "Effect of CeO_2 on microstructure and wear resistance of TiC bioinert coatings on $Ti6Al_4V$ alloy by laser cladding," vol. 11, no. 1, p. 58, 2017.

[10] Z. Zhang, "Influence of Particle Concentration on the Elemental Penetration Region and Properties of Ni-P-SiC Composite Coatings Prepared through Sandblasting and Scanning Electrodeposition on 45 Steel Surfaces," vol. 11, no. 10, p. 1237, 2021.

[11] Aghaie, E, Najafi, A, Maleki-Ghaleh, H and Mohebi, H, "Effect of SiC concentration in electrolyte on Ni–SiC composite coating properties," vol. 29, no. 3, p. 177-182, 2013.

[12] R. Arghavanian, N. P. Ahmadi, S. Yazdani, and B. Bostani, "Investigations on corrosion proceeding path and EIS of Ni–ZrO_2 composite coating," vol. 28, no. 7, p. 508-512, 2012.

[13] M. Sokić, Ž. Kamberović, V. Nikolić, B. Marković, M. Korać, Z. Anđić, and M. Gavrilovski, "Kinetics of NiO and $NiCl_2$ hydrogen reduction as precursors and properties of produced Ni/Al_2O_3 and Ni-Pd/Al_2O_3 catalysts," vol. 2015, 2015.

[14] Y. Bai, Z. Wang, X. Li, G. Huang, C. Li, and Y. Li, "Microstructure and mechanical properties of Zn-Ni-Al_2O_3 composite coatings," vol. 11, no. 5, p. 853, 2018.

[15] A. A. Kasach, D. S. Kharytonau, A. V. Paspelau, J. Ryl, D. S. Sergievich, I. M. Zharskii, and I. I. Kurilo, "Effect of TiO_2 Concentration on Microstructure and Properties of Composite Cu–Sn–TiO_2 Coatings Obtained by Electrodeposition," vol. 14, no. 20, p. 6179, 2021.

[16] B. Łosiewicz, A. Stępień, D. Gierlotka, and A. Budniok, "Composite layers in Ni–P system containing TiO_2 and PTFE," vol. 349, no. 1-2, p. 43-50, 1999.

[17] J. Yu, Y. Wang, X. Zhao, Q. Li, Q. Qiao, J. Zhao, and S. Zhai, "Wear resistance of ni-based alloy coatings," vol. 2019, 2019.

[19] L. Jun, W. Yiyong, W. Dianlong, and H. Xinguo, "The microstructure and wear resistance characteristics of electroformed nickel and partially stabilized zirconia composite coatings," vol. 35, no. 7, p. 1751-1758, 2000.

[20] Aghaie, E, Najafi, A, Maleki-Ghaleh, H and Mohebi, H, "Effect of SiC concentration in electrolyte on Ni–SiC composite coating properties," vol. 29, no. 3, p. 177-182, 2013.

[21] A. Angelastro, S. L. Campanelli, G. Casalino, and A. D. Ludovico, "Optimization of Ni-based WC/Co/Cr composite coatings produced by multilayer laser cladding," vol. 2013, 2013.

[22] E. Pavlatou, M. Stroumbouli, P. Gyftou, and N. Spyrellis, "Hardening effect induced by incorporation of SiC particles in nickel electrodeposits," vol. 36, no. 4, p. 385-394, 2006.

[23] P. Narasimman, M. Pushpavanam, and V. Periasamy, "Synthesis, characterization and comparison of sediment electro-codeposited nickel–micro and nano SiC composites," vol. 258, no. 1, p. 590-598, 2011.

[24] S. Pinate, P. Leisner, and C. Zanella, "Wear resistance and self-lubrication of electrodeposited Ni-SiC: MoS_2 mixed particles composite coatings," vol. 421, p. 127400, 2021.

[25] S. Aruna, V. W. Grips, and K. Rajam, "Ni-based electrodeposited composite coating exhibiting improved microhardness, corrosion and wear resistance properties," vol. 468, no. 1-2, p. 546-552, 2009.

[26] P. Gyftou, M. Stroumbouli, E. Pavlatou, and N. Spyrellis, "Electrodeposition of Ni/SiC composites by pulse electrolysis," vol. 80, no. 3, p. 88-91, 2002.

[27] G. Gyawali, B. Joshi, K. Tripathi, S. H. Kim, and S. Wohn Lee, "Effect of microtexturing on tribological performance of Ni/Ni–SiC composite coatings," vol. 31, no. 9, p. 701-707, 2015.

[28] L. Lai, H. Li, Y. Sun, G. Ding, H. Wang, and Z. Yang, "Investigation of Electrodeposition External Conditions on Morphology and Texture of Ni/SiC w Composite Coatings," vol. 9, no. 18, p. 3824, 2019.

[29] M. Vaezi, S. Sadrnezhaad, and L. Nikzad, "Electrodeposition of Ni–SiC nano-composite coatings and evaluation of wear and corrosion resistance and electroplating characteristics," vol. 315, no. 1-3, p. 176-182, 2008.

[30] F. Kılıç, H. Gül, S. Aslan, A. Alp, and H. Akbulut, "Effect of CTAB concentration in the electrolyte on the tribological properties of nanoparticle SiC reinforced Ni metal matrix composite (MMC) coatings produced by electrodeposition," vol. 419, p. 53-60, 2013.

[31] P. Jin, C. Sun, C. Zhou, L. Shi, and C. Liu, "Effect of SiC particle size on structures and properties of Ni–SiC nanocomposites deposited by magnetic pulse electrodeposition technology," vol. 45, no. 16, p. 20155-20164, 2019.

[32] Y. Yao, S. Yao, L. Zhang, and H. Wang, "Electrodeposition and mechanical and corrosion resistance properties of Ni–W/SiC nanocomposite coatings," vol. 61, no. 1, p. 67-70, 2007.

[33] H. Wang, H. Liu, Y. He, C. Ma, and L. Li, "Ni-SiC composite coatings with good wear and corrosion resistance synthesized via ultrasonic electrodeposition," vol. 30, no. 2, p. 1535-1544, 2021.

[34] K. C. Chan, C. Wang, K. Zhang, and G. Pang, "Superplastic deformation behavior of the electrocodeposited Ni/SiC composite," vol. 51, no. 6, p. 605-609, 2004.

[35] C. W. Su, L. Zhao, Y. Bai, L. Tian, B. Wen, and J. Guo, "Microhardness improvement of Ni-W/SiC composite coatings by high frequency induction heat treatment," vol. 166, no. 8, p. D301, 2019.

[36] R. Chebolu, R. Nallu, and R. Chanamala, "Experimental investigation on mechanical behavior of as cast Zn-Al-Cu/SiC/TiB_2 hybrid metal matrix composite by ultrasonic assisted stir casting technique," 2022.

[37] M. Allahyarzadeh, M. Aliofkhazraei, A. Sabour Rouhaghdam, and V. Torabinejad, "Functionally graded nickel–tungsten coating: electrodeposition, corrosion and wear behaviour," vol. 55, no. 3, p. 303-311, 2016.

[38] N. P. Wasekar, S. M. Latha, M. Ramakrishna, D. S. Rao, and G. Sundararajan, "Pulsed electrodeposition and mechanical properties of Ni-W/SiC nano-composite coatings," vol. 112, p. 140-150, 2016, 140.

[39] Y. Wang, M. Yu, H. Luo, Q. Qiao, Z. Xiao, Y. Zhao, L. Zhao, H. Sun, Z. Xu, K. Matsugi, and J. Yu, "Effect of saccharin on the structure and properties of electrodeposition NiWP alloy coatings," vol. 25, no. 10, p. 4402-4407, 2016.

[40] J. C. Cameron, "Acetylenic compositions and nickel plating baths containing same," éd: Google Patents, 1983.

[41] O. A. Rahman, N. P. Wasekar, G. Sundararajan, and A. K. Keshri, "Experimental investigation of grain boundaries misorientations and nano twinning induced strengthening on addition of silicon carbide in pulse electrodeposited nickel tungsten composite coating," vol. 116, p. 1-7, 2016.

[42] S. Sangeetha, G. P. Kalaignan et J. T. Anthuvan, "Pulse electrodeposition of self-lubricating Ni–W/PTFE nanocomposite coatings on mild steel surface," vol. 359, p. 412-419, 2015.

[43] L. Feng, Y. Y. Ren, Y. h. Zhang, S. Wang, and L. Li, "Direct correlations among the grain size, texture, and indentation behavior of nanocrystalline nickel coatings," vol. 9, no. 2, p. 188, 2019.

[44] B. Li, Y. Huan, H. Luo, and W. Zhang, "Electrodeposition and properties of Ni–B/SiC nanocomposite coatings," vol. 35, no. 2, p. 109-119, 2019.

[45] S. Ahmadiyeh, A. Rasooli, M.G. Hosseini, A. Farhood, "Superior corrosion and wear resistance of pulse plated Ni–W–B/SiC composite coatings," vol. 270, p. 124761, 2021.

[46] K. R. Sriraman, S. Ganesh Sundara Raman, and S. K. Seshadri, "Corrosion behaviour of electrodeposited nanocrystalline Ni–W and Ni–Fe–W alloys," vol. 460-461, p. 39-45, 2007, 39.

[47] Y. Yang, Y. Zhang, Y. Zhang, B. Yan, and F. Mo, "Corrosion properties of ultrasonic electrodeposited nanocrystalline and amorphous patterned Ni–W alloy coatings," vol. 27, no. 19, p. 1341007, 2013.

CHAPTER 11 ARTICLE 6: SYNTHESIS AND CHARACTERIZATION OF NOVEL NIW–CEO_2 COMPOSITE COATING WITH ENHANCED CORROSION AND WEAR RESISTANCE

Authors: Mina Dadvand, Oumarou Savadogo

Article published: Journal of Coatings, 21 June 2022

DOI: https://doi.org/10.3390/coatings12070878

Abstract

Compact and uniform NiW composite coatings filled with ceramic particles such as CeO_2 were electrodeposited on brass substrates using direct current (DC) and a well–designed pulse reverse current waveforms (PRC). PRC coatings exhibited the noblest corrosion potential and lowest current density compared to DC electrodeposited coatings. Among all PRC coatings, PRC–NiW–CeO_2 demonstrated the highest corrosion potential (-4.72×10^{-1} V) and the lowest current density (5.32×10^{-6} V). It also seems that addition of CeO_2 particles to NiW matrix enhanced the wear resistance of the coatings and the lowest wear volume of (133.10×10^{3} μm^3) and the friction coefficient of 0.25 were obtained due to the formation of the uniform, void free and compact structures with high content of CeO_2 particles in the coating.

Keywords: Nickel–tungsten coating, pulsed reverse current electrodeposition, direct current electrodeposition, friction coefficient, corrosion and wear resistance.

11.1 Introduction

In recent years, metal matrix composites (MMCs) with an excellent performance, have been widely used in aerospace, automotive, and electronics applications. These materials are prepared by adding various reinforcing phases [1–3]. Among MMCs, nickel–based alloys have been widely used in different industrial applications due to their outstanding performance and low cost [1]. Among various fabrication techniques, electrodeposition is one of the most common method of producing various metal matrix coatings [1–7]. The reinforcing phases (insoluble materials) are suspended in a conventional electrodeposition bath and co–deposited within the metal matrix during the electrodeposition process. These insoluble components can be in the form of powder, fiber or encapsulated particles. Electrodeposition of various Ni based composites have been reported in which one or more of various metallic oxides such as CeO_2, ZrO_2, Al_2O_3, TiO_2, MoO_2 and carbides such as SiC were added into Ni based electrodeposition baths [1–17]. Substantial improvements in material properties such as microhardness, wear, and corrosion resistance as a result of co–deposition of reinforcements phase(s) into Ni matrix [18–19]. The degree of improvements in the properties depends on various factors such as the type and content of the reinforcements particles as well as their uniformity in distribution within the Ni based matrix, electrodeposition parameters such as operating temperature, agitation modes, applied current density, plating duration, and electrolyte formulation (i.e., type and concentration of ingredients). [1–20]

Among various metal oxides reinforcement particles, CeO_2 can be attractive due to its special physical and chemical characteristics. CeO_2 particles have been used as fillers for fabricating of polytetrafluoroethylene–based composites where the tribological properties of the fabricated composites were improved significantly at high temperatures. [21–23] Co–deposition of CeO_2 particles with Ni have been reported in few articles. It was found that the addition of cerium oxide particles into Ni matrix enhances hardness, wear and oxidation resistance of the matrix [1, 4–6]. However, inclusion of cerium oxide particles within Ni matrix is required to be dispersed uniformly without agglomeration. Therefore, electrodeposition parameters including applied current density and operating temperature as well as plating electrolyte need to be well–designed and optimized [1, 7]. Zhou et al. [8] reported that well dispersion of CeO_2 in Ni matrix enhances mechanical, wear and corrosion properties of the Ni–CeO_2 coating compared to bare Ni. They attributed the enhancement to grain refining effect of CeO_2 on Ni matrix and formation of passivation layer on the surface [8]. The properties of electrodeposited Ni–based composites can be further improved through alloying with other transition metals such as tungsten (W)

[24–30]. To the best of our knowledge, there is no research activities reported on electrodeposition of NiW–CeO_2 composites and investigation on their microstructure and properties.

In this research work, NiW–CeO_2 deposit was fabricated by using DC and PRC process through applying a unique pulsed reverse current waveform on electrodeposition bath chemistry containing specially selected ingredients. It was found that the incorporating of CeO_2 ceramic particles within NiW matrix enhanced the corrosion and wear performance of the deposit and PRC–NiW–CeO_2 possessed superior corrosion and wear performance compared to the DC and PRC electrodeposited Ni and NiW coatings.

11.2 Methodology

11.2.1 Electrolyte components

The Ni electrodeposition bath was composed of nickel sulfate ($NiSO_4.6H_2O$), citric acid, *o*–Benzoic sulfimide (sodium saccharin, $C_7H_5NO_3S$), propargyl–oxopropane–2,3–dihydroxy, and DuPont Capstone Fluorosurfactant F–63. NiW electrodeposition electrolyte was prepared by adding sodium tungstate dehydrate ($Na_2WO_4.2H_2O$) as a source of tungstate ions into the same electrodeposition bath that was used for electrodeposition of Ni. And finally, NiW–CeO_2 bath was made by adding CeO_2 particles and a dispersant agent such as polyethyleneimine into NiW plating solution. Table 11.1 displays the ingredients of the bath chemistry as well as the optimized experimental parameters to obtain uniform and void–free NiW coating with desired mechanical and tribological performance.

Table 11.1 Electrodeposition bath ingredients and optimized experimental parameters

Name of chemicals	**Concentration**
Nickel sulfate	29.5–30 ($g.L^{-1}$)
Sodium tungstate	58–60 ($g.L^{-1}$)
Citric acid	63–67 ($g.L^{-1}$)
Ammonia	58 ($ml.L^{-1}$)
Sulfuric acid	as needed
Propargyl–oxo–propane–2,3–dihydroxy (POPDH)	0.9–1 ($g.L^{-1}$)
DuPont™ Capstone® Fluoro–surfactant FS–63	1.8–2 ($g.L^{-1}$)
Sodium saccharin	0.5–1 ($g.L^{-1}$)
Experimental parameters	
pH	7.8–8.0
Temperature	58–61 ºC
Duration of electrodeposition	30 min

In this formulation, to prevent direct interaction between nickel and tungstate ions, citric acid is used to form stable complexes with tungstate (WO_2^{+4}) and nickel (Ni^{2+}) ions. Such direct interaction would result in formation of non–soluble nickel tungstate compound in electrodeposition bath [31, 32]. Sodium saccharin was used to decrease the internal stress within the coating [33]. We used propargyl–oxo–propane–2, 3–dihydroxy as a brightener and grain refiner to control the Ni ion diffusion towards the cathode. This type of compound is a specific type of propargyl derivative containing a carbon–carbon triple bond (i.e. –C≡C–H) at the end of its molecular chain which has a tendency to deposit preferentially at high current density areas (sharp areas) on the substrate during electrodeposition. Therefore, a uniform, mirror–finish surface and crack–free deposit was obtained [34]. Finally, Capstone fluoro–surfactant FS–63 (DuPont) which is a low foaming type anionic fluoro–surfactant was utilized as a wetting agent to remove hydrogen gas bubbles from the substrate surface and to reduce the surface tensions. [35]

11.2.2 Substrate preparation

The surface of brass substrates were degreased, activated, and rinsed prior to electrodeposition process followed by immersion into 50 $g.L^{-1}$ alkaline soap solution (TEC1001; Technic Inc,

Rhode Island, USA) at temperature of about 50ºC for approximately 1 min. Then the substartes were rinsed with deionized (DI) water and activated by immersing into dilute sulfuric acid (10% v/v) at room temperature for about 10 sec followed by rinsing with DI water. Water break test was performed to evaluate the cleanliness of the substrates. In this testing protocol, the brass substrates were gently rinsed with DI water following the final rinse step. The substrates were considered clean if the water completely wets the surface.

11.2.3 Electrodeposition setup

The electrodeposition bath setup is displayed in Figure 11.1 The electrodeposition setup was composed of an electrodeposition tank containing electrolyte, a filter pump (Flo King Filter System Inc.) to provide adequate agitation, two anodes made of stainless steel mesh, a cathode made of brass as a substrate being electrodeposited, and a reversed pulse plating power supply (Model pe8005, Plating Electronic GmbH, Sexau, Berlin, Germany). The electrodeposition bath was placed inside a water circulating bath operating at 60ºC temperature.

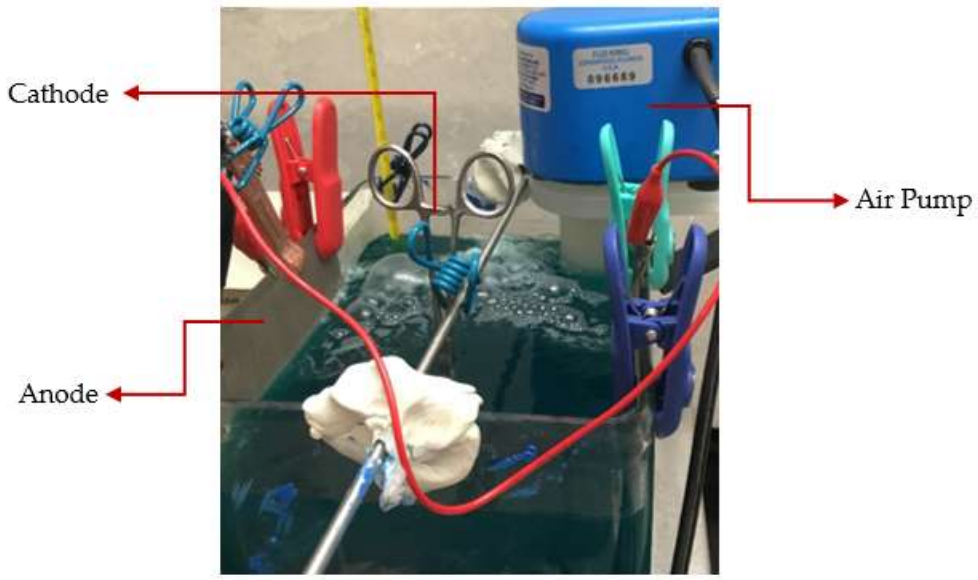

(a)

Figure 11.1 Schematic diagram of electrodeposition setup

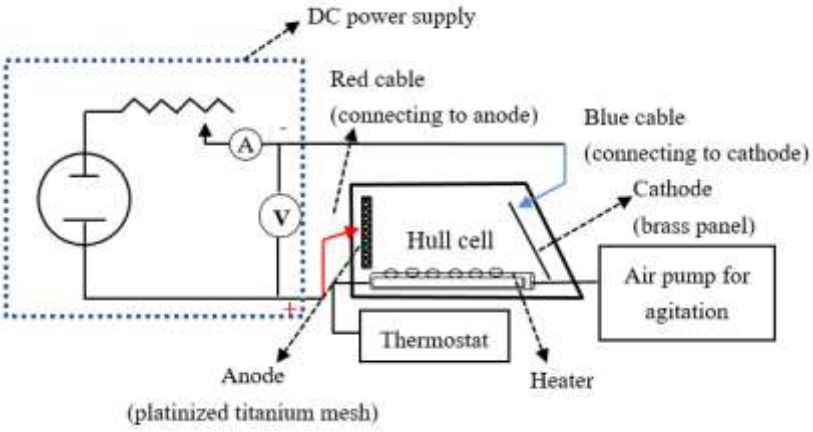

Figure 11.2 Schematic diagram of hull cell equipped with thermostat and air agitation.

A Hull cell (Figure 11.2) equipped with heater, thermostat air agitation and air pump was used to perform the initial electrodeposition experiments to characterize and improve the current density distribution throughout the substrate surface. A brass substrate was used as cathode and a platinized titanium mesh sheet was used as anode.

11.2.4 Optimization of PRC waveform

The PRC current waveform was designed with regards to its forward and reverse current densities (I_f and I_r) and pulse durations (t_f and t_r). The schematic diagram of the applied PRC waveform is displayed in Figure 11.3.

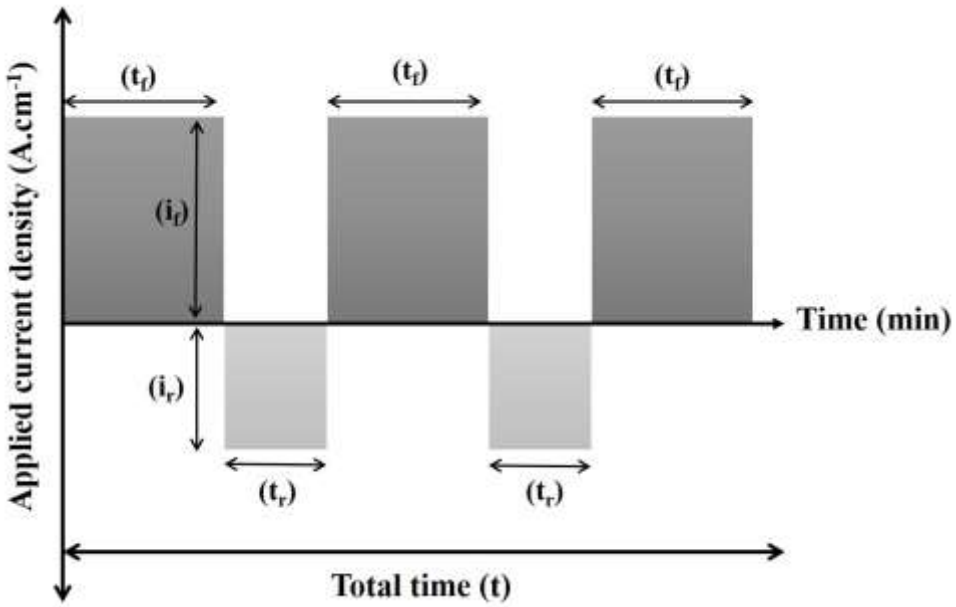

Figure 11.3 Reverse pulse waveform; i_f = 0.15 A.cm^{-2}; i_r = 0.11 A.cm^{-2}; t_f = 16 ms; t_r = 9 ms; and total time = 30 min. i_f = forward current density; i_r = reverse current density; t_f = forward pulse duration; t_r = reverse pulse duration.

11.2.5 Characterization of deposits

The tungsten content, surface morphology of the deposits, and grain size were characterized by energy dispersive spectroscopy (EDS), scanning electron microscopy (SEM, Joel 7600 TFE), and X–ray diffraction (XRD, Bruker D8 Advance) respectively.

Potentiostat (Princeton Applied Research Potentiostat/Galvanostat Model 273A) was used to investigate the corrosion behavior of the deposits. The potentiostat was equipped with CorrWare software enabling to apply potential scans remotely through the software. Potentiodynamic polarization (PP) scans were performed from -0.6 to 1.0 V vs. Ecorr at room temperature and 5 mV.s^{-1} scan rate. For all the PP experiments, silver/silver sulfate electrode and graphite rod were used as reference and counter electrodes, respectively. The surface of the substrate was covered with an insulating 3M tape to expose 1 cm^2 of the surface to corrosive media (artificial sea water). Table 11.2 displays the composition of the artificial sea water.

Table 11.2 Composition of Artificial Sea Water

Ingredients	**Concentrations (wt%)**
NaCl	58.49
Na_2SO_4	9.75
$CaCl_2$	2.765
KCl	1.645
$NaHCO_3$	0.477
KBr	0.238
H_3BO_3	0.071
$SrCl_2.6H_2O$	0.095
NaF	0.007
$MgCl_2$	26.46

Pin–on–disk (Custom–built) and Profilometer (Bruker Dektak XT) were performed to measure the coefficient of friction and wear volume of removed material. The tests were performed under dry air conditions and ambient temperature. Spherical Al_2O_3 steel balls with a diameter of 4.7 mm were used for the friction test. The sliding velocity and the number of revolutions were 180 mm/s and 3500, respectively. For all of the experiments, the applied load was 1N. The coefficients of friction were continuously recorded with respect to the number of revolutions. Each friction experiment was repeated three times and the average results were obtained.

11.3 Results and discussion

11.3.1. Corrosion analysis

11.3.1.1 Cyclic potentiodynamic polarization (CPP)

Figure 11.4 displays the CPP graphs for DC and PRC electrodeposited Ni, NiW, and NiW–CeO_2 coatings. As it can be observed, in anodic polarization scan, potential scanning starts from the corrosion potential (E_{corr}) after reaching the steady state value. The rapid rise in current density before reaching the oxygen evolution potential could be attributed to the following factors: 1) local dissolution of the oxide film in the presence of corrosive ions; 2) defective passive layer that can lead to the instability of the passive film over the passive region. Below the oxygen

evolution potential, these defects are active and will begin to extend resulting in the rise of the current density [36–38]. In order to investigate the material's response to the pitting or localized corrosion after increase of the current density at the pitting corrosion, the scanning direction of potential is changed from positive values towards the negative values. It can be observed that, both DC and PRC deposited NiW–CeO_2 exhibited negative hysteresis loop, depicting repassivation of pits compared to DC and PRC coated Ni and NiW with positive or zero hysteresis loops. In fact, during the reversal scan, reversed anodic curve shifted to lower current densities, in contrast to forward scan. This indicates the uniform corrosion and restoration of the damaged passive film at higher potentials.

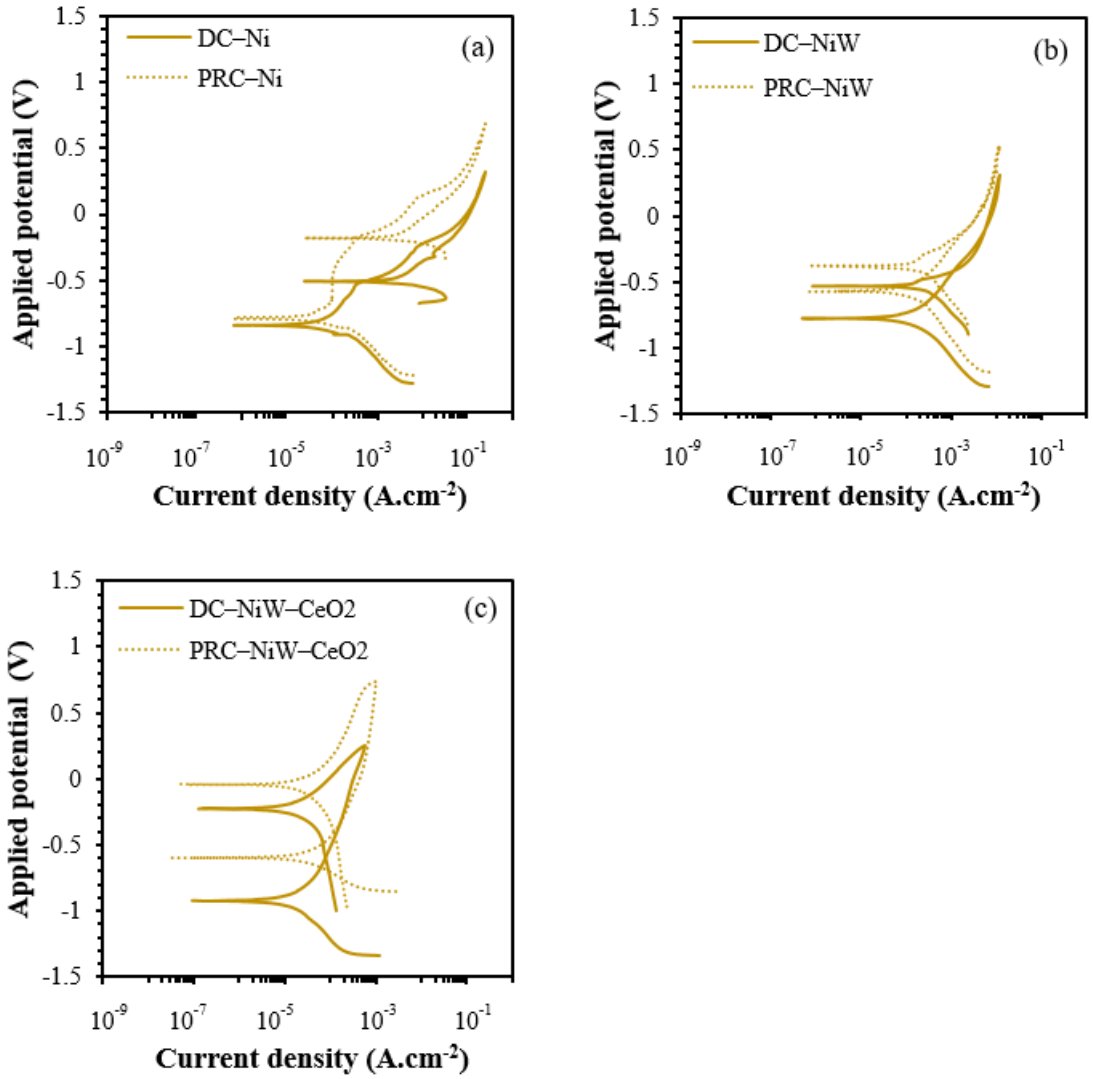

Figure 11.4. Cyclic potentiodynamic polarization graphs of DC and PRC deposited (a) Ni; (b) NiW; and (c) NiW–CeO_2 exposed to artificial sea salt solution.

The corrosion potential values for DC and PRC deposited Ni, NiW, and NiW–CeO_2 extracted from Figure 11.4 are displayed in Figure 11.5. As it can be seen, PRC–NiW–CeO_2 demonstrated the more noble corrosion potential. It was also speculated that the difference in grain structures of coatings deposited by various current waveforms (DC and PRC), and outstanding corrosion properties of CeO_2, were mainly responsible for different corrosion behaviors.

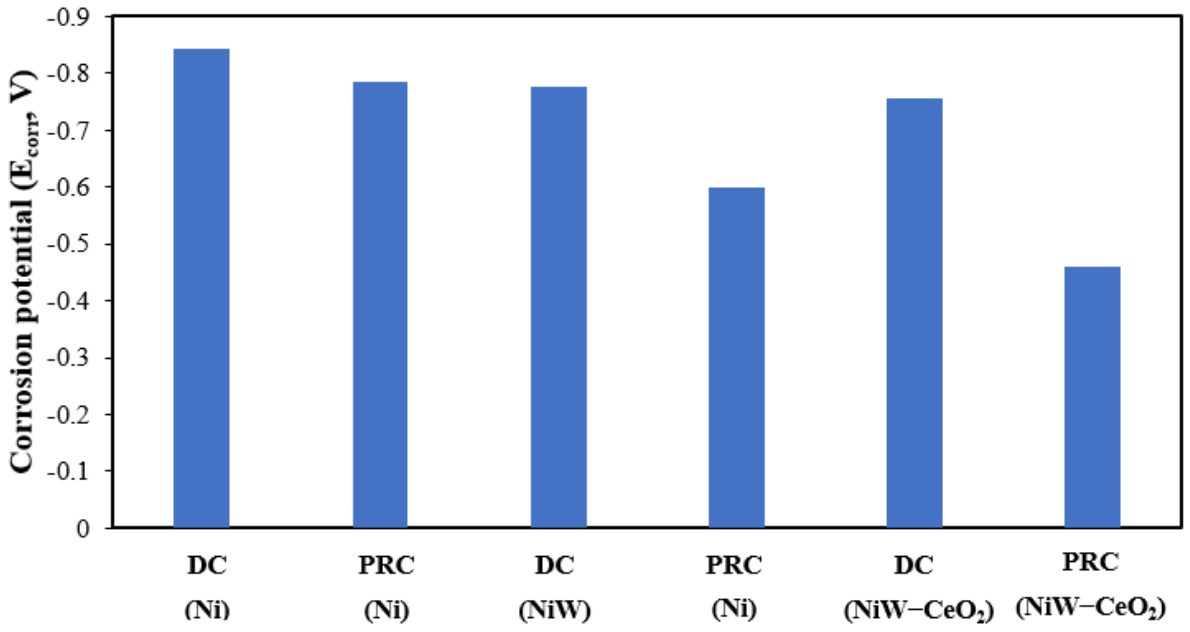

Figure 11.5 Comparison of DC and PRC deposited Ni, NiW, and NiW–CeO_2 coatings with respect to their corrosion potential determined in artificial sea salt solution.

11.3.1.2 Potentiodynamic polarization (PP)

Potentiodynamic polarization graphs of the electrodeposited DC and PRC deposited Ni, NiW, and NiW–CeO_2 are displayed in Figure 11.6. The parameters of corrosion potential (Ecorr) and corrosion current density (I_{corr}) extracted from the polarization graphs in Figure 11.6 are demonstrated in Figure 11.7 for all the deposits. As it can be observed, the corrosion resistance improves in the following order for deposits:

DC–Ni < PRC–Ni < DC–NiW < DC–NiW–CeO_2 < PRC–NiW< PRC–NiW–CeO_2

The sharp increase in anodic current density with increasing potential is attributed to the pitting corrosion that can be seen for all samples. For DC and PRC deposited Ni and NiW coatings, no passive region was established before pitting. However, for DC and PRC coatings, two wide

passive regions were observed. This could be due to higher corrosion resistance and stability of the coatings in the corrosive media. Furthermore, for all coatings, sudden increase of the anodic current density can be observed at higher positive potentials due to local breakdown or dissolution of the passive film which can lead to the failure of the coating. This could be attributed to non–stability of the passive film in corrosive media at higher positive potentials.

Following the PP–tests, the masking tapes were removed from DC and PRC electrodeposited Ni, NiW, NiW, and NiW–CeO_2 specimens and optical micrographs (Figure 11.8 b) were taken from the surface of specimens. Figure 11.8a displays the schematic diagram of the specimen after masking the surface with tape and exposing 1 cm^2 unmasked surface area. As it can be seen from the optical micrographs, the DC and PRC deposited Ni deposits were completely corroded and pulled off the surface, whereas the surface of DC and PRC electrodeposited NiW showed discoloration. This could be due to formation of passive films such as $NiWO_4$ which can act as physical barriers in initiation and propagation of corrosion. No damages were also observed on the surface of DC and PRC deposited NiW–CeO_2 after the PP–test. The optical micrographs in Figure 11.8b are correlated to the PP–test results as demonstrated in Figure 11.6.

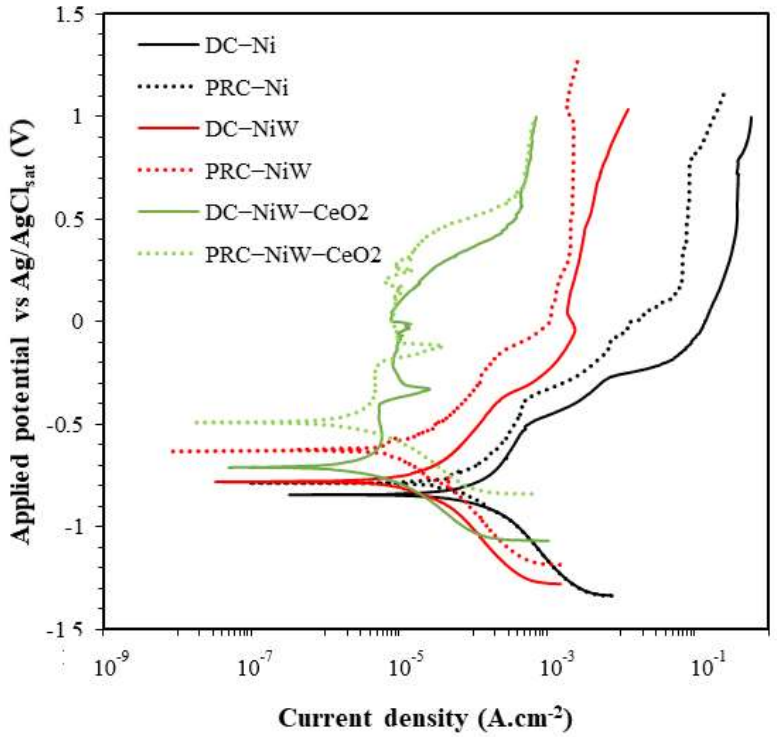

Figure 11.6 Potentiodynamic polarization (PP) of DC–Ni, PRC–Ni, DC–NiW, PRC–NiW, DC–NiW–CeO_2, and PRC–NiW–CeO_2 obtained in artificial sea salt solution.

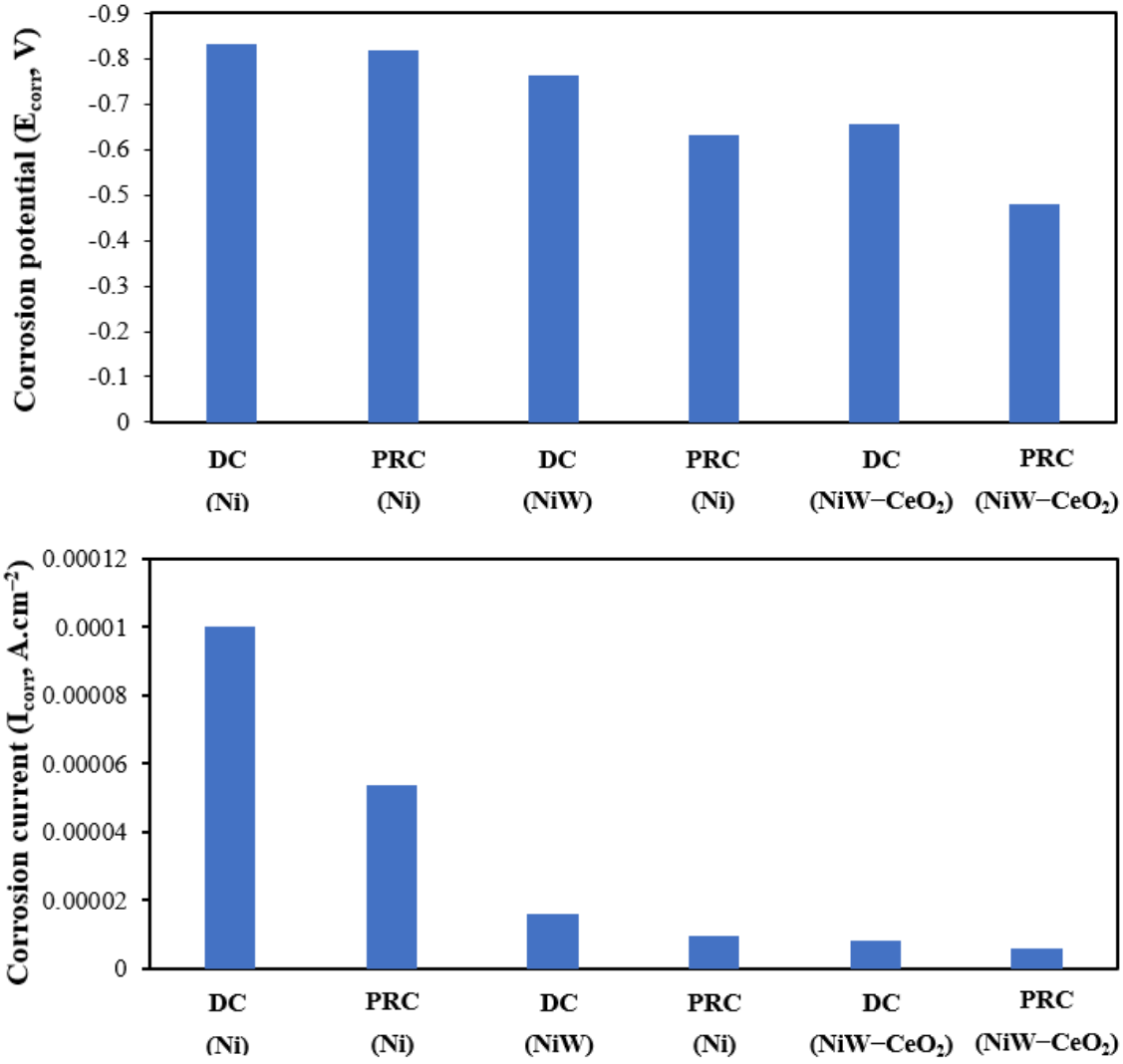

Figure 11.7 Corrosion current density and corrosion potential obtained from potentiodynamic polarizations graphs obtained in artificial sea salt solution for various deposits of DC–Ni, PRC–Ni, DC–NiW, PRC–NiW, DC–NiW–SiC, and PRC–NiW–SiC, DC–NiW–SiC–CeO_2, and PRC–NiW–SiC–CeO_2.

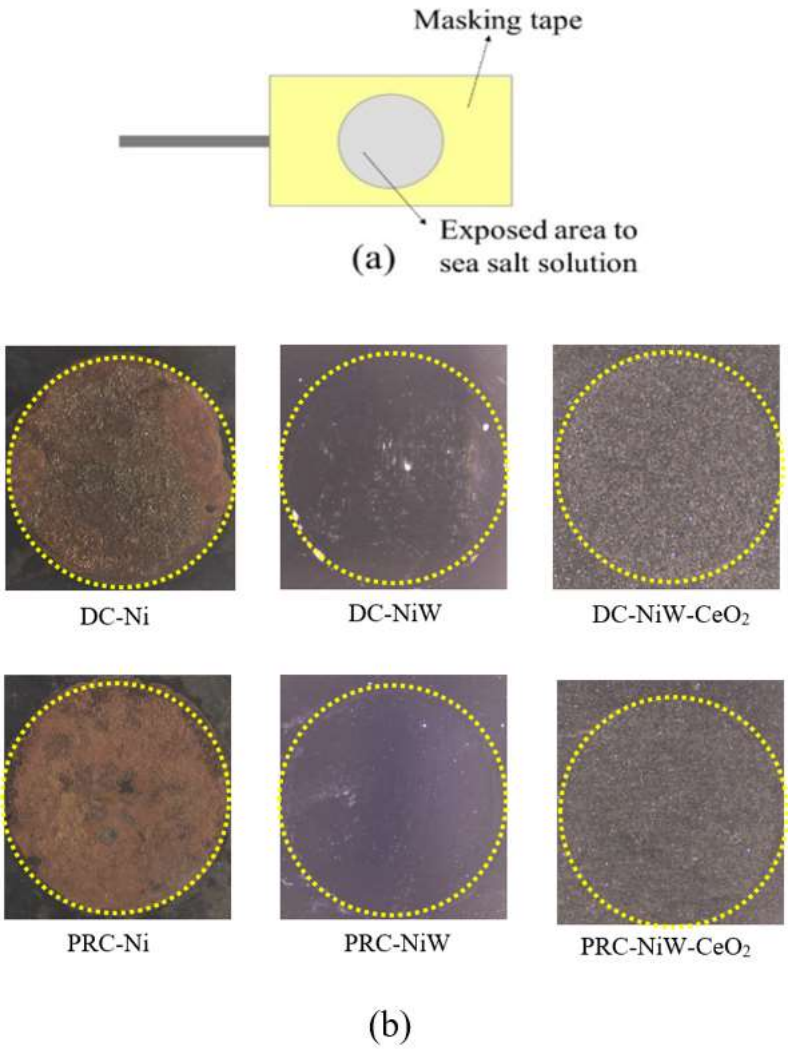

Figure 11.8 (a) schematic diagram of the specimen masked with 3M insulating tape with 1 cm^2 exposed circular area; (b) Optical micrographs taken from the exposed area of various deposits after potentiodynamic polarization of the deposits in artificial sea salt solution. The non–exposed area was protected by applying a masking tape.

11.3.2 SEM/EDS analysis

11.3.2.1 DC and PRC Deposited Ni

SEM micrographs (Figures 11.9 and 11.10) were taken from the surfaces of DC– and PRC–electrodeposited Ni before and after corrosion. No cracks or delamination were observed on the surface of the Ni coatings before corrosion, whereas after corrosion, the DC– and PRC–

electrodeposited Ni were completely corroded and brass substrates were exposed to the surface (Figure 11.9b and 11.10b).

In addition, EDS spectra taken from the surface of the DC– and PRC–electrodeposited Ni before corrosion suggest that Ni was the main element present in the coatings (Figures 11.9a and 11.10a). The reported contents for DC–Ni deposits after corrosion (Figures 11.9b and 11.10b) were 0.2% (Ni), 21.3% (Cu), 59.5% (Zn), and 19% (O) and for the PRC–deposited coating the contents were 1.4% (Ni), 28% (Cu), 52.7% (Zn), and 17.9% (O) accordingly. X–ray mapping results displayed a homogeneous distribution of the coating elements throughout the deposit before and after corrosion (Figures 11.9b and 11.10b).

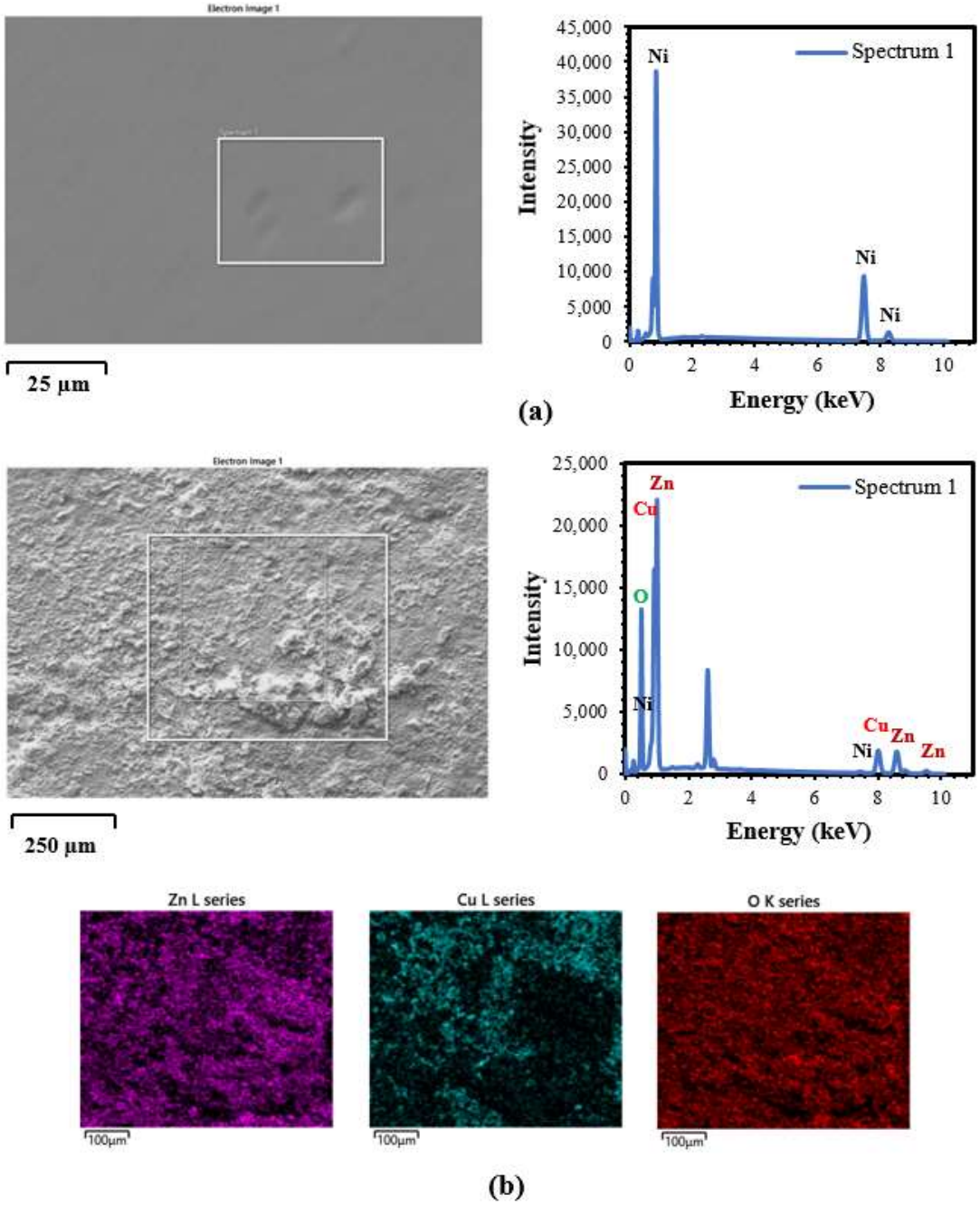

Figure 11.9 SEM micrograph and EDS spectra from the surface of DC−Ni before corrosion. (a) SEM micrograph, EDS spectra and X–ray mapping from the surface of DC−Ni after corrosion.

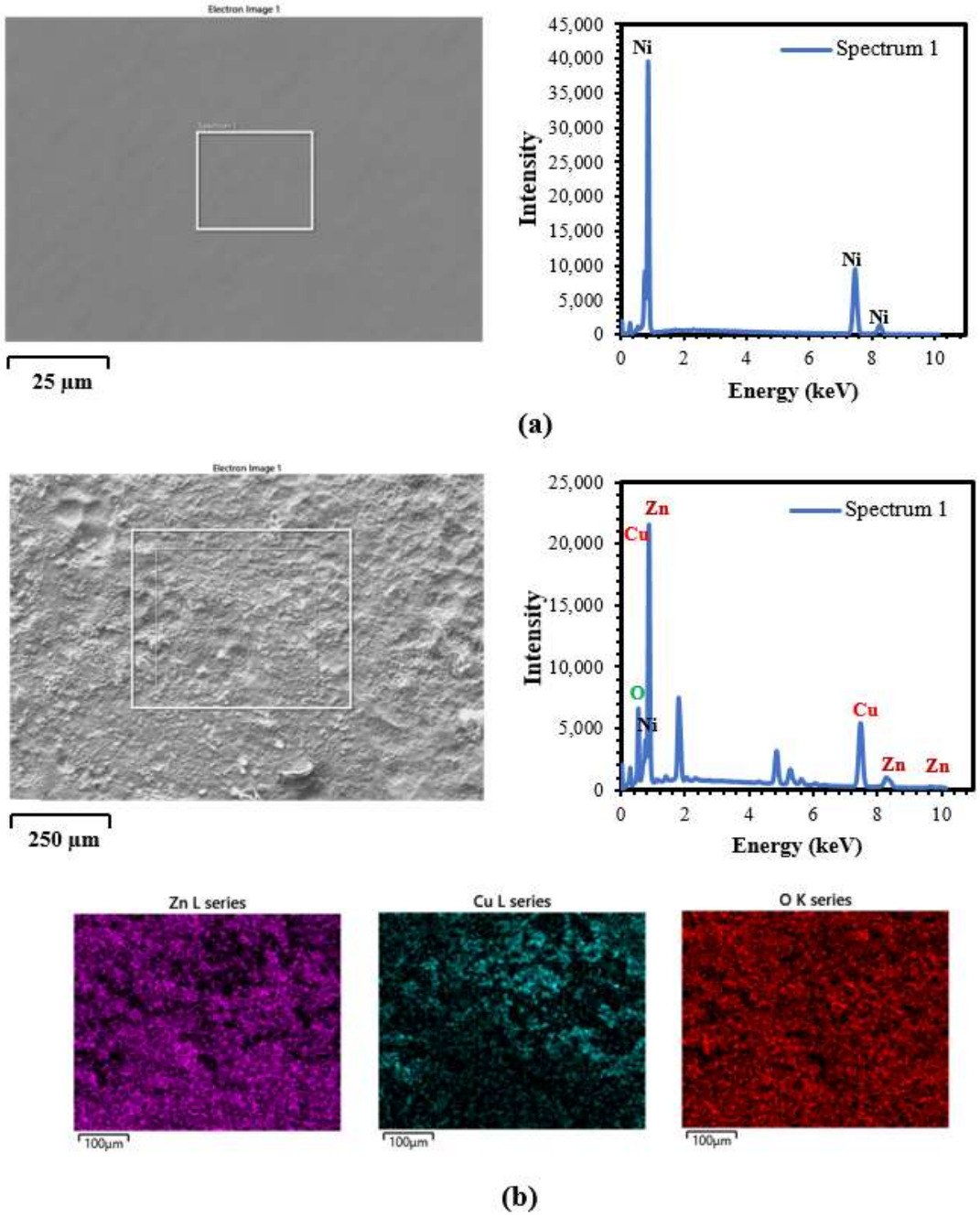

Figure 11.10 SEM micrograph and EDS spectra from the surface of PRC−Ni before corrosion. (a) SEM micrograph, EDS spectra and X–ray mapping from the surface of PRC−Ni after corrosion.

11.3.2.2 DC and PRC Deposited Ni–W

SEM micrographs (Figures 11.11 and 11.12) were taken from the surface of DC– and PRC–electrodeposited NiW before and after corrosion. Before corrosion, the surface of the coatings

were smooth and free of any cracks or defects. However, after corrosion, many defects and pits were observed on the surface of DC–NiW. A few pits were also observed on the surface of PRC–NiW after corrosion (Figures 11.11b and 11.12b).

Moreover, EDS spectra and X–ray mapping taken from the surface of the DC– and PRC–electrodeposited NiW before corrosion suggest that Ni and W are the main elements present in the coatings (Figures 11.11a and 11.12a). The reported contents for DC–NiW deposits were 64.6% (Ni), and 35.4% (W) and for PRC–deposited NiW coatings they were 70% (Ni), and 30% (W) accordingly.

EDS spectra taken from the surface of the DC– and PRC–electrodeposited NiW after corrosion revealed that the coatings contained peaks associated with Ni, W, O, Cu, and Zn (Figures 11.11b and 11.12b). The reported contents for DC–NiW deposits were 5.1% (Ni), 5% (W), 5.8% (Cu), 13.3% (Zn), and 70.8% (O) and for PRC–deposited NiW coating the content were 61.2% (Ni), 33.2% (W), 2.8% (Zn), 2.4% (O), and 0.4% (Cu), respectively.

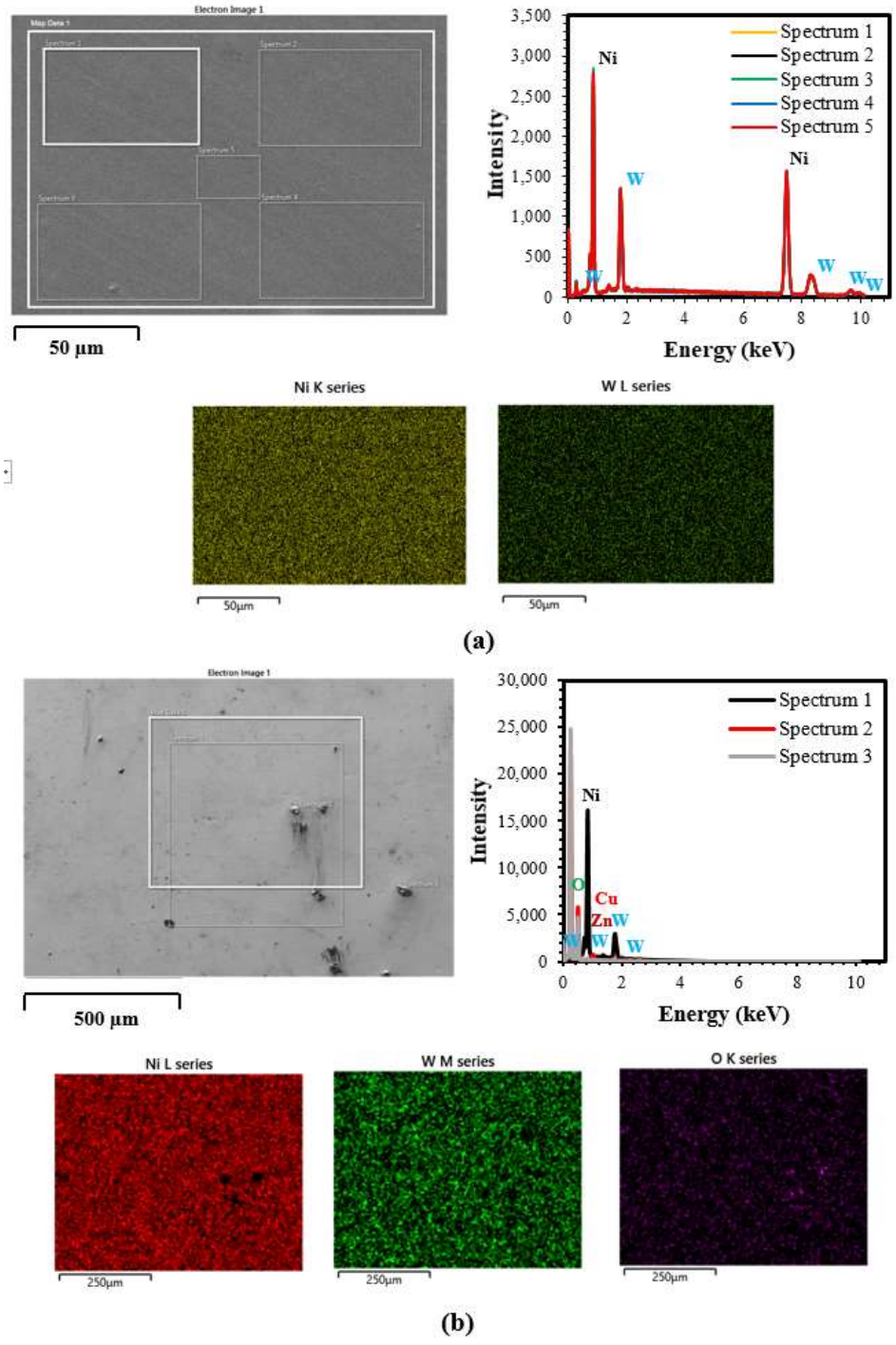

Figure 11.11 SEM micrograph, EDS spectra, and X–ray mapping from the surface of DC–NiW before corrosion. (a) SEM micrograph, EDS spectra, and X–ray mapping from the surface of DC–NiW after corrosion.

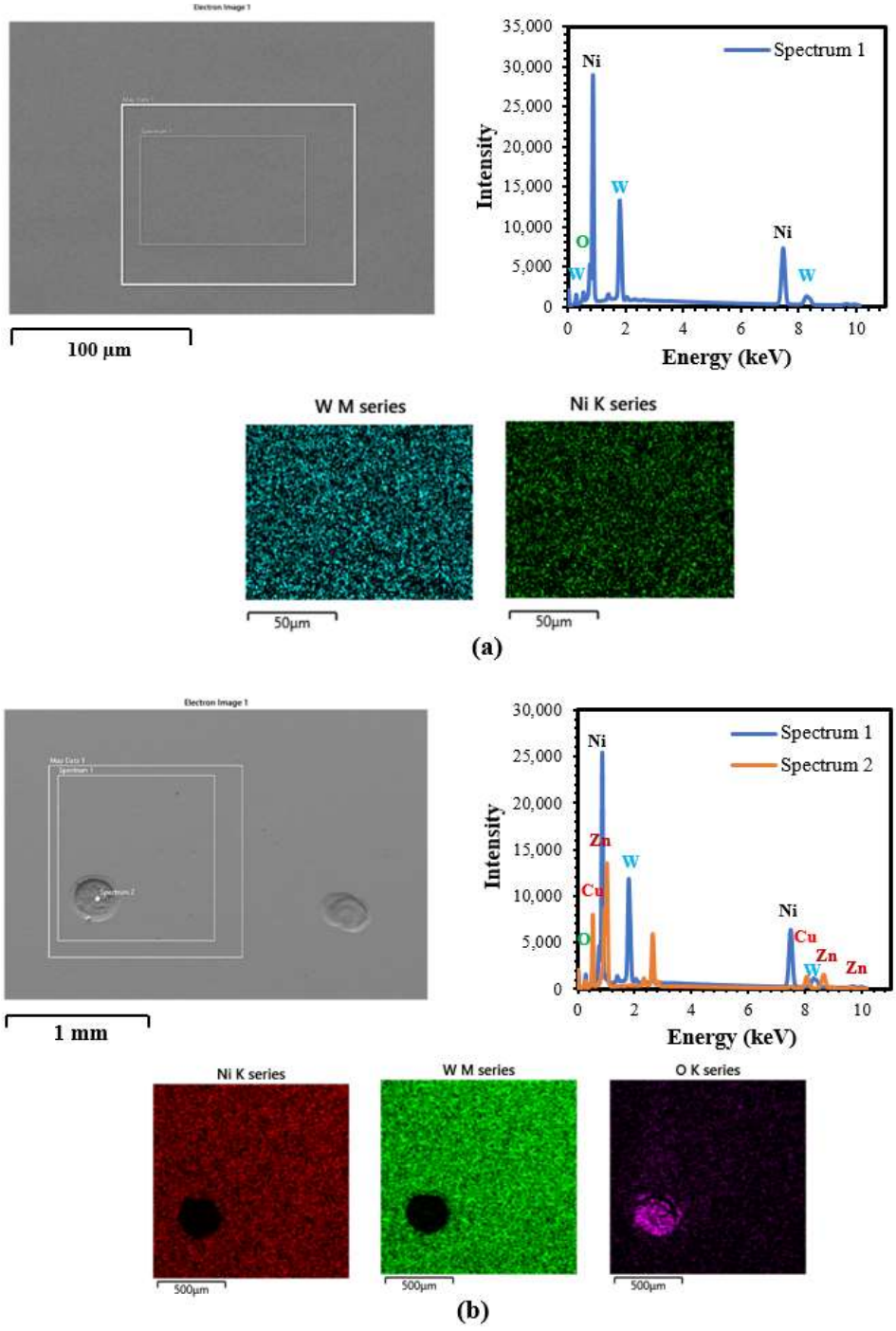

Figure 11.12 SEM micrograph, EDS spectra, and X–ray mapping from the surface of PRC–NiW before corrosion (a); SEM micrograph, EDS spectra, and X–ray mapping from the surface of PRC–NiW after corrosion.

11.3.2.3 DC and PRC Deposited NiW–CeO_2 Composite

SEM micrographs (Figures 11.13 and 11.14) were taken from the surfaces of DC– and PRC–electrodeposited NiW–CeO_2 before and after corrosion. No cracks or delamination were observed on the surface of the coatings. It can be also observed in SEM micrographs that, in PRC–NiW–CeO_2, the majority of the co–deposited CeO_2 particles were embedded within the NiW matrix, while in DC–NiW–CeO_2, the CeO_2 particles were mainly electrodeposited on the surface of the coating. This is due to the fact that in the PRC method, during the anodic pulse (reverse current), greater opportunity will be provided for the arrival of CeO_2 particles on the surface of the cathode and their embedment within the NiW matrix.

Additionally, the EDS spectra taken from the surface of the DC– and PRC–electrodeposited NiW–CeO_2 before and after corrosion suggest that Ni, W, Ce, and O are the main elements present in the coatings (Figures 11.13a and 11.14a). The reported contents for DC deposited coatings before corrosion were 61.4% (Ni), 21.7% (W), 10.9% (Ce), and 3.2% (O) and for PRC deposited coating before corrosion the contents were 55.5% (Ni), 23.9% (W), 15.5% (Ce), and 5.1% (O), accordingly. The higher contents of cerium and oxygen in PRC–NiW–CeO_2 compared to the DC–NiW–CeO_2 could be also related to the increased density of embedded CeO_2 particles in the NiW matrix during the application of the anodic current. The increase in the amount of the particles favors the nucleation rate resulting in the grain refinement of the deposits. This greatly impacts the corrosion resistance of the coating by decreasing the antiparticle distance and formation of highly continuous protective film on the surface of the coating when exposed to the corrosive media.

EDS spectra results from both surfaces of the DC– and PRC–deposited NiW–CeO_2 (Figures 11.13b and 11.14b) after corrosion revealed that the contents for DC–NiW–CeO_2 deposits were 58.6% (Ni), 24.5% (W), 12.9% (Ce), and 4% (O) and for the PRC–NiW–CeO_2 coating the contents were 56.3% (Ni), 26.4% (W), 13.6% (Ce), and 3.7% (O), respectively. The contents of DC– and PRC–deposited NiW–CeO_2 were almost similar before and after corrosion. This could be due to presence of CeO_2 particulates within the NiW matrix covering the surface defects, refining the grains, and acting as a physical barrier to protect the metallic layer underneath from further corrosion. X–ray mapping results displayed a homogeneous distribution of the coating elements throughout the deposit before and after corrosion.

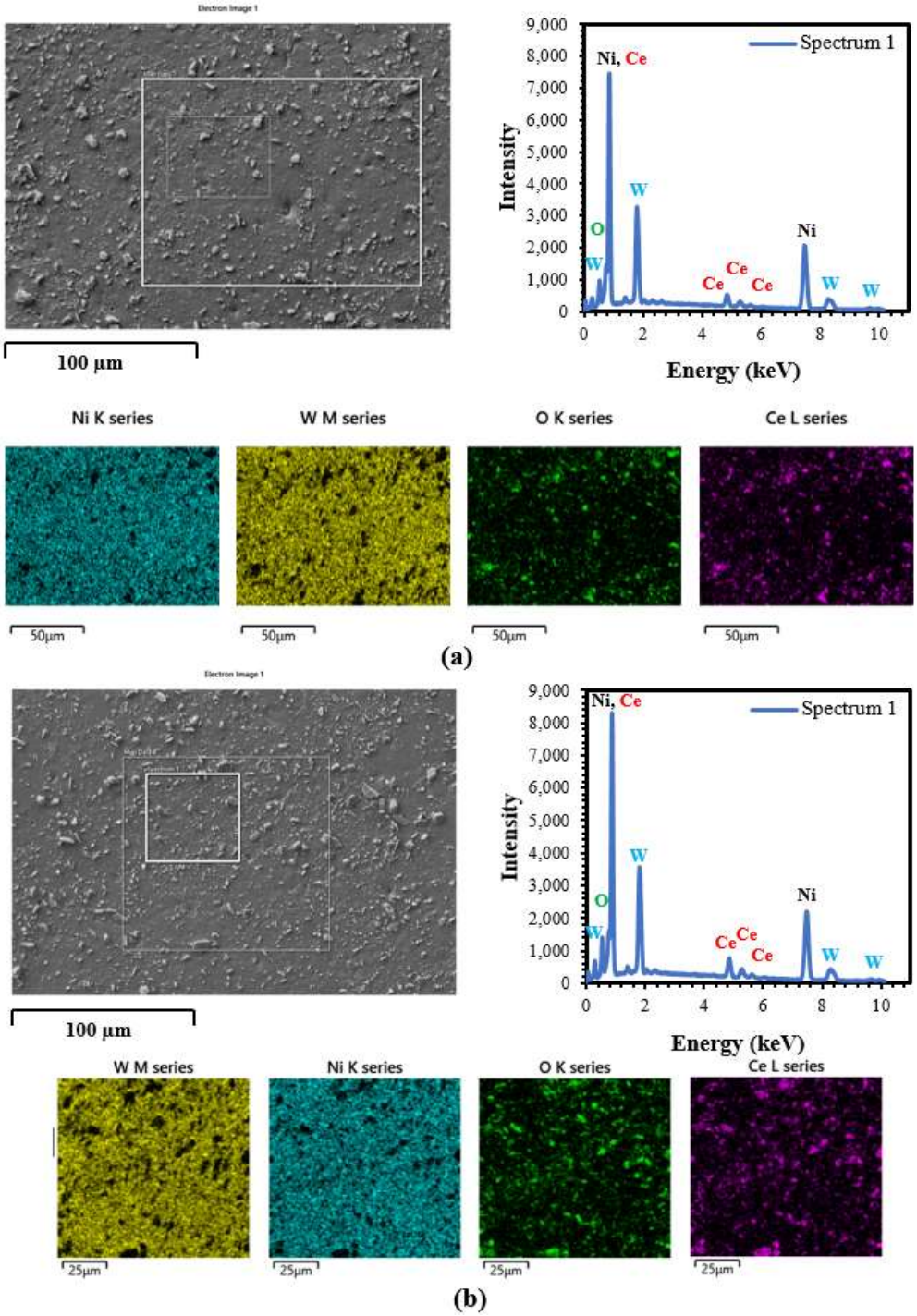

Figure 11.13 SEM micrograph, EDS spectra, and X–ray mapping from the surface of DC–NiW–CeO_2 before corrosion. (a) SEM micrograph, EDS spectra, and X–ray mapping from the surface of DC–NiW–CeO_2 after corrosion. Concentration of CeO_2 in electrolyte was 40 $g.L^{-1}$.

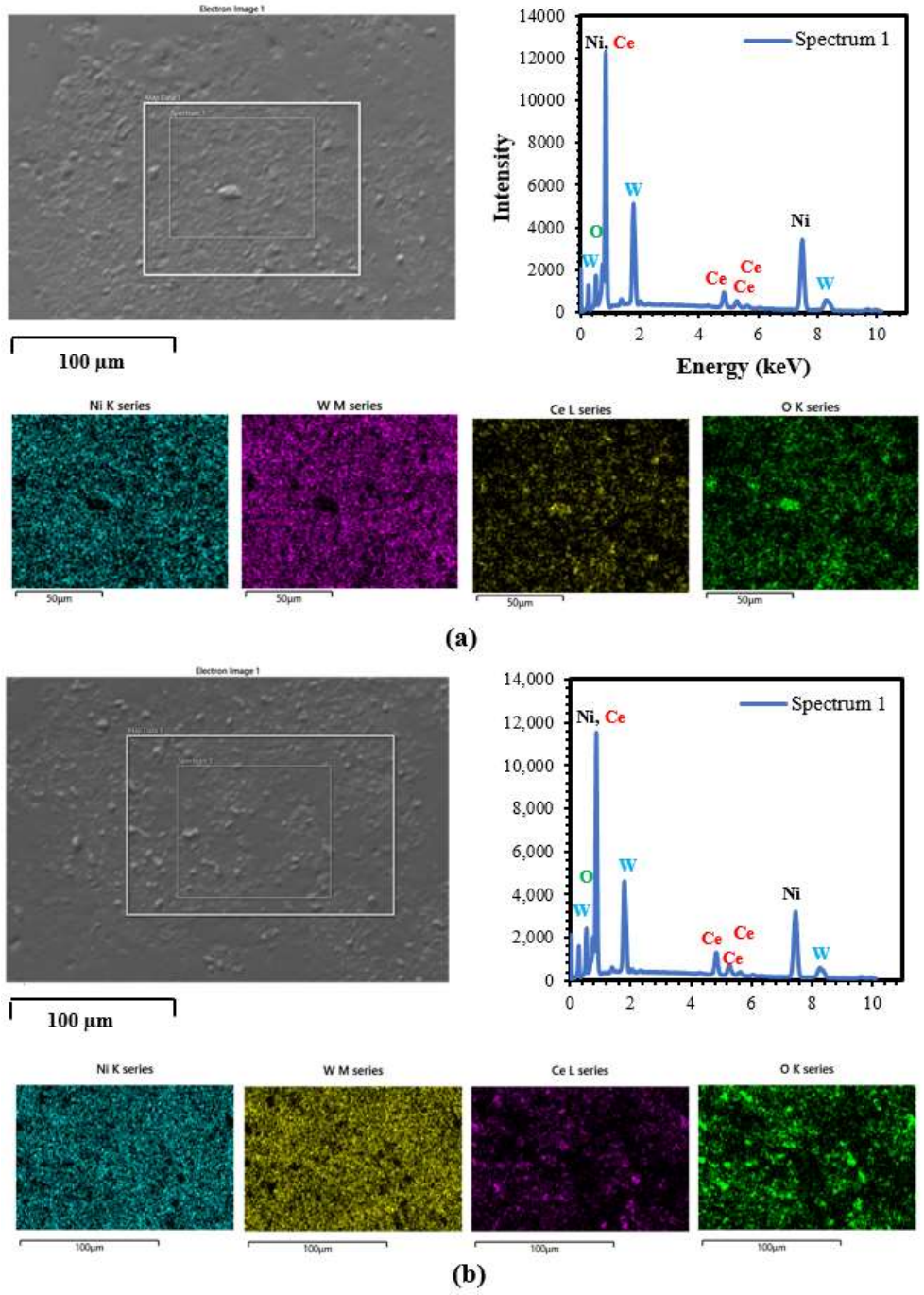

Figure 11.14 SEM micrograph, EDS spectra, and X–ray mapping from the surface of PRC–NiW–CeO_2 before corrosion. (a) SEM micrograph, EDS spectra, and X–ray mapping from the surface of PRC–NiW–CeO_2 after corrosion. Concentration of CeO_2 in electrolyte was 40 $g.L^{-1}$.

11.3.3 Tribological analysis (coefficient of friction and wear rate)

Figure 11.15 displays the variation in the average coefficient of friction for DC and PRC deposited Ni, NiW, and NiW–CeO_2 electrodeposited materials on brass substrates using pin–on–disc wear testing facility. As it can be observed, PRC–NiW–CeO_2 demonstrated the lowest coefficient of friction (0.25) compared to DC–NiW–CeO_2 (0.35), DC–NiW (0.45), PRC–NiW deposits (0.42), DC–Ni (0.67), and PRC–Ni (0.62). The low friction coefficient of PRC–NiW–CeO_2 coating compared to the DC–NiW–CeO_2 and PRC deposited Ni and NiW can be attributed to reduction of the contact between the Al_2O_3 ball and the coating. As well, the formation of stable nickel oxide and tungsten oxide layer during the reverse pulse on the coating surface will effectively reduce the contact between the sliding surfaces.

The low coefficient of friction of the DC and PRC deposited NiW compared to Ni could be related to the solid solution strengthening mechanism by tungsten of nickel matrix. Figure 11.16 displays the wear volume rate of removed material after the friction test.

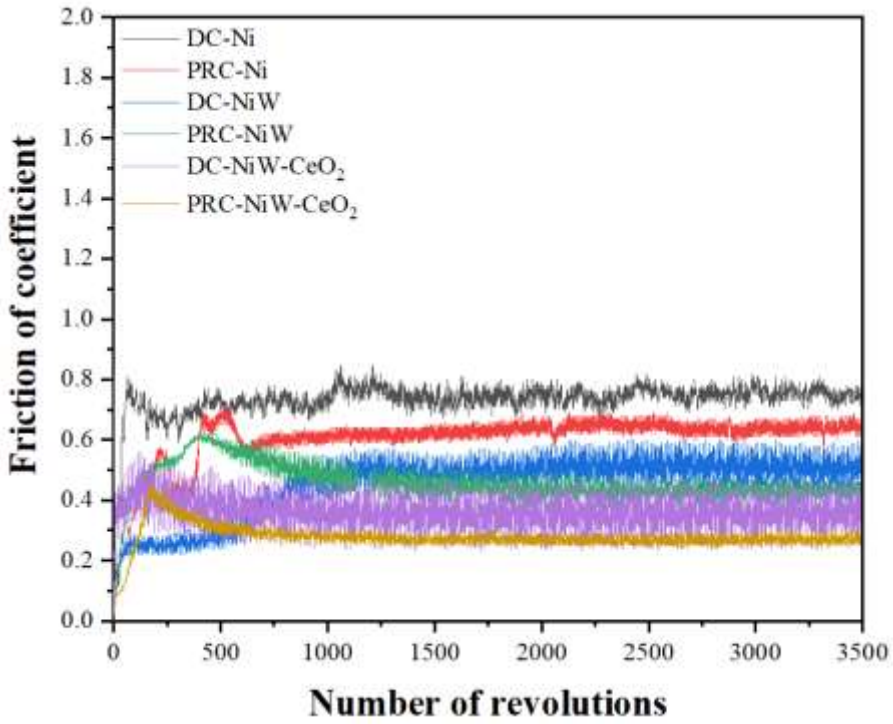

Figure 11.15 Coefficient of friction for the DC and PRC deposited Ni, NiW, and NiW–CeO_2 electrodeposited from an optimized electrolyte on the brass substrate for 3500 revolutions at room temperature and normal applied load of 1N.

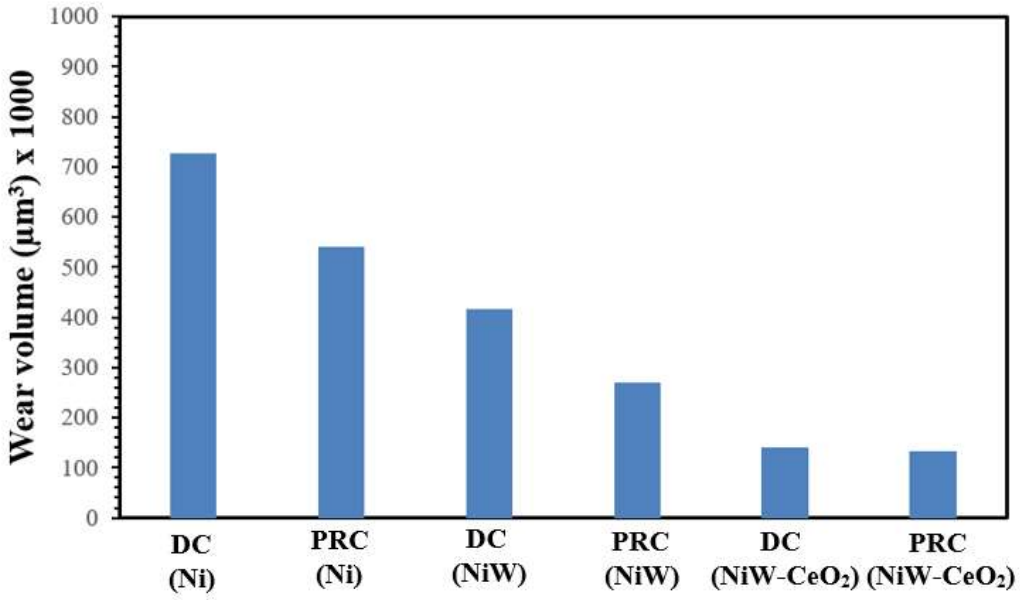

Figure 11.16 Wear volume for the DC and PRC deposited Ni, NiW, and NiW–CeO_2 electrodeposited coatings.

11.3.4 XRD analysis (effect of heat treatment on crystallite sizes of PRC deposited Ni, NiW and NiW–CeO_2)

XRD results were taken from the surfaces of as–deposited and heat–treated PRC electrodeposited Ni, NiW, and NiW–CeO_2 at 350°C and 500°C on brass substrates (Figure 11.17). It was observed that the peak intensity of the heat–treated coatings were higher than that of the as–deposited coating, and hence the crystallite size increased with increase of the annealing temperature which might be attributed to FCC crystal grain growth, and decrease of the internal micro–strains. The crystallites size of the coatings were measured (Table 11.3) from the broadening of the (111) peaks using Scherrer equation. [39]

$$D = K\lambda/\beta\cos\theta \qquad (1)$$

Where D is the crystallite size (nm), K is the Scherrer constant (0.9), λ is the wavelength of the x–ray source (0.15406 nm), β is the FWHM (radians), and θ is the peak position (radians).

XRD spectra taken from the surfaces of as–deposited and heat–treated PRC–Ni (Figure 11a) contained diffraction peaks of Cu (111), Ni (111), Cu (200), Ni (200), Cu (220), Ni (220), Cu, (311), Ni (311), and Ni (222) planes. This demonstrated that PRC–Ni is a polycrystalline coating material. It was also observed that peak intensity and average crystallite size increased from 197 Å up to 1210 Å with increase of the annealing temperature. This was attributed to

increase in degree of coating crystallinity and number of the crystallites. As well, presence of the Cu peaks in XRD spectra indicated its diffusion and segregation from the substrate outward to the coating surface due to higher tendency of Cu for oxidization compared to Ni. [39]

Figure 11.17b displays the XRD spectra taken from the surfaces of as–deposited and annealed PRC–NiW. The XRD spectra contained the peaks of Ni(111), Ni (200), Ni (220), Ni (311), and Ni(222), respectively. It was observed that, the peak intensity of the Ni (111) and Ni (220) was increased and additional peaks of Ni (200) and Ni (311) were formed after annealing at 500^{o}C. Unlike PRC–Ni, no peaks of Cu was observed, indicating better shielding effect of NiW against diffusion of Cu from substrate to Ni. This can have a great influence on the corrosion performance of the coating.

XRD spectra taken from the surfaces of as–deposited and annealed PRC–NiW–CeO_2 at 350^{o}C and 500^{o}C (Figure 11.17c) contained the peaks of Ce (111), Ce (200), Ni (111), Ce (220), Ni (200), Ni (220), Ce (311), and Ni (311). It is worth mentioning that the introduction of CeO_2 into NiW matrix resulted in a decrease in crystallite size of Ni (Table 11.3) which was due to grain refinement effect of CeO_2 particles on the alloy matrix. This can lead to the more compact deposits with improved corrosion and wear performance. It was also noticed that, the intensity of Ce (111), Ni (111), Ni (220), Ni (311) increased with increase of the annealing temperature. As well, some additional peaks of Ce (200), Ni (200), and Ce (311) were appeared after annealing at 500^{o}C. XRD results also revealed that, the average grain size of Ni increased from 110 Å to 158 Å by increase of the annealing temperature up to 500^{o}C.

In all XRD graphs, the peaks of W were not observed. This was due to partial replacement of Ni by W atoms and forming a single–phase solid solutions (W in Ni) with face–centered cubic (F.C.C) structure. Addition of the alloying element of W in Ni, also resulted in peak broadening and reduction in average crystallite size due to decrease of Ni content and lattice distortion. These results on the lattice distortion are in agreement with the results published elsewhere. [43, 44]

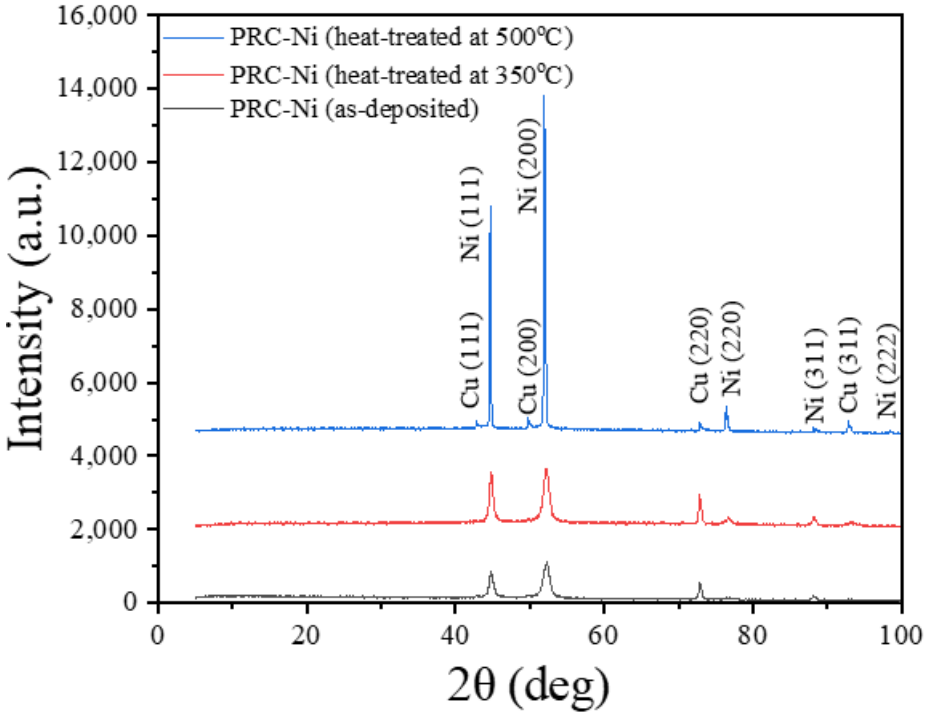
PRC-Ni (heat-treated at 500°C)
PRC-Ni (heat-treated at 350°C)
PRC-Ni (as-deposited)
Ni (111)
Ni (200)
Cu (111)
Cu (200)
Cu (220)
Ni (220)
Ni (311)
Cu (311)
Ni (222)
Intensity (a.u.)
2θ (deg)
16,000
14,000
12,000
10,000
8,000
6,000
4,000
2,000
0
0
20
40
60
80
100

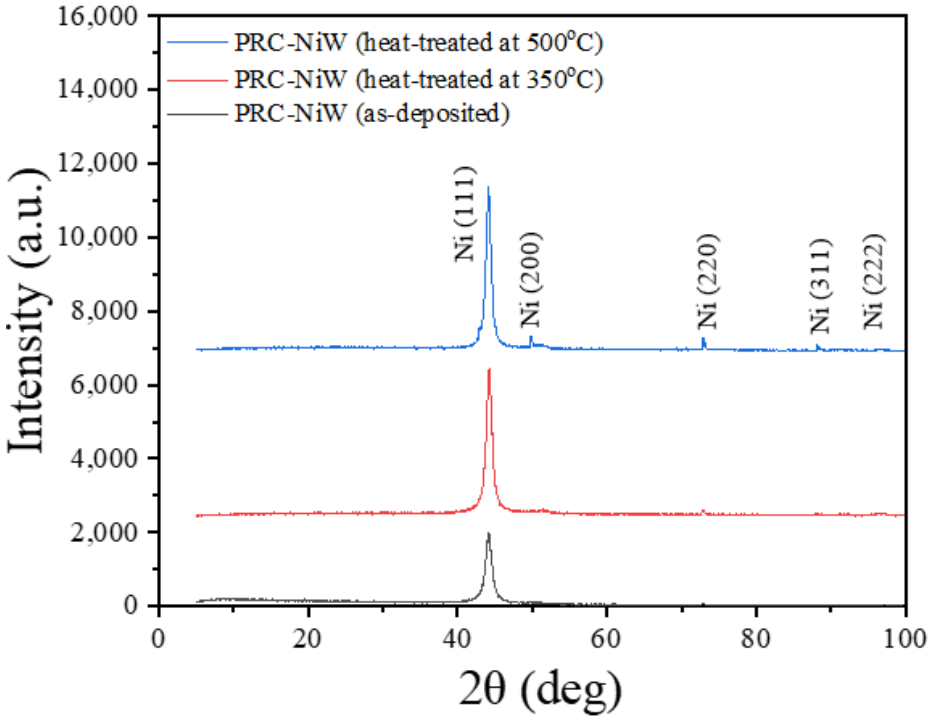
PRC-NiW (heat-treated at 500°C)
PRC-NiW (heat-treated at 350°C)
PRC-NiW (as-deposited)
Ni (111)
Ni (200)
Ni (220)
Ni (311)
Ni (222)
Intensity (a.u.)
2θ (deg)
16,000
14,000
12,000
10,000
8,000
6,000
4,000
2,000
0
0
20
40
60
80
100

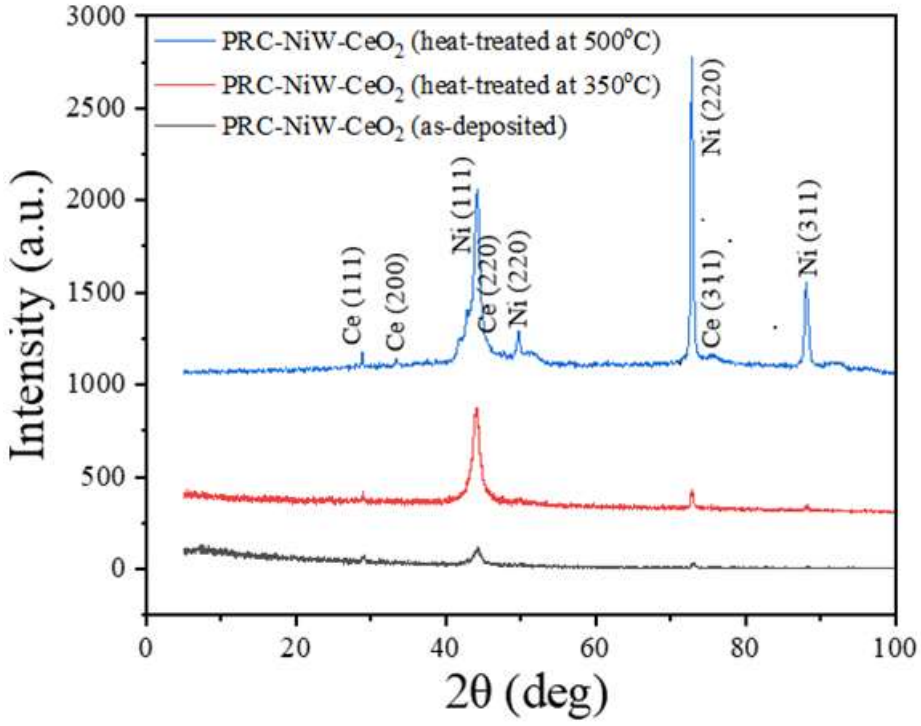

Figure 11.17 XRD spectra from the surface of PRC electrodeposited NiW–CeO_2 (as–deposited and heat–treated at 350°C and 500°C).

Table 11.3 Crystallite sizes of PRC deposited Ni, NiW and NiW–CeO_2

Coatings	**Peak position of (111) [°2Th]**	**FWHM [°2Th]**	**Crystallite size [Å]**
PRC–Ni (as–deposited)	44.712	0.443	197
PRC–Ni (heat–treated at 350°C)	44.810	0.315	280
PRC–Ni (heat–treated at 500°C)	44.651	0.079	1210
PRC–NiW (as–deposited)	44.220	0.630	138
PRC–NiW (heat–treated at 350°C)	44.319	0.433	202
PRC–NiW (heat–treated at 500°C)	44.130	0.386	222
PRC–NiW–CeO_2 (as–deposited)	44.261	0.779	110
PRC–NiW–CeO_2 (heat–treated at 350°C)	44.075	0.692	124
PRC–NiW–CeO_2 (heat–treated at 500°C)	44.214	0.543	158

11.4 Conclusion

Incorporation of CeO_2 ceramic particles within the NiW matrix along with applying the PRC waveform to the electrodposition bath, enhanced the corrosion performance of the NiW coating. Several sets of experiments were performed to investigate the corrosion performance of the NiW coatings reinforced with CeO_2 ceramic particles. It was observed that, the coatings prepared using PRC, exhibited outstanding corrosion resistance when exposed to corrosive media compared to that of DC waveform. It was also revealed that reinforcement of CeO_2 within NiW significantly improved the corrosion performance of the coating and both DC and PRC–NiW–CeO_2 exhibited the highest corrosion performance compared to DC and PRC deposited Ni and NiW. According to pp–test results, the corrosion resistance improved in the following order for deposits:

DC–Ni < PRC–Ni < DC–NiW < DC–NiW–CeO_2 < PRC–NiW< PRC–NiW–CeO_2

From the optical micrographs of the corroded surfaces of DC and PRC electrodeposits, it was found that DC and PRC Ni were completely corroded and pulled off the surface, whereas the surface of DC and PRC–NiW showed discoloration. On the other hand, DC and PRC deposited NiW–CeO_2 were remained almost unaffected after the PP–test.

DC and PRC electrodeposited NiW–CeO_2 demonstrated the lowest coefficient of friction and wear rate compared to other DC and PRC deposited coatings.

Based on the XRD results, as–deposited and annealed PRC electrodeposited Ni, NiW, and NiW–CeO_2 at 350^{o}C and 500^{o}C also revealed that the intensity of the peaks and the average crystallite size increased with increase of the annealing temperature up to 500^{o}C.

11.5 References

[1] R. An-hua, "Effect of Current Density on the Properties of Ni–CeO_2 Composite Coatings prepared using Magnetic Field-Assisted Jet Electrodeposition," 2021, ArticleID:210658.

[2] S. Guo, L. Wang, Y. Jin, N. Piao, Z. Chen, G. Tian, J. Li, C. Zhao, and X. He, "A polymeric composite protective layer for stable Li metal anodes," vol. 7, no. 1, p. 21, Jun 15 2020. [En ligne]. Disponible: https://www.ncbi.nlm.nih.gov/pubmed/32542452

[3] J. Cao, L. Wang, X. He, M. Fang, J. Gao, J. Li, L. Deng, H. Chen, G. Tian, J. Wang, and S. Fan, "In situ prepared nano-crystalline TiO2–poly (methyl methacrylate) hybrid enhanced composite polymer electrolyte for Li-ion batteries," vol. 1, no. 19, p. 5955-5961, 2013.

[4] Y. Yao, H. Dong, L. Jiao, N. Yu, and L. He, "Preparation and electrocatalytic property of PbO_2-CeO_2 nanocomposite electrodes by pulse reverse electrodeposition methods," vol. 163, no. 5, p. D179, 2016.

[5] Y. Y. Xu, Y. J. Xue, F. Yang, C. Y. Liu, and J. S. Li, "Preparation of Ni-ZrO_2-CeO_2 Nanocomposite Coatings by Pulse Electrodeposition," communication présentée à Applied Mechanics and Materials, 2013, p. 174-178.

[6] L. Wang, S. Xing, H. Liu, C. Jiang, and V. Ji, "Improved wear properties of NiTi nanocomposite coating with tailored spatial microstructures by extra adding CeO_2 nanoparticles," vol. 399, p. 126119, 2020.

[7] S. Uhm, Y. Yi, and J. Lee, "Electrocatalytic activity of Pd–CeO_2 nanobundle in an alkaline ethanol oxidation," vol. 138, no. 1, p. 46-49, 2010.

[8] X. Zhou, and Y. Shen, "A comparative study of pure nickel and the Ni–CeO_2 nanocrystalline coatings: microstructural evolution, oxidation behavior, and thermodynamic stability," vol. 49, no. 10, p. 3755-3774, 2014.

[9] Y. J. Xue, X. Z. Jia, Y. W. Zhou, W. Ma, and J. S. Li, "Tribological performance of Ni–CeO_2 composite coatings by electrodeposition," vol. 200, no. 20-21, p. 5677-5681, 2006.

[10] S. K. Kim, and H. J. Yoo, "Formation of bilayer Ni–SiC composite coatings by electrodeposition," vol. 108, p. 564-569, 1998.

[11] I. Garcia, J. Fransaer, and J. P. Celis, "Electrodeposition and sliding wear resistance of nickel composite coatings containing micron and submicron SiC particles," vol. 148, no. 2-3, p. 171-178, 2001.

[12] W. Wang, H. Guo, J. Gao, X. Dong, and Q. Qin, "XPS, UPS and ESR studies on the interfacial interaction in Ni-ZrO_2 composite plating," vol. 35, no. 6, p. 1495-1499, 2000.

[13] S. Banovic, K. Barmak, and A. Marder, "Characterization of single and discretely-stepped electro-composite coatings of nickel-alumina," vol. 34, no. 13, p. 3203-3211, 1999.

[14] G. Wu, N. Li, D. Zhou, and K. Mitsuo, "Electrodeposited Co–Ni–Al_2O_3 composite coatings," vol. 176, no. 2, p. 157-164, 2004.

[15] S. Surviliene, L. Orlovskaja, G. Bikulcius, and S. Biallozor, "Effect of MoO_2 and TiO_2 on electrodeposition and properties of chromium coating," vol. 137, no. 2-3, p. 230-234, 2001.

[16] B. Łosiewicz, A. Stępień, D. Gierlotka, and A. Budniok, "Composite layers in Ni–P system containing TiO_2 and PTFE," vol. 349, no. 1-2, p. 43-50, 1999.

[17] B. Levin, J. DuPont, and A. Marder, "The effect of second phase volume fraction on the erosion resistance of metal-matrix composites," vol. 238, no. 2, p. 160-167, 2000.

[18] J. H. Yun, C. H. Yoon, J. S. Oh, S. B. Kim, B. A. Kang, and K. S. Hwang, "Publication: Journal of Materials Science Pub Date: 2000."

[19] K. Hou, M. Ger, L. Wang, and S. Ke, Wear, "The wear behaviour of electro-codeposited Ni–SiC composites," vol. 253, no. 9-10, p. 994-1003, 2002.

[20] Y. Zhou, F. Xie, X. Wu, W. Zhao, and X. Chen, "A novel plating apparatus for electrodeposition of Ni-SiC composite coatings using circulating-solution co-deposition technique," vol. 699, p. 366-377, 2017.

[21] B. Han, and X. Lu, "Tribological and anti-corrosion properties of Ni–W–CeO_2 coatings against molten glass," vol. 202, no. 14, p. 3251-3256, 2008.

[22] Z. Zhang, Q. J. Xue, W. M. Liu, and W. C. Shen, "Effect of rare earth compounds as fillers on friction and wear behaviors of PTFE-based composites," vol. 72, no. 3, p. 361-369, 1999.

[23] M. Sajjadnejad, S.M.S. Haghshenas, P. Badr, N. Setoudeh, and S. Hosseinpour, Wear, 486-487 (2021), "Wear and tribological characterization of nickel matrix electrodeposited composites: A review," vol. 486-487, 2021, 204098.

[24] G. Cârâc, L. Benea, C. Iticescu, T. Lampke, S. Steinhäuser, and B. Wielage, "Codeposition of cerium oxide with nickel and cobalt: correlation between microstructure and microhardness," vol. 20, no. 5, p. 353-359, 2004.

[25] L. Tarkowski, P. Indyka, and E. Bełtowska-Lehman, "XRD characterisation of composite Ni-based coatings prepared by electrodeposition," vol. 284, p. 40-43, 2012.

[26] N. Atanassov, K. Gencheva, and M. Bratoeva, "Properties of nickel-tungsten alloys electrodeposited from sulfamate electrolyte," vol. 84, no. 2, p. 67-74, 1997.

[27] L. Jinlong, W. Zhuqing, L. Tongxiang, K. Suzuki, M. Hideo, "Effect of tungsten on microstructures of annealed electrodeposited Ni-W alloy and its corrosion resistance," vol. 337, p. 516-524, 2018.

[28] O. Younes-Metzler, and E. Gileadi, "Electroplating of Ni/W Alloys," vol. 149, no. 2, 2002, C100.

[29] M. Klimenkov, A.S.M.A. Haseeb, and K. Bade, "Structural investigations on nanocrystalline Ni-W alloy films by transmission electron microscopy," Thin Solid Films, vol. 517, no. 24, p. 6593-6598, 2009. [En ligne].

Disponible: https://www.cheric.org/research/tech/periodicals/view.php?seq=1062420

[30] K. R. Sriraman, S. Ganesh Sundara Raman, and S. K. Seshadri, "Synthesis and evaluation of hardness and sliding wear resistance of electrodeposited nanocrystalline Ni–W alloys," vol. 418, no. 1-2, p. 303-311, 2006, 303.

[31] Z. Mohammadpour, and H. R. Zare, "Improving the Corrosion Resistance of the Nickel–Tungsten Alloy by Optimization of the Electroplating Conditions," vol. 73, no. 4, p. 937-944, 2020, 937.

[32] N. P. Wasekar, S. M. Latha, M. Ramakrishna, D. S. Rao, and G. Sundararajan, "Pulsed electrodeposition and mechanical properties of Ni-W/SiC nano-composite coatings," vol. 112, p. 140-150, 2016, 140.

[33] Y. Wang, M. Yu, H. Luo, Q. Qiao, Z. Xiao, Y. Zhao, L. Zhao, H. Sun, Z. Xu, K. Matsugi, and J. Yu, "Effect of saccharin on the structure and properties of electrodeposition NiWP alloy coatings," vol. 25, no. 10, p. 4402-4407, 2016.

[34] J. C. Cameron, "Acetylenic compositions and nickel plating baths containing same," éd: Google Patents, 1983.

[35] O. A. Rahman, N. P. Wasekar, G. Sundararajan, and A. K. Keshri, "Experimental investigation of grain boundaries misorientations and nano twinning induced strengthening on addition of silicon carbide in pulse electrodeposited nickel tungsten composite coating," vol. 116, p. 1-7, 2016.

[36] Y. Shi, B. Yang, and P. Liaw, "Corrosion-resistant high-entropy alloys: A review," vol. 7, no. 2, p. 43, 2017.

[37] L. Feng, Y. Y. Ren, Y. h. Zhang, S. Wang, and L. Li, "Direct correlations among the grain size, texture, and indentation behavior of nanocrystalline nickel coatings," vol. 9, no. 2, p.188, 2019.

[38] C.F. Dong, H. Luo, K. Xiao, X.G. Li, and Y.F. Cheng, "In Situ Characterization of Pitting Corrosion of Stainless Steel by a Scanning Electrochemical Microscopy," vol. 21, no. 3, p. 406-410, 2011, 406.

[39] Ahadian, E. Nouri, M. Ranjbar, and A. Dolati, "Diffusion and segregation of substrate copper in electrodeposited Ni–Fe thin films," vol. 443, no. 1-2, p. 81-86, 2007.

[40] L. Liu, Y. Li, and F. Wang, "Influence of grain size on the corrosion behavior of a Ni-based superalloy nanocrystalline coating in NaCl acidic solution," vol. 53, no. 5, p. 2453-2462, 2008.

[41] G. Palumbo, D. Dunikowski, R. Wirecka, T. Mazur, U. Lelek-Borkowska, K. Wawer, and J. Banas, "Effect of Grain Size on the Corrosion Behavior of Fe-3wt.%Si-1wt.%Al Electrical Steels in Pure Water Saturated with CO_2," vol. 14, no. 17, Sep 5 2021. [En ligne]. Disponible: https://www.ncbi.nlm.nih.gov/pubmed/34501174

[42] X. Y. Zhang, M. H. Shi, C. Li, N. F. Liu, and Y. M. Wei, "The influence of grain size on the corrosion resistance of nanocrystalline zirconium metal," vol. 448, no. 1-2, p. 259-263, 2007, 259.

[43] S. Mbugua Nyambura, M. Kang, J. Zhu, Y. Liu, Y. Zhang, and N. J. Ndiithi, "Synthesis and Characterization of Ni–W/Cr_2O_3 Nanocomposite Coatings Using Electrochemical Deposition Technique," vol. 9, no. 12, 2019, 815.

[44] K. R. Sriraman, S. Ganesh Sundara Raman, and S. K. Seshadri, "Corrosion behaviour of electrodeposited nanocrystalline Ni–W and Ni–Fe–W alloys," vol. 460-461, p. 39-45, 2007, 39.

CHAPTER 12 GENERAL DISCUSSION

12.1 General discussions

12.1.1 The role of PRC waveform on corrosion and tribological properties

In this research work, we fabricated a crack–free, uniform and, mirror–like finish surface NiW coatings by using a novel derivative of propargyl compound, propargyl–oxopropane–2,3–dihydroxy, as a brightener and grain refiner into the electrodeposition bath utilizing DC and PRC waveforms. However, a precise control of W content in the coatings was achieved by applying PRC waveform in the electrodeposition bath. Controlling the W content in the coating will enable us to achieve the coating with desired mechanical and tribological properties. This study indicated that the coatings with highest mechanical and wear performance were fabricated when the W content in the coating was 32 wt%.

As well, we demonstrated that both DC and PRC electrodeposited NiW coatings revealed a significant higher resistance to pitting corrosion compared to DC and PRC deposited Ni. Furthermore, PRC electrodeposited NiW displayed the most noble corrosion potential and higher corrosion resistance compared to DC electrodeposited NiW which was attributed to the nano–crystalline structure of the PRC deposited coatings.

12.1.2 The influence of codeposition of ceramic particles on corrosion and tribological properties of NiW

In another study, the influence of incorporation of ceramic particles such as SiC and CeO_2 into NiW matrix on corrosion and tribological properties was studied. NiW–SiC, NiW–CeO_2, and NiW–SiC–CeO_2 deposits were fabricated by using DC and PRC process through applying a unique PRC waveform on electrodeposition bath chemistry containing specially selected ingredients. It was found that the incorporating of CeO_2 and SiC ceramic particles within the NiW matrix enhanced the corrosion and wear performance of the deposits and PRC–NiW–SiC–CeO_2 possessed superior corrosion and wear performance compared to the DC and PRC electrodeposited NiW, NiW–CeO_2, and NiW–SiC coatings.

Finally, the influence of hBN on corrosion and tribological performances of DC–NiW and DC–NiW–SiC was investigated. We found that hBN had a significant influence on the corrosion performance of NiW and NiW–SiC coatings by shifting the corrosion potential to more positive

value and lowering the corrosion current density. It was also noticed that, NiW–hBN demonstrated the lowest wear rate and coefficient of friction compared to Ni, NiW–SiC, and NiW–SiC–hBN deposits.

CHAPTER 13 CONCLUSION AND RECOMMANDATIONS

13.1 Conclusions

Various coatings of Ni, NiW, and NiW reinforced SiC, CeO_2, and hBN were successfully fabricated on brass substrates by applying DC and PRC currents on electrodeposition bath chemistry formulated with specially selected ingredients.

It was found that the tungsten content of the PRC–NiW deposit decreased with the increase in current density and duration of the reversed portion of the applied pulsed reverse current waveform. As well, the increase in bath temperature, increased the W content of the electrodeposited material. It was also found that the increase in W content resulted in the increase in hardness and wear resistance of the PRC–NiW deposit. The increase in hardness and wear resistance was attributed to decrease of grain size due to segregation of the tungsten atoms to grain boundaries of nickel matrix. It was also revealed that, the PRC–NiW–SiC possessed a lower coefficient of friction compared to the DC–NiW, PRC–NiW, and DC–NiW–SiC deposits.

We also investigated the mechanical properties of DC and PRC electrodeposited NiW using nano–indentation techniques. The average modulus for both DC and PRC deposited NiW were found to be similar but the average hardness of samples from DC deposited NiW was slightly higher than those of PRC deposited NiW. This is possibly due to the higher W content in the DC–NiW coating (35 wt.%) compared to that of PRC–NiW (25 wt.%) reported by EDS results. A relationship between the corrosion resistance and the materials microstructure and chemical composition was shown.

Incorporation of CeO_2, SiC, and h–BN ceramic particles within the NiW matrix enhanced the corrosion performance of the NiW coating. Several sets of experiments were performed to investigate the corrosion performance of the NiW coatings reinforced with CeO_2, SiC, and hBN ceramic particles. In the first set of experiment, from the results of PP test, it is concluded that the incorporation of SiC into the alloy matrix, significantly increased the corrosion resistance of the coatings and NiW–SiC composites deposited by PRC waveform had the highest corrosion resistance among all other DC deposited Ni, NiW, NiW–SiC and PRC deposited Ni and NiW coatings. The improvement in corrosion resistance is attributed to the SiC particles acting as physical barriers to initiation and development of defects such as crevices, gaps and micron holes in the composite coatings. SiC particles were also evenly distributed in the alloy

matrix and shifted the corrosion potential of the composite coatings to more positive values resulting in restriction of localized corrosion. It was also observed that, the coatings prepared using PRC, exhibited outstanding corrosion resistance when exposed to corrosive liquid compared to that of DC waveform. In another set of experiment, it was revealed that reinforcement of CeO_2 within NiW–SiC significantly improved the corrosion performance of the coating and PRC–NiW–SiC–CeO_2 exhibited the highest corrosion performance compared to DC deposited Ni, NiW, NiW–SiC, NiW–SiC–CeO_2 and PRC deposited Ni, NiW, NiW–SiC. Potentiodynamic polarization results revealed that, all coatings experience an active–passive transition, and a relatively small passive range are observed which is due to slightly defective passive film.

Following the PP tests, the optical micrographs were taken from the corroded surfaces of the DC–Ni, DC–NiW, DC–NiW–SiC, DC–NiW–SiC–CeO_2 and PRC–Ni, PRC–NiW, PRC–NiW–SiC, PRC–NiW–SiC–CeO_2 and it was found that DC–Ni deposit was completely corroded and pulled off the surface, whereas the surface of DC and PRC–NiW showed significantly small discoloration. The surface of DC deposited NiW–SiC, NiW–SiC–CeO_2 and PRC deposited NiW–SiC, NiW–SiC–CeO_2 deposit were remained almost unaffected after the PP test.

The corrosion potential obtained from CPP graphs for DC–Ni, DC–NiW, PRC–Ni, and PRC–NiW were increased towards less anodically active (i.e. nobler) region as follows: DC–Ni < DC–NiW < PRC–Ni < PRC–NiW. As well, CPP graphs showed that the difference between Ep and Erep for DC and PRC–NiW–SiC–CeO_2 deposit was smaller compared to other DC and PRC deposited coatings. In other words, the NiW–SiC–CeO_2 displayed higher pitting resistance compared to Ni deposit.

It was speculated that the difference in grain structures of DC–NiW and PRC–NiW resulting from the applied current waveforms (DC and PRC) were mainly responsible for different corrosion behaviors. The pulse reverse current waveform produced grains in nanometer sizes whereas the deposits formed by applying DC displayed amorphous structure.

Finally, in the last set of experiment, various coatings of DC–NiW reinforced SiC and h–BN were successfully fabricated on brass substrates. The influence of hBN on corrosion performance of the DC deposited NiW and NiW–SiC was investigated. It was found that, DC–NiW–hBN exhibited nobler corrosion potential compared to NiW. Furthermore, DC–NiW–hBN and DC–NiW–SiC–hBN had similar corrosion potentials. However, DC–NiW–hBN

exhibited lower corrosion current density compared to the DC–NiW–hBN–SiC coating. This was attributed to the chemical inert propertied of the h–BN particles.

In order to study the possible corrosion products formed on the surface of deposits and to obtain information about the species responsible for corrosion behaviors observed during the PP tests, TOFF–SIMS spectra was taken from the surface of DC and PRC deposited Ni, NiW, and NiW–SiC coatings before and after PP tests. In DC and PRC deposited Ni, the nickel layer was completely removed after the PP test and the surface of substrate was exposed. However, in the case of DC–NiW deposit, the Ni layer was not completely removed after the PP test and no exposure of substrate was realized (i.e., no peaks related to Cu and Zn are seen).

Similar observations were noticed for the DC–NiW–SiC and PRC–NiW–SiC deposits. However, in the latter deposits, new positively charged species were observed. These new species were more likely related to oxidation of SiC during the PP test. The oxide form of silicon species might be responsible for further surface passivation and the observed improvement in corrosion resistance of the DC and PRC–NiW–SiC composites compared to DC–NiW deposit. As well, it was found that most of the tungsten containing species was based on the higher oxidation states of tungsten in the case of PRC electrodeposited NiW–SiC. This explains better corrosion performance of PRC deposited NiW–SiC compared to DC deposited NiW–SiC.

The corrosion potential obtained from CPP graphs for DC deposited Ni, NiW, NiW–SiC, NiW–SiC–CeO_2 and PRC deposited Ni, NiW, NiW–SiC, NiW–SiC–CeO_2 were increased towards less anodically active (i.e. nobler) region as follows: DC–Ni < DC–NiW < PRC–Ni < PRC–NiW < DC–NiW–SiC < PRC–NiW–SiC < DC–NiW–SiC–CeO_2 < PRC–NiW–SiC–CeO_2. As well, CPP graphs showed that the difference between Ep and Erep for DC and PRC–Ni deposit was the largest among all coatings. In other words, the NiW–SiC–CeO_2 displayed higher pitting resistance compared to among all coatings.

In order to confirm the TOF–SIMS results and to measure, and compare the surface chemical composition and element valence state before and after the PP test, XPS spectra was taken from the surfaces of PRC deposited Ni, NiW, and NiW–SiC coatings. Results demonstrated that, in all the XPS spectras, the metallic Ni peaks after the pp test were disapeared and other peaks such as NiO, $NiWO_4$, NiOOH, and Ni $(OH)_2$ became more intense and visible. XPS spectra from the surface of NiW–SiC also confirmed the formation of $NiWO_4$ and SiO_2 barrier layers, which could possibly protect the coatings against corrosion.

XRD results were also taken from the surfaces of as–deposited and heat–treated PRC electrodeposited Ni, NiW, NiW–SiC, and PRC–NiW–CeO_2 at 350^{o}C, and 500^{o}C on brass substrate. It was found that the intensity of the peaks and the average crystallite size increased with increase of the annealing temperature. However, in the case of the PRC–NiW–SiC, further increase of the annealing temperature from 350^{o}C up to 500^{o}C did not have any effect on the average grain size of the Ni.

In the tribological section of the experiments, the influence of the current waveform (DC and PRC) on nano–hardness, elastic modulus, and friction coefficient of NiW coating was investigated. The average hardness of DC–NiW was slightly higher than that of PRC–NiW. However, the elastic modulus of the both coatings was approximately similar with increase of the loading rate. It was also revealed that, the DC and PRC–NiW–SiC–CeO_2 possessed a lower coefficient of friction compared to the DC and PRC deposited NiW, NiW–SiC, NiW–CeO_2 deposits due to the reduction of the contact between the Al_2O_3 ball and metal matrix.

Furthermore, influence of hBN on tribological performance of DC deposited NiW and NiW–SiC were investigated. Among all, DC–NiW–hBN exhibited the lowest friction of coefficient and wear rate.

13.2 Recommendations

This thesis primarily focuses on developing high corrosion and wear protective NiW coatings with their composites by controlling the composition and structure of the coatings by applying a well–designed PRC waveform on an electrodeposition bath containing specially selected ingredients. It provides guidelines for controlling the composition, structure, and accordingly the coating properties, which may be of great interest in many industrial applications such as automotive, aerospace, mining, etc.

It is speculated that improving control over the size of reinforcing particles could lead to uniform distribution of particles within the NiW matrix and thus enhances the corrosion and tribological performances of the coatings. This can be attributed to the formation of a uniform and compact passive layer on the surface of the coating after exposure to the corrosive environment.

It is also noteworthy to mention that, the type of current and co-depositing of NiW with ceramic particles could highly affect the grain structure and thus the properties of the coatings.

Therefore, it is suggested to further study the influence of these particles and the type of current on the grain structure of the NiW using characterization techniques such as TEM.

NiCu alloys are amongst the most corrosion-resistant materials, especially in seawater environments. The high corrosion performance of these coatings can be attributed to the formation of an adherent and stable protective passive layer on the underlying metal by the added alloying element. It is suggested to make a comparison between the corrosion performance of this coating material and NiW composite coatings.

REFERENCE

[1] M. H. Allahyarzadeh, M. Aliofkhazraei, A. R. Rezvanian, V. Torabinejad, and A. R. Sabour Rouhaghdam, "Ni-W electrodeposited coatings: Characterization, properties and applications," vol. 307, p. 978-1010, 2016, 978.

[2] S. Whang, "Nanostructured metals and alloys. Woodhead Publ Ltd," éd: Oxford, 2011.

[3] S. Wang, C. Ma, and F. Walsh, "Alternative tribological coatings to electrodeposited hard chromium: a critical review," vol. 98, no. 4, p. 173-185, 2020.

[4] W. Giurlani, G. Zangari, F. Gambinossi, M. Passaponti, E. Salvietti, F. Di Benedetto, S. Caporali, and M. Innocenti, "Electroplating for decorative applications: Recent trends in research and development," vol. 8, no. 8, p. 260, 2018.

[5] K. L. Cwalina, C. Demarest, A. Gerard, and J. Scully, "Revisiting the effects of molybdenum and tungsten alloying on corrosion behavior of nickel-chromium alloys in aqueous corrosion," vol. 23, no. 3, p. 129-141, 2019.

[6] N. P. Wasekar, S. M. Latha, M. Ramakrishna, D. S. Rao, and G. Sundararajan, "Pulsed electrodeposition and mechanical properties of Ni-W/SiC nano-composite coatings," vol. 112, p. 140-150, 2016, 140.

[7] A. Younis, D. Chu, and S. Li, "Cerium oxide nanostructures and their applications," vol. 3, p. 53-68, 2016.

[8] C. H. Huang, "A study of the effects of diammonium citrate on electroformed nickel-tungsten alloy," Plating and Surface Finishing (1997) 62–65.

[9] W. Sassi, L. Dhouibi, P. Berçot, M. Rezrazi, and E. Triki, "Comparative study of protective nickel–tungsten deposit behavior obtained by continuous and pulsed currents from citrate–ammonia media," vol. 206, no. 19-20, p. 4235-4241, 2012.

[10] S. Chhangani, and M. Prasad, "Microstructure, texture and tensile behavior of pulsed electrodeposited Ni–Al composites produced using organic additive-free sulfamate bath loaded with Al nanoparticles," vol. 136, p. 247-256, 2018.

[11] K. H. Hou, H. H. Sheu, and M. D. Ger, "Preparation and wear resistance of electrodeposited Ni–W/diamond composite coatings," vol. 308, p. 372-379, 2014.

[12] I. Matsui, A. Watanabe, T. Uesugi, N. Omura, Y. Takigawa, and T. Yamamoto, "Mechanical properties and microstructures after abnormal grain growth in electrodeposited Ni–W alloys," vol. 8, p. 100481, 2019.

[13]T. Yamasaki, M. Yamada, H. Adachi, T. Nabeshima, and Y. Yokoyama, "Nano-microscale moulding of some metal plates with high strength Ni–W alloy moulds," vol. 20, no. 10, p. 1941-1948, 2014.

[14] Y. Boonyongmaneerat, K. Saengkiettiyut, S. Saenapitak, and S. Sangsuk,, "Effects of WC addition on structure and hardness of electrodeposited Ni–W," vol. 203, no. 23, p. 3590-3594, 2009.

[15] A. Chianpairot, G. Lothongkum, C.A. Schuh, and Y. Boonyongmaneerat, "Corrosion of nanocrystalline Ni–W alloys in alkaline and acidic 3.5 wt.% NaCl solutions," vol. 53, no. 3, p. 1066-1071, 2011.

[16] M. Obradović, R. M. Stevanović, and A. R. Despić, "Electrochemical deposition of Ni–W alloys from ammonia–citrate electrolyte," vol. 552, p. 185-196, 2003.

[17] V. Singh, L. Singh, and P. Tikoo, "Studies on Electrodeposition of Nickel-Cobalt-Tungsten Alloys," vol. 127, no. 3, p. 590, 1980.

[18] L. Namburi, "Electrodeposition of NiW alloys into deep recesses," 2001.

[19] B. Li, W. Zhang, W. Zhang, and Y. Huan, "Preparation of NiW/SiC nanocomposite coatings by electrochemical deposition," vol. 702, p. 38–50, 2017, 38.

[20] R. Xu, J. Wang, L. He, and Z. Guo, "Study on the characteristics of Ni–W–P composite coatings containing nano-SiO_2 and nano-CeO_2 particles," vol. 202, no. 8, p. 1574-1579, 2008.

[21] B. Li, W. Zhang, D. Li, and J. Wang, "Electrodeposition of NiW/ZrO_2 nanocrystalline film reinforced by CeO_2 nanoparticles: Structure, surface properties and corrosion resistance," vol. 229, p. 495-507, 2019.

[22] Y. Boonyongmaneerat, K. Saengkiettiyut, S. Saenapitak, and S. Sangsuk, "Pulse co-electrodeposition and characterization of NiW–WC composite coatings," vol. 506, no. 1, p. 151-154, 2010.

[23] M. K. Das, J. Qin, and P. Karn, "Effect of diamond particles on the microstructure and composition of pulse plated multilayer Ni-W/diamond composite coatings," communication présentée à MATEC Web of Conferences, 2019, p. 03002.

[24] M. Allahyarzadeh, M. Aliofkhazraei, A. S. Rouhaghdam, V. Torabinejad, H. Alimadadi, and A. Ashrafi, "Electrodeposition mechanism and corrosion behavior of multilayer nanocrystalline nickel-tungsten alloy," vol. 258, p. 883-899, 2017.

[25] E. Beltowska-Lehman, P. Indyka, A. Bigos, M. Kot, and L. Tarkowski, "Electrodeposition of nanocrystalline Ni–W coatings strengthened by ultrafine alumina particles," vol. 211, p. 62-66, 2012.

[26] K. H. Hou, H. H. Sheu, and M. D. Ger, "Preparation and wear resistance of electrodeposited Ni–W/diamond composite coatings," vol. 308, p. 372-379, 2014.

[27] P. Indyka, E. Beltowska-Lehman, and A. Bigos, "Microstructural characterization of electrodeposited coatings of metal matrix composite with alumina nanoparticles," vol. 32, 2012, 012010.

[28] D. Vroulias, N. Gkoulemani, C. Papadopoulou, and H. Matralis, "W–modified Ni/Al_2O_3 catalysts for the dry reforming of methane: Effect of W loading," vol. 355, p. 704–715, 2020, 704.

[29] Y. Fan, Y. He, P. Luo, T. Shi, and X. Chen, "Pulse current electrodeposition and properties of Ni-W-GO composite coatings," vol. 163, no. 3, p. D68, 2015.

[30] C. K. Sarangi, B. P. Sahu, B. K. Mishra, and R. Mitra, "Pulse electrodeposition and characterization of graphene oxide particle-reinforced Ni–W alloy matrix nanocomposite coatings," vol. 50, no. 2, p. 265-279, 2020.

[31] X. H. Zhang, X. X. Li, W. J. Liu, Y. Q. Fan, H. Chen, and T. X. Liang, "Preparation and tribological behavior of electrodeposited Ni–W–GO composite coatings," vol. 38, no. 7, p. 695–703, 2018, 695.

[32] T. He, Y. He, H. Li, Z. Su, Y. Fan, and Z. He, "Fabrication of Ni-W-B_4C composite coatings and evaluation of its micro-hardness and corrosion resistance properties," vol. 44, no. 8, p. 9188-9193, 2018.

[33] M.G. Hosseini, H. Teymourinia, A. Farzaneh, and S. Khameneh-asl, "Evaluation of corrosion, mechanical and structural properties of new Ni–W–PCTFE nanocomposite coating," vol. 298, p. 114–120, 2016, 114.

[34] S. Dilek, H. Algül, A. Akyol, A. Alp, H. Akbulut, and M. Uysal, "Pulse electro co-deposition of submicron-sized TiC reinforced Ni–W coatings: tribological and corrosion properties," p. 1–13, 2021, 1.

[35] S. Mbugua Nyambura, M. Kang, J. Zhu, Y. Liu, Y. Zhang, and N. J. Ndiithi,, "Synthesis and characterization of Ni–W/Cr_2O_3 nanocomposite coatings using electrochemical deposition technique," vol. 9, no. 12, p. 815, 2019.

[36] W. Sassi, L. Dhouibi, P. Berçot, M. Rezrazi, and E. Triki, "Study of the electroplating mechanism and physicochemical proprieties of deposited Ni-W-Silicate composite alloy," vol. 117, p. 443-452, 2014.

[37] K. Harachai, N. Kothanam, J. Qin, Y. Boonyongmaneerat, and P. Jaroenapibal, "Hardness and tribological properties of co-electrodeposited Ni-WB/B coatings," vol. 402, p. 126313, 2020.

[38] J. Qin, "Electrodeposition and Mechanical Properties of NiW Matrix Composite Coatings with Embedded Amorphous Boron Particles," p. 9529–9541, 2016, 9529.

[39] Y. Fan, Y. He, P. Luo, T. Shi, and H. Li, "Pulse current electrodeposition and characterization of Ni-W-MWCNTs nanocomposite coatings," vol. 162, no. 7, p. D270, 2015.

[40] T. He, Y. He, H. Li, Y. Fan, Q. Yang, and Z. He, "A comparative study of effect of mechanical and ultrasound agitation on the properties of pulse electrodeposited Ni-W/MWCNTs composite coatings," vol. 743, p. 63-72, 2018.

[41] B. Li, D. Li, T. Mei, W. Xia, and W. Zhang, "Fabrication and characterization of boron nitride reinforced Ni–W nanocomposite coating by electrodeposition," vol. 777, p. 1234–1244, 2019, 1234.

[42]B. Li, W. Zhang, D. Li, Y. Huan, and J. Dong, "Microstructural, surface and electrochemical properties of pulse electrodeposited NiW/Si3N4 nanocomposite coating," vol. 44, no. 16, p. 19907–19918, 2018, 19907.

[43] W. Zhang, Q. Fu, Z. Shi, C. Ji, B. Li, and H. Chu, "Microstructure, surface characteristics and properties of Ni–W composite coatings reinforced by nanoparticles fabricated by electrodeposition route," vol. 9, no. 1, p. 015010, 2021.

[44] E. Beltowska-Lehman, A. Bigos, P. Indyka, A. Chojnacka, A. Drewienkiewicz, S. Zimowski, M. Kot, and M. J. Szczerba, "Optimization of the electrodeposition process of Ni-W/ZrO_2 nanocomposites," vol. 813, p. 39–51, 2018, 39.

[45] E. Beltowska-Lehman, P. Indyka, A. Bigos, M. J. Szczerba, J. Guspiel, H. Koscielny, and M. Kot, "Effect of current density on properties of Ni–W nanocomposite coatings reinforced with zirconia particles," vol. 173, p. 524–533, 2016, 524.

[46] E. Beltowska-Lehman, P. Indyka, A. Bigos, M. J. Szczerba, and M. Kot, "Ni–W/ZrO_2 nanocomposites obtained by ultrasonic DC electrodeposition," vol. 80, p. 1-11, 2015.

[47] B. Li, D. Li, T. Mei, and W. Zhang, "Fabrication and optimization of Ni-W/ZrO_2-CeO_2 composite coating for enhanced hardness and corrosion resistance," vol. 13, p. 102375, 2019.

[48] B. Li, D. Li, J. Zhang, W. Chen, and W. Zhang, "Preparation of Ni-W nanocrystalline composite films reinforced by embedded zirconia ceramic nanoparticles," vol. 114, p. 138-147, 2019.

[49] S. Shajahan, and A. Basu, "Corrosion, oxidation and wear study of electro-co-deposited ZrO_2-TiO_2 reinforced Ni-W coatings," vol. 393, p. 125729, 2020.

[50] W. Zhang, C. Ji, and B. Li, "Synthesis and properties of Ni–W/ZrO_2 nanocomposite coating fabricated by pulse electrodeposition," vol. 13, p. 102242, 2019.

[51] J. A. M. Oliveira, A. F. de Almeida, A. R. N. Campos, S. Prasad, J. J. N. Alves, and R. A. C. de Santana, "Effect of current density, temperature and bath pH on properties of Ni–W–Co alloys obtained by electrodeposition," vol. 853, p. 157104, 2021.

[52] D. G. Portela, T. C. de Morais Nepel, J. M. Costa, and A. F. de Almeida Neto, "Two-stages electrodeposition for the synthesis of anticorrosive Ni–W-Co coating from a deactivated nickel bath," vol. 260, p. 114611, 2020.

[53] D. G. Portela, M. B. Porto, and A. F. de Almeida Neto, "Parameters variation on Ni–Co–W coating electroplating to evaluate improvements in morphology and corrosion resistance," vol. 41, no. 12, p. 1-9, 2019.

[54] P. Bacal, M. Donten, and Z. Stojek, "Electrodeposition of high-tungsten W-Ni-Cu alloys. Impact of copper on deposition process and coating structure," vol. 241, p. 449-458, 2017.

[55] B. Li, and W. Zhang, "Microstructural, surface and electrochemical properties of pulse electrodeposited Ni–W/Si_3N_4 nanocomposite coating," vol. 44, no. 16, p. 19907-19918, 2018.

[56] W. Zhang, B. Li, and C. Ji, "Synthesis and characterization of Ni-W/TiN nanocomposite coating with enhanced wear and corrosion resistance deposited by pulse electrodeposition," vol. 45, no. 11, p. 14015-14028, 2019.

[57] B. Li, D. Li, J. Zhang, W. Chen, and W. Zhang, "Electrodeposition of NiW/TiN–Y_2O_3 nanocrystalline coating and investigation of its surface properties and corrosion resistance," vol. 787, p. 952-962, 2019, 952.

[58] R. Zhang, Z. Li, X. Yu, and G. Cui, "Characterisation and properties of Ni–W–Y_2O_3–ZrO_2 nanocomposite coating," vol. 35, no. 7, p. 578-587, 2019.

[59] A. Farzaneh, M. G. Hosseini, S. K. Asl, and O. Mermer, "Electrochemical, structural and nano tribological behavior of Ni-W-PTFE nanocomposite coatings prepared by tartrate bath," vol. 11, p. 5140-5153, 2016.

[60] L. Ren, Y. Cheng, Q. Wang, and J. Yang, Surface, "Study on the properties of Ni-WP coating with PTFE co-deposition," vol. 7, no. 4, p. 045009, 2019.

[61] S. Sangeetha, G. P. Kalaignan, and J. T. Anthuvan, "Pulse electrodeposition of self-lubricating Ni–W/PTFE nanocomposite coatings on mild steel surface," vol. 359, p. 412-419, 2015.

[62] P. Odetola, P. Popoola, O. Popoola, and D. Delport,, "Parametric Variables in Electro-deposition of Composite Coatings," dans Electrodeposition of Composite Materials, 2016.

[63] Q. J. Wang, and Y. W. Chung, Encyclopedia of tribology: Springer US, 2013.

[64] C. Low, R. Wills, and F. Walsh, "Electrodeposition of composite coatings containing nanoparticles in a metal deposit," vol. 201, no. 1-2, p. 371-383, 2006.

[65] S. H. Whang, "Nanostructured Metals and Alloys," p. 1–804, 201.

[66] F. Walsh, and C. Ponce de Leon, "A review of the electrodeposition of metal matrix composite coatings by inclusion of particles in a metal layer: an established and diversifying technology," vol. 92, no. 2, p. 83-98, 2014.

[67] E. P. Schmitz, S. P. Quinaia, J. R. Garcia, C. K. de Andrade, and M. C. Lopes, "Influence of commercial organic additives on the nickel electroplating," vol. 11, no. 1, p. 983-997, 2016.

[68] E. Pavlatou, M. Stroumbouli, P. Gyftou, and N. Spyrellis, "Hardening effect induced by incorporation of SiC particles in nickel electrodeposits," vol. 36, no. 4, p. 385-394, 2006.

[69] I. Tudela, Y. Zhang, M. Pal, I. Kerr, and A. J. Cobley, "Ultrasound-assisted electrodeposition of composite coatings with particles," vol. 259, p. 363-373, 2014.

[70] Y. Zhou, F. Xie, X. Wu, W. Zhao, and X. Chen, "A novel plating apparatus for electrodeposition of Ni-SiC composite coatings using circulating-solution co-deposition technique," vol. 699, p. 366-377, 2017.

[71] S. Dehgahi, R. Amini, and M. Alizadeh, "Microstructure and corrosion resistance of Ni-Al_2O_3-SiC nanocomposite coatings produced by electrodeposition technique," vol. 692, p. 622-628, 2017.

[72] S. P. Devaneyan, and T. Senthilvelan, "Electro co-deposition and characterization of SiC in nickel metal matrix composite coatings on aluminium 7075," vol. 97, p. 1496-1505, 2014.

[73] P. Gyftou, E. Pavlatou, and N. Spyrellis, "Effect of pulse electrodeposition parameters on the properties of Ni/nano-SiC composites," vol. 254, no. 18, p. 5910-5916, 2008.

[74] E. Rudnik, L. Burzyńska, Ł. Dolasiński, and M. Misiak, "Electrodeposition of nickel/SiC composites in the presence of cetyltrimethylammonium bromide," vol. 256, no. 24, p. 7414-7420, 2010.

[75] F. Danilov, Y. E. Sknar, I. Tkach, and I. Sknar, "Electrodeposition of nickel-based nanocomposite coatings from cerium (III)-ion-containing methanesulfonate electrolytes," vol. 51, no. 4, p. 294-298, 2015.

[76] M.G. Hosseini, M. Abdolmaleki, and J. Ghahremani, "Investigation of corrosion resistance of electrodeposited NiW/SiC composite coatings," vol. 49, p. 247–253, 2013, 247.

[77] M. H. Allahyarzadeh, M. Aliofkhazraei, A.S. Rouhaghdam, V. Torabinejad, H. Alimadadi, and A. Ashrafi, "Electrodeposition mechanism and corrosion behavior of multilayer nanocrystalline nickel-tungsten alloy," vol. 258, p. 883-899, 2017.

[78] A. Karimzadeh, M. Aliofkhazraei, and F.C. Walsh, "A review of electrodeposited Ni-Co alloy and composite coatings: Microstructure, properties and applications," vol. 372, p. 463–498, 2019.

[79] A. Lelevic, and F.C. Walsh, "Electrodeposition of Ni–P alloy coatings: A review," vol. 369, p. 198-220, 2019.

[80] K. Ahmadi, N. Dole, O. Karadavut, F.C.R. Hernandez, T.D. Hall, E.J. Taylor, and S.R. Brankovic, "Crack Free Cr Coatings from Cr^{3+} Electrolyte," vol. 169, no. 1, 2022, 012504.

[81] A. Joseph, B. Kirubasankar, A.M. Mathew, M. Narayanasamy, C. Yan, and S. Angaiah, "Influence of pulse reverse current parameters on electrodeposition of copper-graphene nanocomposite coating," vol. 5, 2021.

[82] Z. Mahidashti, M. Aliofkhazraei, and N. Lotfi, "Review of nickel-based electrodeposited tribo–coatings, Transactions of the Indian Institute of Metals," vol. 71, p. 257–295, 2018.

[83] S. Esmailzadeh, M. Aliofkhazraei, and H. Sarlak, "Interpretation of Cyclic Potentiodynamic Polarization Test Results for Study of Corrosion Behavior of Metals: A Review," vol. 54, no. 5, p. 976-989, 2018, 976.

[84] A. Amadeh, A. Rahimi, B. Farshchian, and H. Moradi, "Corrosion behavior of pulse electrodeposited nanostructure Ni-SiC composite coatings," vol. 10, no. 8, p. 5383-8, 2010.

[85] N. S. Mbugua, M. Kang, Y. Zhang, N. J. Ndiithi, G. V. Bertrand, and L. Yao, "Electrochemical deposition of Ni, NiCo alloy and NiCo–ceramic composite coatings—A critical review," vol. 13, no. 16, p. 3475, 2020.

[86] B. Szczygieł, and M. Kołodziej, "Composite Ni/Al_2O_3 coatings and their corrosion resistance," vol. 50, no. 20, p. 4188-4195, 2005.

[87] Q. Sun, and K. Chen, "Inflection of backward sweep of cyclic polarization curve: Pit transition potential Eptp," vol. 69, no. 12, p. 1729-1740, 2018, 1729.

[88] G. Frankel, "Pitting corrosion of metals: a review of the critical factors," vol. 145, no. 6, p. 2186, 1998.

[89] N. P. Wasekar, N. Hebalkar, A. Jyothirmayi, B. Lavakumar, M. Ramakrishna, and G. Sundararajan, "Influence of pulse parameters on the mechanical properties and electrochemical corrosion behavior of electrodeposited Ni-W alloy coatings with high tungsten content," vol. 165, p. 108409, 2020.

[90] K. R. Sriraman, S. Ganesh Sundara Raman, and S. K. Seshadri, "Corrosion behaviour of electrodeposited nanocrystalline Ni–W and Ni–Fe–W alloys," vol. 460-461, p. 39-45, 2007, 39.

[91] H. Alimadadi, M. Ahmadi, M. Aliofkhazraei, and S.R. Younesi, "Corrosion properties of electrodeposited nanocrystalline and amorphous patterned NiW alloy," vol. 30, no. 4, p. 1356–1361, 2009.

[92] F. Z. Yang, Y. F. Guo, L. Huang, S. K. Xu, and S. M. Zhou, "Electrodeposition, structure and corrosion resistance of nanocrystalline Ni-W alloy," vol. 22, no. 3, p. 228–231, 2004.

[93] L. Elias, and A.C. Hegde, "Electrodeposition of laminar coatings of Ni–W alloy and their corrosion behaviour," vol. 283, p. 61-69, 2015.

[94] P. Indyka, E. Beltowska-Lehman, L. Tarkowski, A. Bigos, and E. García-Lecina, "Structure characterization of nanocrystalline NiW alloys obtained by electrodeposition," vol. 590, p. 75–79, 2014.

[95] Y. Yao, S. Yao, and L. Zhang, "Corrosion behavior of Ni–W/SiC nanocomposite coating in NaCl solution," vol. 13, no. 04, p. 489-494, 2006.

[96] Y. Wu, D. y. Chang, D. s. Kim, and S. c. Kwon, "Effects of 2–butyne-1, 4–diol on structures and morphologies of electroplating NiW alloy," vol. 162, no. 2–3, p. 269–275, 2003.

[97] E. Broitman, "Indentation Hardness Measurements at Macro-, Micro-, and Nanoscale: A Critical Overview," vol. 65, p. 23, 12/28 2016.

[98] T. He, Y. He, H. Li, Z. Su, Y. Fan, and Z. He, "Fabrication of Ni-W-B4C composite coatings and evaluation of its micro-hardness and corrosion resistance properties," vol. 44, no. 8, p. 9188-9193, 2018.

[99] Z. Zhang, and D. Chen, "Contribution of Orowan strengthening effect in particulate-reinforced metal matrix nanocomposites," vol. 483, p. 148-152, 2008.

[100] C. Zhao, Y. Yao, and L. He, "Electrodeposition and characterization of NiW/ZrO_2 nanocomposite coatings," Vol. 37, no. 5, p. 1053–1058, 2014.

[101] S. Xing, L. Wang, C. Jiang, H. Liu, W. Zhu, and V. Ji, Vacuum, "Influence of Y_2O_3 nanoparticles on microstructures and properties of electrodeposited Ni–W–Y_2O_3 nanocrystalline coatings," vol. 181, p. 109665, 2020.

[102] K. H. Hou, H. H. Sheu, and M. D. Ger, "Preparation and wear resistance of electrodeposited Ni–W/diamond composite coatings," vol. 308, p. 372-379, 2014.

[103] D. K. Singh, M. K. Tripathi, and V. Singh, "Electrolytic preparation of Ni-B_4C composite coating and its characterization," vol. 24, no. 3, p. 1213-1219, 2015.

[104] M.D. Ger, "Electrochemical deposition of nickel/SiC composites in the presence of surfactants," vol. 87, no. 1, p. 67–74, 2004, 67.

[105] M. Uysal, H. Algül, E. Duru, Y. Kahraman, A. Alp, and H. Akbulut, "Tribological properties of Ni–W–TiO_2–GO composites produced by ultrasonically–assisted pulse electro co–deposition," vol. 410, p. 126942, 2021.

[106] M. Allahyarzadeh, M. Aliofkhazraei, A. S. Rouhaghdam, and V. Torabinejad, "Electrochemical tailoring of ternary Ni-W-Co (Al_2O_3) nanocomposite using pulse reverse technique," vol. 705, p. 788-800, 2017.

[107] J. Chevalier, L. Gremillard, A. V. Virkar, and D. R. Clarke, "The tetragonal-monoclinic transformation in zirconia: lessons learned and future trends," vol. 92, no. 9, p. 1901-1920, 2009.

[108] B. Li, W. Zhang, D. Li, and J. Wang, "Electrodeposition of NiW/ZrO_2 nanocrystalline film reinforced by CeO_2 nanoparticles: Structure, surface properties and corrosion resistance," vol. 229, p. 495-507, 2019.

[109] Y. Boonyongmaneerat, K. Saengkiettiyut, S. Saenapitak, and S. Sangsuk, "Effects of WC addition on structure and hardness of electrodeposited Ni–W," vol. 203, no. 23, p. 3590-3594, 2009.

[110] J. Zarpellon, H. Jurca, J. Klein, W. Schreiner, N. Mattoso, and D. Mosca,, "Electrodeposition of Fe thin films on Si (1 1 1) surfaces in the presence of sodium saccharin," vol. 53, no. 4, p. 2002-2008, 2007.

[111] M. Surender, B. Basu, and R. Balasubramaniam, "Wear characterization of electrodeposited Ni–WC composite coatings," vol. 37, no. 9, p. 743-749, 2004.

[112] H. Wei, C. Wenjian, W. Shaoping, and M. M. Tomovic, "Mechanical wear debris feature, detection, and diagnosis: A review," vol. 31, no. 5, p. 867-882, 2018.

[113] J. Burwell, and C. Strang, "On the empirical law of adhesive wear," vol. 23, no. 1, p. 18-28, 1952.

[114] A. Gallegos-Melgar, S.A. Serna, I. Lázaro, E. J. Gutiérrez-Castañeda, V. Mercado-Lemus, H. Arcos-Gutierrez, M. Hernández-Hernández, J. Porcayo-Calderón, J. Mayen, and M.D.A. Monroy, "Potentiodynamic polarization performance of a novel composite coating system of Al_2O_3/chitosan-sodium alginate, applied on an aluminum AA6063 alloy for protection in a chloride Ions environment," vol. 10, no. 1, p. 45, 2020.

[115] S. O. Ekolu, S. Diop, and F. Azene, "Potentiodynamic polarization study of the corrosion characteristics of acid mine drainage," dans Construction Materials and Structures: IOS Press, 2014, p. 1436-1441.

[116] https://www.ameteksi.com.

[117] https://www.gamry.com.

[118] O. A. Rahman, N. P. Wasekar, G. Sundararajan, and A. K. Keshri, "Experimental investigation of grain boundaries misorientations and nano twinning induced strengthening on addition of silicon carbide in pulse electrodeposited nickel tungsten composite coating," vol. 116, p. 1-7, 2016.

[119] G. Guillonneau, G. Kermouche, S. Bec, and J. L. Loubet, "Determination of mechanical properties by nanoindentation independently of indentation depth measurement," vol. 27, no. 19, p. 2551–2560, 2012, 2551.

[120] S. Basu, A. Moseson, and M.W. Barsoum, "On the determination of spherical nanoindentation stress strain curves," vol. 21, no. 10, p. 2628–2637, 2011, 2628.

[121] D. J. Shuman, A. L. M. Costa, and M. S. Andrade, "Calculating the elastic modulus from nanoindentation and microindentation reload curves," vol. 58, no. 4, p. 380-389, 2007, 380.

[122] H. Zhang, X. Li, W. Qian, J. Zhu, B. Chen, J. Yang, and Y. Xia, "Characterization of mechanical properties of epoxy/nanohybrid composites by nanoindentation," vol. 9, no. 1, p. 28-40, 2020.